

**New insight in structure-function relations of
water-oxidising cobalt and nickel oxides by
electrochemistry combined with X-ray absorption
spectroscopy**

by

Katharina Klingan

A dissertation submitted to the Physics Department of
Freie Universität Berlin for the degree of

Dr. rer. nat.



Berlin, December 2015

New insight in structure-function relations of water-oxidising cobalt and nickel oxides by electrochemistry combined with X-ray absorption spectroscopy

Katharina Klingan

Department of Experimental Physics, Freie Universität Berlin

First advisor: Prof. Holger Dau

Second advisor: Prof. Christian Limberg

Date of defense: 2016/02/04

Abstract

To understand how structure and function are correlated within amorphous and heterogeneous water oxidation catalysts is of general importance for progress in solar fuel production. Catalysts based on earth-abundant cobalt oxide or nickel oxide electrodeposited as thin films on inert electrodes are studied herein. The structural aspect is investigated by X-ray absorption spectroscopy at synchrotrons and the functional side is addressed by electrochemical techniques.

In this thesis, it is proposed that within the same transition metal catalyst, volume or surface catalysis may occur simultaneously. Both modes of catalysis are essential for an extensive understanding of heterogeneous water oxidation. At very low amounts of deposited cobalt oxide ($< 20 \text{ nmol Co cm}^{-2}$) surface catalysis prevails indicated by an improved relative rate of catalysis. This mode of surface catalysis points to the possibility of a relevant improvement of the rate of catalysis of the CoCat (cobalt-based oxide catalyst) at surface exposed sites or domains. Atomic defects are introduced in these films, as they can be described as catalysts with less ordered oxide layers and/or smaller oxide fragments. Above $20 \text{ nmol Co cm}^{-2}$ catalysis of water oxidation occurs within the bulk volume of the hydrated oxide film, at the margins of cobalt oxide fragments of molecular dimensions. At high current densities, the availability of a proton-accepting base at the catalyst–electrolyte interface controls the rate of water oxidation. The reported findings may be of general relevance for water oxidation catalysed at moderate pH by amorphous transition-metal oxides. Volume activity happens by catalysis at the margins of numerous oxide fragments, which together with an intercalated quasi-electrolyte constitute the bulk catalyst material. It is proposed that the water oxidation volume activity of the bulk material may prevail generally in amorphous and hydrated oxides. At high overpotentials, the protonation state of the buffer base in the bulk electrolyte is a codeterminant of the catalytic rate. An increased catalyst internal proton concentration is found due to rate limitation by proton transfer to the buffer base. As opposed to classical alkaline or acidic water electrolysis, proton transfer to bases of the electrolyte buffer appears to be essential for efficient water oxidation at moderate pH.

Similar to the cobalt oxide catalyst, various oxidation states of a nickel oxide catalyst can be obtained by variation of the electric potential. In contrast to the cobalt oxide catalyst more pronounced nickel oxidation state changes and several distinctly different structures may contribute to the oxygen evolution reaction. Structural motifs consist of edge-sharing sharing NiO_6 octahedra, which are Jahn-Teller distorted at intermediate potentials. Deprotonation of di- μ -hydroxo bridges occurs during the transition from low to intermediate potentials applied to the catalyst.

Zusammenfassung

Eine nachhaltige und industrielle Erzeugung des regenerativen Kraftstoffs H_2 aus Wasser beruht unter anderem auch auf dem Verständnis des Zusammenhangs zwischen Funktionsweise und atomarer Struktur der einsetzbaren Katalysatoren. Amorphe, heterogene Katalysatoren können unter neutralen Bedingungen effizient Wasser oxidieren und dabei molekularen Sauerstoff entstehen lassen. Daher bilden solche Katalysatoren, die basierend auf Kobalt oder Nickel als dünne Filme auf inerten Elektroden elektrochemisch abgeschieden werden, den Fokus dieser Arbeit. Der Frage nach einem vertieften Einblick in Korrelationen zwischen der atomaren Anordnung und ihrer katalytischen Funktion wurde mit quantitativen und qualitativen experimentellen Untersuchungsmethoden, im Besonderen Röntgenabsorptionsspektroskopie, an Elektronenbeschleunigern (Synchrotrons) nachgegangen. Die Ergebnisse zeigen, dass in demselben Übergangsmetalloxidkatalysator Volumen- oder Oberflächenkatalyse simultan stattfinden, die Katalyse in der Volumenphase bei größeren Filmstärken aber überwiegt. Essenziell dabei ist, beide Arten der Katalyse in eine holistische Auffassung der heterogenen Katalyse zu integrieren. Bei sehr dünnen abgeschiedenen Kobaltoxidfilmen dominiert die Oberflächenkatalyse. Eine gesteigerte Katalysenrate an der Katalysatoroberfläche wird wahrscheinlich durch eine erheblich erhöhte Anzahl exponierter Seiten oder Domänen an der Oberfläche erreicht. Enthält der Katalysator mehr als 20 nmol cm^{-2} Kobalt, so erfolgt die Wasseroxidation vorrangig im gesamten Volumen des hydratisierten Oxidfilms, genauer an den Rändern von Kobaltoxidfragmenten molekularer Dimension. Bei hohen Stromdichten wird die Rate der Wasseroxidation von der Verfügbarkeit einer protonen-akzeptierenden Base an der Katalysator/Elektrolyt-Grenzfläche bestimmt. Volumenaktivität bedeutet, dass die Katalyse an den Rändern von zahlreichen Oxidfragmenten, welche zusammen mit einem zwischengelagerten Elektrolyten das *Bulk*-Katalysatormaterial bilden, stattfindet. Eine Begrenzung der Geschwindigkeit des Protonentransfers zu der Base führt zu einer erhöhten inneren Protonenkonzentration des Katalysators. Diese Erkenntnisse könnten von genereller Bedeutung für die katalysierte Wasseroxidation bei moderaten pH-Werten von amorphen Übergangsmetalloxiden sein, wobei die Volumenaktivität des *Bulk*-Materials allgemein in amorphen und hydratisierten Oxiden vorherrschen könnte. Vergleichbar mit dem Kobaltoxidkatalysator können verschiedene Oxidationszustände eines Nickeloxidkatalysators durch das Anlegen eines elektrischen Potentials erhalten werden. Der Letztere zeichnet sich durch die Fähigkeit aus, in einer größeren Spanne von Oxidationszuständen und in mehreren strukturellen Phasen im Potentialbereich der Sauerstoffentwicklungsreaktion vorzuliegen.

Table of contents

Abstract	I
Zusammenfassung	III
Glossary	IX
Chapter 1 Introduction and Motivation	1
1.1 Hydrogen fuel from water electrolysis	2
1.2 The natural and biomimetic way of water oxidation	3
1.3 Transition metal thin-film catalysts	4
1.3.1 The cobalt oxide catalyst (CoCat)	6
1.3.2 The nickel oxide catalyst (NiCat)	10
1.4 Homogenous catalysts	12
1.5 Scope and organisation of the thesis	13
Chapter 2 Volume activity of the CoCat	14
2.1 Experimental detail	16
2.1.1 Sample preparation	16
2.1.2 Total X-ray fluorescence analysis (TXRF)	17
2.1.3 Turnover frequency (TOF)	17
2.1.4 Estimation of the double-layer capacitance with impedance spectroscopy	17
2.1.5 Scanning electron microscopy (SEM)	19
2.1.6 pH titrations	19
2.1.7 X-ray absorption spectroscopy (XAS)	19
2.2 Results	21
2.2.1 Estimation of deposition charge	21
2.2.2 Estimation of reduction equivalents	23
2.2.3 Turnover frequency (TOF)	25
2.2.4 Double-layer capacitance	27
2.2.5 Scanning electron microscopy (SEM)	29
2.2.6 pH titrations	32
2.2.7 Atomic structure	35
2.3 Discussion	36
2.3.1 Outer surface versus bulk material reactivity	36
2.3.2 Noncanonical pH dependence due to electrolyte bases	38
2.3.3 Nonsaturating thickness dependence at high overpotentials	42
2.4 Summary	45

Chapter 3 Surface activity of the CoCat	46
3.1 Experimental detail	48
3.1.1 Sample preparation	48
3.1.2 X-ray absorption spectroscopy (XAS)	48
3.1.3 EXAFS simulations	49
3.2 Results	50
3.2.1 Electrochemical behaviour and redox equivalents	50
3.2.2 Turnover frequency (TOF)	52
3.2.3 Oxidation states and atomic structure	54
3.3 Discussion	58
3.4 Summary	60
Chapter 4 Calcination of the CoCat	61
4.1 Experimental detail	62
4.1.1 Sample preparation	62
4.1.2 X-ray absorption spectroscopy (XAS)	62
4.1.3 EXAFS simulations	63
4.2 Results and Discussion	64
4.2.1 Electrochemical behaviour and redox equivalents	64
4.2.2 Oxidation states	66
4.2.3 Atomic structure	69
4.2.4 Microscopical surface structure	75
4.3 Summary	76
Chapter 5 Structural integrity of a molecular cobalt-polyoxometalate	77
5.1 Experimental detail	79
5.1.1 XAS sample preparation	79
5.1.2 EXAFS simulations	82
5.1.3 UV-vis spectroscopy	82
5.2 Results	84
5.2.1 UV-vis changes	84
5.2.2 Oxidation states	87
5.2.3 Atomic structure	90
5.3 Discussion	95
5.4 Summary	96

Chapter 6 Structural and functional changes in the NiCat	97
6.1 Experimental detail	99
6.1.1 Sample preparation	99
6.1.2 Total X-ray fluorescence analysis (TXRF)	100
6.1.3 Coulometry	100
6.1.4 <i>In-situ</i> electrochemical absorption (UV-vis) changes	101
6.1.5 XAS sample preparation	101
6.1.6 XAS measurements	104
6.1.7 XAS data extraction	104
6.1.8 EXAFS simulations	106
6.2 Results	107
6.2.1 Coulometry	107
6.2.2 Electrochemical absorption changes	107
6.2.3 Electrochemical operation of the NiCat	112
6.2.4 X-ray absorption near-edge structure (XANES)	114
6.2.5 Extended X-ray absorption fine-structure (EXAFS)	119
6.3 Discussion	126
6.3.1 Structural changes by comparison with nickel (oxy)hydroxides	126
6.3.2 Electrochromism of the NiCat	129
6.3.3 Oxidation state changes	130
6.3.4 Possibility of Fe contaminations	132
6.4 Summary	133
Key results	134
References	137
List of publications	154
Selbständigkeitserklärung	157

Glossary

1	$\text{Na}_{10}[\text{Co}_4(\text{H}_2\text{O})_2(\text{PW}_9\text{O}_{34})_2]$
2	$\text{Na}_{17}[\{(\text{Co}(\text{H}_2\text{O}))\text{Co}_2\text{PW}_9\text{O}_{34}\}_2(\text{PW}_6\text{O}_{26})]$
BESSY	Berliner Elektronenspeicherring-Gesellschaft für Synchrotronstrahlung
B_i	Borate buffer pH 9.2
bpy	bpy = tris(2,20-bipyridyl)
C_H^{int}	Internal proton concentration within the catalyst
C_{DL}	Double-layer capacitance
CoCat	The cobalt oxide catalyst, deposited in KP_i (0.1 M, pH7)
CV	Cyclic voltammetry or cyclic voltammogram
DSA	Dimensionally stable anode
ε	Molar extinction coefficient
E_0	Energy shift in EXAFS simulations
EDX	Energy dispersive X-ray spectroscopy
EXAFS	Extended X-ray absorption fine-structure
FT	Fourier-transform
HEPES	2-[4-(2-hydroxyethyl)piperazin-1-yl]ethanesulfonic acid
HER	Hydrogen evolution reaction
HZB	Helmholtz-Zentrum Berlin für Materialien und Energie
ITO	Indium tin oxide
KP_i	Potassium phosphate buffer pH 7
MES	2-(N-morpholino)ethanesulfonic acid
M2P	Methyldiphosphonate
NaP_i	Sodium phosphate buffer
NHE	Normal hydrogen electrode
NiCat	The nickel oxide catalyst, deposited in B_i (0.1 M, pH 9.2)
n_M	Number of electrodeposited atoms (M= Co or Ni)
n_{red}	Number of reduced Co or Ni atoms
OER	Oxygen evolution reaction
PEIS	Potentiostatic electrochemical impedance spectroscopy
PEM	Polymer electrolyte membrane
PET	Polyethylene terephthalate
POM	Polyoxometalate
PS-II	Photosystem II
Q	Charge in general
Q_{dep}	Charge passed during electrochemical deposition
Q_{red}	Charge passed during electrochemical reduction
R_f	Fit quality of EXAFS simulations
R_X	Distance between absorbing atom and backscattering atom of element X
R_Y	Rate of Y in reaction kinetics
σ_X	Debye-Waller parameter in EXAFS simulations
S_0^2	Amplitude reduction factor in EXAFS simulations
SEM	Scanning electron microscopy
TOF	Turnover frequency
TRIS	2-amino-2-hydroxymethyl-propane-1,3-diol
TXRF	Total reflection X-ray fluorescence
WOC	Water oxidation catalyst
XANES	X-ray absorption near-edge structure
XAS	X-ray absorption spectroscopy
XRD	X-ray diffraction

*Chapter 1***Introduction and Motivation**

The common method of production is *inter alia* characterised by the destruction of its own requirements; most prominently as capital is dependent on labour power for the accumulation of value and has the tendency to supersede the same productive labour power by perpetually decreasing the number of workers (Marx 2008 (1876), Kurz 2012). The constant consumption of primary raw materials and fossil fuels (Armaroli and Balzani 2007) is a related constituent for a high-tech economy and an everyday life that is exclusively based on fuels. Thus, drawing on the primary natural resources beyond its regenerative capacity results in exhaustion. Already in 1999, humanity's demand for natural capital lay over 120 % the capacity of the global biosphere (Wackernagel, Schulz et al. 2002).

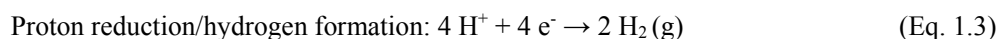
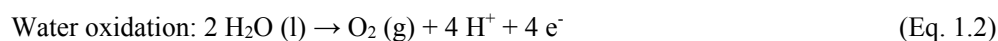
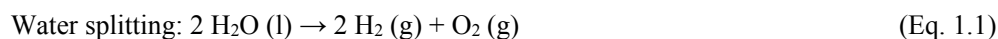
In 2007, on average 1000 barrels of oil a second were consumed and a steady of 13 trillion watts of power demand was necessary to perpetuate global economy (Armaroli and Balzani 2007). During the last decades it has come to common knowledge that after hundreds of years of exploitation of fossil fuels (oil, coal, gas), these soon will be exhausted due to the permanently rising energy demand (Kerr and Service 2005). The obvious storage problem of radioactive waste material and historical disasters of nuclear power plants spare nuclear power as a promising future technology. Not only the escalating need for a safe power supply, but also emissions of CO₂ and other harmful substances which threaten human health and have led to numerous environmental problems such as pollution, global warming and stratospheric ozone depletion, obviously demand renewable and sustainable energy resources. Among these renewable energy sources like solar energy, wind, geothermal heat, tides, biomass, solar energy is the most promising (Nocera 2009), because of its possible realisation as an individual, personalised and secure energy supply with the aid of low-cost and low-tech devices. The bottleneck of personalised solar energy is indeed the storage process, as sun light is not available continuously.

Without doubt the energy crisis is one of the most provoking issues of the 21st century. Related advanced innovations in technology and science try to face challenges on how atmospheric CO₂ levels could be limited to twice their preanthropogenic values and at the same time meet the increased energy demand (Lewis and Nocera 2006). Dihydrogen (H₂) is an ideal candidate for energy storage having an energy density of 142 MJ/kg (Midilli, Ay et al. 2005) (for comparison petrol has an energy density of 44 MJ/kg) (Fischer, Werber et al. 2009). Efficient energy storage *via* chemical bonds is possible *via* electrochemical reactions, for example the electrochemical

splitting of water to form hydrogen and oxygen gas. The subsequent recombination (oxygen reduction and hydrogen oxidation) can furnish clean electrical energy with only water as a by-product (Hong, Risch et al. 2015).

1.1 Hydrogen fuel from water electrolysis

Seeking for new solar fuels, the water oxidation reaction is essential. This reaction still is insufficiently understood, which simultaneously impedes and stimulates progress in the development of applicable technologies for the conversion of light into storable fuels (Dau, Limberg et al. 2010). Nowadays only 4 % of the global hydrogen production stem from electrolysis (Zeng and Zhang 2010), the electrocatalytic splitting of liquid water into hydrogen and oxygen gas using electricity and electrodes. The production of non-fossil fuels needs systems, which primarily involve the use of water as a source of electrons, and hence require efficient water oxidation. The overall reaction of electrolysis is given in Equation 1.1. In detail, the water splitting reaction consists of two half-cell reactions; the oxidation process at the anode, denoted as oxygen evolution reaction (OER); it is the catalysed extraction of four electrons from a water molecule coupled to release four protons and one molecule of dioxygen (Equation 1.2). The other half reaction is the reduction process at the cathode, denoted as hydrogen evolution reaction (HER), which accords to Equation 1.3.



Water electrolysis was first observed in 1789 (see (Trasatti 1999a, Trasatti 1999b) and made its way to a wider audience in 1800 using a voltaic pile by Nicolson and Carlisle (Nicolson 1800). Industrialisation of water electrolysis at the beginning of the 20th century made it possible to produce hydrogen gas for ammonia production (fertiliser industry) and early petroleum refining (LeRoy 1983, Dau, Limberg et al. 2010). Nowadays, even after severe material and system improvements on the whole and on single parts of electrolyzers such as diaphragms (Rosa, Santos et al. 1995), dimensionally stable anodes (DSAs) (Carmo, Fritz et al. 2013), polymer electrolyte membranes (PEMs) (Aricò, Siracusano et al. 2013), other membrane materials such as perfluorosulfonic acid (Pintauro 2015), these reactors still suffer from a series of drawbacks for a

large-scale production of hydrogen fuel. However, water electrolysis can already be coupled with photovoltaic solar energy conversion on a low efficiency level (Yilanci, Dincer et al. 2009).

Among the scientific and technical challenges, the need for advanced but earth-abundant materials is critical to account for the energy-intensive process of water electrolysis for a large scale production of hydrogen fuel, which should be efficient, renewable, low-cost, and regenerative. Mimicking nature can address the problem of the type of input energy for electrolysis, as well as prevention of CO₂ emission; therefore the water oxidation reaction in photosystem II of plants, algae, and cyanobacteria will be briefly described, followed by the artificial mimics of its function and structure.

1.2 The natural and biomimetic way of water oxidation

The protein photosystem II (PS-II) is a multi-subunit pigment protein complex of 700 kDa (Suga, Akita et al. 2015) with enormous complexity, located in the thylakoid membrane, which itself is composed of a dense array of proteins and lipids. This lipid bilayer membrane separates the aqueous compartments of the PS-II acceptor side (lumen) and donor side (stroma) (for references see Dau, Limberg et al. 2010). PS-II catalyses light-driven oxidation of water into dioxygen through the S-state cycle of the oxygen-evolving complex (OEC) ((Dau and Haumann 2008). From a very simplified viewpoint, light is absorbed by antenna pigments; the photon excites chlorophylls, resulting in initiation of a sequence of electron-transfer steps and proton-coupled redox reactions. The catalytic centre of the photosynthetic water oxidation is a pentanuclear and asymmetric Mn₄Ca(μ-O)₅ complex, denoted as oxygen-evolving complex (Figure 1.1). Only the energy supplied by the sun is used to drive the water oxidation reaction. Changes of oxidation state and structure of the Mn₄Ca(μ-O)₅ complex occur during the water oxidation reaction cycle (Dau and Haumann 2008).

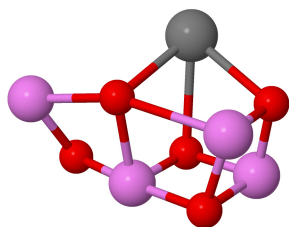


Figure 1.1: Atomic structure (Suga, Akita et al. 2015) of the metal-oxo core of the OEC (Mn₄Ca(μ-O)₅) of PS-II. Colour codes are the following: manganese, violet; calcium, grey; and oxygen, red.

Moreover, in PS-II, photosynthetic water oxidation is coupled to quinone reduction. It is a high efficiency process with a theoretical maximum of 16 % of the solar energy conversion efficiency and a minimum overpotential of 0.3 V (Dau and Zaharieva 2009).

Complete and successful artificial photosynthesis would necessitate a combination of several processes occurring in photosynthesis; light harvesting, charge separation, electron transfer, and water oxidation (oxygen evolution), as well as the hydrogen-forming reaction or the transformation of carbon dioxide into a chemical compound of higher energy content (Bard and Fox 1995, Alstrum-Acevedo, Brennaman et al. 2005, Gust, Moore et al. 2009, Dau, Limberg et al. 2010).

Mimicking the efficient water oxidation reaction of PS-II is currently considered a major bottleneck in the field of biomimetic photosynthesis. The established criteria cover reaching a similar efficiency to that of PS-II, the use of abundant and inexpensive materials, benign conditions, carbon neutrality, low costs, and the exclusive use of sun light to provide a true 'solar fuel' (Nocera 2009, Risch, Klingan et al. 2014, Zou and Zhang 2015). Currently, there is a wide range of diverse artificial catalysts and synthesis methods to produce mimics of biological water oxidation; among these are metal oxides on surfaces (Suntivich, May et al. 2011), bulk metal oxides in suspension (Shevchenko, Anderlund et al. 2011), bulk metal oxides deposited on electrodes (Risch, Ringleb et al. 2015), nanostructures (Meng, Song et al. 2014) and nanoparticles (Zhang, de Respinis et al. 2014, Koroidov, Anderlund et al. 2015), and molecules (metal complexes) (Artero, Chavarot-Kerlidou et al. 2011, Duan, Bozoglian et al. 2012, Sheehan, Thomsen et al. 2015). Recently, a breakthrough has been achieved, as a manganese-calcium cluster has been synthesised (Zhang, Chen et al. 2015), which readily undergoes four redox transitions like the OEC in photosystem II. The synthetic Mn_4Ca -cluster coincides both in structure of the Mn_4Ca -oxo core and the ligating carboxylate groups with the biological core complex, but differences occur in bridging protein ligands and water-binding sites on the 'dangling' Mn atom (Zhang, Chen et al. 2015).

The objects of this thesis are electrochemically deposited oxide catalysts active in the oxygen-evolution reaction; hence a short report of the cornerstones in this area of research will be given in the following.

1.3 Transition metal thin-film catalysts

Many transition metal catalysts which have been obtained by electrodeposition as thin films on supporting electrodes are members of a class of amorphous and hydrated (water-containing) synthetic catalysts which can be viewed best as non-classical solid-state materials with molecular properties that perform heterogeneous catalysis (Risch, Klingan et al. 2014). From a structural and functional point of view, transition metal catalysts based on Co, Ni, and Mn are remarkable water oxidation catalysts (WOCs), which bear a striking similarity to the natural model, the pentanuclear $Mn_4Ca(\mu-O)_5$ complex of PS-II (see Figure 1.2). The metal-oxygen bond length of all these

electrodeposited WOCs is between 1.88 and 1.90 Å in their ‘resting state’ (Risch, Khare et al. 2009, Risch, Klingan et al. 2011, Zaharieva, Chernev et al. 2012), which conforms to the bond length in PS-II (1.8 – 2.0 Å) (Haumann, Müller et al. 2005). Their dominating common motif is the di- $\mu_{2/3}$ -oxo bridging between two corresponding metal ions and two oxygen atoms (distances of 2.81 ± 0.01 Å for CoCat and NiCat, 2.86 Å for MnCat, 2.70 Å for PS-II). Among other factors, this type of bridging is important regarding the need for reducing the overpotential of water oxidation by redox-potential levelling, in other words by keeping a constant redox potential of the Mn_4Ca cluster for exactly the four sequential oxidation steps before dioxygen formation.

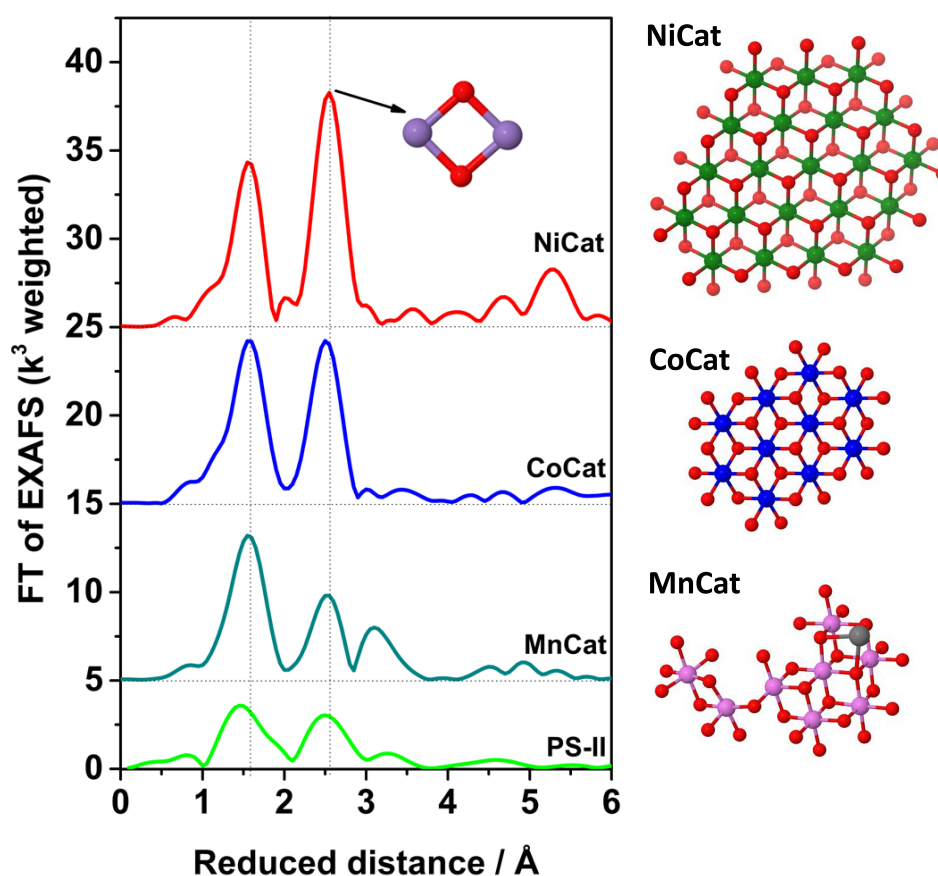


Figure 1.2. Comparison of experimental K -edge Fourier-transformed (FT) EXAFS of the CoCat (Risch, Klingan et al. 2012), NiCat (Risch, Klingan et al. 2011), MnCat (Zaharieva, Chernev et al. 2012), and the Mn-Ca core of the S_1 -state of PS-II (Haumann, Müller et al. 2005). The structural motif assigned to the second peak (di- $\mu_{2/3}$ -oxo bridging) is displayed schematically. Note that the indicated distance is reduced by about 0.3 Å in comparison to the distance obtained by EXAFS simulations. Schematic, idealised structures of perfectly ordered layer fragments of the electrodeposited WOCs are shown on the right side. Colour codes are the following: manganese, violet; calcium, grey; nickel, green; cobalt, blue; and oxygen, red.

1.3.1 The cobalt oxide catalyst (CoCat)

Since the first report of the ‘ancestral’ cobalt oxide catalyst (CoCat) (Coehn and Gläser 1902), more than hundred years must have elapsed for seeing its potential for future energy applications. In 2008 the CoCat was rediscovered by Kanan and Nocera (Kanan and Nocera 2008), who described that a promising OEC can be synthesised using a very simple electrodeposition protocol. The overpotential to oxidise water at pH 7 (for a current of 1 mA cm^2 and in 0.1 M KP_i) was determined as 0.41 V (Kanan and Nocera 2008). From this point on the CoCat has attracted much interested; an avalanche of in-depth investigations into basic and applied aspects of the CoCat has been set off. Its efficiency at neutral pH, its self-repair mechanism and its electrochemical self-assembly from low cost materials are the principal characteristics of the CoCat, making it an ideal candidate for an industrial water oxidation catalyst; as reviewed elsewhere (Risch, Klingan et al. 2014).

It is possible to electrodeposit the CoCat on a variety of substrates, in different electrolytes and under various potentials/pH values (Gerken, Landis et al. 2010, Esswein, Surendranath et al. 2011, Gerken, McAlpin et al. 2011, Liu and Nocera 2014); the surface morphology depends on the deposition time, the composition of the electrolyte, and the applied potential. Interestingly, catalyst operation and formation does not necessarily involve reagent-grade water: the operation of the CoCat in brine, river, and waste water demonstrates that especially chloride does not inhibit the OER catalysed by the CoCat (Surendranath, Dinca et al. 2009, Esswein, Surendranath et al. 2011). In 2009 the structure of the ‘resting state’ of the CoCat was disclosed by extended X-ray absorption fine-structure (EXAFS) measurements (Risch, Khare et al. 2009) and afterwards several times confirmed (Risch, Ringleb et al. 2009, Kanan, Yano et al. 2010, Du, Kokhan et al. 2012, Risch, Klingan et al. 2012, Risch, Klingan et al. 2014). As the atomic structure of the CoCat is highly amorphous, conventional diffraction techniques such as X-ray diffraction (XRD) cannot resolve the atomic framework, therefore bulk methods being sensitive to amorphous materials have to be used; e.g. X-ray spectroscopy (XAS) at synchrotrons. The detected cobalt oxide fragments mainly consist of octahedrally coordinated Co^{III} ions which are interconnected *via* bridging oxygen atoms (O^{2-}) in form of di- μ -oxo bridges. Di- μ -oxo bridging is equivalent to edge-sharing of $\text{Co}^{\text{III}}\text{O}_6$ octahedra (see Figure 1.2). For electrodeposition at pH 7 in 0.1 M KP_i , the size of an active CoCat cluster contains 9-16 Co atoms (EXAFS analysis, Figure 1.2) (Risch, Khare et al. 2009). Models for the amorphous CoCat are based on crystalline structures like layered ACoO_2 (all incomplete cubanes, A denotes a cation). Small oxide fragments or defect-rich variants of ACo_2O_4 are very conceivable for amorphous Co-based catalysts (Risch, Klingan et al. 2014). While in the natural paragon, the core-complex of PS-II, a Ca ion is bound specifically in the $\text{Mn}_4\text{Ca}(\mu\text{-O})_5$ structure, potassium and other

monovalent cations bind largely unspecifically with the incomplete Co-oxo cubanes of the CoCat. This gives a picture similar (obviously aside from the amorphous structure, defects, and vacancies) to layered oxides like LiCoO_2 , where the cations are located in between of the Co containing sheets (Risch, Klingan et al. 2012).

Regardless of the electrolyte (KCH_3CO_2 , LiCH_3CO_2 , KCl , CaCl_2 , KPi) used for electrodeposition, atomic structures of the CoCat are highly similar (edge-sharing CoO_6 octahedra). However, the type of anion influences the size of the Co-oxo clusters and the corresponding catalytic currents. Monovalent cations like K^+ , Na^+ , Li^+ probably exist as hydrated ions bound largely unspecifically between the layers, but Ca^{2+} ions participate to an extent up to 40 % in the formation of $\text{CaCo}_3(\mu\text{-O})_4$ cubanes (Risch, Klingan et al. 2012).

The formation process of the CoCat has been suggested to occur *via* nucleation resulting in nanosized domains in the beginning of the deposition process, which then arrange into extended clusters of the CoCat for the amorphous catalyst film (Surendranath, Lutterman et al. 2012, Liu and Nocera 2014). Hereby, phosphate plays a key role as proton acceptor not only for the OER of the CoCat (Surendranath, Kanan et al. 2010, Klingan, Ringleb et al. 2014), but also for growth and self-repair of the catalyst (Lutterman, Surendranath et al. 2009, Surendranath, Lutterman et al. 2012).

The mechanistic aspect of the oxygen evolution reaction has been studied in great detail: First and foremost, a key event in water oxidation, the proton-coupled electron transfer (PCET) has been a relevant focus of the research efforts (McClintock and Blackman 2010, Surendranath, Kanan et al. 2010, Mattioli, Risch et al. 2011, Symes, Surendranath et al. 2011, Wang and Van Voorhis 2011, Risch, Klingan et al. 2012, Bediako, Costentin et al. 2013, Farrow, Bediako et al. 2013, Symes, Lutterman et al. 2013, Risch, Ringleb et al. 2015).

The general mode of catalysis at the CoCat can be described by interconversion of three structural motifs, A, B, C, as displayed in Figure 1.3 and recently demonstrated by a combination of EXAFS, *in-situ* electrochemical UV-vis spectroscopy, and differential electrochemical mass spectroscopy at different potentials and pH values (Risch, Ringleb et al. 2015). Cobalt ions at the margins of the CoCat of Co-oxo fragments (9-16 Co ions interconnected *via* di- $\mu_{2/3}$ -oxo bridges) undergo chemical changes, characterised by two redox transitions, at 1.0 V ($\text{Co}^{\text{II}}_{0.4}\text{Co}^{\text{III}}_{0.6} \leftrightarrow \text{all-Co}^{\text{III}}$) and at 1.2 V vs. NHE at pH 7 ($\text{all-Co}^{\text{III}} \leftrightarrow \text{Co}^{\text{III}}_{0.8}\text{Co}^{\text{IV}}_{0.2}$), which are coupled to structural changes. Motif A represents a mixed-valence state $\text{Co}^{\text{II/III}}$, the lowest oxidation state of the CoCat. When increasing the potential (or the pH), motif B becomes dominant with a Co oxidation state of +3.0. Further increase in the potential may result in deprotonation of a $\mu\text{-OH}$ bridge and oxidation of Co, so that

motif C is formed with a mean Co oxidation state of +3.2 in the material. In the process of water oxidation, oxidation equivalents are accumulated by the CoCat ($A \rightarrow B \rightarrow C$) before the onset of O_2 -formation, water oxidation and O_2 -formation are coupled to cobalt reduction. This means that the onset of O-O bond formation is the rate-determining step, and not the accumulation of oxidising equivalents (Risch, Ringleb et al. 2015). Risch and co-workers (Risch, Ringleb et al. 2015) proposed four stages involved in the general mode of catalysis in the hydrated, amorphous, and volume-active CoCat material (see Figure 1.3):

- (1) Dynamic equilibrium between the three structural elements (A, B, and C)
- (2) Formation of an active site of the water oxidation chemistry involving two or more Co^{IV}
- (3) O-O bond formation and cobalt reduction at the transiently formed active site
- (4) Fast electrochemical Co reoxidation and return to (1)

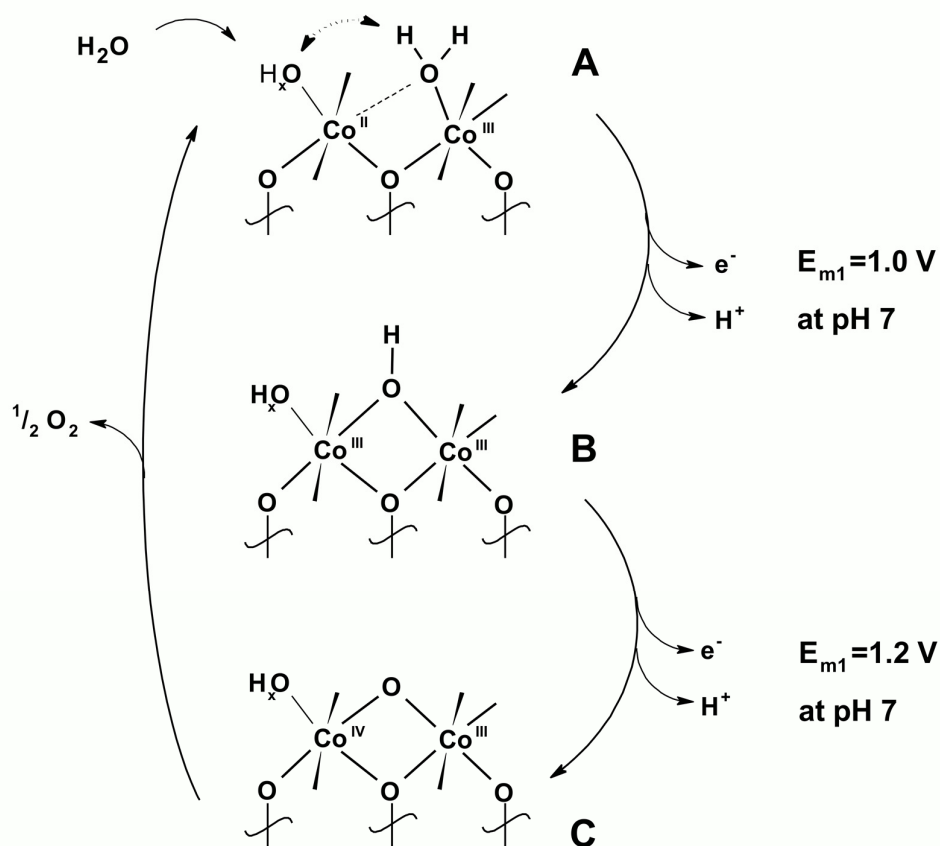


Figure 1.3. Structural motifs A, B, and C in the CoCat during the OER (Risch, Ringleb et al. 2015). Oxygen evolution occurs in the transition from C to A. The shown structural changes probably arise at the margins of Co-oxo fragments (9-16 Co ions) (Risch, Ringleb et al. 2015). Figure reproduced from Risch, Ringleb et al. 2015 with permission from The Royal Society of Chemistry.

The use of the CoCat for directly light-driven water oxidation is a promising alternative for the utilisation of solar light energy. Technical requirements are: (i) the substrate electrode is replaced by a light absorbing and charge separating material, (ii) an adequate life-time of photo-generated charges and efficient transfer to the CoCat must be guaranteed, (iii) the use of rare chemical elements should be avoided to realise low final cost on large scale (Lewis and Nocera 2006, Risch, Klingan et al. 2014). These approaches cover either water oxidation at photoanodes or quasi homogenous systems. An example for the latter is the combination of a photosensitiser, $[\text{Ru}(\text{bpy})_3]^{2+}$ (bpy=2,2'-bipyridine), persulfate as an electron acceptor, and the CoCat which is present in a suspension in form of nanoparticles, stabilised by methylenediphosphonate (M2P) (Shevchenko, Anderlund et al. 2011).

More prominent are attempts to deposit the CoCat on semiconducting anodes, which consist of a light absorbing/charge separating material. The efficiency of the semiconductor based photoanodes is limited by (i) short hole-diffusion length, best solved by using nanostructured materials, and (ii) strong electron hole-recombination, best decreased by another catalyst at the photoanode (such as the CoCat) (Li, Luo et al. 2013, Risch, Klingan et al. 2014). This is why semiconductor photoanodes like TiO_2 (Bledowski, Wang et al. 2012), WO_3 (Seabold and Choi 2011), ZnO (Steinmiller and Choi 2009), TaON (Higashi, Domen et al. 2012), BiVO_6 (Abdi and van de Krol 2012, Ding, Shi et al. 2013), wolfram doped BiVO_6 (Ye, Park et al. 2011, Zhong, Cornuz et al. 2011, Abdi, Furet et al. 2012), molybdenum doped BiVO_6 (Pilli, Furtak et al. 2011), $\text{SiO}_2\text{-BiVO}_6$ (Pilli, Deutsch et al. 2012), and with especially good prospects hematite $\alpha\text{-Fe}_2\text{O}_3$ (Sivula, Le Formal et al. 2011), dopants of silicon (Hong, Liu et al. 2011) and Nb (Barroso, Cowan et al. 2011) on hematite have been used in the field of water oxidation (Risch, Klingan et al. 2014). The formation of the CoCat directly at the surface on to the semiconductor could be accomplished by electrodeposition (Yamazaki, Shouji et al. 2010, Young, Martini et al. 2012). Thus, of special interest is the photodeposition of the CoCat on photoanodes, which bears the advantage of forming the CoCat faster at locations where the holes are especially accessible (Steinmiller and Choi 2009, McDonald and Choi 2011, Zhong, Cornuz et al. 2011, Khnayzer, Mara et al. 2012, Pilli, Deutsch et al. 2012, Young, Martini et al. 2012).

Another system, which allows water oxidation directly driven by light without the help of any oxidising agents, is a solution consisting of semiconducting nanoparticles (yttrium-doped BiVO_4), where the CoCat, and Pt clusters as cocatalyst for proton reduction are deposited on (Wang, Li et al. 2012).

Generally, all these photoanodes coupled to the CoCat can only be used as parts for complete systems for overall water splitting. The most straightforward design of direct and wireless solar to hydrogen conversion has been achieved by the design of the 'artificial leaf' (Reece, Hamel et al.

2011). The ‘artificial leaf’ consists of a triple-junction silicon solar cell (light absorbance and formation of an electrode potential necessary to split water), a protection layer of ITO (indium tin oxide) against photoinstability, and only the CoCat to catalyse water oxidation. In the ‘artificial leaf’ this CoCat/Si photoanode is combined with a NiMoZn alloy cathode on stainless steel, so that oxygen and hydrogen can be produced upon illumination in a borate buffer at pH 9.2. In this wireless device the solar-to-fuel efficiency is 2.5 % (Reece, Hamel et al. 2011).

1.3.2 The nickel oxide catalyst (NiCat)

Likewise the history as well as the structural and functional characteristics of the CoCat, other transition metal catalysts can be deposited as thin films exhibiting similar electrocatalytic water oxidation properties. After the wave of interest to search for potential amorphous water oxidation catalyst has aspired, it was first reported (Dincă, Surendranath et al. 2010) that a nickel oxide catalyst (NiCat) can easily be electro-synthesised from a Ni^{2+} solution in borate buffer (B_i) under benign conditions (optimal pH 9.2). The overpotential of the NiCat (at a current density of 1 mA cm^{-2} in B_i at pH 9.2) was reported as 0.43 V and the oxygen yield as 104 % (Dincă, Surendranath et al. 2010). By Ni-*K*-edge XAS of the electrodeposited NiCat and comparison of the resulting spectra to the atomic arrangement of the CoCat, the structure of the resting state of the NiCat could be identified and related to that of γ -NiOOH (Risch, Klingan et al. 2011). The structure of the NiCat is remarkably similar to the one of the CoCat, both contain edge-sharing $\text{M}(=\text{Ni or Co})\text{O}_6$ octahedra. Its composition could be identified as extended fragments, which are separated by water and borate of a layered $\text{Ni}^{\text{III/IV}}\text{OOH}_{n<1}$ structure. The NiCat has more metal-metal interactions, in other words a higher degree of long-range order than the CoCat. The EXAFS analysis of a $\text{Ni}_{21}\text{O}_{59}$ cluster in Figure 1.2 results in 4.5 Ni-Ni interactions at 2.8 Å and about 3 Ni-Ni interactions at both 2.9 Å and 5.6 Å (Risch, Klingan et al. 2011). Both the NiCat and the CoCat are amorphous metal oxides and feature extensive di- μ -oxo bridging, while mono- μ -oxo bridging could not be detected between the redox-active ions (Risch, Klingan et al. 2011).

With the use of molecular precursors (amine complexes) the activity and robustness of the NiCat could be noteworthy enhanced. The corresponding catalyst films were more uniform on the surface, exhibited an overpotential reduced by 20 mV, and catalytic current densities increased by ~50 %, which did not change for the period of six hours (Singh, Chang et al. 2013). Another increase in activity (overpotential of 0.20 V at pH 9.2 and a Faradaic efficiency of > 95 % in the oxygen

evolution regime) could be achieved by electrodepositing the NiCat on multi-walled carbon nanotubes.

The kinetic profile of anodised NiCat films (Bediako, Surendranath et al. 2013), which had undergone an activation protocol by voltammetry in order to enhance their catalytic performance, correspond to a rather low Tafel slope (30 mV/decade at 25 °C, pH 8.5 - 14) and an inverse third order rate dependence on H^+ activity (Bediako, Surendranath et al. 2013). On the other hand, directly as-deposited films without further anodisation probably suffer from a limiting electron transfer, suggested by a loss in catalyst activity of almost three orders in magnitude. Based on the results from this electro-kinetic study a reaction cycle has been proposed: (1) Reversible dissociation of borate anion from the resting state, (2) Equilibrium between two electrons and three protons by deprotonation of a bridging and two terminal hydroxyl groups, (3) Chemical turnover-limiting step, which involves O-O bond formation and/or Ni-O scission. Besides, the role of the buffer electrolyte B_i is dualistic, being both an inhibiting adsorbate and a proton acceptor for the proton coupled electron transfer (Bediako, Surendranath et al. 2013). An *in-situ* XAS investigation revealed the oxidation state of the anodised NiCat as +3.6, whereas non-operated films have an oxidation state of +3.0 and further exhibit a distortion in their Ni^{III} centres, a common characteristic for a Jahn-Teller effect of β -NiOOH (Bediako, Lassalle-Kaiser et al. 2012). Contradicting results were reported by *in-situ* Raman spectroscopy in 0.1 M KOH electrolyte buffer, where the more active phase in aging of nickel electrodes was identified with β -NiOOH (Yeo and Bell 2012).

Moreover, the NiCat can be used to functionalise Si photoanodes with cost effective sol-gel approaches to create photoelectrochemical cells with an efficient and transparent photo-oxidation catalyst (conversion efficiency of the n-Si | NiCat is 1.34 %) (Sun, Park et al. 2012). In such systems the NiCat (prepared by either sol-gel or sputtering synthesis) also functions as a protection layer for the silicon photoanode, which is sensitive to corrosion, both in KOH media at pH 14 and borate electrolyte at pH 9.5 (Kenney, Gong et al. 2013). The NiCat protection layer bears many advantageous characteristics like being transparent, antireflective, conductive, chemically stable, and inherent catalytic, thus the NiCat can stabilise many other semiconducting photoanodes in their operating conditions (Sun, McDowell et al. 2015, Sun, Saadi et al. 2015).

1.4 Homogenous catalysts

A promising class of compounds of homogenous water oxidation catalysts (WOCs) with sufficient hydrolytic stability are polyoxometalates (POMs). Their overall characteristic is their fast reaction kinetics (Quionero, Kaledin et al. 2010), and they belong to the best WOCs existing till now. The earliest POMs contained Ru as metal core (Geletii, Botar et al. 2008, Sartorel, Carraro et al. 2008, Geletii, Huang et al. 2009), while newer approaches synthesised POMs containing of abundant transition metal elements, either Co or Ni (Car, Guttentag et al. 2012, Lv, Geletii et al. 2012, Tanaka, Annaka et al. 2012, Zhu, Glass et al. 2012). A purely inorganic Co₄-POM **1** Na₁₀[Co₄(H₂O)₂(PW₉O₃₄)₂] based on earth-abundant cobalt is an active oxygen-evolving catalyst together with either a chemical (Yin, Tan et al. 2010) or a photochemical oxidant (Huang, Luo et al. 2011). This interesting finding was first reported by Yin and co-workers (Yin, Tan et al. 2010) decades after the synthesis and structure of **1** had been published (Finke, Droege et al. 1987). In the following it set off an avalanche of research on Co₄-POM under various conditions with the help of several different methods (Huang, Luo et al. 2011, Ohlin, Harley et al. 2011, Natali, Berardi et al. 2012, Vickers, Lv et al. 2013, Schiwon, Klingan et al. 2014). The stability against hydrolysis of **1** under oxygen turnover conditions is essential when determining **1** as an active WOC, otherwise hydrolytic products are the main catalysts. In 2011 it was argued (Stracke and Finke 2011) that **1** is not stable at pH 8 in electrochemical experiments; it rather partially dissolves into Co²⁺, which deposits as the CoCat at the working electrode. Then, laser flash photolysis investigations in photocatalytic cycles with [Ru(bpy)₃]²⁺ as a photosensitiser (Natali, Berardi et al. 2012) favoured a transformation of **1** during catalysis. Both of the latter noted that decomposition of **1** might be dominating under the experimental conditions used in the studies (electrocatalysis and laser flash photolysis). The open question, on how to determine the real catalyst, was addressed by another electrochemical survey (Stracke and Finke 2013), where further evidence was found for the electrocatalytic instability of **1**, and yet results also within electrochemical experiments are conflicting due to different conditions. Sodium phosphate buffer and pH values above 7.5 – 8 can represent hydrolytically unstable conditions for the Co₄POM (Finke, Droege et al. 1981, Lieb, Zahl et al. 2011, Ohlin, Harley et al. 2011), debasing the role of **1** as effective WOC. Recently, this has been challenged throughout a systematic examination on the influence of pH, ionic strength, buffer medium, and buffer concentration on the stability and reactivity of **1** (Vickers, Lv et al. 2013). Generally, it is of high importance to elucidate the kinetic stability or instability in water oxidation by addressing in detail the behaviour of **1** under a variety of conditions (Swierk and Mallouk 2013). This will be the route to follow for a general decision, whether **1** can or cannot be a promising WOC.

1.5 Scope and organisation of the thesis

The primary goal is to contribute to the current research on electrochemical water splitting by biomimetic transition metal catalysts. A key role herein is the determination of structure-function correlations of amorphous cobalt and nickel metal catalysts during the OER. Questions like “What is the true mode of catalysis within the CoCat - volume catalysis or surface catalysis?”, “Why does the NiCat change its colour during the OER?”, “Can the Co₄-POM **1** be viewed as a more defined version of the CoCat?” are addressed in this work. Understanding, not improving the catalytic performances of the catalysts is the ambition of this thesis.

The chapters are organised as follows:

- Chapter 2** investigates crucial determinants of electrocatalytic activity for a CoCat film electrodeposited at various thicknesses (between 2 and 200 mC cm⁻² of Co) on inert electrodes by voltammetry, titration curves in different buffer electrolytes, and X-ray spectroscopy (XAS) at the cobalt *K*-edge.
- Chapter 3** examines the mode of water oxidation of the CoCat at very low amounts of deposited cobalt (≤ 2 mC cm⁻² of Co) with the aid of voltammetry and Co *K*-edge XAS.
- Chapter 4** addresses the role of calcination for the CoCat. A structural comparison between the CoCat and high-temperature exposed CoCats is given.
- Chapter 5** interrogates the integrity of homogenous cobalt-polyoxometalates (POMs) during the water oxidation reaction detected by cobalt *K*-edge XAS, demonstrated by comparison of Na₁₀[Co₄(H₂O)₂(PW₉O₃₄)₂] (**1**) with the heterogeneous CoCat, a Co²⁺ product of hydrolysis, and Na₁₇[((Co(H₂O))Co₂PW₉O₃₄)₂(PW₆O₂₆)] (**2**).
- Chapter 6** scrutinises different potential-induced states of a NiCat during the OER and compares them to the corresponding results of the CoCat by electrochemical *in-situ* UV-vis spectroscopy and Ni *K*-edge XAS.

At the beginning of each chapter, a succinct abstract outlines key results and applied methods. Experimental detail is described in the following. The main part of each chapter contains description of results and their discussion. At the end of each chapter a concise summary is given. All the chapters in this thesis are self-contained with regard to scientific content. The theoretical background is covered in each chapter by citations of standard textbooks and leading reviews. This presentation approach supersedes the need for independent theory and experimental chapters.

Chapter 2

Volume activity of the CoCat

Classical heterogeneous catalysis is characterised by surface and interface reactions, where the bulk of the catalyst is mainly unaffected by the reaction pathway, so that fabrication of customary heterogeneous catalysts results in a preferably huge surface area. The main properties of the transition metal oxide thin films (as described in Chapter 1.3) hint that that they behave non-classical. They may be members of the same class of amorphous, hydrated oxide materials with specific functional properties that set them aside from classical heterogeneous catalysts.

Herein, we investigated two aspects of the CoCat function, namely, the question of water oxidation activity within the bulk of the oxide material and the surprising role of ‘buffer bases’ in the electrolyte. Both aspects are of basic conceptual importance and of direct relevance for the design of efficient technological systems.

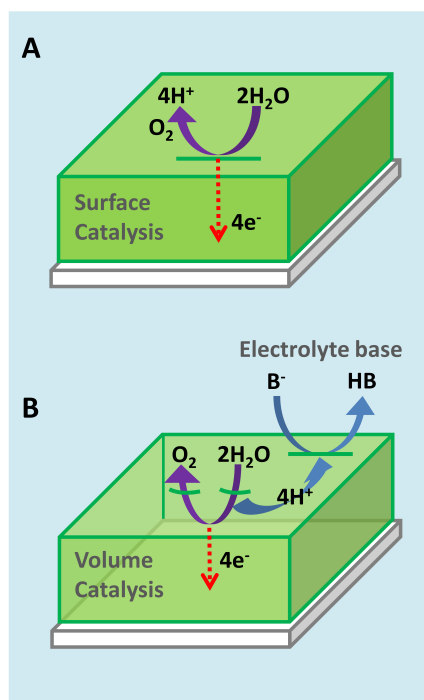


Figure 2.1. Surface (A) versus volume catalysis (B). (B) Volume catalysis as a working mode of the CoCat: Water oxidation may prevail within the bulk of the amorphous oxide materials, but the proton transfer to an electrolyte buffer base (abbreviated as B⁻) at the bulk oxide surface. After water oxidation at oxide fragments inside of the bulk material, protons are transported through multiple hopping steps involving the numerous potentially protonatable groups within the CoCat. In the bulk oxide/bulk electrolyte interface region, these protons are transferred to the unprotonated molecular bases present in the electrolyte solution at high concentration.

Crucial determinants of electrocatalytic activity and structural changes were investigated for a cobalt-based oxide film (CoCat) electrodeposited at various thicknesses on inert electrodes with voltammetry, electrochemical impedance spectroscopy, pH titrations, X-ray absorption spectroscopy (XAS), and scanning electron microscopy (SEM). For water oxidation at low current densities, the turnover frequency (TOF) per cobalt ion of the bulk material stayed fully constant for variation of the thickness of the oxide film by a factor of 100 (from about 15 nm to 1.5 μm). Thickness variation changed neither the nanostructure of the outer film surface nor the atomic structure of the oxide catalyst significantly. These findings imply catalytic activity of the bulk hydrated oxide material. Nonclassical dependence on pH was observed. For buffered electrolytes with pK_a values of the buffer base ranging from 4.7 (acetate) to 10.3 (hydrogen carbonate), the catalytic activity reflected the protonation state of the buffer base in the electrolyte solution directly and not the intrinsic catalytic properties of the oxide itself. It is proposed that catalysis of water oxidation occurs within the bulk hydrated oxide film (Figure 2.1) at the margins of cobalt oxide fragments of molecular dimensions. At high current densities, the availability of a proton-accepting base at the catalyst–electrolyte interface controls the rate of water oxidation. The reported findings may be of general relevance for water oxidation catalysed at moderate pH by amorphous transition-metal oxides.

Complemented by additional information this entire chapter has been published as:

K. Klingan, F. Ringleb, I. Zaharieva, J. Heidkamp, P. Chernev, D. Gonzalez-Flores, M. Risch, A. Fischer, and H. Dau, *ChemSusChem*, 2014, 7(5):1301-1310, <http://dx.doi.org/10.1002/cssc.201301019>

Reproduced with permission from Wiley-VCH. Copyright 2014 Wiley-VCH.
<http://www.interscience.wiley.com/>

K. Klingan prepared the samples, conducted all electrochemical experiments, evaluated the data, and performed XAS
F. Ringleb recorded the specific conductivity of the CoCat in dependence of the phosphate concentration
I. Zaharieva, J. Heidkamp, P. Chernev, D. Gonzalez-Flores, M. Risch supported the synchrotron measurements
A. Fischer performed SEM measurements
P. Chernev wrote software for data evaluation

2.1 Experimental detail

2.1.1 Sample preparation

All electrochemical experiments including CoCat deposition were performed in a single-compartment, three-electrode setup driven by an SP-200 potentiostat (Bio-Logic SAS, Claix). The working electrodes were glass slides coated with ITO (12Ω per square, VisionTek Systems Ltd, Cheshire, UK), where a conductive area of 1.5 cm^2 was exposed to the solution. To guarantee electrical contact between the ITO and a clamp, copper tape (Farnell GmbH) was used. The conductivity of the working electrode was tested before every experiment using a digital multimeter. A platinum grid ($25 \times 25 \text{ mm}^2$) served as the counter electrode and the reference was a mercury sulphate electrode ($\text{Hg}/\text{Hg}_2\text{SO}_4/\text{K}_2\text{SO}_4$, $+650 \text{ mV vs. NHE}$). The platinum grid was cleaned consecutively with concentrated acids, H_2SO_4 and HCl , rinsed with needful amounts of miliQ water, then flame-cut with a laboratory burner, to guarantee the absence of possible metals traces other than from the buffered deposition solution. The single-compartment cell was rinsed with the just mentioned acids and miliQ water; the reference electrode was rinsed with miliQ water, then with the later used Co-free buffer electrolyte. All chemicals used for film deposition of buffers were purchased and used without further purification. The anodic electrodeposition of the CoCat films refined from a 0.1 M KP_i buffer ($\sim 40\% \text{ KH}_2\text{PO}_4$ and $\sim 60\% \text{ K}_2\text{HPO}_4$) at pH 7 containing 0.5 mM Co^{2+} ions from a $\text{Co}(\text{OH})_2(\text{NO}_3)_2$ solution at $1.05 \text{ V vs. the normal hydrogen electrode (NHE)}$ (with iR compensation). The deposition potential was carefully chosen to avoid catalytic currents leading to water oxidation and dioxygen evolution, instead solely ensuring Co^{2+} to Co^{3+} oxidation. Filtration of this solution was not necessary as no solid cobalt precipitate was observed. The resistance between the ITO working electrode and the reference electrode was determined by impedance spectroscopy (typical value of 50 Ohm) and the iR drop was compensated at 80% for all electrochemical measurements.

The anodic electrodeposition was stopped when the integration of current density over time reached the desired value of charge density: 2.0, (5.0), 5.5, 8.0, 16.7, 22.2, 30.0, 38.0, 45.0, 100, 150, 200 mC/cm^2 . After deposition each CoCat film was rinsed with essential amounts of 0.1 M KP_i , pH 7 electrolyte and a cyclic voltammograms with a scan rate of 20 mV s^{-1} was recorded in 0.1 M KP_i at pH 7. The cell geometry stayed unchanged for all the following electrochemical characterisations (distance between working and reference electrode $\sim 1 \text{ cm}$).

2.1.2 Total X-ray fluorescence analysis (TXRF)

The amount of deposited cobalt was identified with total X-ray fluorescence analysis (TXRF). TXRF measurements were performed by using an AXS PicoFox (Bruker) instrument. After the above described sample preparation, the CoCat films were dissolved in a particular amount of 30% HCl. To the dissolved CoCat, gallium standard ($\text{Ga}(\text{NO}_3)_3$, 10 mgL^{-1} , Fluka TraceCert), was added. After mixing this solution, a drop of this mixture was dried on a silicon-coated quartz glass sample plate before TXRF measurements were initiated.

2.1.3 Turnover frequency (TOF)

After deposition of the CoCat film, the buffer medium was changed to a cobalt-free phosphate buffer (0.1 M KP_i , pH 7.0). Therefore, electrodeposition of cobalt ions is terminated and interference of electrodeposition with catalytic currents is largely excluded. Then the Faraday currents (that is, catalytic currents) were estimated by potentiostatic measurement of current densities at 1.20, 1.25, 1.30, 1.35, and 1.40 V (vs. NHE) after equilibration at the respective potential for 1 min.

Herein, the turnover frequency is related to a single Co-atom and O_2 molecule.

$$TOF (s^{-1}) = \frac{i}{n_{e^-} \cdot e \cdot n_{Co}} \quad (\text{Eq. 2.1})$$

In Equation 2.1, i is the current density (mA cm^{-2}), n_{e^-} is the number of participating electrons in water oxidation, e the elementary charge (C), and n_{Co} the number of deposited cobalt atoms. The turnover frequency is a measure of the reaction kinetics. At a given overpotential, the TOF can be understood as the number of reaction products (generated oxygen molecules) produced per active site (Co atom) and time (s). Notably, the TOF values are calculated by taking into account all deposited cobalt ions. Higher values would result from taking into account the still unknown number of cobalt ions per active site (e.g., four cobalt ions per single active site) and/or a fraction of ‘buried’ or otherwise catalytically inactive cobalt ions.

2.1.4 Estimation of the double-layer capacitance with impedance spectroscopy

Potentiostatic electrochemical impedance spectroscopy (PEIS) was employed using sinusoidal potential modulation (amplitude of 10 mV) at an electrode potential of 0.75 V (vs. NHE) in 0.1 M KP_i at pH 7. At 0.75 V, changes in the electrode potential induce neither variation in the catalytic

currents nor cause changes to the oxidation state of the cobalt ions (the latter means that the so-called pseudocapacitance is zero).

The electrochemical double-layer capacitance (DLC), C_{DL} , was estimated by two methods. First, C_{DL} was calculated at a frequency, f , of 33 Hz with the corresponding imaginary part of the impedance, Z (Equation 2.2).

$$C_{DL} = (-2\pi \cdot f \cdot \text{Im} |Z|)^{-1} \quad (\text{Eq. 2.2})$$

Secondly the DLC was determined by simulating the experimental impedance data with an equivalent circuit (shown in Figure 2.2) in a frequency domain between 10 Hz and 100 kHz. The fit was accomplished with EC-Lab software (Bio-Logic SAS, Claix).

Determination of an equivalent circuit is a common approach to the dynamical electrochemical behaviour of porous electrodes (Conway and Pell 2003). To model the CoCat different equivalent circuits were simulated to fit the experimental data. The best compliance delivered an equivalent circuit shown in Figure 2.2, consisting of three resistors and two constant phase elements, which imply surface factors and impurities deviating from ideal capacitors. A very similar type of equivalent circuit has been proposed to model hydrated metal oxides electrodes during the oxygen evolution reaction (OER) (Doyle, Godwin et al. 2013). The first resistance, R_{Ω} , corresponds to the solution resistance, whereas Q_{DL} models the double-layer capacitance. The charge transfer resistance, R_P , is related to the overall reaction rate. The relaxation of charge is associated with the reaction intermediates of the OER, Q_S . The related ease of which these intermediates are formed is reflected in R_S (Doyle, Godwin et al. 2013).

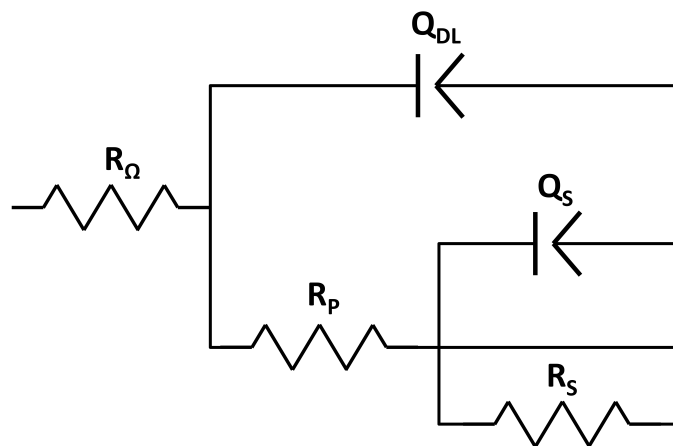


Figure 2.2. Model equivalent circuit for CoCat films of various thicknesses in the resting state of catalysis (absence of redox reactions and water oxidation). Data from potentiostatic electrochemical impedance spectroscopy (PEIS) measurements are used for simulation.

2.1.5 Scanning electron microscopy (SEM)

SEM was performed with a JEOL 7401F instrument operated at 10 kV. CoCat were prepared as described above, the only modification concerned the working electrode. ITO was substituted to glassy carbon (HTW Hochtemperatur-Werkstoffe GmbH) to avoid electrostatic charging from the glass substrate during the SEM experiments. SEM was performed by Dr. Anna Fischer at TU Berlin, Department of Chemistry.

2.1.6 pH titrations

For investigation of the role of buffer bases, we prepared solutions from (0.1 M) CH₃COOK (acetate), KH₂PO₄ (phosphate, KP_i), 2-amino-2-hydroxymethyl-propane-1,3-diol (TRIS), 2-(N-morpholino)ethanesulfonic acid (MES), 2-[4-(2-hydroxyethyl)piperazin-1-yl]ethanesulfonic acid (HEPES), NH₂CH₂COOH (glycine), B(OH)₃ (borate), and KHCO₃ (carbonate). For each buffer system, a new CoCat film was used, which had been deposited for 600 s at 1.05 V (in 0.1 M KP_i, pH 7), resulting in a deposition charge and estimated film thickness of about 3 mC cm⁻² and 25 nm. Currents were detected by employing 80% *iR* compensation with a typical *R* value of 50 Ω. Because about 40 Ω stemmed from the ITO resistance and only about 10 Ω related to the solution resistance, the decrease of *R* by protonation of the anionic bases was predicted to be negligibly small. The titration was performed from low to high pH by the addition of NaOH under continuous stirring (~700 rpm) and simultaneous pH detection by an electrode; currents were recorded after stabilisation of the current (equilibration) at the given pH.

2.1.7 X-ray absorption spectroscopy (XAS)

The XAS experiments were performed at the KMC-1 bending-magnet beamline (Schaefer, Mertin et al. 2007) at the BESSY synchrotron operated by the Helmholtz-Zentrum Berlin (HZB). The spectra were collected at the Co *K*-edge at 20 K. The excitation energy was selected by a Si-111 double-crystal monochromator. The measurements were performed at 20 K in a liquid-helium cryostat (Oxford-Danfysik). The cobalt *K_α* emission was detected using a windowless, energy-resolving 13-element detector (Ultra-LEGe germanium elements, Canberra). The scan range for cobalt *K*-edge was 7600-8750 eV.

The XAS samples were electrodeposited as explained in 2.1.1 on thin glassy carbon sheets (HTW Hochtemperatur-Werkstoffe GmbH) of dimensions 100 μm x 1.9 cm x 2.1 cm, which were mounted such that the angle between the CoCat surface and the incident beam was 45°. The fluorescence detector was installed perpendicular to the X-ray beam. In order to minimise the

radiation damage to the investigated samples, the cryostat was installed about 3 m away from the focal point of the beamline optics, thereby decreasing the X-ray intensity (per area) by increasing the spot size. At the out-of-focus position, the area irradiated by the X-rays was about 1 mm x 0.5 mm. A filter foil (12.5 μm Fe) was put directly in the sample compartment between the CoCat surface and the window facing the fluorescence detector. The energy resolution was tested with a ^{55}Fe source (5.9 keV) and is approximately 150 eV for a shaping time of 2.5 μs . The 13 detector elements (nominal active area is 50 mm² per element) were operated windowless. The detector was operated at 500 V and the signals were amplified by integrated pre-amplifiers (type, 3102 D). The signal processing was done using analogue components, namely 13 shaping amplifiers of type 2026 and 13 single channel analysers of type 2030. The energy window was set to the K_{α} -emission of cobalt. Only the 12 of 13 channels working according to specifications were analysed. Each spot on the CoCat sample was exposed for less than 35 min to synchrotron radiation. We changed the spot on the sample by 0.5 mm (vertically) after each scan. The spectra of the 12 channels were averaged for each spot on the samples. At least 5 different spots on each sample were taken (Risch, Klingan et al. 2012).

Energy calibration was performed by recording simultaneously the fluorescence data and the spectra of an energy reference (Co foil, 10 μm , 99.9 %, Goodfellow GmbH). Fluorescence data were aligned according to the energy reference. Then, the energy axis of the experimental data was shifted by an offset such that the first maximum in the derivative of the reference signal aligned with the value of 7709.0 eV (reported by Bearden and Burr 1967) (Risch, Klingan et al. 2012). Details of the data extraction for the CoCat at the Co K -edge are described in Risch, Klingan et al. 2012.

2.2 Results

2.2.1 Estimation of deposition charge

Examples for CoCat electrodeposition and typical CoCat cyclic voltammograms (CVs) at pH 7 in 0.1 M KP_i are given in Figure 2.3. At 1.05 V the integrated deposition current results in a value of the ‘deposition charge’, which reflects the amount of deposited cobalt ions properly. By increasing the deposition time, the deposition charge was varied between 2 and 200 mC cm^{-2} .

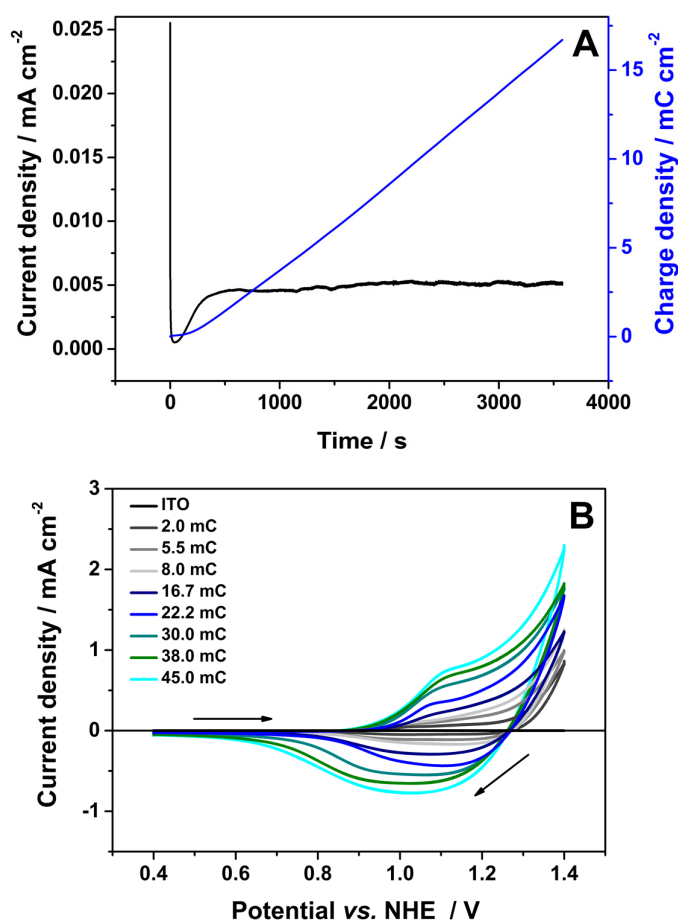


Figure 2.3. (A) Electrodeposition of a 16.7 mC cm^{-2} CoCat from 0.1 M KP_i (pH 7) and 0.5 mM $\text{Co(OH)}_2(\text{NO}_3)_2$ at 1.05 V vs. NHE. The blue line corresponds to the charge of the deposited Co ions (per cm^2). (B) CVs for the electrode substrate (ITO on glass) and different thick CoCats in 0.1 M KP_i at pH 7 with a scan rate of 20 mV s^{-1} .

Assuming that the deposition at 1.05 V involves one-electron oxidation of dissolved Co^{2+} ions to deposited Co^{3+} , the number of electrodeposited cobalt ions, n_{Co} (in mol) is predicted to be equal to the deposition charge, Q_{dep} , divided by the elementary electron charge (e) and the Avogadro constant (N_A), as shown in Equation 2.3:

$$n_{\text{Co}} = (Q_{\text{dep}}/e) \cdot N_A^{-1} \quad (\text{Eq. 2.3})$$

To verify the validity of Equation 2.3, the number of deposited cobalt ions was determined independently by total X-ray fluorescence analysis (TXRF), involving complete dissolution of the films in acidic solution and determination of the cobalt content in the obtained solution.

It is clearly visible in Figure 2.4 that the number of deposited cobalt ions determined by X-ray fluorescence analysis is in very good agreement with the number of cobalt ions, n_{Co} , determined by the electrochemical approach. We conclude that for electrodeposition at noncatalytic potentials, the deposition charge provides a reliable measure of the amount of deposited cobalt ions. Albeit circumstantially, this result also confirms that the cobalt oxidation state in the deposited catalyst film is Co^{3+} , as reached by one-electron oxidation of the Co^{2+} ions of the buffer solution.

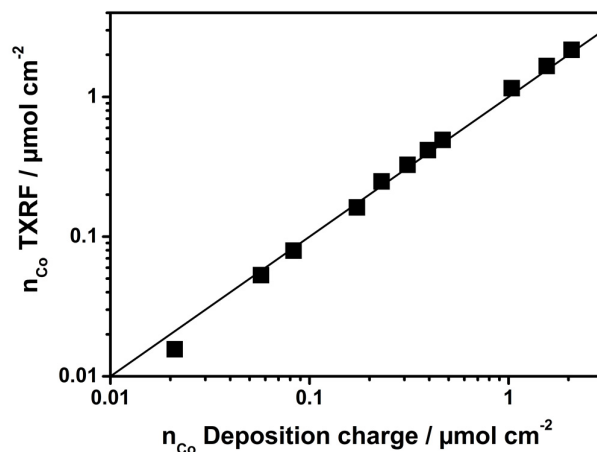


Figure 2.4. Relationship between the amounts of cobalt ions deposited, as determined by elementary analysis (y axis) and calculations from the integrated deposition current (x axis). The amount of cobalt given on the y axis was determined by total reflection X-ray fluorescence (TXRF) after film dissolution in acidic solution. The amount on the x axis was calculated from the deposition charge, Q_{dep} . The solid line corresponds to exactly equal values for TXRF determination and current integration.

2.2.2 Estimation of reduction equivalents

The CVs in Figure 2.3 B and Figure 2.5A show an oxidative, noncatalytic wave in the anodic scan (increasingly positive potentials) before onset of the catalytic wave (> 1.2 V) and the corresponding reductive wave in the cathodic scan. Noncatalytic oxidative and reductive wave are explainable, most likely, by oxidation and reduction of cobalt ions. Integration of the reductive current facilitates an estimation of the number of cobalt ions undergoing oxidation-state changes (see also Risch, Klingan et al. 2012). Upon increasing the film thickness by a factor of 100, the estimated number of redox-active cobalt ions increased by a factor of about 80 (Figure 2.5 B).

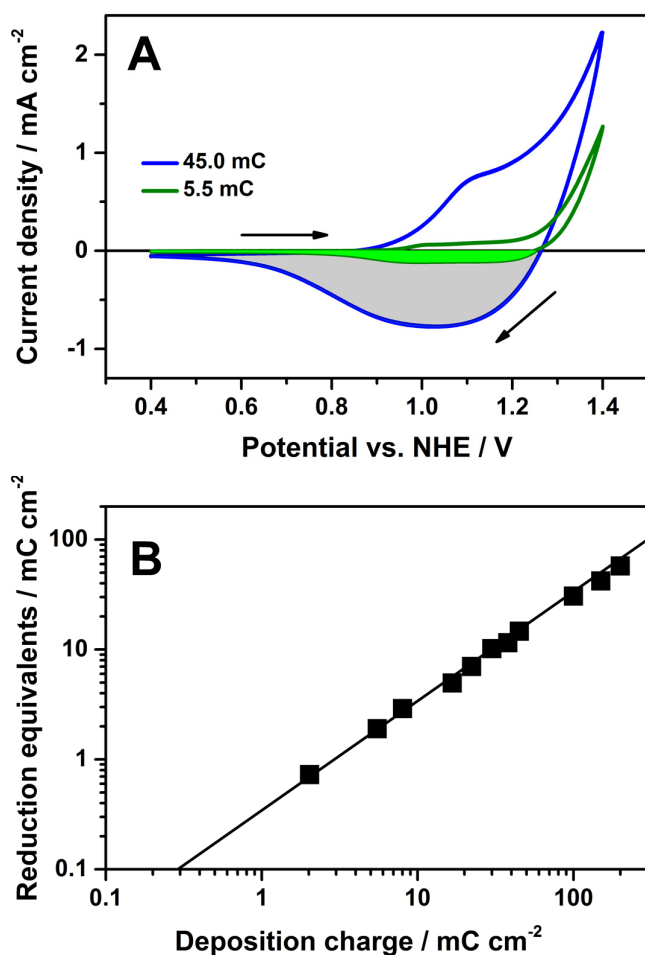


Figure 2.5. CVs and estimated amount of redox-active cobalt ions. **(A)** CVs collected for oxide films with a deposition charge of 5.5 and 45.0 mC cm⁻² at a scan rate of 20 mV s⁻¹. **(B)** Amount (in terms of charge) of redox-active cobalt ions for deposition charges ranging from 2 to 200 mC. The charge that corresponds to the amount of redox-active cobalt ions has been estimated from integration of the reductive current and is several-fold larger for deposition of 45.0 than for 5.5 mC cm⁻² (compare the grey and green areas in A).

As observed in Figure 2.6, the percentage of redox-active cobalt ions estimated from the integration of the reductive cyclic voltammetry current changes from 36 (thin films) to 28 % (thick films). It is conceivable that the fraction of redox-active cobalt ions is even fully independent of the film thickness; the observed changes could relate to an underestimated value of redox-active cobalt ions resulting from increased overlap of catalytic and redox-state currents.

We conclude that, to a good approximation, both the catalytic current (at low potentials) and the number of redox-active cobalt ions is proportional to the film volume and largely unrelated to the geometric interface area separating the bulk oxide and the bulk electrolyte.

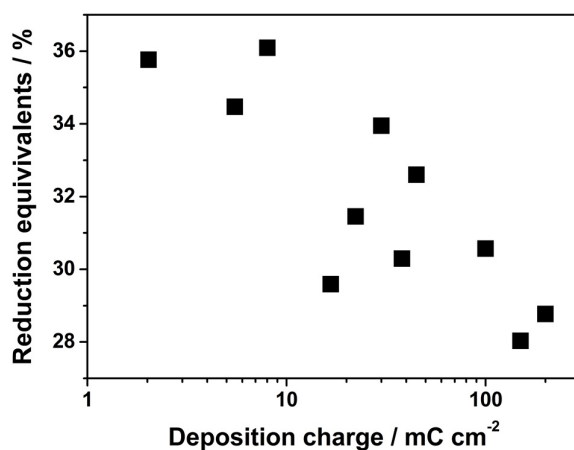


Figure 2.6. Reduction equivalents of the CoCat film followed by cyclic voltammetry. The reduction equivalents measure oxidative charging as a fraction of the one electron oxidation equivalent, n_{red}/n_{Co} , in percent. This was calculated by dividing the number of reduced cobalt atoms (n_{red} , from Q_{red} of CVs) by the total number of deposited cobalt atoms (n_{Co} ; from TXRF). The number of reduced cobalt atoms, n_{red} , was calculated from the reductive charge, Q_{red} , which was obtained by integration of the negative values of the cathodic scan of CVs.

2.2.3 Turnover frequency (TOF)

The current density/deposition charge dependence shown in Figure 2.7 A is remarkable: At all potentials, the relationship between the logarithm of the catalytic current ($\log i$) and the logarithm of the deposition charge (and thus, the number of deposited cobalt ions, $\log n_{Co}$) is linear. However, the slope (m) changes from close to unity at low overpotentials (1.20 and 1.25 V) to about 0.5 at high overpotentials (1.35 and 1.45 V). Thus, Equation 2.4 and consequently Equation 2.5 are obtained:

$$\log i = m \cdot \log n_{Co} + \log i_0 \quad (\text{Eq. 2.4})$$

$$i = i_0 \cdot n_{Co}^m \quad (\text{Eq. 2.5})$$

This means that, with increasing overpotential, the n_{Co} dependence changes from being direct proportionality ($m=1$) to a square-root dependence ($m=0.5$). For application of low potentials to the CoCat film (1.20 and 1.25 V), the catalytic current increased linearly with the deposition charge, and thus, with the amount of cobalt ions in the film (Figure 2.7, $m \sim 1$).

Consequently, for variation in the number of cobalt ions by more than two orders of magnitude, the TOF per cobalt ion stayed fully constant, if this were calculated by taking into account all cobalt ions of the film (Figure 2.7 B). This finding contradicts the simple picture of the CoCat as a solid metal oxide film, for which catalysis takes place only at the interface between the solid oxide material and the bulk electrolyte. The constant TOF is most straightforwardly explained by assuming that, at low electrode potentials, catalysis takes place with equal ease at any position within the bulk of the cobalt oxide material, irrespective of the distance to the bulk–electrolyte interface. The catalytic reactions may take place at internal sites more or less homogeneously distributed within the bulk oxide so that the amount of reactive sites is proportional to the catalyst volume (see section 2.3 Discussion). Albeit unlikely, a 100-fold increase in the electrolyte-exposed surface area of the oxide film might explain the 100-fold increase in catalytic current. To address this possibility, we investigated the nanostructure of the oxide by SEM and the electrochemical surface area quantitatively by impedance spectroscopy.

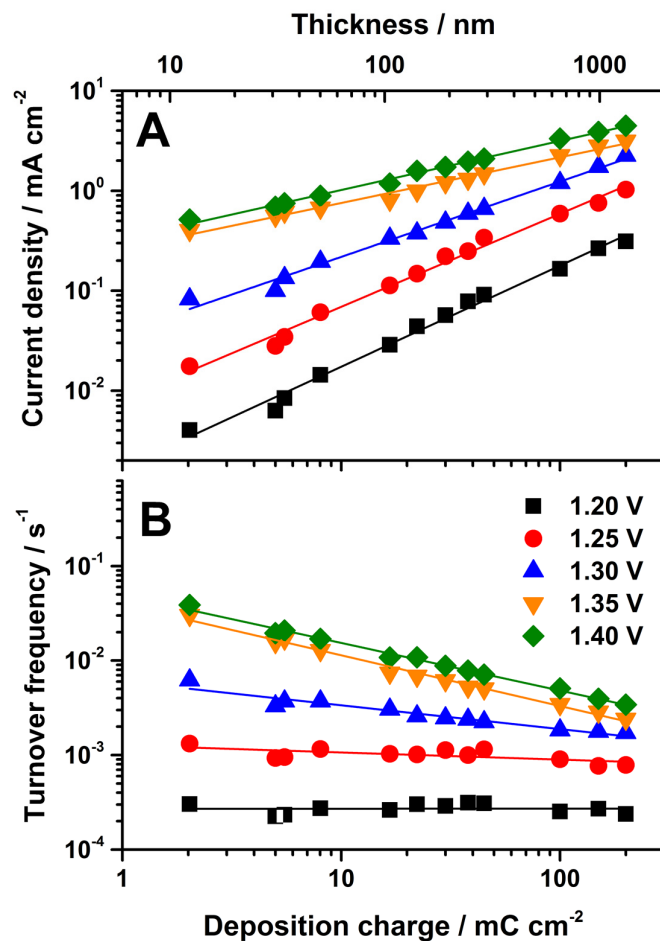


Figure 2.7. (A) Stationary current densities (catalytic currents) for variation of the deposition charge from 2 to 200 mC, at five potentials (vs. NHE, pH 7, in 0.1 M KP_i) applied to the catalyst films previously deposited on the working electrode. (B) Turnover frequency (TOF) per cobalt ion and formed O₂ molecule. The bottom scale (x axis of B) provides the number of deposited cobalt ions in terms of the corresponding deposition charge; 1 mC cm⁻² corresponds to about 10 nmol cm⁻². The top scale in A) provides a thickness estimate based on the electron micrographs shown in Figure 2.11. The current was measured after equilibration for 60 s at the given potential (80% *iR* compensation; *R* of about 50 Ω, as determined by impedance spectroscopy). In A) and B), the lines were obtained by a least-squares fit. In A), the slope values of the straight lines are 0.99 (1.20), 0.91 (1.25), 0.73 (1.30), 0.46 (1.35), and 0.49 (1.40 V) in units of $\log i$ per $\log Q_{dep}$. A slope of 1.0 indicates that the current is proportional to the deposition charge; a slope of 0.5 indicates that the current is proportional to the square root of the deposition charge. In B), the corresponding slopes are 0.02 (1.20), 0.09 (1.25), 0.27 (1.30), 0.54 (1.35), and 0.51 (1.45 V).

2.2.4 Double-layer capacitance

The electrical capacitance of the oxide–electrolyte interface (double-layer capacitance) is predicted to increase with increasing surface area (Levine and Smith 1971). In the CoCat film, the area of the outer film surface, that is, the area of the bulk oxide/bulk electrolyte interface, may determine the double-layer capacitance.

The double-layer capacitance appears due to accumulation and extension of ionic and/or electrical charges at the interface of a solid electrode and the buffered solution (Conway, Birss et al. 1997). In aqueous electrolytes representative values range from 15 to 50 $\mu\text{F cm}^{-2}$ (Grahame 1947, Conway, Birss et al. 1997). However, redox reactions, chemisorption of anions with potential dependent partial Faradaic transfer of an electronic charge (electrosorption valency), and co-occurrence of non-Faradaic double-layer charging and Faradaic surface processes require a modified thermodynamic quantity, the pseudocapacitance (Conway, Birss et al. 1997), where the processes of charging/discharging are described by electron transfer of Faradaic nature. At 0.75 V vs. NHE, the pseudocapacitance influence likely is negligible in the CoCat.

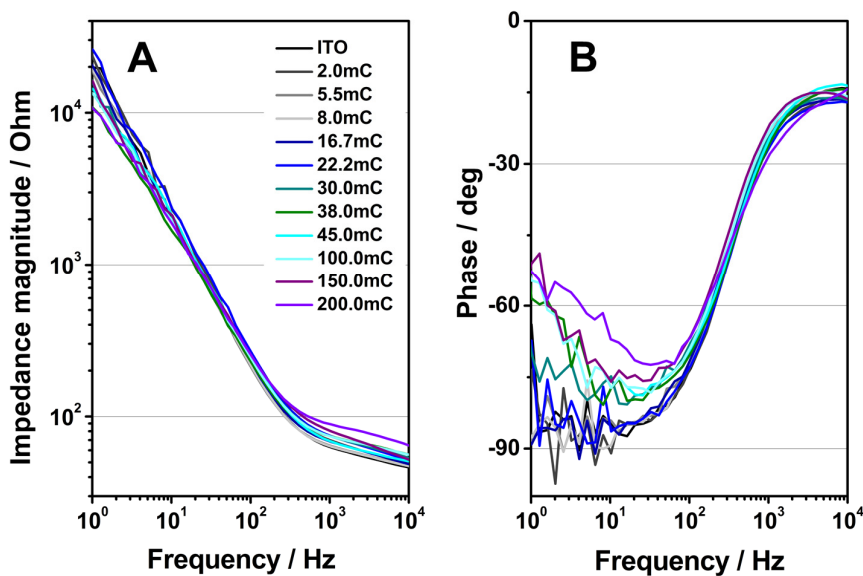


Figure 2.8. Bode representations of impedance with (A) impedance magnitudes (B) and phase shifts in dependence of the frequency, obtained by potentiostatic electrochemical impedance spectroscopy for CoCat films of various thicknesses (various deposition charges). Potentiostatic electrochemical impedance spectroscopy was performed at 0.75 V in 0.1 M KPi at pH 7.

Figure 2.8 shows a typical Bode plots of CoCat films of different thickness (variation of deposition charge as described in 2.1.1), where the impedance magnitude and the phase response are plotted as a function of the frequency. In the high frequency region the system is mostly resistive, as the phase shift approaches 0° . The deviation from the phase angle of 0° may be due to consequences of the amorphous, layered, and hydrated components of the CoCat, as 0° is predicted for ideal model interfaces. At low frequencies the phase angle for all CoCat $< 30 \text{ mC cm}^{-2}$ are approaching -90° , which means that the system behaves like a pure capacitor. Thicker CoCat films exhibit a slightly higher phase angle between 0 and 10 Hz after undergoing a minimum, which may be due to a vanishing influence of the ITO substrate.

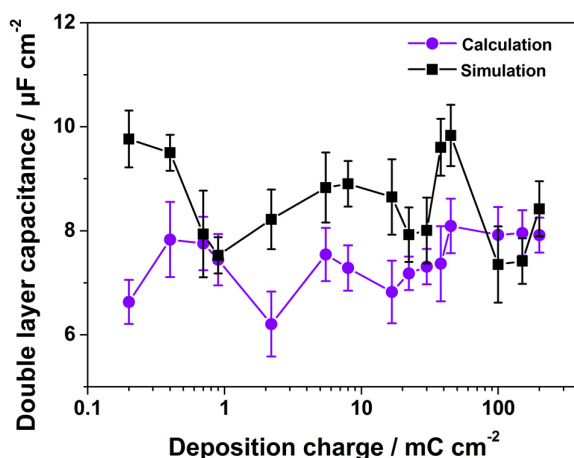


Figure 2.9. Calculated (purple circles) and simulated (black squares) values for the double-layer capacitance from electrochemical impedance spectroscopy data of Figure 2.8. Values were calculated from the imaginary parts of impedance at 33 Hz assuming that this value is predominantly determined by the double-layer capacitance. Simulation was performed with an equivalent circuit displayed in Figure 2.2. The lines are a guide for the eye.

As we monitored the CoCat at 0.75 vs. NHE with impedance spectroscopy, thus in absence of redox reactions and water oxidation, the determination of the double-layer capacitance is straightforward and independent of the model. Already visual inspection of the impedance spectra illustrates that the surface capacitance is thickness independent (about $8 \mu\text{F}$; Figure 2.8 and 2.9). The results of calculating and fitting (equivalent circuit) the double-layer capacitance are displayed in Figure 2.9. Double-layer capacitance values fluctuate between 6 and $10 \mu\text{F cm}^{-2}$ within partially overlapping error ranges ($7.4 \pm 0.5 \mu\text{F cm}^{-2}$ for the calculation and $8.5 \pm 0.6 \mu\text{F cm}^{-2}$ for the simulation, the ITO exhibits $7.2 \pm 0.3 \mu\text{F cm}^{-2}$ and $8.2 \pm 0.4 \mu\text{F cm}^{-2}$ respectively). We are aware that the double-layer (surface) capacitance does not necessarily reflect the outer surface area directly. In

the CoCat film, the presence of mobile water molecules and ions may lend the properties of a conducting electrolyte to the bulk material, as suggested previously (Burke and O'Sullivan 1981) for amorphous iron oxide layers. Consequently, the experimentally determined double-layer capacity might relate rather to the interface between the well-conducting indium tin oxide (ITO) electrode and the CoCat material than to the bulk oxide/bulk electrolyte interface.

As there is no observable change in the DLC for a variation of the deposition charge from 2 to 200 mC cm^{-2} , we may deduce that the surface area of the different thick CoCats does not change with increasing deposition charge. Therefore, we conclude conservatively that impedance spectroscopy does not provide any positive indication for a surface area increase.

2.2.5 Scanning electron microscopy (SEM)

As illustrated by the SEM images in Figures 2.10 and 2.11, increasing amounts of deposited cobalt ions result in a proportional increase of the thickness of the cobalt oxide films: for variation of the deposition charge by a factor of 10 (from 5 to 50 mC), the layer thickness increased from about 50 to 500 nm. In the SEM images in Figure 2.11, the bulk of the oxide film appears to be homogeneous. The surface is rough in both films, but the extent of roughness appears to be similar (irregular thickness variations by about ± 10 nm). We note that crack formation (Kanan and Nocera 2008) and detachment from the electrode surface result from vacuum drying of the CoCat film during the SEM measurements, as confirmed by environmental SEM (ESEM) on wet films (Esswein, Surendranath et al. 2011). The latter experiments have not provided any evidence for further drastic morphology changes caused by the vacuum drying statement. In conclusion, upon increasing the volume of deposited oxide 10-fold, there are no indications for a corresponding increase in the area of the external film surface exposed to the electrolyte bulk phase.

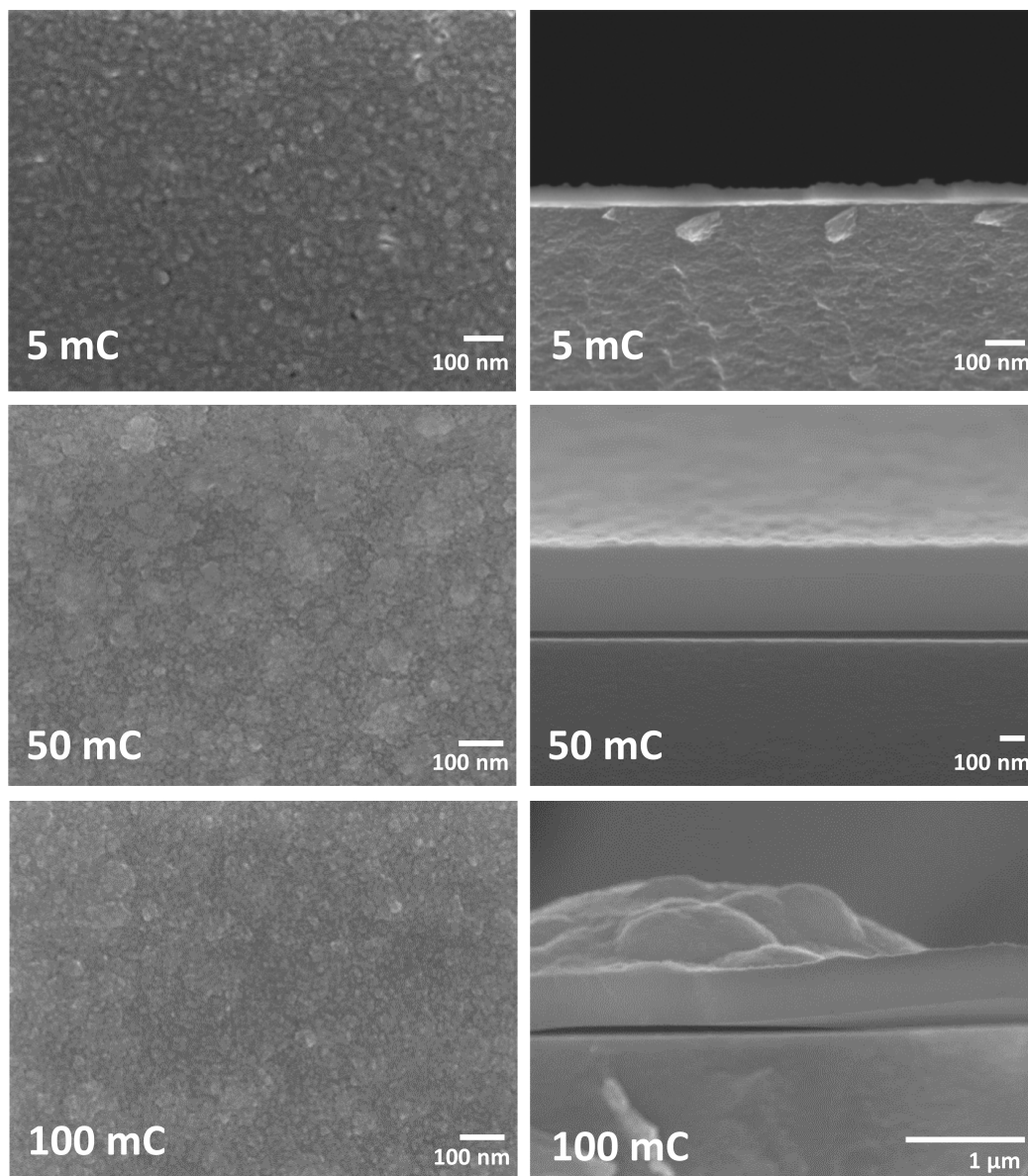


Figure 2.10. Scanning electron microscopy (SEM) measurements of CoCat films electrodeposited on ultrathin glassy carbon slides with increasing deposition charges of 5 mC, 50 mC and 100 mC cm⁻². The CoCat films were dried under nitrogen after deposition and measured without any surface modification. Due to the good contact between the CoCat film and the GC wafer no overcharging was observed ensuring a good resolution of the surface structures. The left column represents the top-view images of the film surface and the right column the respective cross-section. From the top-view image it can be seen that in all the cases the films exhibit a homogeneous granular surface structure with grain sizes around 3-5 nm. Cross-section measurements evidence a homogeneous structure of the film throughout the full film thickness. Film thicknesses of 39±6 nm, 344±9 nm, and 460±20 nm were measured. Especially the number for the 100 mC film may be highly imprecise because of severe modification by dehydration caused by the vacuum conditions of the SEM measurements.

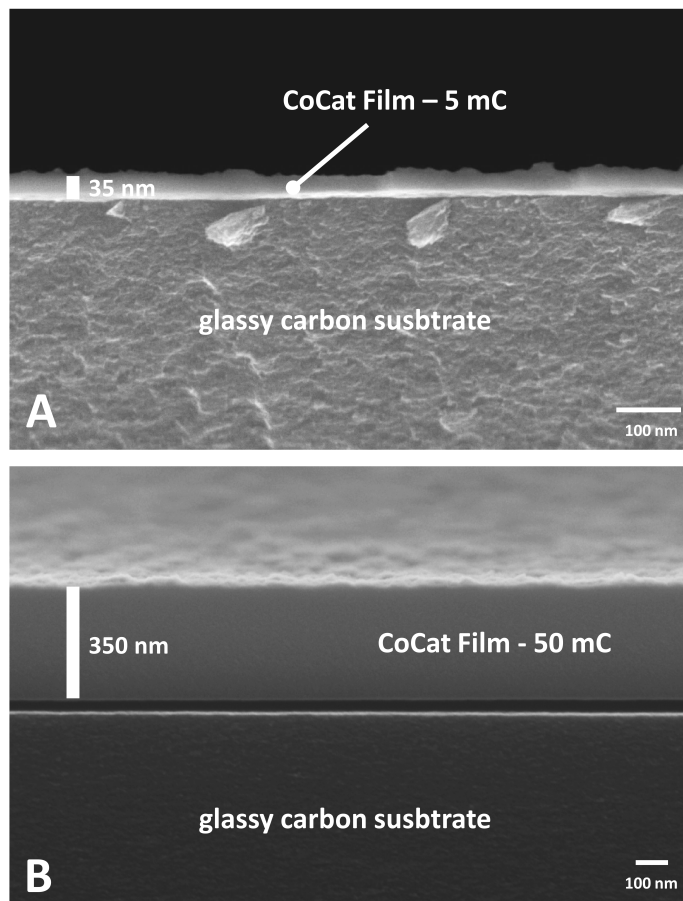


Figure 2.11. SEM images for the electrodeposition of 5 (A) and 50 mC cm^{-2} (B) of cobalt ions on glassy carbon. In B), the catalyst material became detached from the glassy carbon electrode (gap between electrode and catalyst film); this can be explained by tension resulting from partial dehydration of the hydrated oxide during the SEM experiment. The SEM images suggest an increase in the film thickness by about 7 nm per mC of cobalt ions deposited per square centimetre (1 mC corresponds to about 10 nmol). This estimate represents a lower limit of the *in-situ* thickness because severe dehydration during the SEM measurements (performed under vacuum) may have caused shrinkage (or deswelling) of the film. The length of the white bars indicating the thickness of the CoCat film correspond to 35 and 350 nm, respectively; more precise measurement of the film thicknesses resulted in values of (39 ± 6) and (344 ± 9) nm.

2.2.6 pH titrations

As clearly visible in Figure 2.7, the catalytic current is proportional to the amount of deposited cobalt ions, but only at the low current densities achieved at low electrode potentials. At high current densities, seemingly a second factor becomes a decisive codeterminant of the catalytic rate. Because mass transport limitation related to a limited availability of water is unlikely, we focused on the role of the molecules employed as a pH buffer in the aqueous electrolyte.

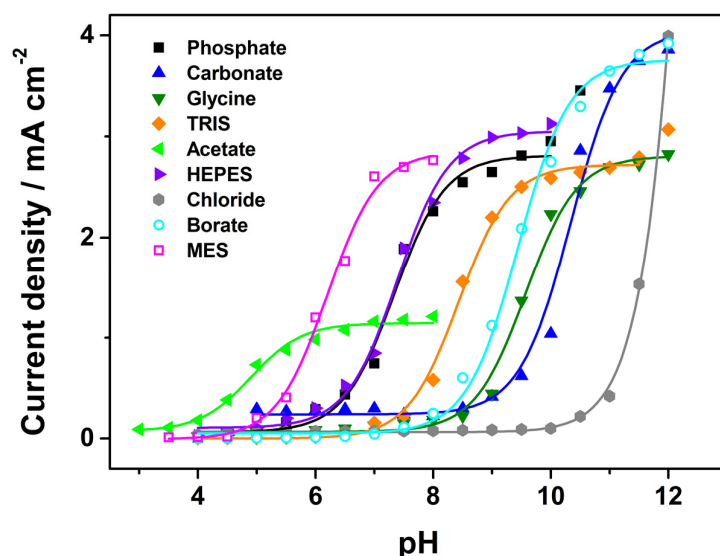


Figure 2.12. pH titrations of the catalytic current at 1.35 V (vs. NHE) in various buffer systems. The respective electrolyte consisted of the indicated buffer system at a concentration of 0.1 M. The lines were obtained by means of simulations assuming that the catalytic activity was proportional to the relative concentration of base. The respective pK_a values were determined by curve fitting, which is shown for glycine in Figure 2.13. The titration was performed from low to high pH by the addition of NaOH under continuous stirring (~ 700 rpm) and simultaneous pH detection by an electrode; currents were recorded after stabilisation of the current (equilibration) at the given pH.

By using a variety of buffer molecules, pH titrations of the stationary (catalytic) current were performed for application of a constant electrode potential. The selected potential of 1.35 V was well within the potential regime at which the proportionality of deposition charge and catalytic current breaks down. The resulting titration curves are shown in Figure 2.12. The observed pH dependence differs from the canonical behaviour of electrocatalysts, as discussed further below (section 2.3), and resembles the titration curves of a base in aqueous solution. Therefore, we approached simulation of these curves by assuming that the catalytic current was proportional to the relative concentration of the base, that is, the unprotonated buffer molecule. All pH titration

curves could be simulated with reasonable quality (solid lines in Figure 2.12 and example of glycine in Figure 2.13); the resulting pK_a values are shown in Figure 2.14. The data agree remarkably well with the known pK_a values of the respective buffer base in aqueous solution.

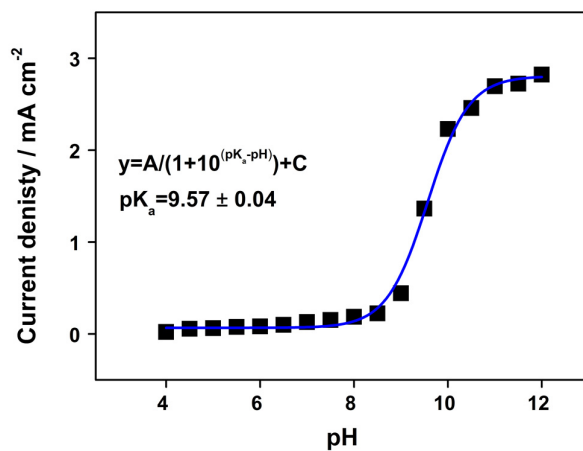


Figure 2.13. Example of the simulation of a titration curve of the CoCat in 0.1 M glycine. The titration was performed from low to high pH by the addition of NaOH under continuous stirring (~700 rpm) and simultaneous pH detection by an pH-electrode; currents were recorded after stabilisation of the current (equilibration) at the given pH.

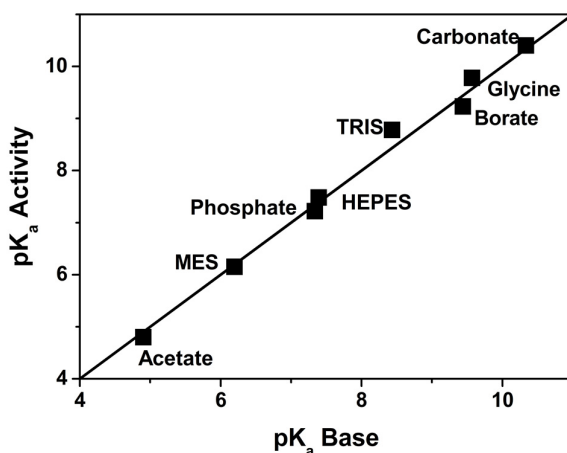


Figure 2.14. Comparison of pK_a values determined by simulation of the pH dependence of the catalytic current (y axis) and the pK_a of the respective buffer molecule (x axis). The solid line of unity slope corresponds to exactly equal pK_a values.

It has been shown before that the Faradaic efficiency of oxygen evolution equals, within experimental accuracy limits, 100 % for the phosphate buffer system (Kanan and Nocera 2008). Similarly the oxidative side reaction in the borate and carbonate buffer can essentially also be excluded. In the other buffer systems, we cannot definitely exclude that, aside from water, the respective carbon-containing buffer molecule is also oxidised (see footnote 5 in Gerken, McAlpin et al. 2011) in a reaction exhibiting the same pH dependence as water oxidation, but consider this unlikely.

The above analysis of the pH dependence at constant, relatively high electrode potential indicates that the catalytic current at higher electrode potentials is proportional to the absolute or relative concentration of the unprotonated form of the buffer molecule in the electrolyte solution, irrespective of the buffer system used. The availability of unprotonated buffers in the electrolyte appears to control the catalytic current.

2.2.7 Atomic structure

The structure at the atomic level was investigated by X-ray absorption spectroscopy (XAS) at the cobalt *K*-edge (Figure 2.15). The spectra resulting from application of this bulk-sensitive method show that neither the average cobalt oxidation state nor changes of the atomic structure are caused by variation of the layer thickness of the catalyst film.

We conclude that, irrespective of the film thickness, the same nanosized clusters of di- μ -oxo bridged Co^{3+} ions were formed (Risch, Khare et al. 2009, Risch, Ringleb et al. 2009, Kanan, Yano et al. 2010, Du, Kokhan et al. 2012, Risch, Klingan et al. 2012), as recently reviewed in detail elsewhere (Risch, Klingan et al. 2014).

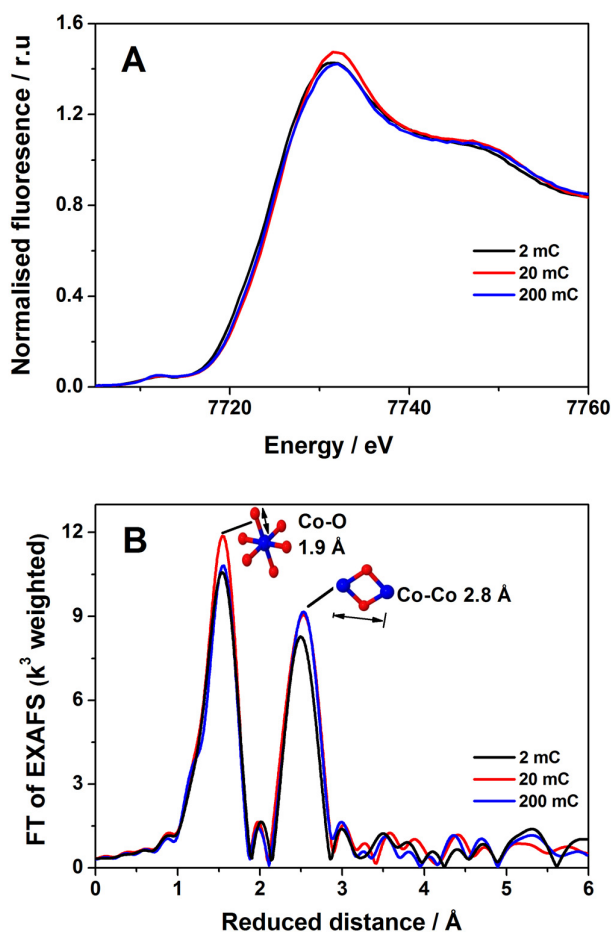


Figure 2.15. (A) Co *K*-edge XANES spectra and (B) Fourier-transforms (FT) of experimental EXAFS spectra of the cobalt catalyst for various amounts of deposited Co ions (measured in terms of the indicated deposition charge).

2.3 Discussion

Herein, the rate of electrochemical water oxidation catalysed by an amorphous cobalt oxide film was investigated by means of 1) variation of the film thickness and 2) pH titration in various electrolyte buffer systems. These experiments provide insight into the relative importance of reactivity and transport phenomena proceeding 1) within the bulk of the oxide film or 2) at the outer film surface facing the bulk electrolyte, as discussed in the following.

2.3.1 Outer surface versus bulk material reactivity

At low overpotentials, the rate of catalysis is proportional to the number of deposited cobalt ions (Figure 2.7). Thickness variation affects neither the atomic structure nor the electrolyte-exposed surface area significantly (Figures 2.10, 2.11, and 2.15). Thus, we conclude that, for variation of the volume-to-surface ratio by a factor of 100, the activity per volume of the catalyst film stays constant. This finding implies that the bulk volume of the oxide material is catalytically active. Similarly the redox activity, that is, the capability to undergo oxidation-state changes, also appears to be a volume property of the catalysts film (Figure 2.5 B).

Relationships between structure of (micro-)crystalline oxides of various elemental composition and their activity in water oxidation have been reported for series of metal oxides since the 1980s (Trasatti 1980, Trasatti 1984, Harriman, Pickering et al. 1988), and recently (Suntivich, May et al. 2011, Gardner, Go et al. 2012, Landon, Demeter et al. 2012, Trotochaud, Ranney et al. 2012, Bajdich, García-Mota et al. 2013, Calle-Vallejo, Inoglu et al. 2013, Grimaud, Carlton et al. 2013, Grimaud, May et al. 2013, Louie and Bell 2013, Robinson, Go et al. 2013, Smith, Prévot et al. 2013). Recent spectroscopic investigations indicate that the surface structure of some oxide crystallites can differ significantly from that of the crystalline phase (Lee, Carlton et al. 2012, May, Carlton et al. 2012, Su, Gorlin et al. 2012, Doyle, Godwin et al. 2013, Gorlin, Lassalle-Kaiser et al. 2013, Risch, Grimaud et al. 2013, Bergmann, Martinez-Moreno et al. 2015, Gonzalez-Flores, Sanchez et al. 2015), akin to the model of Burke and O'Sullivan (Burke and O'Sullivan 1981), which is outlined further below. Nonetheless, often the site of catalysis has been assumed (implicitly or explicitly) to be an original or only moderately restructured crystal surface, without any volume activity of the oxide particles or films. In the light of these and numerous other reports on heterogeneous catalysis at surface sites, the finding of the volume activity of the CoCat film may come as a surprise. However, it depends on the viewpoint to what extent the volume activity of the CoCat film is conceived as being surprising. In the structurally closely related cobalt oxides employed in lithium-ion batteries (LiCoO_2 | CoO_2) (Amatucci, Tarascon et al. 1996) and

electrochemical supercapacitors (*e.g.*, $\text{Co}(\text{OH})_2 \mid \text{CoOOH}$) (Conway 1991, Fedorov, Linnemann et al. 2013), the redox activity of all cobalt ions of the oxide is essential for optimal charging capacity; similarly important is the diffusion of lithium ions within the battery oxide (Thomas, Bruce et al. 1985, Zhang, Lu et al. 2007) or protons within the supercapacitor material (Srinivasan and Weidner 2002). In research on battery and capacitor oxides, it is commonly assumed that redox activity and cation diffusion is not restricted to (nano)particle surfaces or grain boundaries, but can extend over the bulk of the material.

In research on alkaline water oxidation, metal electrodes previously exposed to a potential-cycling protocol have been discussed in terms of a three-layer concept, involving 1) a metal layer, 2) a compact oxide, and 3) the electrolyte-exposed ‘hydrous oxide’ (Burke and O’Sullivan 1981, Doyle, Godwin et al. 2013). Burke and O’Sullivan state: “*The skeletal nature of the (hydrous) oxide is clearly a major advantage from an electrocatalytic viewpoint as it permits a major increase in the number of oxycations participating in the electrode reaction.* (Burke and O’Sullivan 1981)” Although quantitative assessment by experiments analogous to the ones reported in Figure 2.7 has not been approached before this one (to the best of our knowledge), the participation of the majority of iron ions within the hydrous oxide layer in water-oxidation catalysis is experimentally well supported; for a comprehensive review, see Doyle, Godwin et al. 2013. We propose that the hydrous oxide layers are comparable to the amorphous cobalt oxide investigated herein, which means that they share volume activity and other functionally crucial properties.

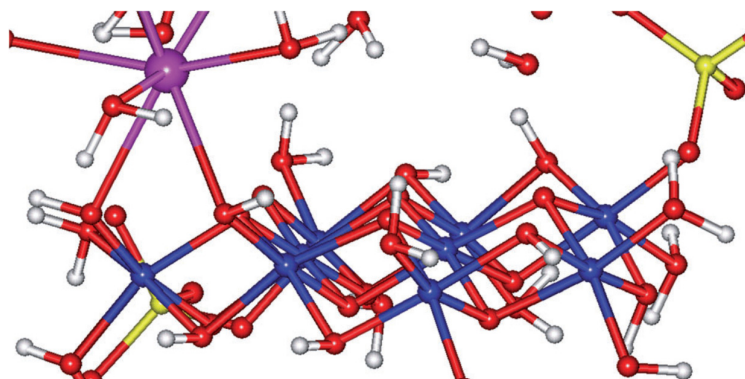


Figure 2.16. Illustration of a cobalt oxide fragment and the surrounding quasiaelectrolyte consisting of potassium and phosphate ions and water molecules; nine cobalt ions are interconnected by bridging oxygen atoms. Water oxidation is assumed to take place at the margins of the planar cobalt–oxo fragment involving terminally coordinated water species or $\mu_2\text{-O}(\text{H})$ bridges at the fragment margins. Potassium or phosphate ions could interconnect various cobalt–oxo fragments; cross-linking by mono- μ -oxo bridges between cobalt ions is also not excluded. This picture serves merely for illustrative purposes and was not obtained by quantitative molecular modelling. Colour codes are the following: cobalt, blue; potassium, violet; phosphor, yellow; oxygen, red; and hydrogen white.

The volume activity of the CoCat material can be understood in terms of its structural properties (Figure 2.16). We (Risch, Khare et al. 2009, Risch, Ringleb et al. 2009, Risch, Klingan et al. 2012) and others (Kanan, Yano et al. 2010, Du, Kokhan et al. 2012, Khnayzer, Mara et al. 2012, Farrow, Bediako et al. 2013) found that the amorphous oxide consisted of cobalt oxide fragments with intrafragment connection of the octahedrally coordinated cobalt ions by di- μ -oxo bridges (edge-sharing of CoO_6 octahedra). Water molecules, anions (phosphate), and cations (potassium) are predicted to occupy the space between $\text{Co}_n(\mu\text{-O})_{2n-m}$ fragments (Dau, Limberg et al. 2010, Gerken, McAlpin et al. 2011), which are likely to involve cation binding to $\mu\text{-O}$ atoms of the oxide particle (Risch, Klingan et al. 2012) and possibly anion binding at terminal cobalt coordination sites (Risch, Klingan et al. 2012, Risch, Shevchenko et al. 2012). Whether the oxide fragments form fully disordered polymeric networks of metalate units or whether planar fragments are stacked, as found in layered manganese oxides of the birnesite or busserite type (Golden, Chen et al. 1987, Post 1999), with one (birnesite) or two (busserite) cation–water layers between oxide fragments, is still unknown.

The outlined picture of cobalt oxide fragments of molecular dimensions embedded in a quasi-electrolyte consisting of water, anions, and cations (Figure 2.16) renders the catalytic activity of the bulk material less surprising. Water oxidation can take place at the outer margins or at internal vacancies of oxide fragments; proton transfer can occur within networks of hydrogen-bonded phosphate ions, water molecules, and bridging hydroxides found at the margins of oxide fragments (Mattioli, Risch et al. 2011, Bediako, Costentin et al. 2013). Water oxidation at the margins of oxide fragments is supported by the inverse correlation between fragment size and catalytic activity described in Risch, Klingan et al. 2012. Thus, we propose that the volume activity of the CoCat material results from reactive sites present throughout the CoCat film at the margins (edges) of the individual oxide fragments. Continuous catalysis of water oxidation is maintained by the capability of the quasioelectrolyte present between oxide fragments to conduct protons effectively from the bulk phase toward the bulk–electrolyte interface (Figure 2.1).

2.3.2 Noncanonical pH dependence due to electrolyte bases

The role of proton-accepting electrolyte bases was investigated by pH titration of the current density at relatively high electrode potential of 1.35 V (vs. NHE), for bases covering a wide range of pK_a values. The observed pH dependence is nonclassical in several regards. The often-observed ‘classical’ behaviour is that the electrocatalytic current rises exponentially for increasing pH, resulting in a linear increase of the current logarithm.

For the CoCat film at low electrode potentials, the current logarithm indeed increases linearly with increasing pH; the slope is close to unity ($\log_{10}i = s \cdot \text{pH}$ with $s \sim 1$ (Surendranath, Kanan et al. 2010)). At 1.35 V, however, this behaviour is not observed in any of the buffer systems used (clearly visible in Figure 2.12 and Figure 2.17). Second, the pH dependence of the electrocatalytic current is typically assumed to reflect the pH dependence of the rate-determining step of the catalyst, and thus, is predicted to be independent of the buffer system used (Koper 2013). In clear contrast, the data of Figures 2.12 and 2.17 imply that the electrochemical overpotential needed to reach a current level of 1 mA changed by more than 0.2 V from below 0.5 V in MES buffer to about 0.7 V in carbonate buffer.

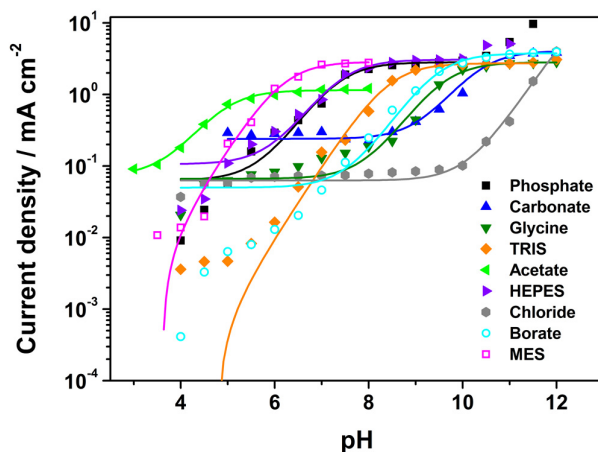


Figure 2.17. Titration curves of the CoCat film at a catalytic current of 1.35 V vs. NHE in various buffer systems. The shown data points and simulations are fully identical to ones shown in Figure 2.12, but the current density is displayed using a logarithmic scale.

In Figures 2.12 and 2.17 the maximal currents reached at high pH values mostly do not depend significantly on the pK_a of the electrolyte base. Only in the case of acetate, we observed reproducibly lower catalytic currents, suggesting that its lower proton binding energy might have resulted in diminished rates of proton uptake by the acetate base. In this context, it is of interest that a significant catalytic current at pH values below eight is found when using carbonate buffer. This may be explainable by the capability of the HCO_3^- base to accept protons (pK_a of 3.6), albeit at clearly lower rate than that of the CO_3^- base (pK_a of 10.3). It is also remarkable that the catalytic current stays low until pH 10 and rises steeply at higher pH values in the absence of specific buffer molecules (chloride electrolyte in Figure 2.12). This behaviour is most likely explainable by OH^- ions acting as especially efficient proton acceptors.

In conclusion, the efficiency of the bases acting as proton acceptors appears to be largely independent of the pK_a for values ranging from five to ten. Bases with lower pK_a (in acetate or hydrogen carbonate) may be (slightly) less efficient proton acceptors; the hydroxide ion with its high pK_a appears to act as an especially efficient proton acceptor at high pH. Future in-depth investigation into the role of the buffer pK_a on the rate or efficiency of proton removal from the water-oxidation catalyst will be of high interest.

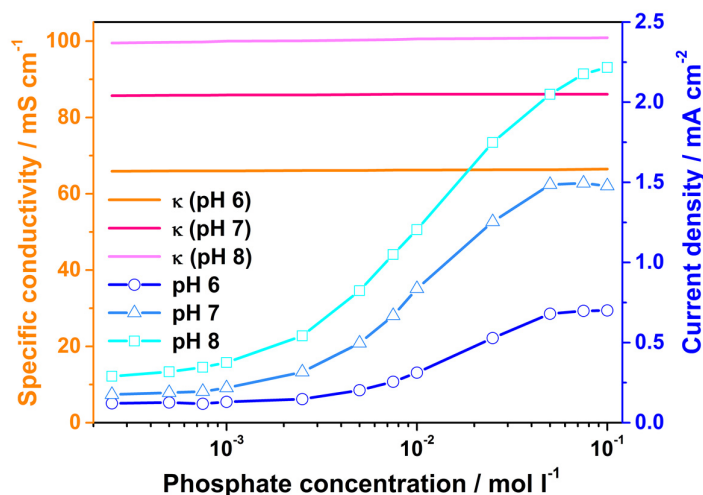


Figure 2.18. Phosphate concentration dependence of the catalytic current measured at 1.35 V (vs. NHE). The right axis provides the current density, the left axis the specific conductivity (κ) of the electrolyte as measured with a conductivity meter (GMH 3410, Greisinger GmbH, Germany). The phosphate concentration was varied by stepwise addition of increasing amounts of a phosphate buffer (1 M phosphate) to a potassium sulphate (K_2SO_4 , 100 mL) solution of approximately identical specific conductivity. The pH was adjusted by changing the ratio of K_2HPO_4 and KH_2PO_4 in the phosphate buffer solution and controlled by measurements using a calibrated pH electrode. Inside of the electrochemical cell, the electrolyte was continuously stirred. Each addition of the phosphate buffer solution (to the electrolyte in the electrochemical cell) was followed by a mixing and equilibration phase of about 2 min; the indicated current densities were detected at the end of the equilibration period. The CoCat films used in this experiment had been deposited for 1.5 h at a potential of 1.35 V vs. NHE resulting in ‘thick films’ with about 500 nm of cobalt ions per cm^2 . We note that the half-saturation value at pH 7 and pH 8 is close to 10 mM phosphate; at pH 6 it may be slightly higher (close to 20 mM). Figure reproduced from diploma thesis of Franziska Ringleb, 2009.

In the following, the site of proton uptake by the buffer base is discussed. Recently, Bediako et al. investigated the transport processes in water oxidation by the CoCat films by comprehensive simulations based on a set of equations describing reaction kinetics and diffusion processes (Bediako, Costentin et al. 2013). When modelling the contributing processes, they assumed that the deprotonated, negatively charged base (HPO_4^{2-}) diffuses through the complete film from the outer surface of the bulk oxide towards the oxide layer at the surface of the conducting substrate electrode (e.g., ITO on glass), where proton uptake by the base takes place (formation of $H_2PO_4^-$).

To reconcile this hypothesis from Bediako et al. with our experimental findings in a reasonably straightforward way, one would need to assume that, at the surface of the substrate electrode and in the special environment of the hydrated cobalt oxide, the protonation state of the buffer base corresponds exactly to the respective protonation state in the bulk electrolyte, which is unlikely. Moreover, the relatively large buffer bases investigated herein (for example HEPES) would also need to diffuse twice through the complete CoCat film without resulting in diminishment of the catalytic current by diffusion limitations. Therefore, we consider it more likely that proton uptake by the buffer base proceeds at the bulk oxide/bulk electrolyte surface involving either adsorbed buffer molecules or collisional proton transfer. The phosphate concentration dependence of the catalytic current exhibits saturation behaviour as displayed in Figure 2.18, and thus, may support the former option, namely, adsorption of the buffer base involving either chemical binding (chemisorption) or physical association (physisorption).

To proof the structural similarity of CoCat films deposited at 1.05 V and 1.35 V (used in the experiment in Figure 2.18), Fourier-transforms (FT) of experimental EXAFS spectra are displayed in Figure 2.19.

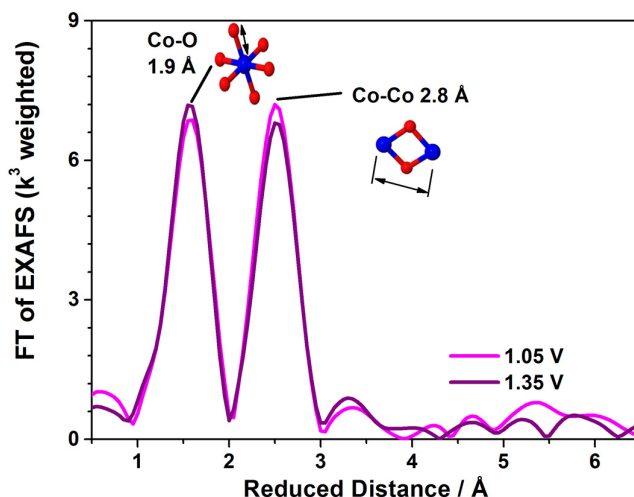


Figure 2.19. Fourier-transforms (FT) of experimental EXAFS spectra of the cobalt catalyst deposited at 1.35 V vs. NHE for 47 nmol Co (purple) and at 1.05 V for 48 nmol Co (magenta) are shown. Structural motifs corresponding to the two peaks are schematically displayed.

Final clarification on the exact mechanism of water oxidation in transition metal oxide films needs to await more extensive experimental characterisation. Experimental tracking of location and diffusion of the buffer molecules would be desirable, but will require new methodical developments.

The availability of a special proton-accepting base in the aqueous electrolyte appears to be an essential requirement for efficient water oxidation at moderate pH. We emphasise that the observed pH dependence is not a classical ‘thermodynamic’ overpotential dependence, but results from a kinetic pH effect, namely, the requirement that unprotonated buffer bases facilitate kinetically efficient proton removal from the catalyst. Classical electrolyzers operate either at extremely high pH (alkaline electrolysis, *e.g.*, in KOH solutions of at least 0.1 M) (Zeng and Zhang 2010) or low pH (acid electrolysis, for example in sulfuric acid) (Carmo, Fritz et al. 2013), and mechanistic investigations have mostly been focused on unravelling either the alkaline or the acidic reaction (Dau, Limberg et al. 2010, Carmo, Fritz et al. 2013). In alkaline water oxidation, the presence of hydroxide ions renders an additional acceptor base superfluous; in acidic water oxidation, proton transfer to water molecules is kinetically efficient enough. Today, however, water oxidation at moderate pH values is also of high technological interest, for which proton-acceptor bases are clearly pivotal. We see the need for more extensive investigations into their mechanistic role and transport properties to facilitate the rationale design of technological systems for water splitting in the moderate pH regime.

2.3.3 Nonsaturating thickness dependence at high overpotentials

To our surprise, we did not observe saturation of the catalytic current for increasing amounts (n_{Co}) of deposited cobalt ions. Instead the current increases proportionally to the square root of n_{Co} at 1.35 and 1.45 V (see Figure 2.7 and Equation 2.4 and 2.5). Is the observed nonsaturating, square-root dependence compatible with a limitation by proton transfer to the buffer base? The approximate quantitative model described in the following addresses this question.

At high overpotentials, the internal proton concentration, C_H^{int} , within the catalyst film is assumed to exceed the external proton concentration in the bulk electrolyte. Neglecting diffusion limitations and reversibility of proton transfer, the rate of proton transfer to the buffer molecules of the bulk electrolyte is described by Equation 2.6:

$$R_H = k_H \cdot C_H^{int} \quad (\text{Eq. 2.6})$$

Here, k_H depends on the concentration and type of employed buffer base, on pH (through the protonation state of the buffer base), and on other factors.

By measurements at low current densities, the catalytic current has been found to increase by a factor of close to 10 per pH unit; this implies that the intrinsic rate of catalysis (per cobalt ion),

k_{Cat}^{int} , is inversely proportional to the proton concentration (Surendranath, Kanan et al. 2010). Thus, we can describe, to a first approximation, the rate of catalysis by Equation 2.7;

$$R_{Cat.} = n_{Co} \cdot k_{Cat.}^{int} / C_H^{int} \quad (\text{Eq. 2.7})$$

in which $k_{Cat.}^{int}$ depends on the electrode potential and other factors, but not on the proton concentration. After equilibration of the catalytic current, $R_{Cat.}$ equals $4R_H$. Exploiting this equality, mathematically straightforward rearrangements result in Equation 2.8:

$$R_{Cat.} = n_{Co}^{1/2} \cdot (4k_H \cdot k_{Cat.}^{int})^{1/2} \quad (\text{Eq. 2.8})$$

We emphasise that this highly approximate description is applicable only to the situation at high overpotentials. Extension of the above model by also taking into account the reversibility of the proton transfer step is straightforward and predicts proportionality between catalytic currents and n_{Co} at low rates of catalysis (low overpotentials). Extension by inclusion of diffusion limitations by internal proton transport will be more intricate (Bediako, Costentin et al. 2013), but may explain the intermediate slope at intermediate overpotentials of 1.30 V vs. NHE. In any event, the outlined simplistic model can explain that the catalytic current rises proportionally to the square root of n_{Co} , without displaying saturation behaviour.

In conclusion, the experimentally observed nonsaturating, square-root-type thickness dependence of the catalytic current is compatible with both catalytic activity throughout the bulk oxide material and limitation of the catalytic rate by proton transfer to the buffer base.

The observed thickness dependence of the catalytic current is also consequential with regard to technological application. It could mean that increasingly thick layers of the oxide film will result in increasingly higher catalytic current densities. Indeed, for electrodeposition of very high amounts of cobalt ions on a nickel foam electrode, current densities of 100 mA cm⁻² have been reached at an overpotential of only 360 mV (Esswein, Surendranath et al. 2011). We find that proton transfer to the electrolyte base becomes a limiting factor at higher overpotentials, but even then the catalytic current increases with the square root of the amount of deposited cobalt ions. However, at high overpotentials and a layer thickness beyond the range investigated herein, severe transport limitations assignable, for example, to proton transport within the catalyst material and diffusion of the buffer base might become a limiting factor, as discussed in Bediako, Costentin et al. 2013, for which the existence of an optimal layer thickness has been predicted and beyond which the current does not increase further.

Concluding, the results reported herein imply a continuous increase of the catalytic current density with increasing thickness of the amorphous catalyst film. An optimal thickness is reached either only for deposition charges clearly exceeding 200 mC cm^{-2} (clearly exceeding $2 \text{ } \mu\text{mol cobalt per cm}^2$) or is never reached at any practicable thicknesses level, as suggested by other results (Esswein, Surendranath et al. 2011). An increase in the layer thickness is apparently a useful strategy toward improved catalytic performance.

2.4 Summary

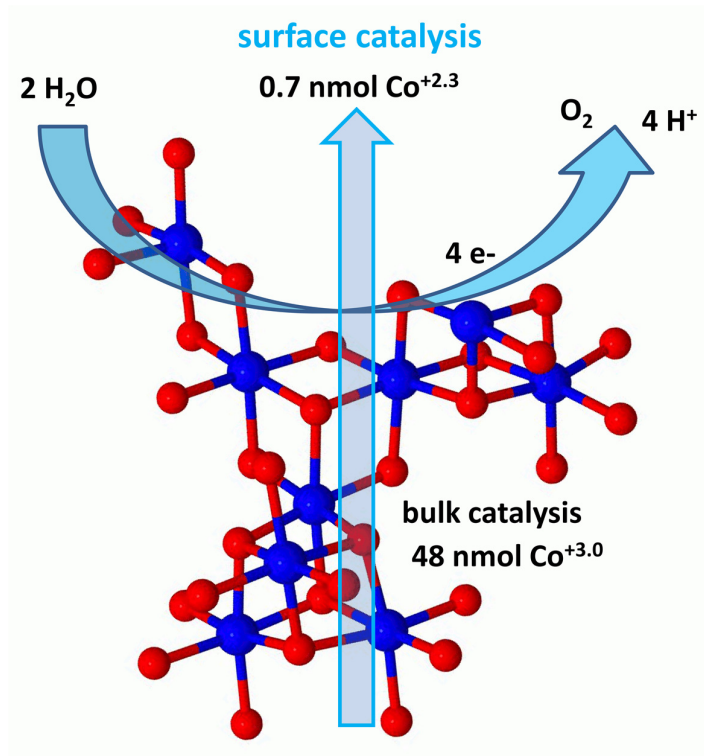
In the amorphous and hydrated cobalt oxide, catalysis of water oxidation does not take place exclusively at the bulk oxide/bulk electrolyte surface, but throughout the hydrated oxide material. Therefore, at low overpotentials, the current density is directly proportional to the amount of deposited cobalt ions, and thus, the catalyst volume. We explained this volume activity by catalysis at the margins of numerous oxide fragments, which together with an intercalated quasi-electrolyte constitutes the bulk catalyst material. A lack of correlation between surface area and catalytic activity was also noted before for amorphous and hydrated manganese oxide particles that were active in water oxidation (Zaharieva, Najafpour et al. 2011, Wiechen, Zaharieva et al. 2012, Baktash, Zaharieva et al. 2013). On these grounds, we propose that the water oxidation volume activity of the bulk material may prevail generally in amorphous and hydrated oxides.

At high overpotentials, however, the protonation state of the buffer base in the bulk electrolyte becomes a codeterminant of the catalytic rate. This may also be a general property of water oxidation catalysis at near-neutral pH (see pH dependence of catalysis by amorphous manganese oxides (Bergmann, Zaharieva et al. 2013)). Surprisingly, we found that, at the highest investigated overpotentials, the catalytic current increases proportionally with the square root of the amount of deposited cobalt ions, which was explained by an increased catalyst internal proton concentration due to rate limitation by proton transfer to the buffer base. As opposed to classical alkaline or acidic water electrolysis, proton transfer to bases of the electrolyte buffer appears to be essential for efficient water oxidation at moderate pH. Further investigations are required to elucidate where and how this proton transfer takes place.

*Chapter 3***Surface activity of the CoCat**

Herein, the activity of the CoCat, containing very low amounts of Co, was scrutinised. Compared to Chapter 2, very 'thin' CoCat films (between 0.14 and 2.00 mC cm⁻²) were investigated by voltammetry, SEM, XANES, and also EXAFS. At very low levels of the amorphous material, high turnover frequencies imply catalysis at surface sites. This effect of surface catalysis is accompanied by minimal structural differences in terms of a lower oxidation state and a shorter long-range order for CoCats.

Within the same transition metal catalyst, bulk and surface catalysis may occur simultaneously; the film thickness determines the dominating mode of catalysis. It is of high importance to consider both modes of catalysis for a comprehensive understanding of heterogeneous water oxidation.



Portions of this paper have been published, whereupon in this chapter only my own contributions are presented:

D. González-Flores, I. Sánchez, I. Zaharieva, K. Klingan, J. Heidkamp, P. Chernev, P. W. Menezes, M. Driess, H. Dau, and M. L. Montero, *Angewandte Chemie International Edition*, 2015, **54**(8): 2472-6, <http://dx.doi.org/10.1002/anie.201409333>

Adapted with permission from Wiley-VCH. Copyright 2015 Wiley-VCH.
<http://www.interscience.wiley.com/>

D. González-Flores made EC, XAS, and ATR-FTIR experiments with the pakhomovskiytes.

I. Sánchez synthesised the pakhomovskiytes, performed XRD, and SEM experiments

K. Klingan made all CoCat experiments

I. Zaharieva, J. Heidkamp, P. Chernev supported the synchrotron measurements

P. Chernev wrote software for data evaluation

P. W. Menezes assisted in electro-preparation of pakhomovskiytes

3.1 Experimental detail

The applied experimental methods including electrochemistry, TXRF, SEM, and XAS are described in detail in Chapter 2.1.

3.1.1 Sample preparation

CoCats were electrodeposited for a total charge of 0.14, 0.44, 0.70, 0.89, 2.0 mC cm⁻² and compared to a more concentrated 5.00 mC cm⁻². The anodic electrodeposition of the CoCat films refined from a 0.1 M KP_i (~40 % KH₂PO₄ and ~60 %K₂HPO₄) at pH 7 containing 0.5 mM Co²⁺ ions from a Co(OH)₂(NO₃)₂ solution at 1.05 V vs. the normal hydrogen electrode (NHE) (with *iR* compensation). Electrodeposition was employed in a three-electrode setup driven by an SP-200 potentiostat (Bio-Logic SAS, Claix). The working electrodes were glass slides coated with ITO (12 Ω per square, VisionTek Systems Ltd, Cheshire, UK).

3.1.2 X-ray absorption spectroscopy (XAS)

The Co *K*-edge X-ray absorption spectroscopy (XAS) data were collected at the KMC-1 bending-magnet beamline (Schaefers, Mertin et al. 2007) of the BESSY synchrotron operated by the Helmholtz-Zentrum Berlin (HZB). The excitation energy was selected by a Si-111 double-crystal monochromator (scan range 7600-8750 eV). The measurements were performed at 20 K in a liquid-helium cryostat (Oxford-Danfysik). The cobalt *K_α* emission was detected using a windowless, energy-resolving 13-element detector (Ultra-LEGe germanium elements, Canberra). The CoCats on ITO were mounted such that the angle between the sample surface and the incident beam was 45°. The fluorescence detector was installed perpendicular to the X-ray beam. A filter foil (12.5 μm Fe, ≥ 99.99 %, Goodfellow, Bad Nauheim, GER) was put directly in the sample compartment between the CoCat surface and the window facing the fluorescence detector. Each spot on the CoCat sample was exposed for less than 35 min to synchrotron radiation. We changed the spot on the sample by 0.5 mm (vertically) after each scan. The spectra of the 11 channels were averaged for each spot on the samples. At least 4 different spots on each sample were taken. Details of the data collection can be found in section 2.1.7, the data extraction at Co *K*-edge is described in detail in Risch, Klingan et. al. 2012.

3.1.3 EXAFS simulations

All simulations were performed using the in-house software package ‘SimXLite’ (developed by Dr. P. Chernev, FU Berlin, Biophysics and Photosynthesis, AG Dau). After extraction of experimental EXAFS data, these were k^3 weighted and simulated with least-squares fit in k -space without any Fourier-filtering. The sum of contributions of n_{shell} atomic shells (*i.e.* group of elements with identical atomic number and very similar distances from the X-ray absorbing atom) determine an EXAFS spectrum, $\chi(k)$. The following equation describes the spectrum in EXAFS simulations (Teo 1986, Penner-Hahn 1999, Rehr and Albers 2000, Risch, Klingan et al. 2012):

$$\chi(k) = S_0^2 \cdot \sum_i^{n_{shell}} A(R_i, k)_i \cdot N_i \cdot \exp(-2\sigma_i^2 \cdot k^2) \cdot \sin(2k \cdot R_i + \phi_i) \quad (\text{Eq. 3.1})$$

where S_0^2 is the amplitude reduction factor, $A(R, k)_i$ the scattering amplitude, ϕ the phase correction, N_i the number of neighbours in the i^{th} atomic shell, σ_i the Debye-Waller parameter of the i^{th} atomic shell, and R_i the distance between the X-ray absorbing atom and the atoms of the i^{th} atomic shell. The fit error, which quantifies the deviations between experimental and simulated spectra relative to the overall magnitude of the experimental spectrum is given by Equation 3.2 (Risch, Klingan et al. 2012);

$$R_f = \frac{\sum_i^n |\chi(k, \mathbf{a})_i^* - y_i^*|}{|y_i^*|} \quad (\text{Eq. 3.2})$$

where the asterisk denotes the operation of Fourier-isolation for the R-range of interest, \mathbf{a} corresponds to a vector of all fit parameters, $\chi(k, \mathbf{a})$ to the EXAFS model function, and y_i to the unfiltered experimental data of n data points. In general, R_f -values are a useful measure of the quality of the fit. In the same way as in previous works (Risch, Klingan et al. 2012, Risch, Ringleb et al. 2015), for the simulation at the Co K -edge, the coordinates were obtained from a fragment of the LiCoO₂ structure (CoO₂ layer) with 10 cobalt atoms and 32 oxygen atoms (*i.e.* 5 incomplete Co₃(μ -O)₆ cubanes). The phase functions for the EXAFS spectrum were obtained by *ab-initio* calculations using Feff 9.05 (Ankudinov, Ravel et al. 1998, Rehr, Kas et al. 2009). The scattering paths were obtained up to a radius of 6 Å for up to ‘four-legged’ paths. Data extraction of experimentally obtained spectra followed a previous described method (Risch, Klingan et al. 2012), summarised with a spline range of 7711- 8511.65 eV, number of knots = 2, $E_0 = 7710$, weighted by k^3 and simulated (leastsquares fit) in k -space (without any Fourier-filtering). Curve-fitting of the data was accomplished within a k -range of 3 Å⁻¹ to 11.5 Å⁻¹. The amplitude reduction factor, S_0^2 , was 0.7 and the energy axis of the fit was shifted by 3.5 eV relative to the initially selected E_0 of 7710 eV.

3.2 Results

3.2.1 Electrochemical behaviour and redox equivalents

From CV scans of ‘thin’ CoCat films in Figure 3.1 it is apparent that the main redox and activity waves are already present even in films containing extremely low deposition charges. In this regime of low deposition charges ($< 2 \text{ mC cm}^{-2}$), the CoCat does not cover the substrate electrode, but rather starts to grow in form of isolated islands (Surenranath, Lutterman et al. 2012) (see section 3.3 Discussion). Oxidation of cobalt ions ($\text{Co}^{\text{II}} \rightarrow \text{Co}^{\text{III}} + \text{e}^-$) and water ($2 \text{ H}_2\text{O} \rightarrow \text{O}_2 + 4 \text{ e}^- + 4 \text{ H}^+$) relates to positive currents, while reduction of cobalt ions ($\text{Co}^{\text{III}} + \text{e}^- \rightarrow \text{Co}^{\text{II}}$) occurs at negative currents. For higher Co concentrations the activity rises, the overpotential slightly decreases.

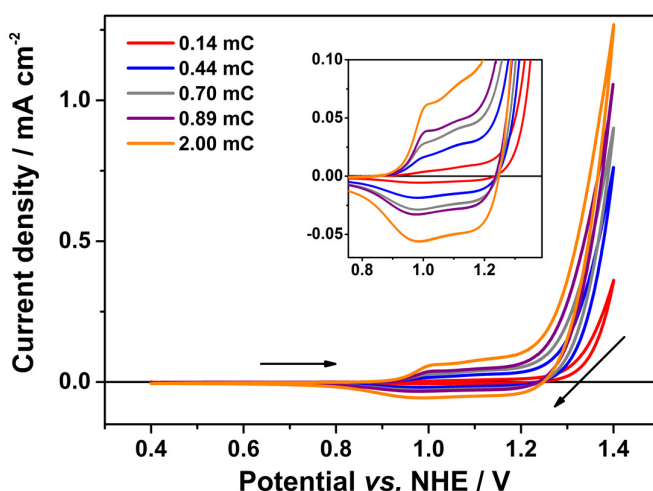


Figure 3.1. CVs for a 0.14 (red), 0.44 (blue), 0.70 (grey), 0.89 (purple), 2.00 (orange) mC cm^{-2} CoCat in 0.1 M KP_i at pH 7 with a scan rate of 20 mV s^{-1} . All CVs were corrected for 80 % iR drop during the experiments. The insight gives an enlarged picture of the Co^{II} to Co^{III} oxidation and the Co^{III} to Co^{II} reduction wave.

A closer examination of the redox transition corresponding to cobalt oxidation and reduction is performed by determination of the peak potentials from the maxima and minima of the 4th derivatives of the respective CV scan. The peak potentials for 2.00 and 0.89 mC cm^{-2} are 0.98 V (anodic peak potential) and 0.90 V (cathodic peak potential), for the lower concentrated films 0.97 V (anodic peak potential) and 0.89 V (cathodic scan). From these minimal changes also in the midpoint potentials (0.94 V for 2.00 and 0.89 mC cm^{-2} versus 0.93 V for ‘thinner’ CoCats) it may be concluded that the only drastic electrochemical change (from ‘thinner’ to ‘thicker’ films) is the overall rising activity in the oxygen evolution regime. The overlapping of the current waves

originating from the redox couple $\text{Co}^{\text{III/IV}}$ and the onset of water oxidation makes it difficult to determine the exact value of the water oxidation overpotential only from electrochemical data.

Figure 3.2 provides an overview of the percentage of reduction equivalents in dependence of the deposition charge. Upon increasing the deposition charge from 0.14 to 5.00 mC cm^{-2} , the estimated number of redox-active cobalt ions is increased by a factor of about 1.7 only. The amount of cobalt in these catalyst films ranges from 0.7 nmol for the ‘thinnest’ sample (0.14 mC cm^{-2}) over 16.2 nmol (2.0 mC cm^{-2}) to 48.0 nmol (5.0 mC cm^{-2}) (determination with TXRF).

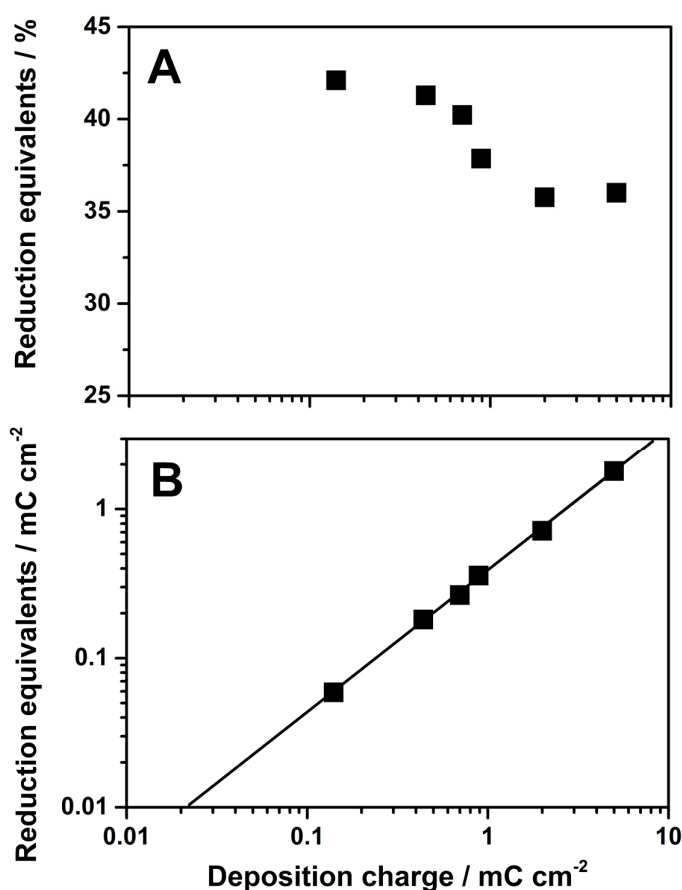


Figure 3.2. (A) Percentage of the reduction equivalents of ‘thin’ CoCat films in dependence of the deposition charge. The one-electron reduction equivalent (n_{red}/n_{Co} ; in percent) was calculated by dividing the number of reduced cobalt atoms (n_{red} , from integration of the negative values of the cathodic scan of the CV) by the total number of cobalt atoms (n_{Co} , TXRF). (B) Amount (in terms of charge) of redox-active cobalt ions for deposition charges ranging from 0.14 to 5.00 mC . The charge that corresponds to the amount of redox-active cobalt ions has been estimated from integration of the reductive current.

The percentage of redox-active cobalt ions estimated from the integration of the reductive cyclic voltammetry current changes slightly from 42 (0.14 mC film) to 36 (5.0 mC film). This fits to the

trend in Chapter 2 for ‘thicker’ films (Figure 2.5 B), where the percentage of reduction equivalents is minimally higher for ‘thinner’ films, so that the overall number of redox-active cobalt ions is proportional to the film volume and moreover independent of the geometric interface area between the oxide and electrolyte. Overall, the relative capacity for accumulating reduction equivalents is not considerably affected, when the amount of electrodeposited Co ions is decreased.

3.2.2 Turnover frequency (TOF)

In Chapter 2 (Figure 2.7) the Co amount within the CoCat was altered from 2 to 200 mC cm⁻²; an increase of Co by two orders of magnitude. In this regime of the deposition charge (2 – 200 mC cm⁻²) the catalytic activity of water oxidation is independent of the Co concentration, which points to equal catalytic activity throughout the bulk volume of the catalyst.

From now on we will focus also on highly ‘thin’ CoCat films (up to 140 μC cm⁻²) in order to give an extended insight into the activity, in terms of turnover frequency of the CoCat.

Figure 3.3 shows the stationary current density and the turnover frequency per O₂ and cobalt ion for potentials of 1.20, 1.25, 1.30, 1.35, and 1.40 V for a wide range of CoCat films of different thickness (between 0.7 nmol and 2.2 μmol Co per cm²). For CoCats containing a very low amount of Co (0.14 to 2.03 mC cm⁻²) current density slope values are evanescently small, if the current density stays below the level of proton transport limitation (0.15 and 0.18 log_{mC}(mA) for 1.20 V and 1.25 V) and for very high overpotentials (0.14 for 1.40 V). Compared to thicker films (> 5 mC cm⁻²), which cover completely the ITO surface, the turnover frequency (TOF) is quite high for these very ‘thin’ catalyst films (0.85 s⁻¹ at 1.40 V for a 0.14 mC cm⁻² CoCat). The TOF per cobalt ion is increased by one order of magnitude at 1.20 V from the highest to the lowest level of Co amount. This effect is even stronger for higher overpotentials at 1.35 V and 1.40 V; when scaling up the deposition charge from 0.14 to 200 mC cm⁻², the TOF is reduced by two orders of magnitude. Interestingly, between 0.14 mC and 2.03 mC cm⁻² the activity of the CoCat is fully dependant on the amount of Co. Below the level of complete catalyst coverage of the substrate electrode, the following correlation is observed: The lower the Co concentration within the catalyst film, the higher the turnover frequency.

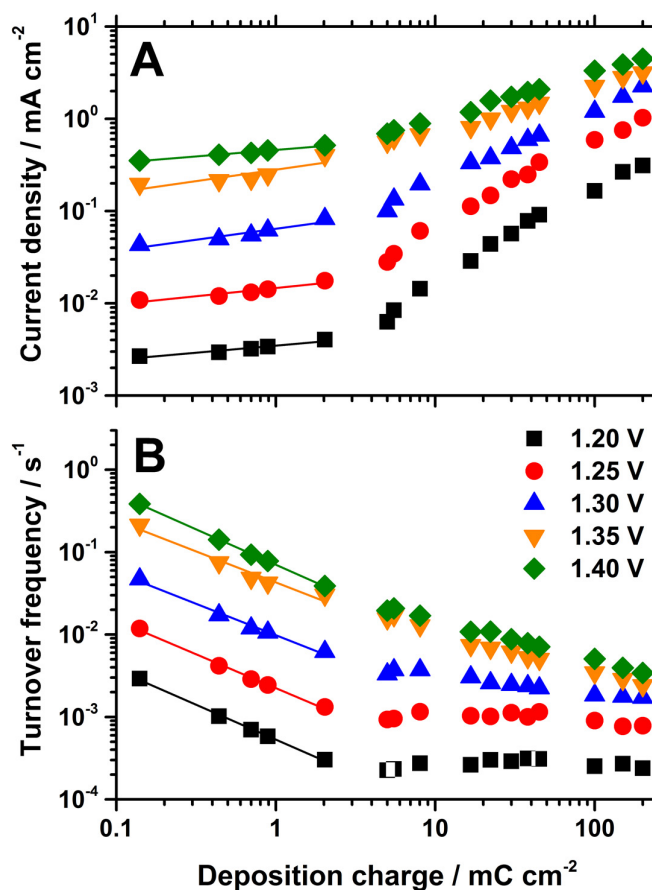


Figure 3.3. Turnover frequency per O₂ and cobalt ion at various potentials vs. NHE. All measurements were performed in 0.1 M KP_i at pH 7 and the data points correspond to current densities 60 s after the potential jump. **(A)** Stationary current densities (catalytic currents) for variation of the deposition charge from 0.14 mC cm⁻² to 200 mC cm⁻², at five potentials (vs. NHE, pH 7, in 0.1 M KP_i) applied to the catalyst films previously deposited on the working electrode. **(B)** Turnover frequency (TOF) per cobalt ion and formed O₂ molecule. The bottom scale (x axis of B) provides the number of deposited cobalt ions in terms of the corresponding deposition charge; for CoCat films ≥ 5 mC, 1 mC cm⁻² corresponds to about 10 nmol cm⁻². The current was measured after equilibration for 60 s at the given potential (80% *iR* compensation; *R* of about 50 Ω, as determined by impedance spectroscopy). In A) and B), the lines were obtained by a least-squares fit. In A), the slope values of the straight lines are 0.15 (1.20), 0.18 (1.25), 0.24 (1.30), 0.25 (1.35), and 0.14 (1.40 V) in units of $\log i$ per $\log Q_{dep}$. In B), the corresponding slopes are 0.85 (1.20), 0.82 (1.25), 0.76 (1.30), 0.75 (1.35), and 0.85 (1.45 V). The data for deposition charges ranging from 2 to 200 mC is identical to the data of Figure 2.7.

3.2.3 Oxidation states and atomic structure

The X-ray absorption near-edge structure (XANES) can provide useful information about the oxidation state and coordination environment of the metals in amorphous metal oxides.

Figure 3.4 displays the Co *K*-edge XANES spectra for deposition charges of 5.00, 0.44, and 0.14 mC cm⁻². The main edge positions of ‘thinner’ catalyst films are considerably shifted to lower energy values. Such a change is usually interpreted as a shift to lower oxidation states (Natoli 1984, Teo 1986, Dau and Haumann 2003, de Vries, Hozoi et al. 2003, Glatzel, Smolentsev et al. 2009). Moreover, the amplitude of the shoulder at 7740 eV in the XANES spectrum in Figure 3.4 decreases for samples with smaller amounts of deposited Co ions, which indicates a reduced number of neighbouring atoms affected by the high fraction of surface atoms due to the existence of only a few Co-oxo layers (Kühn, Caliebe et al. 2011). Commonly, lower oxidation states in amorphous transition metal oxides can also be witnessed by a pronounced decrease of the pre-edge area in absence of any severe changes in symmetry (Yamamoto 2008). Due to their lower Co concentration, the averaged XANES spectra are noisier for 0.44 mC cm⁻² and all the more for 0.14 mC cm⁻², so that any definitive predications of a change in pre-edge area of CoCats with a varying amount of Co ions is not possible.

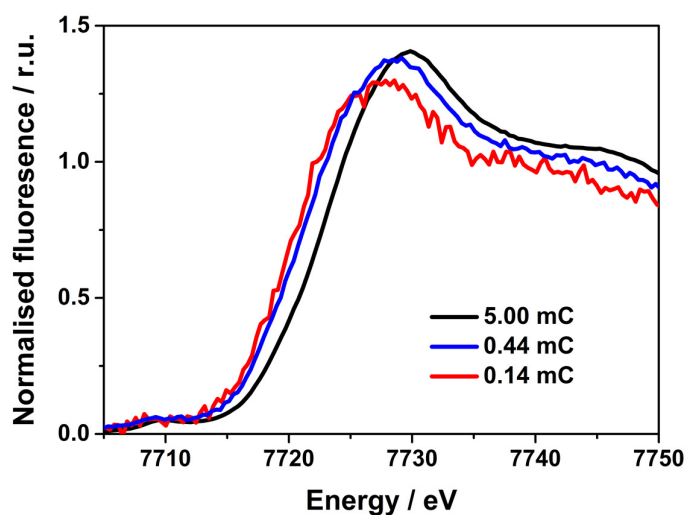


Figure 3.4. Co *K*-edge XANES spectra at 20 K of the CoCat for various amounts of deposited Co ions measured in terms of the indicated deposition charge, 5 mC cm⁻² (black), 0.44 mC cm⁻² (blue), and 0.14 mC cm⁻² (red).

In previous works (Risch, Khare et al. 2009, Risch, Ringleb et al. 2009) the existence of the local geometry of CoO_6 octahedra within the CoCat was confirmed by comparison of Co-*K*-edge XANES spectra of LiCoO_2 and $[\text{Co}(\text{OH}_2)_6]^{2+}$ with the CoCat. The spectra presented here in Figure 3.4 are very similar in shape and position, so that the conclusion of an octahedral coordination of cobalt by six oxygen ligands is evident for the 5.00 mC sample.

Table 3.1. Edge positions* of the different CoCat films of various deposition charges and the calculated oxidation states. . The amount of cobalt in the samples, n_{Co} , was determined with elemental analysis (TXRF). (*)The integral method (Dau, Liebisch et al. 2003) was used with limits $0.15 < \mu < 1.0$

Sample	n_{Co}	Edge position* (eV)	Oxidation state	% Co^{II}	% Co^{III}	% Co^{IV}
0.14 mC cm^{-2}	0.7 nmol	7719.23	2.30 ± 0.06	0.70	0.30	-
0.44 mC cm^{-2}	2.1 nmol	7719.81	2.55 ± 0.07	0.45	0.55	-
5.00 mC cm^{-2}	48.0 nmol	7720.91	3.03 ± 0.07	-	0.97	(0.03)

Applying the integral method (Dau, Liebisch et al. 2003) to localise the edge positions, results in lower energy values for ‘thinner’ CoCat films (Table 3.1). The well-established method of using the known oxidation state and the experimentally determined one of a range of different cobalt oxides in a calibration curve (Risch, Klingan et al. 2012) was used to calculate the oxidation states of CoCats deposited at 1.05 V vs. NHE in 0.1 M KPi , pH 7 for 5.00 mC cm^{-2} ($\sim \text{Co}^{+3.0}$), 0.44 mC cm^{-2} ($\sim \text{Co}^{+2.6}$), and 0.14 mC cm^{-2} ($\sim \text{Co}^{+2.3}$) (Table 3.1). The formal valence of cobalt found herein varies from +2.30 over +2.55 to +3.03 by increasing the amount of deposited Co. A film consisting of fewer cobalt ions in terms of the deposition charge exhibits a lower oxidation state and thus incorporates a higher amount of Co^{II} ions.

The extended X-ray absorption fine-structure oscillations in Figure 3.5 were obtained by Fourier-filtering between 3 and 11.5 \AA^{-1} on a reduced distance scale. Generally, the location of the peaks in the FT can be assigned to average distances between the absorbing cobalt atom and its backscattering neighbours. However, the x-axis in Figure 3.5 is 0.3 \AA shorter than the corresponding atom-atom distance from simulations.

Visual inspection of the experimental data (Figure 3.5) suggests that the two peak positions of 5.00 mC cm^{-2} and 0.44 mC cm^{-2} are at akin reduced distances. From this it follows that similar Co-O and Co-Co bond lengths can be obtained for a varying amount of Co within the CoCat.

The coordination number of the absorber atom is usually reflected in the peak height in the FT. The Co-O peak and the Co-Co peak of the more concentrated film are higher indicating a more ordered oxide or larger oxide fragments. This finding should not be confused with a misleading

understanding of a higher degree of crystallinity. Obviously, both CoCat samples are amorphous materials, but a higher degree of order denotes the size of interconnected CoCat domains (CoO_6 octahedra interconnected *via* di- μ -oxo bridges).

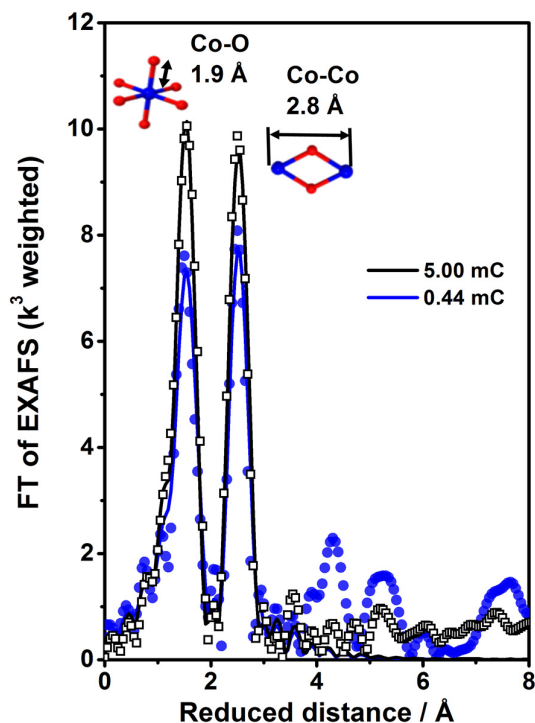


Figure 3.5. Experimental (symbols) and simulated (solid lines) EXAFS spectra of a 5.00 mC cm^{-2} CoCat (black) and a 0.44 mC cm^{-2} CoCat film (blue). The reduced distances were obtained by Fourier-transforming the unfiltered k -space data between 3 and 11.5 \AA^{-1} . Structural motifs corresponding to the two peaks are displayed schematically.

Quantitative information about the number of the cobalt ligands and inter-atomic distances can be obtained by simulation of the experimental EXAFS spectra (Table 3.2). A small difference is distinguishable between the two Co-O bond lengths of films containing a different cobalt amount. Although unaltered within error range, this likely reflects the lower oxidation state of 2.55 resulting in an elongated Co-O bond length of 1.91 ± 0.01 \AA in the 0.44 mC catalyst film, while the higher oxidation state of 3.03 of the ‘standard’ CoCat film results in a Co-O distance of 1.89 ± 0.01 \AA . The average bond lengths of Co-O compounds are the following; 1.90 \AA for hexacoordinated Co^{III} , 2.04 \AA for pentacoordinated Co^{II} , and 2.09 \AA for hexacoordinated Co^{II} (Wood and Palenik 1998).

If the substrate electrode is covered completely with the CoCat, the atomic structure of the latter can be identified with edge-sharing $\text{Co}^{\text{III}}\text{O}_6$ octahedra, which are interconnected *via* di- μ -oxo bridges, as it has been discussed in previous works (Risch, Khare et al. 2009, Risch, Klingan et al.

2012). Thus, the deposition time or the deposition charge influences the coordination behaviour; less ordered oxide fragments occur within the 0.44 mC CoCat. Its coordination number of 5.3 is reduced compared to the ‘standard’ CoCat ($N_O=6.3$). This finding could be interpreted in a way that the low-amount CoCat film (0.44 mC) contains besides six coordinated Co^{III} ions, also a considerable amount of five coordinated Co^{II} .

Table 3.2. EXAFS simulation results for the differently thick CoCat films. Parameters were used for simulation of FT EXAFS spectra displayed in Figure 3.5.

Sample	N_o	Co-O		N_{Co}	Co-Co	
		$R_o(\text{Å})$	σ_o		$R_{Co}(\text{Å})$	σ_{Co}
0.44 mC cm ⁻²	5.3±1.4	1.91±0.01	0.074±0.019	2.7±1.2	2.81±0.01	0.055±0.022
5.00 mC cm ⁻²	6.3±0.7	1.89±0.01	0.064±0.007	4.6±0.8	2.81±0.01	0.065±0.008

All parameters were obtained by curve-fitting to the data (k -range of 3 Å^{-1} to 11.5 Å^{-1}). The amplitude reduction factor, S_o^2 , was 0.7 and the energy axis of the fit was shifted by 3.5 eV relative to the initially selected E_o of 7710 eV. The errors accord to 68 % confidence interval. R_f -values were 12.

In the CoCat cobalt-oxo distances of ~ 2.8 Å are usually identified with di- μ -oxo-bridges (incomplete cobalt-oxo cubanes, edge sharing octahedra) (Risch, Khare et al. 2009, Risch, Klingan et al. 2012). The characteristic Co-Co distance of 2.81 Å represents about 4.6 cobalt-cobalt interactions in case of the 5.00 mC film and 2.7 for the 0.44 mC film (Table 3.2, simulated N values are overlapping within error ranges). The film with a lower Co amount accounts for fewer interactions, probably being less ordered. The lower extent of order could result from a five-coordinated Co^{II} ions and a corresponding loss of di- μ -oxo bridging. Thus, CoO_6 octahedra are present already at low deposition times or charges, but to a smaller extent than in the thicker film. The fraction of Co^{III} is presumably reduced from 97 % to 55 % (Table 3.1). However, we may state that the trend for various thick CoCats (see also Figure 2.15 in Chapter 2) is the unmodified existence of the same fragments with a change in the order of the oxide and/or the size of the oxide fragments.

In conclusion, X-ray absorption spectroscopy revealed that by deposition of small amounts of cobalt ions, the overall atomic structure in terms of cobalt oxide fragments, which consist of octahedrally coordinated Co interconnected by di- μ -oxo bridges, is basically maintained. Nevertheless more defects arise for the low-amount CoCat in terms of five coordinated Co^{II} and less edge-sharing of CoO_6 octahedra. Irrespective of the amount of deposited cobalt ions, edge-sharing CoO_6 octahedra represent the prevailing structural motif.

3.3 Discussion

For electrodeposition of a cobalt oxide catalyst, containing 0.44 mC cm^{-2} Co, the ITO substrate is incompletely covered and isolated CoCat fragments are found on top of the supporting electrode at this low Co deposition charge (SEM picture in Figure 3.6). The growth process of the CoCat was studied in detail by Surendranath et al. (Surendranath, Lutterman et al. 2012). They found 65 % coverage at a deposition charge of $\sim 1 \text{ mC cm}^{-2}$ and that the process of catalyst formation happens *via* nucleation from discontinuous islands (Surendranath, Lutterman et al. 2012). The CoCat cluster in Figure 3.6 is rather large, while the main portion of the surface seems to be uncovered. This obviously does not reflect the true situation of CoCat coverage of the ITO substrate, where nanosized CoCat islands should have started to coalesce with coverage up to 39 % (Surendranath, Lutterman et al. 2012). The ITO substrate itself has a rather rough surface and in an uncovered state the ITO features suffer from a blurred appearance. If the CoCat is deposited on the ITO, then most surface features are better resolved; probably caused by present fractions of the CoCat. Not only the indicated CoCat cluster (blue circle) is present on the ITO surface in Figure 3.6, a large part of CoCat particles is not detectable with this choice of substrate and the applied method.

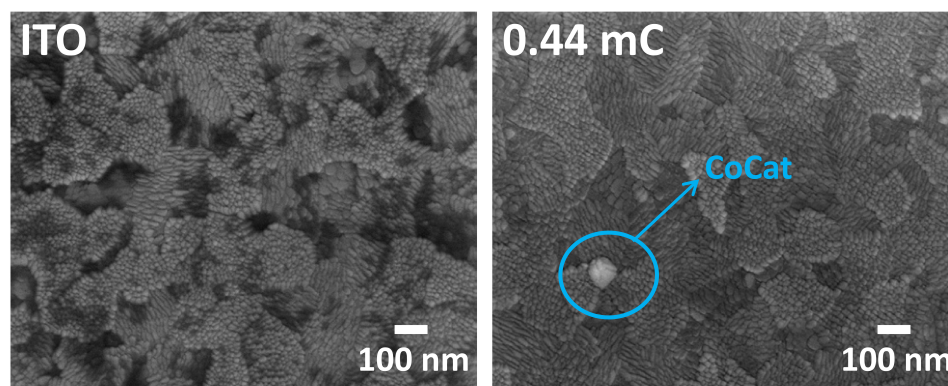


Figure 3.6. SEM images of blank ITO without CoCat, and after deposition of 0.44 mC cm^{-2} CoCat. The blue circle indicates the Co-oxo cluster on top of the ITO surface. The CoCat films were dried under nitrogen after deposition and measured without any surface modification. SEM was performed by Dr. Anna Fischer at TU Berlin.

The following explanation is proposed for the increased turnover frequency (TOF) at low deposition charge: As we have seen for deposition of thick films ($>10 \text{ nm}$, see Chapter 2, Figure 2.7), catalysis within the bulk volume of the film preponderances and the corresponding TOF is very low (10^{-3} s^{-1} at 1.25 V , Figure 2.7). However, at lower levels of deposited cobalt ions (Figure 3.3, between 0.14 mC and 2.03 mC cm^{-2}), the activity of the CoCat per Co ion depends on the

amount of Co ions; more precise, the lower the Co concentration within the catalyst film, the higher the turnover frequency. This finding is a common effect in surface catalysis so that we may infer that for very 'thin' CoCat films surface catalysis dominates. The corresponding TOF per cobalt ion and O₂ is significantly higher than observed for volume catalysis (minimally by one order of magnitude, 10⁻² s⁻¹ at 1.25 V), in line with recent findings reported in Gonzalez-Flores, Sanchez et al. 2015. Hence, this outcome denotes that in the CoCat the rate of catalysis could be enhanced significantly at electrodes below 2 mC cm⁻² of Co. Regarding the mechanistic behaviour of ultrathin amorphous transition metal catalysts, these films obviously carry more easily accessible and potentially especially reactive surface sites for water oxidation.

The higher concentrated CoCat films (2 – 200 mC cm⁻²) probably contain a clear majority of catalytic sites for electrolysis within the bulk volume of the film. In conclusion, the improved rate of catalysis per Co ion within the CoCat for very 'thin' films is probably due to an overall higher ratio of surface exposed sites to internal sites, and suggests that surface catalysis predominates in this case. The elevated activity per Co ion in films containing a small Co amount may be related to the decreased order and the presence of more defects in the CoCat. Quantitative and qualitative analysis of X-ray spectroscopy data at the Co-*K* edge demonstrated that the 'special' properties of the 0.44 mC sample are the reduced oxidation state of 2.55 and the co-existence of Co^{II}O₅. Hence, a less ordered oxide has a distinct impact on the oxygen-evolving activity per Co ion; more defects give higher relative activity.

For the understanding of water oxidation catalysis of crystalline materials this finding implies, that high turnover frequency values may not entirely be attributed to surface sites, but as well to (surface) amorphisation of the initially crystalline materials (compare to TOF values of crystalline and amorphous pakhomovskiyite in Gonzalez-Flores, Sanchez et al. 2015).

3.4 Summary

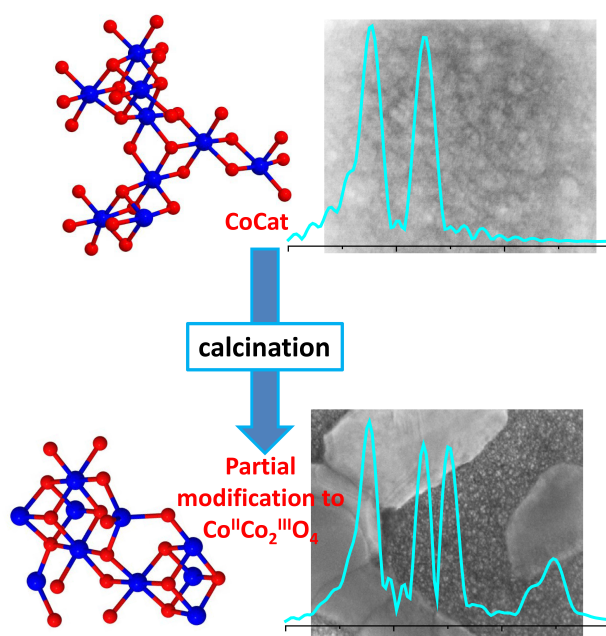
The low-cobalt films (0.7 nmol cm^{-2} for a 0.14 mC film and 2.1 nmol cm^{-2} for a 0.44 mC film) exhibit a low average Co oxidation state (2.30 for 0.14 mC cm^{-2} , and 2.55 for 0.44 mC cm^{-2}); more Co^{II} ions are incorporated into the film. Atomic defects are introduced in these films, which can be described as catalysts with less ordered oxide layers and/or smaller oxide fragments.

The mode of water oxidation of the CoCat at very low amounts of deposited cobalt could be identified as surface catalysis. As the corresponding turnover frequency per cobalt ion is significantly higher than observed for volume catalysis (minimally by one order of magnitude, at 1.25 V , and maximally by two orders of magnitude at 1.35 and 1.45 V), the mode of surface catalysis points to the possibility of a relevant improvement of the rate of catalysis of the CoCat at surface exposed sites or domains.

*Chapter 4***Calcination of the CoCat**

In this chapter ‘thick’ CoCat films (45 mC cm^{-2} deposition charge) were subjected to a temperature treatment in order to compare the changing electrochemical parameters of water oxidation, the rearrangement in atomic structure, as well as the modifications in microscopical surface morphology to the respective properties of the as-deposited CoCat film. The results of these investigations provide an insight into how the CoCat film changes its performance after an exposure to elevated temperatures.

With the help of electrochemical, XAS, and SEM techniques the hypothesis is deployed that calcined films undergo a structural transition towards a Co_3O_4 spinel-like type. The absolute catalytic activity of calcined CoCat films is drastically reduced, suggesting that only parts of the calcined CoCat remain active.



Portions of this chapter have been prepared for publication.

4.1 Experimental detail

TXRF, SEM, XAS, and EXAFS are performed and evaluated as described in the previous chapters (see experimental details of 2.1 and 3.1).

4.1.1 Sample preparation

CoCats were electrodeposited for a total charge of 45 mC cm^{-2} , which translates into a cobalt amount of $0.47 \text{ } \mu\text{mol cm}^{-2}$ (identified by TXRF), or $\sim 300 \text{ nm}$ (identified by SEM) at 1.05 V vs. NHE in KP_i at pH 7 on ITO/glass ($12 \text{ } \Omega$ per square, VisionTek Systems Ltd, Cheshire, UK). All experiments were corrected for 80 % iR drop. After film deposition a CV of the CoCat was recorded in KP_i at pH 7 (scan rate 20 mV s^{-1}), then dried for one day in a desiccator prior to calcination in air (heating rate 100°C/hour , each film held at the desired calcination temperature for 2 hours, accomplished at TU Berlin, Chemistry Department, Dr. Anna Fischer). The obtained films were ready for further characterisation.

4.1.2 X-ray absorption spectroscopy (XAS)

The Co K -edge X-ray absorption spectroscopy (XAS) data were collected at the KMC-1 bending-magnet beamline (Schaefers, Mertin et al. 2007) of the BESSY synchrotron operated by the Helmholtz-Zentrum Berlin (HZB). The excitation energy was selected by a Si-111 double-crystal monochromator (scan range $7600\text{-}8750 \text{ eV}$). The measurements were performed at 20 K in a liquid-helium cryostat (Oxford-Danfysik). The cobalt K_α emission was detected using a windowless, energy-resolving 13-element detector (Ultra-LEGe germanium elements, Canberra). The data extraction at Co K -edge for the CoCat was performed as described in Risch, Klingan et. al. 2012.

The nonstoichiometric $\text{Co}^{\text{II/III}}_3\text{O}_4$ ($\geq 99.995 \%$, Sigma Aldrich Chemie GmbH Munich, GER) and the stoichiometric $\text{Co}^{\text{II}}_3(\text{PO}_4)_2$ powder ($\geq 99.5 \%$, Sigma Aldrich Chemie GmbH Munich, GER) were diluted with boron nitride (Sigma Aldrich Chemie GmbH Munich, GER) in a ratio of 1:20 and measured in absorption mode. The CoCats on ITO were measured in fluorescence mode and mounted such that the angle between the sample surface and the incident beam was 45° . The fluorescence detector was installed perpendicular to the X-ray beam. A filter foil ($12.5 \text{ } \mu\text{m Fe}$, $\geq 99.99 \%$, Goodfellow, Bad Nauheim, GER) was put directly in the sample compartment between the CoCat surface and the window facing the fluorescence detector. Each spot on the CoCat sample was exposed for less than 35 min to synchrotron radiation. We changed the spot on the sample by

0.5 mm (vertically) after each scan. The spectra of the 11 channels were averaged for each spot on the samples. At least 5 different spots or scans on each sample were taken.

4.1.3 EXAFS simulations

For the simulation of the distances related to the CoCat at the Co *K*-edge the coordinates were obtained from a fragment of the LiCoO₂ structure (CoO₂ layer) with 10 cobalt atoms and 32 oxygen atoms (*i.e.* 5 incomplete Co₃(μ-O)₆ cubanes) (Risch, Klingan et al. 2012, Risch, Ringleb et al. 2015). The phase functions for the EXAFS spectrum were obtained by *ab-initio* calculations using Feff 9.05 (Ankudinov, Ravel et al. 1998, Rehr, Kas et al. 2009). For the CoCat the scattering paths were obtained up to a radius of 6 Å for up to ‘four-legged’ paths. For the Co₃O₄ multi-scattering paths were obtained up to a radius of 5.4 Å for up to ‘four-legged’ paths. All multi-scattering distances were simulated by carefully chosen corresponding phase functions taking into account a ‘three-legged’ path and simultaneously a ‘four-legged’ path. Data extraction of experimentally obtained spectra was accomplished with a spline range of 7711- 8511.65 eV, number of knots = 2, $E_0 = 7710$, and weighted by k^3 and simulated (least-squares fit) in k -space (without any Fourier-filtering). Curve-fitting of the data was accomplished within a k -range of 3 Å⁻¹ to 12 Å⁻¹. The amplitude reduction factor, S_0^2 , was 0.7 and the energy axis of the fit was shifted by 3.5 eV relative to the initially selected E_0 of 7710 eV.

4.2 Results and Discussion

4.2.1 Electrochemical behaviour and redox equivalents

Cyclic voltammograms (CV) of the CoCat films ‘as-deposited’ and after a certain temperature exposure are displayed in Figure 4.1. After calcination of the respective CoCat films, the maximum activity in the oxygen evolution regime decreases with increasing calcination temperature in the following order: ‘as-deposited’ > 350 °C > 400 °C > 450 °C > 550 °C > 600 °C. The maximum current density of the calcined films decreases by ~65 to 75 % compared to the ‘as-deposited’ CoCat at high potentials.

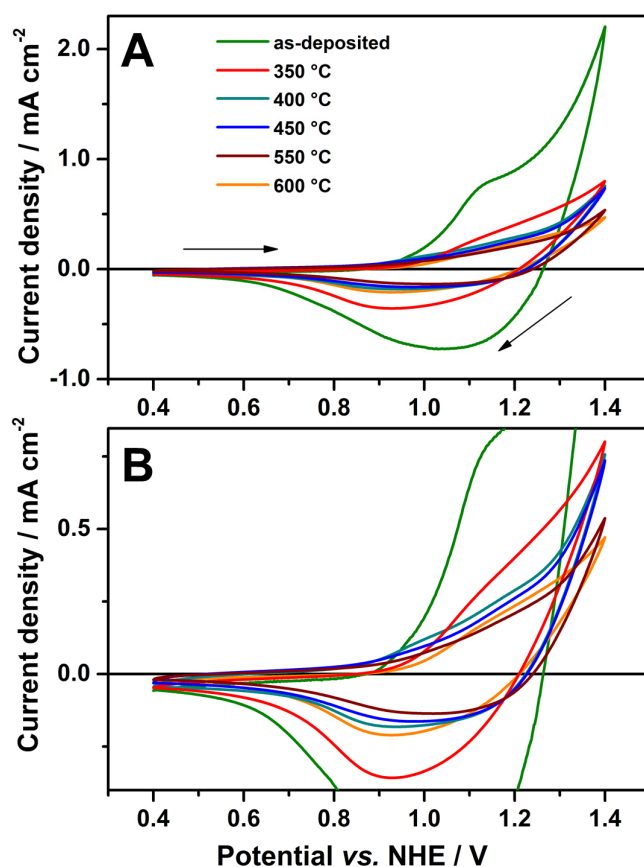


Figure 4.1. Cyclic voltammograms of CoCat films ‘as-deposited’ (45 mC cm⁻²) (olive), calcined at 350 °C (red), 400 °C (dark cyan), 450 °C (blue), 550 °C (wine), and 600 °C (orange) in 0.1 M KPi at pH 7 (scan rate of 20 mV s⁻¹). (A) The complete current range is displayed. The arrows indicate the scan direction. (B) Enlarged picture of A) for better distinction of calcined films.

Moreover, upon temperature exposure the characteristic and pronounced $\text{Co}^{\text{II}}/\text{Co}^{\text{III}}$ oxidation wave at ~ 1.15 V vs. NHE smears out into a very broad feature. TXRF control experiments of the calcined CoCat films did not detect any significant loss in the amount of cobalt. This finding together with the data from Figure 4.1 emphasises that only parts of the initially active Co-oxo centres will remain active.

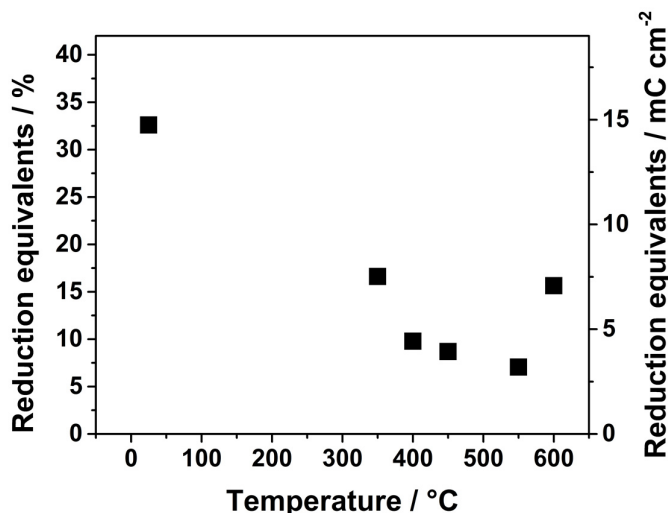


Figure 4.2. (A) Percentage of reduction equivalents of the ‘as-deposited’ (25 °C) and calcined CoCat films at different temperatures. The redox-charging (n_{red} / n_{Co} , in percent) was calculated by dividing the number of reduced cobalt atoms (n_{red} , from integration of the negative values of the cathodic scan of the CV) by the total number of cobalt atoms (n_{Co} , TXRF). (B) Amount (in terms of charge) of redox-active cobalt ions for ‘as-deposited’ and calcined CoCat films with calcination temperatures between 350 °C and 600 °C. The charge that corresponds to the amount of redox-active cobalt ions was estimated from integration of the reductive current.

As the quantitative character of cobalt oxidation in the CoCat is of high interest for the performance of a water oxidation catalyst, the reduction equivalents of CoCats, ‘as-deposited’ and calcined between 350 and 600 °C are given in Figure 4.2. In the same way as in previous chapters, the redox equivalents were determined by dividing the number of reduced cobalt atoms (n_{red} , from integration of the negative values of the cathodic scan of the CV) by the total number of cobalt atoms (n_{Co} , from TXRF). During the calcination process the CoCat obviously loses most of its capacity for storing and accumulating redox equivalents. Within the temperature series 350, 400, 450, 550, and 600 °C the redox equivalents are reduced from $\sim 15\%$ or 33 mC cm^{-2} (‘as-deposited’ CoCat) to respectively 8, 4, 4, 3, 7 % or $17, 10, 9, 7, 16 \text{ mC cm}^{-2}$. Overall, after being subjected to a calcination protocol only 5.2 ± 1.9 % (average redox equivalents of all temperatures) of the cobalt population of the catalyst film gets oxidised by one unit from the fully reduced state to the completely oxidised state.

4.2.2 Oxidation states

The X-ray absorption near-edge structure (XANES) can give evidence about the oxidation state and coordination environment of the metals in amorphous metal oxides. Oxidation state changes can be deduced from a shift of the edge position in a XANES spectrum (Natoli 1984, Teo 1986, Dau, Liebisch et al. 2003, de Vries, Hozoi et al. 2003, Glatzel, Smolentsev et al. 2009). We have shown in Chapter 3 those CoCats with a very low concentration and growing as isolated islands cause such a shift (Figure 3.4).

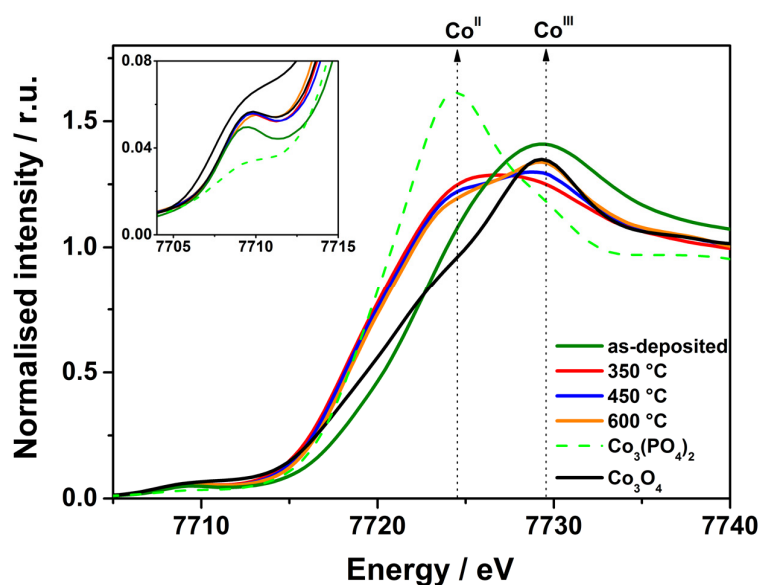


Figure 4.3. Co *K*-edge XANES spectra of powders Co_3O_4 (black line), $\text{Co}_3(\text{PO}_4)_2$ (green dashed line) and catalyst films ‘as-deposited’ (dark green line), calcined at 350 °C (red line), calcined at 450 °C (blue line), and calcined at 600 °C (orange line). The inset magnifies the pre-edge region. The arrows indicate the spectral contribution of Co^{II} and Co^{III} .

In a similar manner the XANES spectra of the temperature treated CoCats exhibit a shift to lower energies, suggesting a lower oxidation state. Here, Figure 4.3 depicts the Co *K*-edge XANES spectra for the calcined CoCats and a reference spectrum of Co_3O_4 powder is also presented. The maximum of the 350 °C calcined CoCat is broadened in comparison to the ‘as-deposited’ CoCat. Furthermore, it becomes obvious for the 450 °C and 600 °C CoCat that two peaks contribute as a superposition to the shape of the white line (principal edge maximum). The first main edge feature of all the calcined films derives from a Co^{II} contribution (for comparison see listed edge positions

in Table 4.1 and the spectrum of the $\text{Co}^{\text{II}}_3(\text{PO}_4)_2$ reference in Figure 4.3). The second feature in the absorption edge of the 450 and 600 °C is indicative of a Co^{III} contribution.

The inset in Figure 4.3 magnifies the pre-edge region for the different samples. Pre-edge features in XANES spectra are sensitive to the oxidation state and the degree of symmetry around the metal centre (Yamamoto 2008). All pre-edge heights of the calcined CoCats are higher than the ‘as-deposited’ CoCat, which points to a lowering of the symmetry in the temperature exposed films. Usually, the pre-edge peak intensity increases with decreasing coordination number (Yamamoto 2008), which points to the assumption that the calcined CoCats have a lower coordination number than the ‘as-deposited’ CoCat.

Moreover, the oxidation state cannot be deduced from pre-edge intensities. Higher calcination temperature shifts the main edge to lower energy values indicating lower oxidation states. In contrast, the pre-edge heights increase for higher calcination temperature. Hence, coordination and symmetry affects may play an outstanding role for the properties of the pre-edge of calcined CoCat films.

Table 4.1. Edge positions* and the corresponding calculated oxidation states of $\text{Co}_3(\text{PO}_4)_2$ and Co_3O_4 powder references, and of the CoCat films; ‘as-deposited’ and treated with the temperature protocol described in 4.1.1. (*) The integral method (Dau, Liebisch et al. 2003) was used with limits $0.15 < \mu < 1.0$.

Sample	Edge position* (eV)	Oxidation state
350 °C	7718.55	2.00±0.06
450 °C	7718.70	2.07±0.06
600 °C	7718.89	2.15±0.06
as-deposited	7720.68	2.93±0.07
$\text{Co}^{\text{II}}_3(\text{PO}_4)_2$	7718.65	2.04±0.05
$\text{Co}^{\text{II}}\text{Co}^{\text{III}}_2\text{O}_4$	7720.09	2.67±0.03

The edge positions and the calculated cobalt oxidation states (for calibration curve see Supporting Information of Risch, Klingan et al. 2012) from the Co *K*-edge XANES spectra in Figure 4.3 can be found in Table 4.1. If the ligands are not affected by any major alterations, one can expect a shift of 2.3 eV per Co oxidation state in the edge position (Risch, Klingan et al. 2012). All the heated CoCats scatter closely around an oxidation state of ~2, while the untreated film has an oxidation state of ~3. The oxidation state of the powder spinel $\text{Co}^{\text{II}}\text{Co}^{\text{III}}_2\text{O}_4$ was experimentally determined as 2.67, which matches perfectly the theoretical value.

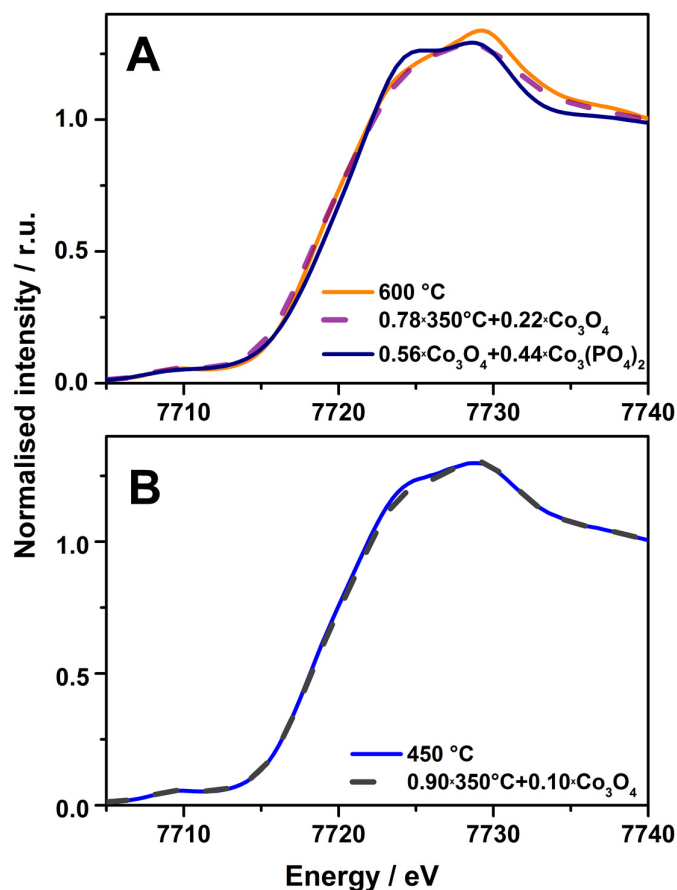


Figure 4.4. Co K-edge XANES spectra of (A) catalyst film calcined at 600 °C (orange line), linear combination $0.78 \cdot 350^\circ\text{C} + 0.22 \cdot \text{Co}_3\text{O}_4$ (dashed violet line), linear combination $0.56 \cdot \text{Co}_3\text{O}_4 + 0.44 \cdot \text{Co}_3(\text{PO}_4)_2$ (navy line) and (B) catalyst film calcined at 450 °C (blue line), linear combination $0.90 \cdot 350^\circ\text{C} + 0.10 \cdot \text{Co}_3\text{O}_4$ (dashed grey line). Linear combinations were selected by least-square fits (with the weighting factors as fit parameters).

In Figure 4.3 the second edge maximum of the calcined Co-containing films is very similar to the shape and position of the principal edge maximum of $\text{Co}^{\text{II}}\text{Co}^{\text{III}}_2\text{O}_4$. The higher the calcination temperature the higher this feature becomes. To investigate the calcined samples referring to their possible Co-spinel contribution, linear combinations of the XANES spectra of 350 °C and the $\text{Co}^{\text{II}}\text{Co}^{\text{III}}_2\text{O}_4$ spinel were calculated, which are displayed in Figure 4.4. Although the real Co^{III} contribution is still underestimated, the 600 °C calcined Co-film may contain at least 22 % Co-spinel (Figure 4.4 A). A linear combination of 90 % of the 350 °C Co-film and 10 % Co-spinel reproduces well the 450 °C calcined sample (Figure 4.4 B). The amount of Co-spinel obviously rises for a higher calcination temperature. The fraction or amount of Co-spinel refers to the ligand environment of the Co^{II} and Co^{III} ions in the spinel structure. This does not necessarily imply the formation of a Co-spinel phase, but the presence of atomic motifs related to $\text{Co}^{\text{II}}\text{Co}^{\text{III}}_2\text{O}_4$ spinel.

4.2.3 Atomic structure

To illuminate the atomic structure of CoCat films exposed to an elevated temperature program, we analysed EXAFS spectra at the Co *K*-edge. The Fourier-transformed (FT) EXAFS spectra are illustrated in Figure 4.5. Visual inspection of spectra alludes that the 450 °C and 600 °C sample obviously contain structural motifs up to a radius of 6 Å which are also present in the Co-spinel. Compared to the latter and to the ‘as-deposited’ Co-film their oscillations are lower, pointing to a smaller abundance of the present structural fragments.

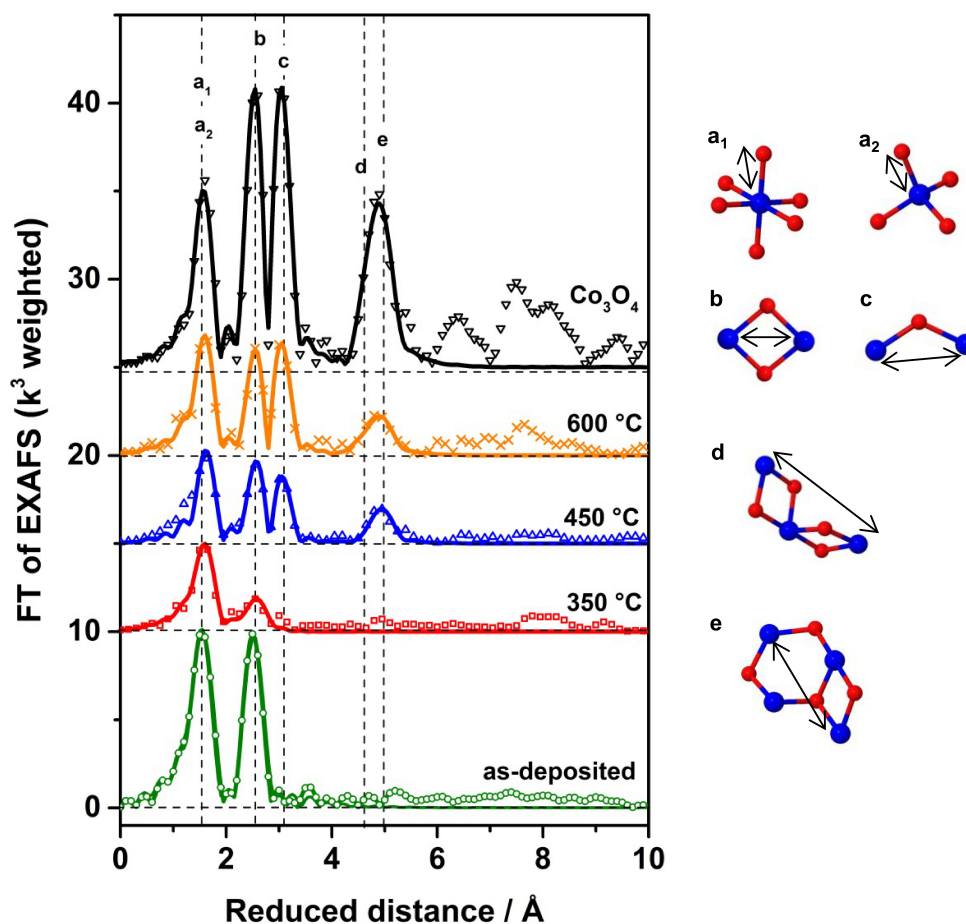
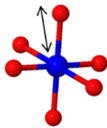
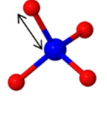
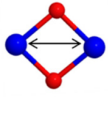
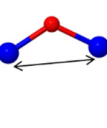
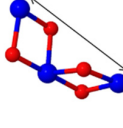
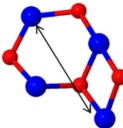


Figure 4.5. Experimental (symbols) and simulated (solid lines) FT Co *K*-edge EXAFS spectra of crystalline Co₃O₄ (black), the CoCat ‘as-deposited’ (olive), calcined at 350 °C (red), 450 °C (blue), and 600 °C (orange). The reduced distances were obtained by Fourier-transforming the unfiltered *k*-space data between 3 and 12 Å⁻¹. Unfiltered *k*-space EXAFS may be found in Figure 4.6. Structural motifs a_x, b, c, d, e are schematically displayed on the right side. Colour codes are the following: cobalt, blue; and oxygen, red.

Table 4.2 Selected prominent distances, R , coordination numbers, N , and main structural motifs of Co_3O_4 spinel (Smith and Hobson 1973, Liu and Prewitt 1990) are shown (within 5.3 \AA). This information was used as basis for EXAFS simulations of Figure 4.5 and Table 4.3. Note that Co_3O_4 possess more Co and O distances than the ones shown herein.

Co-O distance (a_1)	Co-O distance (a_2)	Co-Co ₁ distance (b)	Co-Co ₂ distance (c)	Co-Co ₃ distance (d)	Co-Co ₄ distance (e)
					
$R=1.89 \text{ \AA}$ $N_{ocr}=6$ -	$R=1.99 \text{ \AA}$ - $N_{tet}=4$	$R=2.86 \text{ \AA}$ $N_{ocr}=6$ -	$R=3.35 \text{ \AA}$ $N_{ocr}=6$ $N_{tet}=12$	$R=4.94 \text{ \AA}$ $N_{ocr}=12$ -	$R=5.25 \text{ \AA}$ $N_{ocr}=8$ $N_{tet}=14$
$N_O=5.33$		$N_{Co}=6$	$N_{Co}=8$	$N_{Co}=12$	$N_{Co}=10$

Quantitative information about the number of the ligands of the X-ray absorbing cobalt atoms and the inter-atomic distances can be obtained by simulation of the measured EXAFS spectra. The CoCat film, ‘as-deposited’ was simulated without any parameter restrictions (all parameters were allowed to vary freely) as demonstrated previously (Risch, Klingan et al. 2012). The procedure for EXAFS simulations of the calcined films was the following: mean coordination numbers of the prominent motifs of experimental Co K -edge EXAFS data of Co_3O_4 spinel were fixed according to the crystal structure of Co_3O_4 (Smith and Hobson 1973, Liu and Prewitt 1990). An overview of the weighted mean coordination numbers is illustrated in Table 4.2. The obtained Debye-Waller parameters were fixed for all calcined samples to the one gained for Co_3O_4 spinel (when the coordination numbers were set to the ones in Table 4.2) in order to obtain only the change in coordination number. The results of these EXAFS simulations are summarised in Table 4.3 and shown in Figure 4.5. This simulation approach lacks any information concerning the distribution of distances or the extent of disorder in the calcined films. Hence, Table 4.4 illustrates the simulation parameters for the first coordination sphere for the calcined Co-films, if all parameters are allowed to vary freely.

Table 4.3. Complete EXAFS simulation results for the ‘as-deposited’ CoCat, CoCats calcined at different temperatures, and Co₃O₄ powder. Parameters were used for spectra in Figure 4.5.

Sample	N_o	Co-O (a _x)		N_{Co}	Co-Co ₁ (b)	
		$R_o(\text{Å})$	σ_o		$R_{Co}(\text{Å})$	σ_{Co}
as-deposited	6.3±0.7	1.89±0.01	0.064±0.007	4.6±0.8	2.81±0.01	0.065±0.008
350 °C	3.3±0.4	1.95±0.01	0.050*	0.7±0.3	2.85±0.01	0.049*
450 °C	3.4±0.4	1.94±0.01	0.050*	1.6±0.3	2.85±0.01	0.049*
600 °C	4.1±0.4	1.94±0.01	0.050*	2.0±0.3	2.85±0.01	0.049*
Co ₃ O ₄	5.33*	1.90±0.01	0.050±0.001	6.0*	2.84±0.01	0.049±0.003
Sample	N_{Co}	Co-Co ₂ (c)		N_{Co}	Co-Co ₃ (d)	
		$R_{Co}(\text{Å})$	σ_{Co}		$R_{Co}(\text{Å})$	σ_{Co}
450 °C	1.6±0.3	3.35±0.01	0.047*	1.7±0.8	4.96±0.01	0.054*
600 °C	2.9±0.3	3.35±0.01	0.047*	2.2±0.8	4.96±0.01	0.054*
Co ₃ O ₄	8.0*	3.35±0.01	0.047±0.003	12.0*	4.96±0.01	0.054±0.007
Sample	N_{Co}	Co-Co ₄ (e)				
		$R_{Co}(\text{Å})$	σ_{Co}			
450 °C	1.5±0.7	5.29±0.01	0.023*			
600 °C	2.3±0.7	5.29±0.01	0.023*			
Co ₃ O ₄	10.0*	5.29±0.01	0.023±0.007			

The parameters marked by an asterisk (*) were fixed; all other parameters were determined by curve fitting to the experimental data (k -range of 3 Å⁻¹ to 12 Å⁻¹). The amplitude reduction factor, S_o^2 , was 0.7 and the energy axis of the fit was shifted by 3.5 eV relative to the initially selected E_o of 7710 eV. The errors accord to 68 % confidence interval and the maximum value of the R_f -factor was 13.8.

Table 4.4. EXAFS simulation result of the first ‘shell’ for calcined Co-films at different temperatures. In contrast to Table 4.3 all parameters were obtained by curve-fitting to the data (k -range of 3 Å⁻¹ to 12 Å⁻¹) in absence of any fixations (all parameters simulated without restrictions).

Sample	Co-O (a _x)		
	N_o	$R_o(\text{Å})$	σ_o
350 °C	4.2±0.8	1.95±0.01	0.068±0.011
450 °C	4.5±0.8	1.94±0.01	0.068±0.011
600 °C	5.0±0.8	1.94±0.01	0.066±0.011

The amplitude reduction factor, S_o^2 , was 0.7 and the energy axis of the fit was shifted by 3.5 eV relative to the initially selected E_o of 7710 eV. The errors accord to 68 % confidence interval and the maximum value of the R_f -factor was 14.

The first inter-atomic Co-O peak is detectable in all Co-films and in the micro-crystalline spinel-type Co₃O₄. We find a varying Co-O bond length between 1.89 Å and 1.95 Å for the first peak (Co-O, peaks a_x in Table 4.3). For the ‘as-deposited’ CoCat the distance at 1.89 Å corresponds to the coordination of six oxygen atoms (Risch, Ringleb et al. 2009) (Co-O, peak a₁). On the other side, the calcined CoCats exhibit Co-O bond lengths, which are 0.05 - 0.06 Å longer. The 350 °C treated CoCat has the longest Co-O distance of 1.95 Å, whereas 450 °C and 600 °C (Co-O, peak a₂) have an identical value within error ranges. The average bond length for tetrahedral coordinated Co^{II} is

1.96 Å (Wood and Palenik 1998), which corroborates the prevalence of Co^{II} in the calcined samples. If the Debye-Waller parameter, σ_o , is fixed (in relation to Co₃O₄, Table 4.3), a tetrahedral coordination is found for the 600 °C CoCat. For the lower temperature exposure a coordination number of four is still feasible within error ranges. At lower calcination temperatures the ordering may probably be reduced, which results in a reduced coordination number. Higher values (between 4.2 and 5.0) for Co-O coordination numbers are obtained, if the Debye-Waller parameters are allowed to vary freely (Table 4.4).

The spinel Co₃O₄ possess besides two thirds of distorted octahedrally coordinated Co^{III} also one third of tetrahedral coordinated Co^{II}, their Co-O distances differ only by 0.1 Å (Table 4.2) (Smith and Hobson 1973), so that the resulting experimental FT EXAFS spectrum in Figure 4.5 reproduces perfectly well only one Co-O peak at a distance of 1.90 Å.

The second peak (b) in Figure 4.5 reflects the shortest Co-Co distance. This distance of about 2.8 Å (peak b in Figure 4.5, Co-Co₁ in Table 4.3) can be attributed to cobalt ions that are interconnected by (μ-O)₂ or (μ-O)(μ-OH) bridges (Risch, Khare et al. 2009, Risch, Ringleb et al. 2009, Risch 2011, Risch, Klingan et al. 2012). This kind of di-μ-oxo bridging between cobalt ions can be specified as edge-sharing between CoO₆ octahedra for the ‘as-deposited’ CoCat and the Co₃O₄ reference. In large part upon temperature exposure the abundance of the main structural motif of the Co^{III}O₆ octahedra is drastically reduced ($N_{Co} \leq 2.0$, Table 4.3).

As the calcined CoCats are still highly amorphous materials lacking extended long-range order, the coordination number at the first Co-Co interaction may be related to the size of ordered fragments of incomplete Co₃(μ-O)₄ cubanes or the order within these extended structures determined by cobalt or oxygen vacancies. The coordination number for the Co-Co₁ distance appears to increase from around 0.7 for the 350 °C film *via* 1.6 for the 450 °C film to 2.0 for the 600 °C Co-film. Possible explanations are that upon heating the nuclearity of the intrinsically ordered fraction of interconnected incomplete cubanes could be lowered significantly or a high number of cobalt vacancies could be induced during the heating process. However, edge-sharing between tetrahedral motifs can be excluded on the whole, because the larger O-Co-O angle of 109.5 ° would result in a Co-Co₁ (b) distance of 2.26 Å, while the EXAFS result give distances of 2.85±0.01 Å for the calcined films.

Longer Co-Co distances at 3.35, 4.96 Å and 5.29 Å could only be found in the FT EXAFS spectra of the calcined 450 and 600 °C films and the micro-crystalline Co₃O₄ reference powder. Due to higher exposure temperatures parts of the CoCat probably transform at temperatures of 450 and 600 °C partially to motifs present in crystalline Co₃O₄. An indication in favour of this hypothesis is

the occurrence of the 3.35 Å distance for 450 and 600 °C calcined films, which corresponds to interconnected cobalt ions *via* a mono- μ -oxygen bridge (peak c in Figure 4.5, Table 4.3 Co-Co₂). This structural motif is not found in the ‘as-deposited’ CoCat and the 350 °C calcined film. In Co₃O₄ both Co atoms of tetrahedral and octahedral sites bind at a distance of 3.35 Å; it is indicative for mono- μ -oxo bridging in three situations, first bridging between CoO₄ and CoO₆ motifs, second bridging between CoO₄ and OCo₄ tetrahedra, and last corner-sharing of CoO₆ octahedra. These types of motifs may also be present in the 450 °C and 600 °C samples, generally mono- μ -oxo bridging between Co ions is peremptory. The other commonly shared motives between the 450, 600 °C film and Co₃O₄ occur at distances of 4.96 Å (peak d in Figure 4.5, Table 4.3 Co-Co₃) and 5.29 Å (peak e in Figure 4.5, Table 4.3 Co-Co₄) which belong to atomic fragments shown in Table 4.2 and Figure 4.5. The ‘as-deposited’ CoCat lacks both of these distances. Thus, under certain conditions the CoCat can possess a somewhat similar and 0.34 Å longer distance than peak e (Co-Co₄). CoCats electrodeposited under elevated potential (70 min at 1.40 V) exhibit a low amplitude Co-Co EXAFS distance of 5.63 Å, which can be explained by two (complete or incomplete) cubanes sharing a cobalt corner (Risch, Khare et al. 2009). To a minor extent this double Co-Co₁ distance may also be reflected as a small shoulder on peak e the cobalt spinel Co₃O₄. Thus, the structural motif found for the distance at 5.29 Å is quite different for the calcined samples and the crystalline Co₃O₄ powder (Table 4.2 and Figure 4.5) than for the CoCat and LiCoO₂. It could be identified as the backscattering distance between a tetrahedrally coordinated cobalt ion and a cobalt ion of edge-sharing octahedra. With higher calcination temperature the order of these three representative structural Co₃O₄ motifs (c,d,e) is increased within the calcined CoCats as their coordination numbers rise.

Figure 4.6 shows the experimental EXAFS oscillations in *k*-space and their corresponding simulations for the data presented in Figure 4.5. Commonly, the as-isolated EXAFS oscillations contain the same structural information than the Fourier-transforms. The 450 °C and 600 °C treated CoCats exhibit a striking similarity in their spectra, while the 350 °C one represents an intermediate form between the ‘as-deposited’ and the higher temperature calcined CoCats. The interesting region of the *k*-space oscillations can be found between 8 and 12 Å⁻¹. There, the calcined CoCats strongly differ from the ‘as-deposited’ CoCat, and moreover after being exposed to higher temperature their oscillations converge to a larger extend the ones of Co₃O₄. In general, the spectral intensities of the calcined film obviously discern from the micro-crystalline Co₃O₄, because the calcined samples lack the long-range order of the Co₃O₄. As the amplitude is directly proportional to the number of scattering atoms, the increase within the temperature series film corresponds to the formation of additional μ -oxo bridges. Generally, it is highly implausible to form a complete

Co₃O₄ spinel structure from the CoCat as a starting product. The CoCat, electro-deposited at pH 7, in 0.1 M KP_i always contains some phosphate (~28 %) and potassium (~26 %), where the majority of potassium ions is supposedly distributed rather randomly between Co-oxo layers in the form of largely hydrated ions (Risch, Klingan et al. 2012).

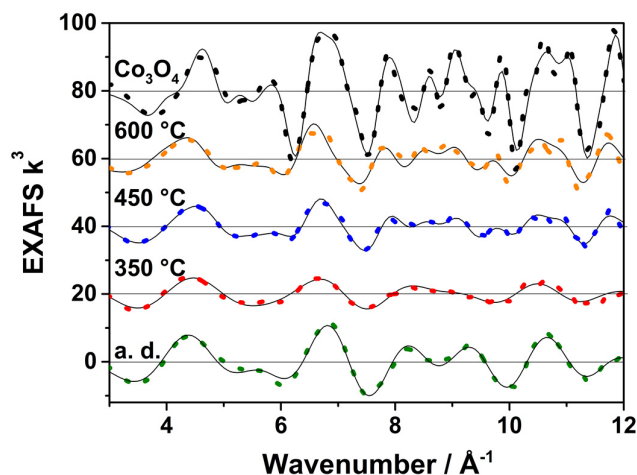


Figure 4.6. Experimental EXAFS oscillations in k -space (dotted coloured lines) and their simulation between 3 and 12 \AA^{-1} (black fine lines) for CoCat films ‘as-deposited’ (olive), calcined at 350 °C (red), 450 °C (blue), and 600 °C (orange), and for Co₃O₄ (black). The corresponding Fourier-transforms are shown in Figure 4.5.

Overall the XAS analysis delivered insight into the change of atomic structure when CoCats are heated up to temperatures of 350, 450 and 600 °C. The oxidation state of these samples is reduced to ~2 from ~3 for the original CoCat. Accompanied by the lower oxidation state is a transformation from octahedrally coordinated Co^{III} (CoCat) to an oxide with a major fraction of four coordinated Co^{II} (calcined samples). At 450 and 600 °C, the films possess at least three more common structural motifs with Co₃O₄, namely a mono- μ -oxygen bridge at ~3.4 \AA , a ~5.0 \AA distance between Co atoms of two adjacent Co^{III}O₆ octahedra, and Co interactions between a Co ion of edge-sharing octahedral and a tetrahedral CoO₄ at ~5.3 \AA . Although the effect of temperature does not change the CoCat into a crystalline material, a structural change towards motifs of the Co₃O₄ is observed. The local composition of the material of the calcined films may consist of two contributions: a rather unordered fraction and some motifs relating to Co-spinel.

4.2.4 Microscopical surface structure

Scanning electron microscopy (SEM) images of cobalt catalyst surfaces deposited on ITO, and cobalt catalysts undertaken a temperature program are depicted in Figure 4.7. These micrographs show how the surface of the catalyst changes upon heating.

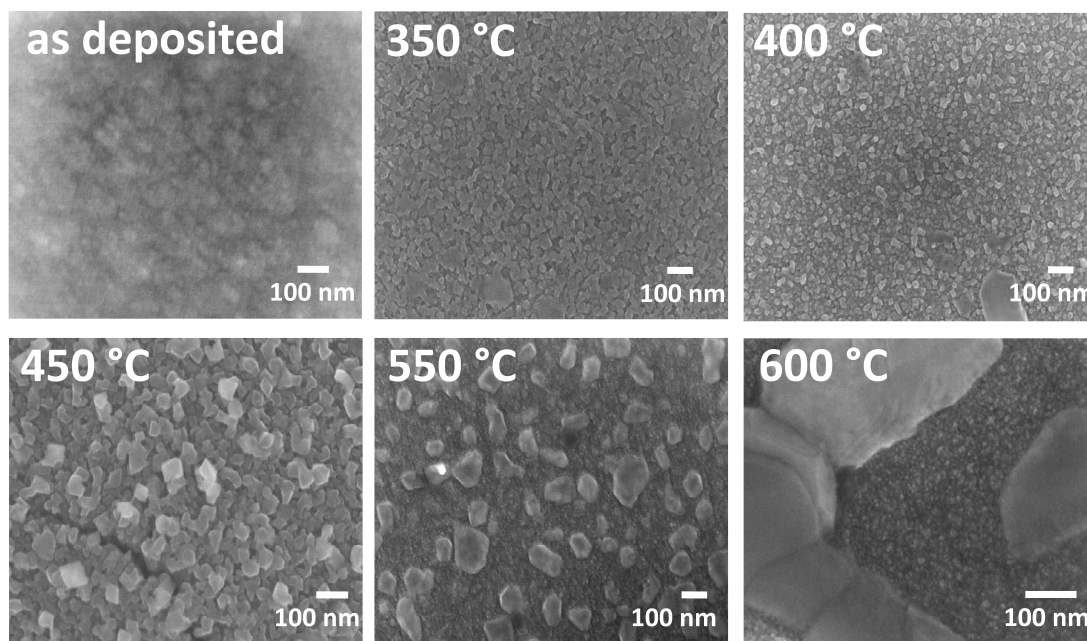


Figure 4.7. SEM images of CoCats, ‘as-deposited’ (45.0 mC cm^{-2}), calcined at 350, 400, 450, 550, and at 600 °C. CoCats were electrodeposited at 1.05 V vs. NHE from 0.1 M KP_i at pH 7 on ITO. SEM was performed by Dr. Anna Fischer at TU Berlin.

The ‘as-deposited’ CoCat of 45 mC cm^{-2} produces a relatively smooth, but still amorphous surface (Risch, Klingan et al. 2012, Klingan, Ringleb et al. 2014), while the 350 °C heated CoCat shapes into a distinct texture of cobalt-oxo grains. These fragments are sharper after a calcination of 400 °C. At 450 °C the clusters on top become bigger and more ordered, forming cubic shaped nuggets, which resemble a lot the surface structure of Co_3O_4 cubes (Xiao, Liu et al. 2012). At 550 °C and 600 °C a phase separation at the surface is striking. The morphology can be described as a film of fine grains, which is over-layered by bigger nodules, both exhibiting the same Co concentration (detected by EDX). The average size of cobalt-oxo clusters on the ITO surface was estimated from the micrographs (shown in Figure 4.7) as $28 \pm 15 \text{ nm}$ (350 °C), $32 \pm 16 \text{ nm}$ (400 °C), $54 \pm 14 \text{ nm}$ (450 °C), $110 \pm 60 \text{ nm}$ (550 °C), and $325 \pm 90 \text{ nm}$ (600 °C). In summary, the surface morphology exhibits with increasing temperature a bigger Co-oxo cluster size. Presumably all the calcined samples contain a phase separation of mainly unordered material and a Co_3O_4 spinel like material on top.

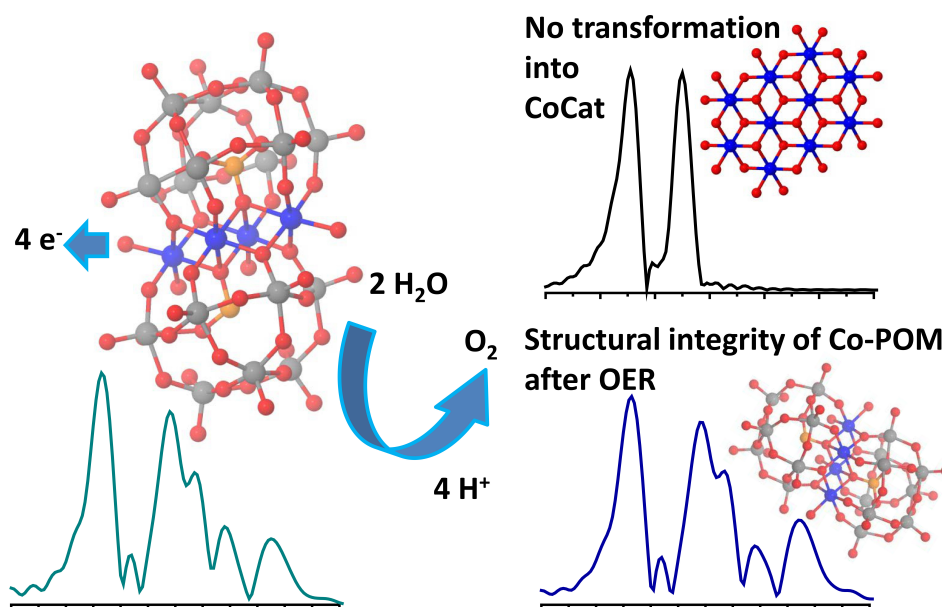
4.3 Summary

The atomic structure of the CoCat deposited in KP_i, which is dominated by edge-sharing CoO₆ octahedra, undergoes a major conversion upon calcination at different temperatures. X-ray absorption spectroscopy at the *K*-edge of Co revealed that the oxidation state of Co-films which are treated with high temperatures (at 350, 450, and 600 °C) is reduced from the initially Co^{III} in the ‘as-deposited’ catalyst to ~Co^{II}. After calcination the symmetry in the local geometry of the Co-films is lowered, as the abundance of the octahedral CoO₆ motif is drastically reduced and instead CoO₄ tetrahedra become a major contribution. Moreover, the 450 °C and 600 °C films contain the same structural motifs of Co^{II}Co₂^{III}O₄ spinel at atomic distances of ~3.35, 4.96 and 5.29 Å. All of these distances are not found in the CoCat. The two films calcined at 450 and 600 °C contain besides di-μ-oxo bridges also mono-μ-oxo-bridges as predicted for a Co^{II}Co₂^{III}O₄ spinel structure. A higher long-range order is found within the temperature series. The surface features of the calcined films exhibit larger clusters on top of finer grains. These changes in structure result in a severe loss of catalytic activity.

Chapter 5

Structural integrity of a molecular cobalt-polyoxometalate

In this chapter the integrity of a molecular cobalt-polyoxometalate (POM) (**1**) after the water oxidation reaction is scrutinised by X-ray absorption spectroscopy (XAS). Two different POM materials, $\text{Na}_{10}[\text{Co}_4(\text{H}_2\text{O})_2(\text{PW}_9\text{O}_{34})_2]$ (**1**) and $\text{Na}_{17}[\text{Co}(\text{H}_2\text{O})\text{Co}_2\text{PW}_9\text{O}_{34}(\text{PW}_6\text{O}_{26})]$ (**2**), the amorphous cobalt oxide (CoCat), and a potential Co^{2+} product of hydrolysis are compared. As a result, XAS reveals the integrity of **1** uncompromised by oxidant-driven water oxidation, which proceeds without formation of catalytic cobalt oxide, respectively the CoCat.



Artificial photosynthesis tries to mimic, *inter alia*, the transformation of water into oxygen and hydrogen (fuel). On one side heterogeneous transition metal oxide catalysts like the CoCat are robust, fast, and inexpensive water oxidation catalysts and potentially promising for industry application (Kanan and Nocera 2008, Kanan, Surendranath et al. 2009, Nocera 2012, Symes, Lutterman et al. 2013). On the other hand beyond doubt, the experimental research on homogenous catalysts like cobalt-polyoxometalates, which are promising water oxidation catalysts (WOCs) for production of non-fossil fuels, is also developing rapidly (Cady, Crabtree et al. 2008, Romero 2008, Brimblecombe, Dismukes et al. 2009, Sala, Romero et al. 2009, Yagi, Syouji et al. 2009, Dau, Limberg et al. 2010, Natali, Berardi et al. 2012). Due to the hindered oxidative ligand degradation, defective POM derivatives are very interesting (tailor-made). A breakthrough in the design of POMs has been achieved (Yin, Tan et al. 2010) as the purely inorganic POM $\text{Na}_{10}[\text{Co}_4(\text{H}_2\text{O})_2(\text{PW}_9\text{O}_{34})_2]$, **1**, functioned as an active WOC with $[\text{Ru}(\text{bpy})_3](\text{ClO}_4)_3$ (bpy = tris(2,20-bipyridyl)) as the oxidant. No wonder that **1** has been the subject of further studies (Lieb, Zahl et al. 2011, Ohlin, Harley et al. 2011, Stracke and Finke 2011). Certainly, a necessary condition is, that **1** is stable as such under turnover conditions. The latter has been put into question (Stracke and Finke 2011, Natali, Berardi et al. 2012). Therefore the hydrolytic stability and possible catalyst degradation during catalysis by Co *K*-edge XAS was investigated. Moreover, this system seemed to be an interesting subject for X-ray absorption spectroscopy (XAS) studies as it may be potentially viewed as a molecular and perhaps more defined version of the heterogeneous CoCat.

The structural data presented in this chapter reveals that Co-POMs can be stable under catalytic conditions and therefore are indeed promising WOCs. This important finding of the stability of **1** implies that the previous hypothesis of representing **1** as a starting material for the CoCat film has to be dismissed.

Most results reported in this chapter have been published:

R. Schiwon, K. Klingan, H. Dau, and C. Limberg, *Chemical Communications*, 2014, **50**(1): 100-102, <http://dx.doi.org/10.1039/c3cc46629a>

Adapted with permission from The Royal Society of Chemistry.

R. Schiwon synthesised **1**, **2**, and $[\text{Ru}(\text{bpy})_3](\text{ClO}_4)_3$, and recorded most of the UV-vis spectra

K. Klingan performed XAS, XAS data extraction and evaluation, EXAFS simulations, CoCat electrodeposition, recorded some UV-vis spectra, and Clark electrode measurements

H. Dau, C. Limberg supervised

5.1 Experimental detail

5.1.1 XAS sample preparation

Synthesis of **1**, **2**, and $[\text{Ru}(\text{bpy})_3](\text{ClO}_4)_3$ had been accomplished by Dr. Rafael Schiwon, HU Berlin, Department of Chemistry (AG Limberg). The synthesis of $\text{Na}_{10}[\text{Co}_4(\text{H}_2\text{O})_2(\text{PW}_9\text{O}_{34})_2]$ (**1**) has been performed according to a method established previously (Finke, Droege et al. 1987). Its basic structure and purity was confirmed by single-crystal X-ray diffraction (XRD, Figure 5.1, parameters listed in Table 5.1), mass spectroscopy, FT-IR, EXAFS, and UV/Vis spectroscopy. The synthesis of $\text{Na}_{17}[\text{Co}(\text{OH}_2)(\text{Co}_2\text{PW}_9\text{O}_{34})_2(\text{PW}_6\text{O}_{26})]$ (**2**) was accomplished according to literature (Ritorto, Anderson et al. 2004) and its structure and purity checked by FT-IR and EXAFS. Synthesis of $[\text{Ru}(\text{bpy})_3](\text{ClO}_4)_3$ was accomplished according to a modified literature synthesis (McDermott, Jones et al. 2011), described in detail in Schiwon, Klingan et al. 2014.

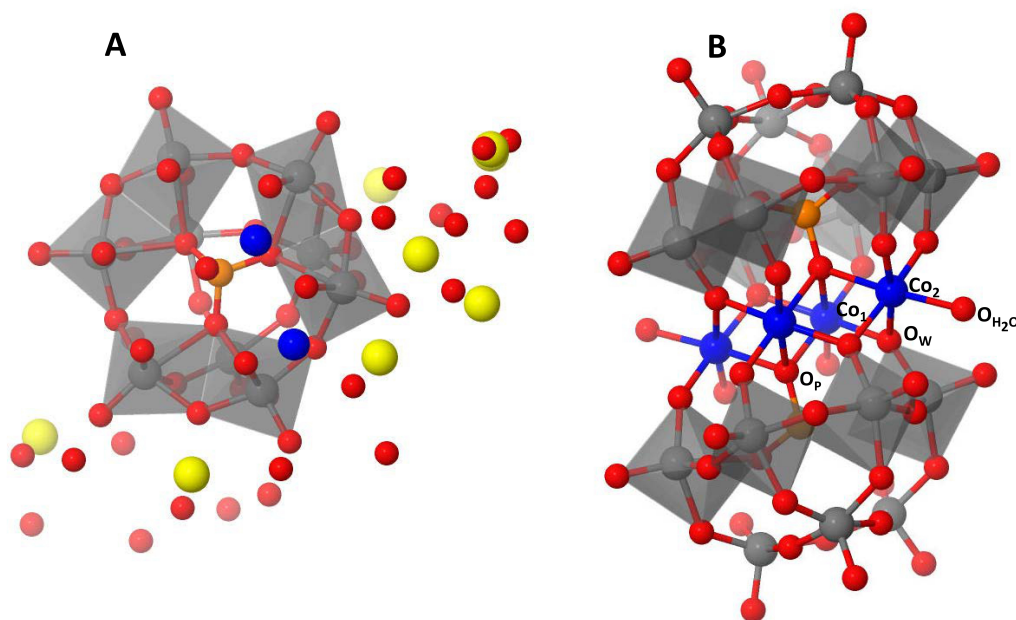


Figure 5.1. Coordination polyhedra representation of $[\text{Co}_4(\text{H}_2\text{O})_2(\text{PW}_9\text{O}_{34})_2]^{10-}$ based on the single crystal X-ray diffraction data of **1**·27 H₂O. Hydrogen atoms are omitted for clarity. **(A)** The unit cell of **1** in plane (1 1 0). **(B)** The planar tetra-cobalt core with two trans coordinated water molecules sandwiched by two polyoxometalate ligands. Selected bond lengths (Å) and angles (°): Co₁-Co₂ 3.1796(18), Co₁-O_P 2.194(8), Co₁-O_W range 1.998(8)-2.063(7), Co₂-O_W range 2.088(8)-2.096(8), Co₂-O_{H₂O} 2.113(7), O_W-Co₂-O_W range 82.5(3), O_W-Co₂-O_{H₂O} range 98.3(3)-101.1(3). Colour codes are the following: cobalt, blue; tungsten, grey; oxygen, red; phosphor, orange; and sodium, yellow.

Table 5.1. Crystal data and refinement parameters for the X-ray structure of **1**.

Complex	1
molecular formula	Co ₄ H ₂₀ Na ₁₀ O ₁₀₈ P ₂ W ₁₈
formula wt. (g mol ⁻¹)	5564.86
temperature (K)	100(2)
radiation (λ , Å)	0.71073
crystal system	triclinic
space group	<i>P</i> -1
<i>a</i> (Å)	11.4798(2)
<i>b</i> (Å)	13.2770(3)
<i>c</i> (Å)	18.2209(4)
α (°)	71.135(2)
β (°)	73.672(2)
γ (°)	73.251(2)
Volume (Å ³)	2461.78(9)
<i>Z</i>	1
Density (calculated)	3.754 mg/m ³
μ (mm ⁻¹)	21.786
<i>F</i> (000)	2444
crystal size (mm ³)	0.200 x 0.173 x 0.140
θ range for data collection	2,10 to 29.00 °
index ranges	-15 $\leq h \leq$ 15, -18 $\leq k \leq$ 16, -24 $\leq l \leq$ 24
reflections collected	69901
independent reflections	13066 [R(int) = 0.1638]
absorption correction	numerical
max. and min. transmission	0.1353 and 0.0376
refinement method	full-matrix least-squares on <i>F</i> ²
data / restraints / parameters	13066 / 0 / 651
goodness-of-fit on <i>F</i> ²	0.998
final R indices [R > 2 σ (I)]	<i>R</i> 1 = 0.0477, <i>wR</i> 2 = 0.1161
R indices (all data)	<i>R</i> 1 = 0.0602, <i>wR</i> 2 = 0.1211
largest diff. peak and hole	6.352 and -5.573 e.Å ⁻³

All samples for XAS analysis are listed in Table 5.2. The powder of **1** was diluted with boron nitride (Sigma Aldrich Chemie GmbH Munich, GER)) at a ratio of 1:10. A first layer of Kapton tape (25 μ m, Goodfellow, Bad Nauheim, GER) was fixed on one side of the custom-made sample-holder frame. The frame was a 3 mm thick polyoxomethylene sheet with a 0.5 x 1.5 cm² window hole through which the samples are accessible in XAS measurements. The powder samples were filled into the frame backed by the first Kapton tape. The cavity filled with the sample powder was closed by a second Kapton tape. XAS samples of **2** were prepared in the same way.

Table 5.2. Samples for XAS analysis

1, 2	powder
3.2 μM 1 , 30 mM NaPi, pH 8	solution
3.2 μM 1 , 30 mM NaPi, 1.5 mM [Ru(bpy) ₃](ClO ₄) ₃ , pH 8	solution
1 mM 1 , 30 mM NaPi, pH 8	solution
1 mM 1 , 30 mM NaPi, 8 mM [Ru(bpy) ₃](ClO ₄) ₃ , pH 8	solution
CoCat	thin-film on ITO

The liquid-sample mounts were manufactured as described above and closed with Kapton tapes on each side resulting in an initially empty volume between the Kapton layers of 200 μL . In variance to the powder-sample holders described above, the polyoxomethylene frame contained two holes (or channels) with a diameter of about 1 mm to facilitate injection of a solution using a gas-tight syringe.

For measurements on **1** after completion of the oxygen-evolution reaction, solutions of [Ru(bpy)₃](ClO₄)₃ and **1** in 30 mM NaPi were de-aerated by bubbling with argon gas for 10 minutes. Then the two solutions were quickly combined yielding the final concentrations indicated in Table 5.2. Within about 10 seconds after mixing, they were injected with a gastight Hamilton syringe (Sigma Aldrich Chemie GmbH Munich, GER) into the liquid-sample holders (volume of 200 μL) through one of its holes. In separate control experiments using a Clark-type O₂-electrode, we had verified that the reaction is relatively fast and essentially completed within 50 s (> 90 % of maximal amount of O₂ formation). Accordingly, the samples were promptly frozen in liquid nitrogen after a reaction time in the sample holder of 40 s yielding an overall reaction time of about 50 s (10 s before and during injection into the sample holder and 40 s after injection).

The CoCat film was prepared using a SP-200 potentiostat (Bio-Logic SAS, Claix, France). Potentiostatic electrodeposition was carried out at 1.05 V vs. NHE in 0.1 M KPi, pH 7 (prepared as a mixture of 40 % KH₂PO₄ and 60 % K₂HPO₄ followed by adjustment of the pH) and 0.5 mM Co²⁺ in a three electrode setup. Potentials were corrected for 80 % *iR* drop, *R* was equal to 50 Ω (for the entire cell). Deposition was completed, when a charge of 5 mC·cm⁻² had passed. The working electrode was a thin layer of conducting indium tin oxide (ITO) on glass with dimensions of 1.0 cm x 2.5 cm, the counter electrode a platinum wire, and the reference a mercury sulphate electrode (Hg/Hg₂SO₄/K₂SO₄, +650 mV vs. NHE) electrode. The resulting CoCat sample was carefully rinsed with 0.1 M KPi. Then, the sample was conditioned at 1.05 V in Co-free electrolyte for 2 min. Finally, the sample was quickly blow-dried using dry air. A single layer of Kapton tape (50 μm , Goodfellow GmbH) was used to fix the sample on its mount (custom-made, 1 mm thick polyvinyl

chloride (PVC) sheet which has a 1.1 x 1.5 cm² window). Finally, the mounted CoCat was frozen in liquid nitrogen within 1 min after conclusion of the conditioning step. All samples were stored for no longer than two weeks in liquid nitrogen before the synchrotron measurement. Data collection was performed as described in 2.1.7.

5.1.2 EXAFS simulations

All simulations were performed using the in-house software package ‘SimXLite’ (developed by Dr. P. Chernev, FU Berlin, Biophysics and Photosynthesis, AG Dau). The EXAFS data were extracted as described elsewhere (Risch, Klingan et al. 2012) (spline range 7711- 8511.65 eV, number of knots = 2, $E_0 = 7710$), then weighted by k^3 and simulated (least-squares fit) in k -space (without any Fourier-filtering). The phase functions for the EXAFS spectrum were obtained by *ab-initio* calculations using Feff 9.05 (Ankudinov, Ravel et al. 1998, Rehr, Kas et al. 2009). For the simulation of all **1** containing samples, the coordinates were obtained from the XRD data of **1**, in contrast for simulation of POM **2** the phase functions were calculated from its own structure. The energy shift of E_0 (relative to the value used for extraction of the experimental EXAFS data, that is, 7710 eV) was 3.5 eV.

5.1.3 UV-vis spectroscopy

Optical absorption spectra were recorded on an AGILENT 8453 diode array spectrometer in kinetics mode, mostly by Dr. Rafael Schiwon, HU Berlin, Department of Chemistry (AG Limberg). The total reaction volume in the cell was 2 mL, which was constantly stirred. The cell was charged with solid $[\text{Ru}(\text{bpy})_3](\text{ClO}_4)_3$ in a glove box and sealed with a septum; the remaining head space was floated with argon during the measurement. Argon was bubbled for 10 minutes through an aqueous 30 mM NaP_i buffer solution. An aqueous solution of 0.64 mM in **1** in 30 mM NaP_i was obtained through dissolution of 3.5 mg **1** in 1 mL of a 30 mM solution of NaP_i which after bubbling argon gas through the solution for exactly 10 minutes was immediately injected to the cell. The decomposition reaction of $[\text{Ru}(\text{bpy})_3](\text{ClO}_4)_3$ was started with addition of 2 mL of the 30 mM NaP_i buffer solution to 2.6 mg solid $[\text{Ru}(\text{bpy})_3](\text{ClO}_4)_3$ with a syringe and spectra were recorded every 3 seconds (Figures 5.2 and 5.3). Within 20 seconds 10 μL of a solution of 0.64 mM in **1** in 30 mM NaP_i buffer were added, which accelerated decrease of the absorption band of $[\text{Ru}(\text{bpy})_3]^{3+}$ at 670 nm immediately (Figures 5.4 and 5.5). The final reaction concentrations were 3.2 μM in **1** and 1.5 mM in $[\text{Ru}(\text{bpy})_3](\text{ClO}_4)_3$. Under air 1 mL of a 2 mM aqueous solution of **1** was mixed with 1 mL

of H₂O or 1 mL of a 60 mM solution in NaP_i (30 mM in NaP_i) or 1 mL of a 800 mM solution in NaP_i (400 mM in NaP_i) to get a 1 mM solution in **1** and spectra were recorded every 10 seconds for 90 minutes in a quartz cuvette (1 cm path length). Spectra were corrected by subtracting the average extinction between 700-800 nm. All three time traces (H₂O, 30 mM and 400 mM in NaP_i) with peak extinction at 579 nm were normalised for a better comparison (Figure 5.6).

5.2 Results

5.2.1 UV-vis changes

UV-vis spectra have been recorded, because of conflicting reports on the stability of **1** in solution and during, respectively after catalysis (Yin, Tan et al. 2010, Stracke and Finke 2011, Natali, Berardi et al. 2012). That is why we started to check the decomposition and accordingly the absorption behaviour of the oxidant $[\text{Ru}(\text{bpy})_3](\text{ClO}_4)_3$ (Creutz, Schwarz et al. 1984) used herein. Figure 5.2 shows that the absorption maximum at 670 nm of $[\text{Ru}(\text{bpy})_3](\text{ClO}_4)_3$ in 30 mM NaP_i at pH 8 exhibits a redox degradation with a $\tau_{1/2}$ of 75 s. During the reaction, a new product is formed, suggested by the new band at 800 nm. The time course of this reduction reaction from $\text{Ru}(\text{bpy})_3^{3+}$ to $\text{Ru}(\text{bpy})_3^{2+}$ is depicted in Figure 5.3.

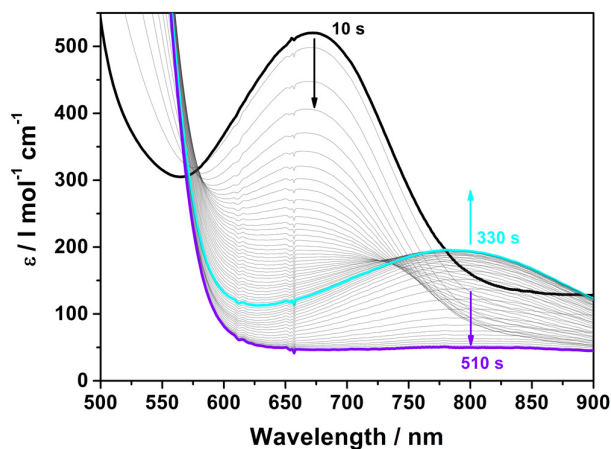


Figure 5.2. UV-Vis spectra of aqueous solutions of 1.5 mM $[\text{Ru}(\text{bpy})_3](\text{ClO}_4)_3$ in 30 mM NaP_i buffer at pH 8. $[\text{Ru}(\text{bpy})_3]^{3+}$ is slowly reduced to $[\text{Ru}(\text{bpy})_3]^{2+}$. Arrows indicate where the absorbance is increasing or decreasing with progressing time.

Thus, the OER reaction between 3.2 μM of **1** in 1.5 mM $[\text{Ru}(\text{bpy})_3](\text{ClO}_4)_3$ and 30 mM NaP_i shows a fast bleaching of the 670 nm absorption band of $\text{Ru}(\text{bpy})_3^{3+}$ (Figure 5.4 and 5.5). Reduction of $[\text{Ru}(\text{bpy})_3]^{3+}$ to $[\text{Ru}(\text{bpy})_3]^{2+}$ is faster when catalyst **1** is present. However, degradation of $[\text{Ru}(\text{bpy})_3]^{3+}$ via redox-decomposition is hindered compared to the previous case of absence of **1** (compare the 800 nm band in Figure 5.2 and 5.4). Hence, the reaction catalysed by **1** yielded 66.7 % O_2 as already demonstrated by Yin et al. 2010 (Yin, Tan et al. 2010).

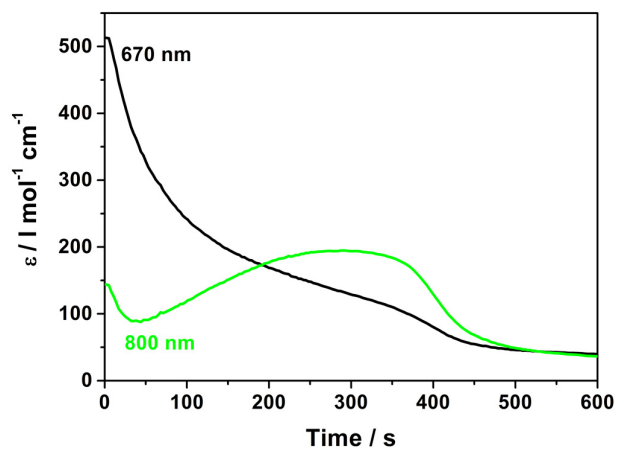


Figure 5.3. Monitoring of the reduction as a line diagram of ϵ vs. time at the designated wavelengths (670 nm black, 800 nm green) of aqueous solutions of 1.5 mM $[\text{Ru}(\text{bpy})_3](\text{ClO}_4)_3$ in 30 mM NaPi buffer at pH 8.

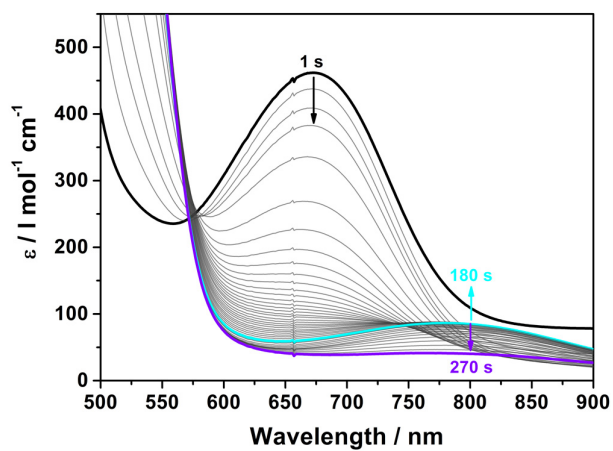


Figure 5.4. UV-vis spectra of aqueous solutions of 3.2 μM of **1** and 1.5 mM $[\text{Ru}(\text{bpy})_3](\text{ClO}_4)_3$ in 30 mM NaPi buffer at pH 8 from 0 to 270 seconds. Arrows indicate where the absorbance is increasing or decreasing with progress of time.

However, when we tested the stability of POM **1** in pure water, we observe unlimited stability of the catalyst (Figure 5.6). At pH 8 and buffer conditions (30 mM NaP_i and 3.2 μM of **1**) a slow decrease of the absorption band at 580 nm was observed in literature (Yin, Tan et al. 2010). We detected that the rate of slow decomposition depends on the NaP_i concentration as depicted in Figure 5.6. Within 1.5 h in 30 mM NaP_i, Co₄-POM **1** shows a decrease of 2 % in its main absorption band, while a concentration of 400 mM NaP_i yielded a decrease of 3.5 %. Recently, it was demonstrated (Vickers, Lv et al. 2013) that such an aging process does not influence the catalytic activity at all as different species (Co₄-POM **1**, CoCat, Co_{aqu.}²⁺) exhibit a very different kinetic behaviour as a function of pH, buffer identity, and buffer concentration.

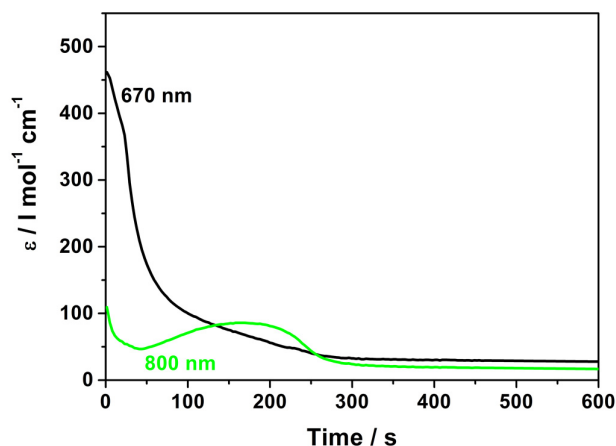


Figure 5.5. Monitoring of the catalytic reaction as a line diagram of ϵ vs. time at the indicated wavelengths (670 nm black, 800 nm green) of aqueous solutions of 1.5 mM $[\text{Ru}(\text{bpy})_3](\text{ClO}_4)_3$ and 3.2 μM of **1** in 30 mM NaP_i buffer at pH 8. Injection was performed after 20 s.

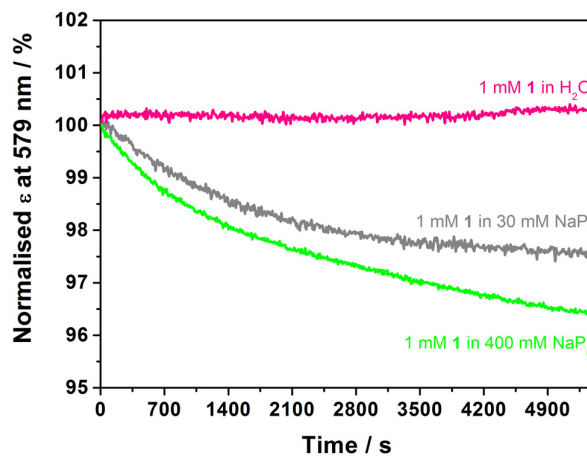


Figure 5.6. Normalised peak extinction at 579 nm vs. time of 1 mM solutions of **1** in water (pink), in 30 mM NaP_i buffer (pH 8.0, grey) and in 400 mM NaP_i buffer (pH 8.0, green). For 90 minutes, spectra were taken every 10 seconds.

5.2.2 Oxidation states

As the X-ray absorption near-edge structure (XANES) region is sensitive mostly to oxidation states and the coordination geometry in the first coordination sphere, we investigated the following Co-POM samples (Table 5.2) by Co *K*-edge X-ray absorption spectroscopy (XAS) at 20 K:

- (a) microcrystalline powder of **1**,
- (b) microcrystalline powder of **2**,
- (c) 3.2 μM of **1**,
- (d) 3.2 μM of **1** with 1.5 mM $[\text{Ru}(\text{bpy})_3]^{3+}$,
- (e) 1 mM of **1**,
- (f) 1 mM of **1** with 8 mM $[\text{Ru}(\text{bpy})_3]^{3+}$; where solution samples (c–f) always contained **1** in an aqueous buffer of 30 mM NaP_i at pH 8.

By collecting scans of two different Co-POMs, we verified the ability of XAS to detect structural changes in the cobalt oxo core of Co₄-POM (**1**), whose stability had been put into question (Stracke and Finke 2011, Natali, Berardi et al. 2012). Therefore, the well described (Co₃)₂-POM Na₁₇[((Co(H₂O))Co₂PW₉O₃₄)₂(PW₆O₂₆)] (**2**), with a different metal oxo core (Ritorto, Anderson et al. 2004) was synthesised and, after verification of its structure by FTIR (not shown here), investigated by XAS in form of a microcrystalline powder.

The oxidant containing samples (d) and (f) were frozen after water oxidation catalysis at an overall reaction time of 50 s and all other samples were immediately frozen. XANES analysis was employed to investigate **1** in aqueous solution at the same low concentration (3.2 μM) used previously for assessment of its catalytic performance (Yin, Tan et al. 2010). Since at this low concentration the signal to noise ratio after collection of 6 spectra (with simultaneous collection of 13 fluorescence signals) is only sufficient for interpretation of XANES; that is the information about the oxidation state of cobalt and major ligand modifications, but impossible for simulation of EXAFS data (information about atom-atom distances and coordination numbers), a reasonable higher concentration was inevitable for identification of the atomic structure. This clearly higher concentration of **1** (1 mM) facilitated collection of high-quality EXAFS spectra, while the water oxidation reaction remained unaffected by a change in concentration.

Figure 5.7 compares the cobalt *K*-edge XANES spectra of these samples to the heterogeneous CoCat (Risch, Klingan et al. 2012, Risch, Klingan et al. 2013), and a solution of Co²⁺. As a general rule, the edge positions on the energy axis are influenced by the oxidation state of the transition metal as well as its ligand environment (Teo 1986, Glatzel, Smolentsev et al. 2009). Usually,

higher oxidation states shift the edge position to higher energies, if the ligand coordination environment is largely conserved.

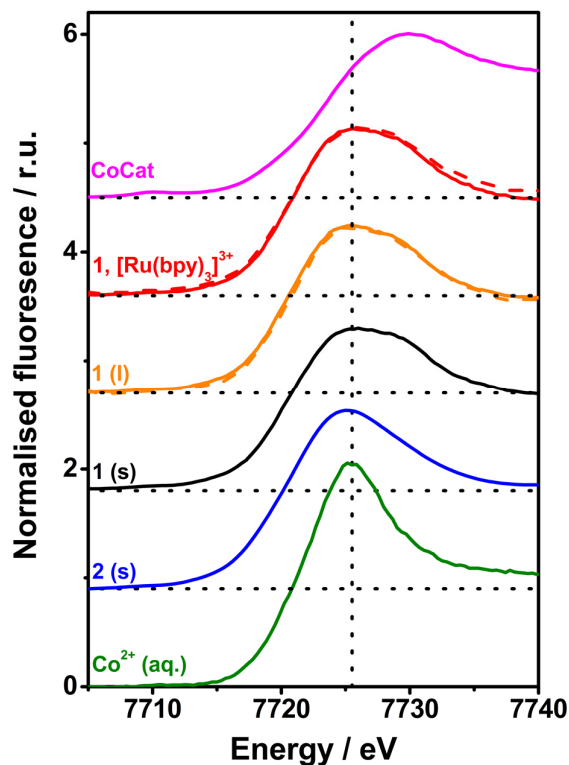


Figure 5.7. Cobalt *K*-edge XANES spectra for the heterogeneous CoCat (CoCat) (magenta), 3.2 mM of **1** with 1.5 mM $[\text{Ru}(\text{bpy})_3]^{3+}$ in 30 mM NaP_i (red dashed line), 1 mM of **1** with 8 mM $[\text{Ru}(\text{bpy})_3]^{3+}$ in 30 mM NaP_i (red), 3.2 mM of **1** in 30 mM NaP_i (orange dashed line), 1 mM of **1** in 30 mM NaP_i (orange), microcrystalline powder of **1** (black), microcrystalline powder of **2** (blue), and $[\text{Co}^{\text{II}}(\text{H}_2\text{O})_6](\text{NO}_3)_2$ in aqueous solution (green). All samples were frozen in liquid nitrogen before XAS data collection at 20 K.

The positions of the absorption edges of all samples containing **1** are identical within error ranges (Table 5.3). No matter whether **1** exists as microcrystalline powder, in 30 mM NaP_i buffer or after the OER with $[\text{Ru}(\text{bpy})_3]^{3+}$ in 30 mM NaP_i , the energy edge positions, which are a direct measure for the Co oxidation state remain identical in the whole XANES region. This is the first perception of the complete conservation of the basic structure of **1** after the water oxidation reaction.

In another work (Risch, Klingan et al. 2012), an empirical relation between the integral edge position and the oxidation state was revealed for Co *K*-edge spectra, which led to a calibration curve for Co-O compounds. Applying this calibration curve to herein presented XANES data, the averaged oxidation state of the Co atoms within all POM containing samples is 2.0 (Table 5.3). The integral edge position of the CoCat is substantial higher, namely close to +3.0, as reported before

(Risch, Khare et al. 2009). Therefore, we may infer that the oxidation state of **1** is conserved after water oxidation, and is the same as in the crystallographically (XRD) characterised form of **1**.

Profound differences between compounds **1** and **2** are not detectable by XANES due to the high similarity of **1** and **2** in the first coordination sphere and their identical oxidation state of +2. A minor distinction of the Co-POM **2** spectrum is that it is characterised by a narrower main fluorescence edge than all XANES spectra relating to **1**.

Concluding the analysis of the oxidation states of the sample set, it could be shown with the aid of XANES that for **1** dissolved at low and high concentration (3.2 μM and 1 mM), the spectra recorded before and after the Ru^{III} -driven oxygen evolution reaction (OER) are identical to its microcrystalline powder. We note that this finding does not exclude that higher cobalt oxidation states are formed during water oxidation at some point, because the herein investigated samples were frozen at a point where water oxidation had come to an end because of exhaustion of the $[\text{Ru}(\text{bpy})_3]^{3+}$ oxidant.

Table 5.3: X-ray edge position energies and estimated Co oxidation states for XANES Co *K*-edge spectra of Figure 5.7.

(*¹) The integral method described elsewhere (Dau, Liebisch et al. 2003) was used (integration: $0.15 < \mu < 1.0$) for determination of edge energies.

(*²) The energy at the half-height ($\mu = 0.5$) of the normalised spectra is shown for comparison.

The indicated error ranges are based on standard deviations obtained by analysis of three or more XANES spectra per sample type. Oxidation states were determined by a mathematical relation obtained from a calibration curve of Co-oxide powders (for more information see Risch, Klingan 2012).

Sample	Edge position* ¹ (eV)	Edge position* ² (eV)	Oxidation state
$\text{Co}^{\text{III}}\text{Cat}$	7720.7 \pm 0.1	7720.4 \pm 0.1	2.9 \pm 0.1
1 (l), $[\text{Ru}(\text{bpy})_3]^{3+}$	7718.6 \pm 0.2	7718.4 \pm 0.2	2.0 \pm 0.2
1 (l)	7718.5 \pm 0.2	7718.3 \pm 0.2	2.0 \pm 0.2
1 (s)	7718.5 \pm 0.2	7718.3 \pm 0.2	2.0 \pm 0.2
2 (s)	7718.2 \pm 0.2	7718.0 \pm 0.2	1.8 \pm 0.2
$[\text{Co}(\text{H}_2\text{O})_6]^{2+}$	7718.4 \pm 0.1	7718.3 \pm 0.1	2.0 \pm 0.2

5.2.3 Atomic structure

Analysis of extended X-ray absorption fine-structure (EXAFS) spectra obtained at the cobalt K -edge is necessary for the explication of the structure of **1** dissolved in aqueous NaP_i and of **1** after the oxygen evolution reaction. A scheme of atomic structures of **1**, **2** and their identified EXAFS distances are given in Figure 5.8. The five prevalent peaks of all Co-POM samples in Figure 5.9 may be assigned to distances from the X-ray-absorbing Co ion and its respective backscattering atom (atom pairs a-e, α , β indicated by arrows in Figure 5.8 and Table 5.4).

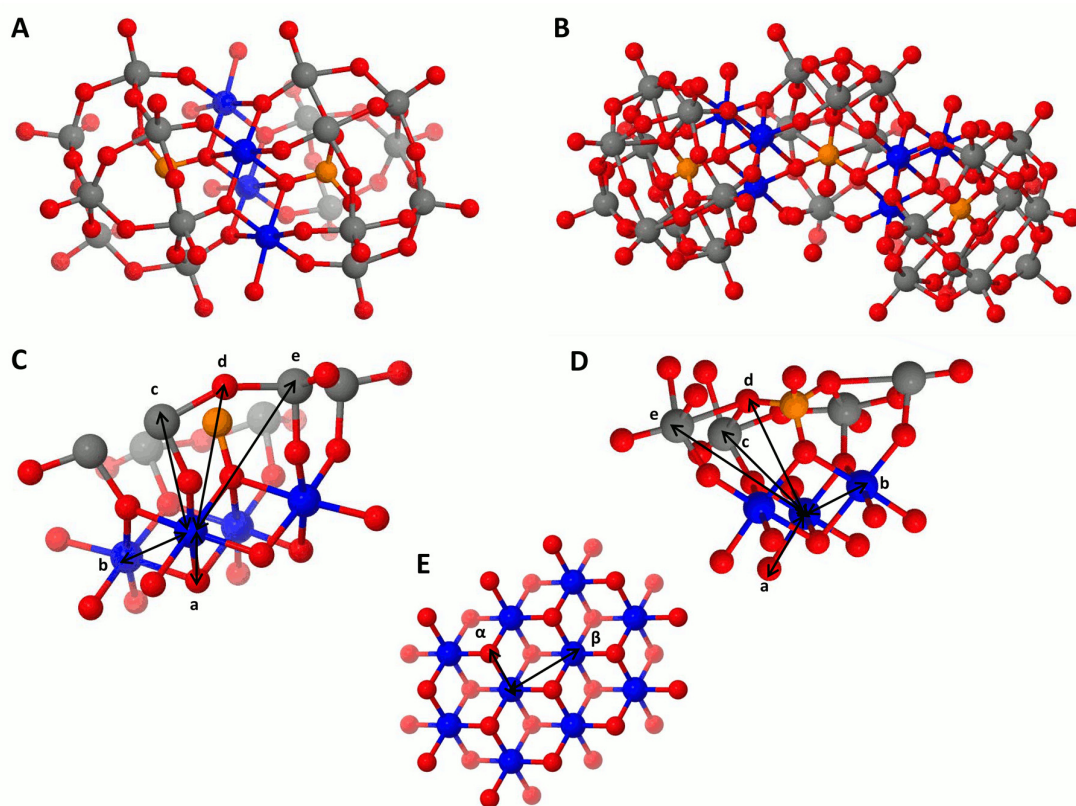


Figure 5.8. (A) Structure of **1**. (B) Structure of **2**. (C) EXAFS distances (a-e) could be identified between the absorbing cobalt ion and its backscattering neighbours of compound **1**. Herein a schematic representation of a $\text{Co}_4\text{P}_1\text{W}_6\text{O}_{23}$ fragment of **1** is given. For detailed information of EXAFS simulation results see Table 5.4. (D) Enlarged picture of the quantified distances of EXAFS simulation results of a $\text{Co}_3\text{P}_1\text{W}_4\text{O}_{25}$ fragment of **2**. (E) Structure of the CoCat with distances α (Co-O) and β (Co-Co). Colour codes are the following: cobalt, blue; tungsten, grey; oxygen, red; and phosphorus, orange.

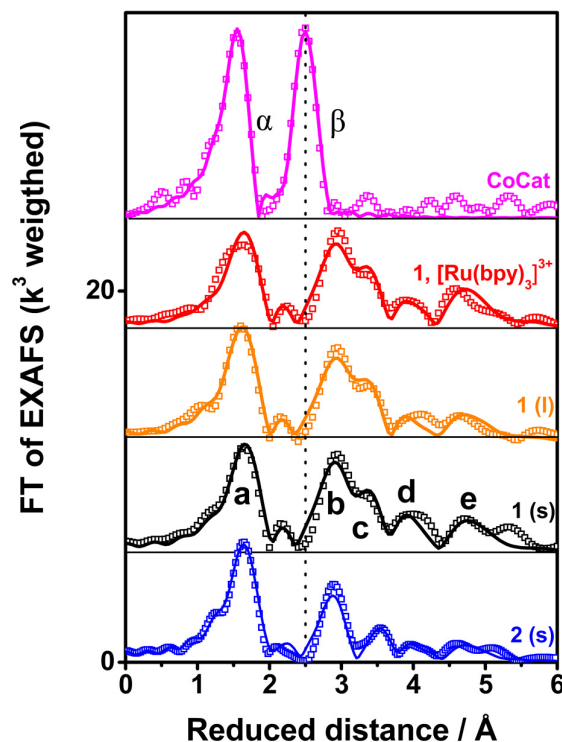


Figure 5.9. Fourier-transformed EXAFS spectra of CoCat (deposited in KP_i) (magenta), 1 mM **1** and 8 mM $[\text{Ru}(\text{bpy})_3]^{3+}$ in 30 mM NaP_i (red), 1 mM **1** in 30 mM NaP_i (orange), powder of **1** (black), and powder of **2** (blue) are shown. Experimental data are indicated by symbols and EXAFS simulations (parameters given in Table 5.4) are shown as lines. Note that the distance on the x-axis is reduced by 0.35 Å relative to the real distance. Peaks (a–e) as well as α and β correspond to distance vectors shown in Figure 5.8.

Figure 5.9 compares Fourier-transformed (FT) EXAFS spectra of the cobalt K -edge belonging to **1**, **2**, 1 mM **1** in 30 mM NaP_i , and 1 mM **1** dissolved in 30 mM NaP_i after reaction with 8 mM $[\text{Ru}(\text{bpy})_3](\text{ClO}_4)_3$ to the product of oxidative transformation, namely the CoCat spectrum.

The x-axis indicates the reduced distance between the X-ray-absorbing Co ion and ‘backscattering atoms’ of the first and higher coordination spheres. The indicated reduced distances are by 0.35 Å shorter than the real distances obtained by EXAFS simulations and presented in Table 5.4. Comparing the EXAFS spectra (Figure 5.9) as well as the structural parameters determined by simulation (Table 5.4), the high similarity between all **1** containing Co-POMs shows that neither dissolving **1** in aqueous buffer nor oxidant exposure and water oxidation catalysis causes structural modification. Also the Co–Co peak at a distance of 2.81 Å, which is typical of edge-sharing octahedra (di- μ -oxo bridges) in CoCat for Co^{III} (FT peak labelled as β) is fully absent for **1**, before and after catalysis of water oxidation.

For all investigated POM samples containing complex **1**, the five major FT peaks were found at the same distances within error ranges (Figure 5.9 and Table 5.4). The amplitude of peaks in the FT of the EXAFS spectra reflects the number of atoms occurring at the corresponding distances (a-e). Minor changes in peak height in the different POM containing samples do not indicate real modifications in the atomic structure of **1**, but rather may be associated with data spread.

Table 5.4. Complete parameters of the EXAFS simulations. N_i , EXAFS coordination number (atoms per X-ray absorbing Co atom); R_i , atom-atom distance; σ_i , Debye-Waller parameter. The parameter errors correspond to the 68% confidence interval. The Debye-Waller parameters labelled by an asterisk (*) have been fixed for reproduction of the known coordination numbers of **1** in microcrystalline form. All parameters were determined by curve-fitting of k^3 -weighted EXAFS data (before Fourier-transformation, k -range of 3–13 Å⁻¹). The amplitude reduction factor, S_0^2 was 0.78, and the energy axis of the fit was shifted by +3.5 eV relative to the initially selected E_0 of 7710 eV.

Sample	Co-O (a)			Co-Co (b)			R_f
	N_o	$R_o(\text{Å})$	$\sigma_o(\text{Å})$	N_{Co}	$R_{Co}(\text{Å})$	$\sigma_{Co}(\text{Å})$	
CoCat	6.0±0.3	1.89±0.01	0.064±0.002	4.3±0.3	2.81±0.01	0.068±0.002	17
1 , Ru(bpy) ₃	5.9±0.8	2.05±0.01	0.081*	2.4±0.4	3.19±0.01	0.044*	20
1 (l)	6.7±0.8	2.04±0.01	0.081*	2.5±0.4	3.19±0.01	0.044*	20
1 (s)	6.0±0.8	2.05±0.01	0.081*	2.5±0.4	3.19±0.01	0.044*	20
2 (s)	6.5±0.4	2.05±0.01	0.081*	1.5±0.2	3.18±0.01	0.044*	22
Sample	Co-W (c)			Co-O (d)			R_f
	N_W	$R_W(\text{Å})$	$\sigma_W(\text{Å})$	N_o	$R_o(\text{Å})$	$\sigma_o(\text{Å})$	
1 , Ru(bpy) ₃	3.2±0.8	3.54±0.01	0.063*	6.2±1.0	4.38±0.03	0.053*	20
1 (l)	3.3±0.8	3.55±0.01	0.063*	6.6±1.0	4.38±0.03	0.053*	20
1 (s)	3.2±0.8	3.55±0.01	0.063*	6.7±1.0	4.38±0.03	0.053*	20
2 (s)	1.7±0.4	3.62±0.01	0.063*	2.4±1.0	4.40±0.04	0.053*	22
Sample	Co-W (e)			R_f			
	N_W	$R_W(\text{Å})$	$\sigma_W(\text{Å})$				
1 , Ru(bpy) ₃	6.5±2.0	4.94±0.02	0.059*	20			
1 (l)	4.8±2.0	4.95±0.02	0.059*	20			
1 (s)	5.2±2.0	4.96±0.02	0.059*	20			
2 (s)	2.1±1.0	4.92±0.02	0.059*	22			

Simulation of the FT EXAFS spectra provides quantitative information about the coordination number of the X-ray absorbing atom and its interatomic distances in first and higher coordination spheres (Co-O, Co-Co, Co-W). The structure of the as synthesised **1** was already known from XRD analysis (Table 5.1 and Figure 5.8). Hence, for a simulation we fixed the EXAFS coordination numbers to the XRD coordination numbers for **1** (powder) and ran a simulation. The Debye-Waller factors, which were calculated in these simulations, were fixed in the following simulations to the value obtained previously, when EXAFS coordination number and distance were treated as unrestricted.

The first simulated distance for the POM samples can be assigned to a distorted Co^{II}-O octahedra with an average bond length of 2.04 or 2.05±0.01 Å. The first sphere Co-O bond length is dependent on the coordination state of Co. The Co^{III}Cat therefore has a shorter Co-O bond length than the Co^{II}-POMs. Thus, the Co-O in the CoCat is hexacoordinated and exhibits a characteristic bond length of 1.89 Å for Co^{III}.

Complex **1** consists of four Co atoms with an expected coordination number of 2.5 for the second Co-Co sphere at an average cobalt distance of 3.19±0.01 Å, which is retrieved by EXAFS simulations for all **1** POMs. In the third coordination sphere the Co-W bond length was identified as 3.54 or 3.55±0.01 Å. The XRD data predict a coordination of 3.5, which is in good agreement with the simulation result (3.2, 3.3±0.8). Furthermore, another Co-O bond length at 4.38±0.03 Å could be quantified in the EXAFS spectrum, here again the simulation results remain unvaried within error ranges for the different **1** samples. In the fifth coordination sphere, the simulation confirms an average, after catalysis unmodified Co-W bond length of 4.94, 4.95, 4.96±0.02 Å. Unfortunately, the Co-Co distance at 5.51 Å cannot be distinguished distinctly from the noise level, which would contain a difference in coordination number between complex **1** and **2** (**1** possess a Co₄ core, while **2** has two Co₃ cores).

To test the sensitivity of EXAFS to small structural changes and thus its reliability for the identification of **1**, we have investigated **2**, a closely related Co-based POM. Compound **2** contains three cobalt atoms in two Co cores, whereas compound **1** possesses only one core with four cobalt atoms (Figure 5.8). The geometry of **2** in the first coordination sphere corresponds as well to distorted Co^{II}-O octahedra. Differences in the atomic structure of **1** and **2** may be seen in all other coordination spheres.

As already mentioned, three Co atoms are situated in POM **2**; respectively simulations yielded an EXAFS coordination number of 1.5±0.2. However, an additional interaction with a Co-W vector at 3.4 Å may lower the actual coordination number to a small extent. The contribution of the Co-W

distances is deduced at 3.62 ± 0.01 Å, thus **2** exhibits a longer Co-W distance and a lower coordination than **1**. Moreover, the structural distinction between **1** and **2** becomes also evident in the lower EXAFS coordination number for the fourth coordination sphere (Co-O (d), 2.4 ± 1.0). In the fifth coordination sphere a slightly reduced Co-W bond length of 4.92 ± 0.02 Å and a smaller coordination of 2.1 ± 1.0 for complex **2** is observed than for **1**.

Comparing Co *K*-edge EXAFS spectra of **1** and **2** illustrated the high sensitivity of the EXAFS method to structural changes within Co-oxo cores. We may state that the detection of even the loss of a single Co ion for Co₄-POM **1** is observable by qualitative and quantitative EXAFS analysis.

Altogether, the herein presented EXAFS analysis has revealed that the complete atomic structure of **1** is preserved in buffer solution and after the water oxidation reaction. Moreover, the recently proposed hydrolytic fragmentation of **1** into soluble species (Natali, Berardi et al. 2012), which then perform the catalysis, could be rebutted by this XAS study. If hydrolysis of **1** occurred during the OER, then these fragments reassemble to give back **1** after catalysis, according to our results.

5.3 Discussion

Lately, it was shown that electrocatalytic water oxidation with **1** proceeds *via* a partial decomposition and release of Co^{2+} which leads to the deposition of a CoCat film as the ultimate catalyst (Stracke and Finke 2011). However, the conditions chosen (beside the presence of an electrode) were slightly different from those utilised in the original and this work. Based on the fact that all oscillations of the XANES spectra of **1** in NaP_i are identical to the as synthesised powder spectrum, hydrolytic decomposition can clearly be ruled out here. Solvated Co^{2+} cations (see spectrum of $[\text{Co}(\text{H}_2\text{O})_6]^{2+}$ in Figure 5.7) exhibit a $\sim 30\%$ higher intensity in the absorption maximum and also their XANES oscillations between 7730-7750 differ from **1**. The comparison of **1** to two conceivable products of hydrolytic decomposition (Co^{2+} solution) or oxidative transformation (CoCat) reflects that the coordination of the scattering atom and its oxidation state are preserved.

The sensitivity limit of the methods allows that maximally estimated 5% of the Co ions might be transformed into CoCat-type oxides. If these 5% of the Co ions were responsible for water oxidation catalysis, their turnover frequency would exceed 2 s^{-1} though, whereas the TOF for the CoCat is clearly below 0.1 s^{-1} (see Chapter 2, Figure 2.7 and Chapter 3, Figure 3.3). Thus, it is highly unlikely that a minor fraction of Co ions present in oxide form could be responsible for water oxidation. A further recent proposal has been hydrolytic fragmentation of **1** into soluble species (Natali, Berardi et al. 2012), which then perform the catalysis. If at all, these fragments reassemble to give back **1** after catalysis according to our results, or they would exhibit an extremely high activity. This scenario is quite unlikely as another recent work (Vickers, Lv et al. 2013) examined very closely the different reaction kinetics and thermodynamics of **1** and its possible transformation products under a variety of different concentrations, pH values, and buffer solutions. The initial reported conditions (Yin, Tan et al. 2010) of $3.2 \mu\text{M}$ **1**, 1.5 mM $[\text{Ru}(\text{bpy})_3](\text{ClO}_4)_3$, and 30 mM NaP_i at pH 8 and room temperature probably preserve 98 % of **1** according to Vickers et al. The decomposition product Co^{2+} of 2 % can neither affect the kinetics of the OER nor the oxygen yield as illustrated by control experiments when the same amount of $\text{Co}(\text{NO}_3)_2$ was added to the reaction mixture (Vickers, Lv et al. 2013). Moreover, CoCat formation would show an induction period on the timescale of the OER, which was not detected for the reaction of **1** (Vickers, Lv et al. 2013).

Overall, careful selection of the reaction conditions like pH, concentration, buffer systems, and non-invasive experimental methods regarding the stability of Co-POMs have to be chosen, when characterising the oxygen-evolving properties of Co-POMs. In this work, the reaction conditions were chosen as initially described by Yin, Tan et al. 2010 and then cautiously up-scaled for qualitative EXAFS analysis. In this way the stability of **1** after the OER could be demonstrated.

5.4 Summary

In conclusion, this X-ray absorption spectroscopy study corroborates the absence of hydrolytic or oxidative transformation of **1**. As other works suggested that not **1** but the amorphous CoCat is the water oxidation catalyst (Stracke and Finke 2011), because of partial decomposition of **1**, release of Co^{2+} , and followed CoCat deposition during electrocatalytic water oxidation, we investigated the stability of **1**. The previous hypothesis of hydrolytic or oxidative transformation of **1** could be rejected, because XANES data, qualitative EXAFS data (FT), and quantitative EXAFS analysis (curve fitting) do not contain any evidence for these possible transformation products.

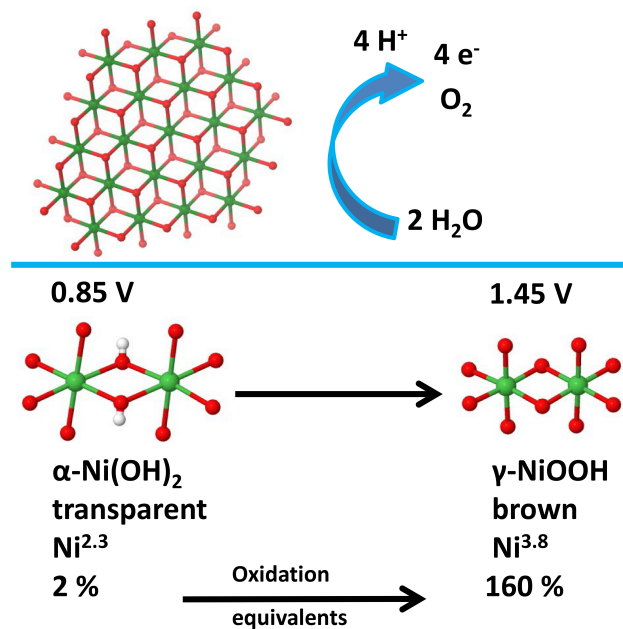
The sensitivity of the EXAFS investigation was checked by comparing two Co-POMs, which differ mostly in the number of atoms interconnected by oxo-bridges and sandwiched between oxo tungstates (four Co in **1** versus three Co in **2**). The predicted difference was reproduced perfectly well by EXAFS simulations ($N_{\text{Co-Co}}$ of 2.5 in **1** and of 1.5 in **2**, Table 5.4).

Avoiding relatively harsh electrocatalytic conditions and using a chemical oxidant at neutral pH, there are no indications for formation of a catalytically active Co oxide during homogenous POM water oxidation. Consequential, Co-POM **1**, which is composed exclusively of chemical elements of relatively high abundance, can be stable under catalytic conditions and thus is indeed a promising WOC.

Chapter 6

Structural and functional changes in the NiCat

Using X-ray absorption spectroscopy (XAS), we investigated the structure of a nickel-oxo catalyst (NiCat) during different modes of its operation. In a previous work (Risch, Klingan et al. 2011) the atomic structure of the NiCat has been identified in its ‘resting state’ as an amorphous layered oxide with layer fragments consisting of edge-sharing $\text{Ni}^{\text{III/IV}}\text{O}_6$ octahedra. Herein, we studied the X-ray absorption fine-structure (EXAFS) for different states of the NiCat obtained by variation of the electrochemical potential. The NiCat equilibrated at different potentials (non-catalytic as well as catalytic) was investigated by electrochemical, *in-situ* electrochemical UV-vis, and XAS experiments. Alterations in the different electrochemical states of the NiCat are accompanied with a change in oxidation state, atomic and electronic re-arrangement of the film. Moreover, the NiCat exhibits the characteristic colour changes of electrochromic materials (Svensson and Granqvist 1986). Regarding its functional and structural behaviour during water oxidation, the NiCat is far more complex than the CoCat, and the extent of nickel oxidation is 2.8 fold higher than for the cobalt catalyst film (Risch, Ringleb et al. 2015).



Applying a rather low potential of 0.85 V vs. NHE to the nickel-oxo catalyst film results in an EXAFS Ni-O distance of 2.03 Å and a Ni-Ni bond length of 3.08 Å. The elongation of the di- μ -oxo-bridges is probably caused by protonation (hydrogen bonding of OH groups). An identical Ni-Ni distance exists in α -Ni(OH)₂ (Pandya, O'Grady et al. 1990). Moreover, an oxidation state of ~2.3 was estimated for an electrochemical steady state of 0.85 V applied to the NiCat. The capacity for accumulation of redox equivalents is only ~2 %. Almost all the light can pass through the nickel-oxo catalyst.

At high electrode potential (1.45 V vs. NHE) the NiCat has an oxidation state close to 3.8 and can be associated with a nickel oxide with extended layer fragments similar to γ -NiOOH·xH₂O. The redox capacity is essentially increased to 160 %, as the NiCat can use and 1.6 electrons per nickel centre for oxidation/reduction. The absorption values are abruptly increased, beginning at 0.98 V, and continuously enhanced till 1.45 V, resulting in a brownish film

Portions of this chapter have been prepared for publication:

K. Klingan, R. M. Mohammadi, I. Zaharieva, P. Chernev and H. Dau

K. Klingan performed all experiments related to the 'non-operated' NiCat

R. M. Mohammadi tested long-term operation of the NiCat

I. Zaharieva, P. Chernev assisted in synchrotron measurements and valuable discussions

P. Chernev wrote software for data evaluation

H. Dau supervised

6.1 Experimental detail

6.1.1 Sample preparation

Electrochemical experiments including NiCat deposition were performed in a single-compartment, three-electrode setup driven by an SP-200 potentiostat (Bio-Logic SAS, Claix). Before anodic deposition all parts were cleaned. The platinum grid was cleaned consecutively with concentrated acids; H₂SO₄, HNO₃, and HCl, rinsed with needed amounts of miliQ water, then flame-cut with a laboratory burner to guarantee the absence of possible metals traces other than from the buffered deposition solution. The single-compartment cell was rinsed with the just mentioned acids and miliQ water, while the reference electrode was flushed with miliQ water and then with the later used Ni-free buffer electrolyte.

The NiCat was anodically electrodeposited from 0.1 M B(OH)₃ (B_i) and 0.5 mM Ni(NO₃)₂ at pH 9.2 and a deposition potential of 1.15 V *vs.* NHE. The buffer solution of 0.1 M B(OH)₃ was adjusted to pH 9.2 with small amounts of a saturated NaOH solution. After addition of Ni(NO₃)₂, filtration of this solution was necessary as solid nickel precipitate was observed. The deposition was stopped at a charge of 20 mC cm⁻² (or ~140 nmol nickel). All electrochemical measurements of ‘non-operated’¹ NiCats were performed with 80 % *iR* compensation (~40 Ω for the entire cell). The counter electrode was a platinum grid (25 x 25 mm²), the reference electrode was a mercury sulphate electrode (Hg/Hg₂SO₄/K₂SO₄, +650 mV *vs.* NHE), and as working electrode served ITO coated on glass (12 Ω per square, VisionTek Systems Ltd, Cheshire, UK), where a conductive area of 1.5 cm² was exposed to the solution. To enhance the electrical contact between the ITO and the clamp, copper tape (Farnell GmbH) was applied to the ITO/glass and tested with a multimeter. After the electrodeposition, the NiCat was washed with the buffering electrolyte (0.1 M B(OH)₃ pH 9.2), the reference electrode was rinsed with miliQ water, then buffering electrolyte, the Pt grid cleaned as before the electrodeposition. Then a CV of the NiCat in 0.1 M B(OH)₃ pH 9.2 was recorded with a scan rate of 20 mV s⁻¹.

For testing the long-term performance of catalyst films a Gamry Interface 1000TM (Gamry Instruments, Warminster, USA) with 8 potentiostats, having in total 10 channels (10 simultaneous experiments), each one in a three electrode setup, was used. The reference electrodes were saturated Ag/AgCl electrodes (+202 mV *vs.* NHE, Methrom), the counter electrodes were Pt wires, the working electrode ITO/glass. Active *iR*-drop compensation was not possible to conduct with

¹ ‘Non-operated’ denotes throughout the text that the NiCat has been brought to an electrochemical steady state by applying a constant potential for 3 minutes. No long-term operation (3 h or 24 h) has been performed on these samples.

this potentiostat and resistances were $\sim 90 \Omega$. Thinner films (containing 40 nmol nickel) were used in the experiments of the long-term performance in order to prevent an overall dissolution or dropout of the catalyst film. Buffer and other conditions stayed the same. Long-term electrolysis at selected potentials of 0.90 V and 1.40 V were performed for 24 h (Ohmic drop 1 - 2 mV), after every 30 min a CV (in a reduced scan range to prevent severe modifications of the film) was taken. Note that the shift of current waves in the CV is due to uncompensated resistances. Long-term performance was tested by Mohammad Reza Mohammadi (FU Berlin, Biophysics and Photosynthesis, AG Dau).

6.1.2 Total X-ray fluorescence analysis (TXRF)

As the nickel deposition occurs at 1.15 V vs. NHE, two processes are overlapping: deposition, *i.e.* oxidation from dissolved Ni^{2+} to solid Ni^{3+} , and oxygen evolution. At pH 9.2 the required electrode potential for water oxidation (25 °C) is 0.69 V vs. NHE. An electrochemical method which simply relates the number of electrodeposited nickel ions to the overall deposited charge is incorrect in this case due to oxygen evolution. Hence, the amount of deposited nickel was identified with total X-ray fluorescence analysis (TXRF). TXRF measurements were performed by using an AXS PicoFox (Bruker) instrument. After electrodeposition the NiCat was completely dissolved in a certain amount of 30% HCl and mixed with a gallium standard ($\text{Ga}(\text{NO}_3)_3$, 10 mg L⁻¹, Fluka TraceCert). A CV of the NiCat free ITO substrate was taken (which was lacking the nickel redox-waves) to control the complete dissolution of the NiCat for elemental analysis. A drop of the solution was dried on a silicon-coated quartz glass sample plate before TXRF measurements were initiated. As a result, a NiCat deposition stopped at 20 mC cm⁻² gives a film consisting of 138±4 nmol or 13.31±0.4 mC cm⁻² Ni (average of four different NiCat films). The iron content of the same sample was estimated as maximally 0.41±0.2 nmol, *i.e.* $\sim 0.3 \%$ of the total nickel concentration.

6.1.3 Coulometry

Coulometry was performed for the estimation of the amount of redox-charging in NiCats at different potential values. After electrodeposition of a 20 mC cm⁻² NiCat film, the catalyst was held at the desired potential in 0.1 M B(OH)₃ pH 9.2 for 3 min (time to reach a steady state value), then the potential was decreased to 0.45 V for 3 min. Background subtraction of the very same experiment in absence of the NiCat (blank ITO) was employed in order to compensate for electrochemical processes of the substrate electrode. The charge of the ITO was 0.5 % of the total charge. For every potential value a freshly prepared NiCat has been used. For the determination of

the reductive charge, Q_{red} , the cumulative charge of the potential jump from X V to 0.45 V was integrated. The reduction charging was expressed as a fraction of the one-electron reduction equivalent, Q_{red}/Q_{dep} in percent, where Q_{dep} was identified by TXRF analysis ($Q_{dep}=13.31\pm 0.4$ mC cm⁻²). If the one-electron reduction equivalent is 100 %, a change of one oxidation state by one electron is implied.

6.1.4 *In-situ* electrochemical absorption (UV-vis) changes

In-situ electrochemical absorption (UV-vis) spectra were recorded simultaneously with the SP-200 potentiostat and a Cary 50 UV-Vis spectrophotometer (Varian GmbH, Waldbronn). The three electrodes were put in a 20 mm dye-laser quartz cuvette. The counter electrode consisted of twisted Pt wires; otherwise all electrochemical conditions were kept the same. All spectra are background subtracted; the spectrum of ITO coated glass (12 Ω per square, VisionTek Systems Ltd, Cheshire, UK), in 0.1 M B(OH)₃ pH 9.2 at the corresponding potential was subtracted. A range of different potentials between 0.80 V and 1.45 V was applied and spectra were collected after the current densities were in a steady-state (after 3 min). For every generated potential a freshly prepared NiCat was used in order to prevent leaching of nickel ions into the solution or activity/structure modifications due to long-term operation.

The molar extinction coefficient, $\varepsilon(\lambda)$ (l mol⁻¹ cm⁻¹) has been calculated from a generalised equation (Risch, Ringleb et al. 2015) for the solid-state NiCat. For this special case Equation 6.1 takes into account that the absorption of the background and the spatial distribution of ions can be neglected, so that the extinction coefficient only depends on the differences in intensity between I_0 , the starting intensity, and I , the intensity after having passed the sample, as well as n_{Ni} , the molar density of nickel ions (mol cm⁻²) in the NiCat (determined by TXRF).

$$\varepsilon(\lambda) = \frac{-\log(I/I_0)}{n_{Ni} \cdot 10^3} \quad (\text{Eq. 6.1})$$

6.1.5 XAS sample preparation

Solid reference powders Ni^{II}O, LiNi^{III}O₂, and K₂Ni^{IV}(H₂IO₆)₂, were diluted with boron nitride (Sigma Aldrich Chemie GmbH Munich, GER) in a volume ratio of 1:10 and measured in absorption mode. The liquid [Ni^{II}(OH₂)₆]²⁺ reference sample was prepared in a concentration of 20 mM.

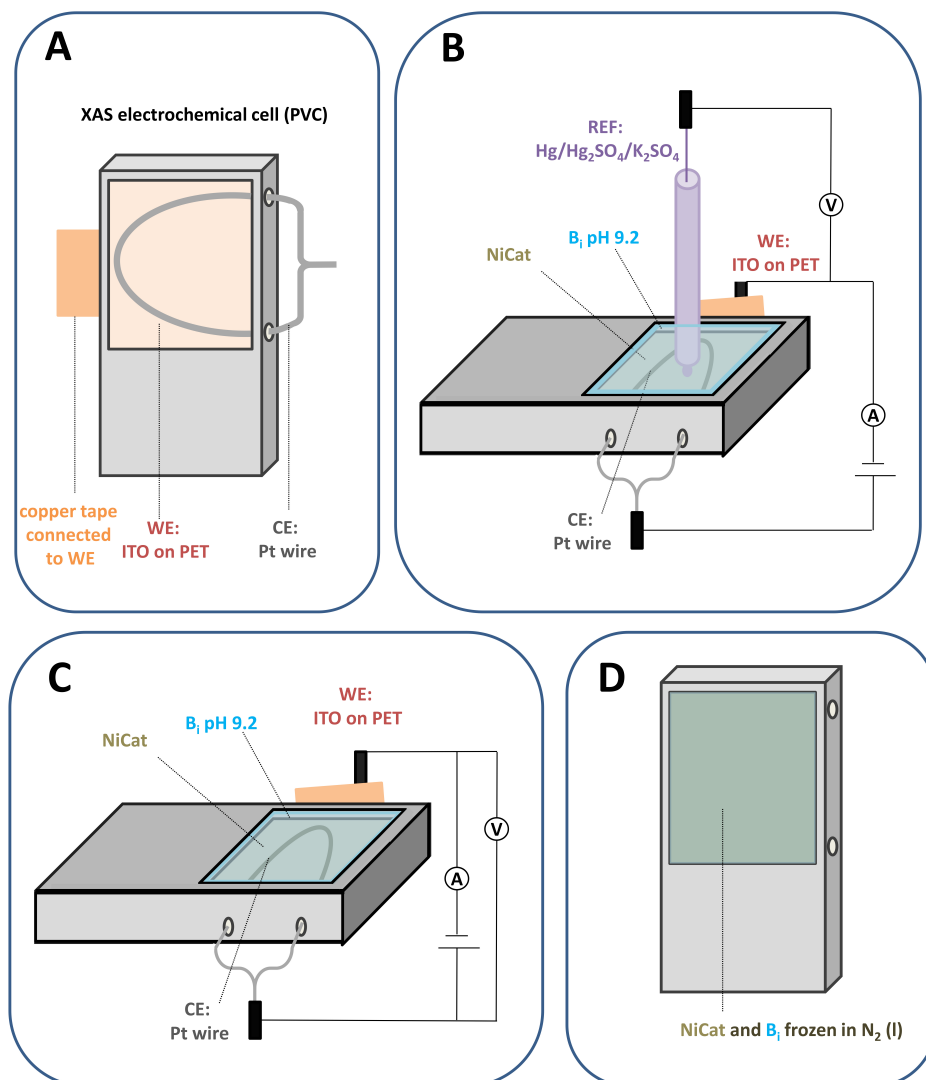


Figure 6.1. Preparation of NiCat samples for X-ray absorption spectroscopy (XAS). **(A)** Electrochemical cell made of transparent PVC with a window (14 mm x 14 mm) and two holes. Behind the window, the working electrode (WE) consisting of an ITO film coated on polyethylene terephthalate (PET) was glued. Copper tape was stuck on the corner of the working electrode for clamp connection. Through the holes of the cell a platinum wire as counter electrode (CE) was looped. **(B)** After electrodeposition of the NiCat, ~250 μl of electrolyte (0.1 M B_1 , pH 9.2) were filled in the cell and the desired potential was applied for 3 minutes with three electrodes. The reference electrode (REF) was a mercury sulphate electrode ($\text{Hg}/\text{Hg}_2\text{SO}_4/\text{K}_2\text{SO}_4 + 650 \text{ mV vs. NHE}$). **(C)** The reference electrode was removed. The potential applied between the working and counter electrode corresponded to the previous value measured after 3 minutes of potentiostatic coulometry. **(D)** After 3 minutes the whole sample cell was quickly and carefully frozen in liquid nitrogen under continuous voltage application between counter and working electrode. After the whole cell was frozen, the electrode clamps were detached and the copper tape was cut off, all in liquid nitrogen. Finally, the Pt wire was removed and the samples were stored in liquid nitrogen before synchrotron measurements.

A schematic overview of the preparation of the NiCat samples with an electrochemically induced steady state is given in Figure 6.1. The electrode substrates for the NiCats were ITO coated polyethylene terephthalate sheets (ITO on PET, Sigma Aldrich Chemie GmbH Munich, GER), which were cut to fit the sample holders (18 mm x 20 mm), cleaned with ethanol and one corner was contacted with copper tape for the electrode clamp connection. An in-house construction of small electrode cells (*i.e.* sample holders) from transparent PVC was used. These sample holders consisted of a window of 14 mm x 14 mm size, which assured an adequate size for multiple XAS scans on different spots, and 2 holes for mounting the counter electrode. Behind the window, the working electrode (an ITO film on a PET foil, resistance 60 Ohm/sq.), was glued and dried. A platinum wire (99.99 %, 0.5 mm diameter, Sigma Aldrich Chemie GmbH Munich, GER) served as counter electrode and was looped through the holes. The reference electrode was again a mercury sulphate electrode. Deposition was carried out in the same way as described above in 6.1.1 (for an overall charge of 20 mC cm^{-2} with 80 % compensation for Ohmic drop). We ensured by electrochemical control experiments that the ITO/PET substrate did not influence the behaviour of the NiCat. After deposition, the small cell was cleaned with 0.1 M B(OH)₃, the electrolyte was exchanged to nickel free 0.1 M B(OH)₃, pH 9.2 buffer, and a CV was conducted with 20 mV s^{-1} to further investigate only excellent quality NiCat samples, which exhibit the same CV as the ones synthesised and investigated in larger electrode cells. Then, the desired electro-conditioning was applied with potentials of 0.80 V, 0.85 V, 0.90 V, 1.00 V, 1.25 V, or 1.45 V for 3 min in 0.1 M B(OH)₃ at pH 9.2. The potential between the counter electrode and the working electrode was recorded. Consecutively, the reference electrode was removed and further sample preparation was achieved with a two electrode setup and a power supply, which was set to the potential measured between the working and counter electrode (after 3 min of potentiostatic coulometry). After 3 min the whole sample cell was quickly and carefully frozen in liquid nitrogen under continuous application of a voltage between working and counter electrode. Subsequently, the electrode clamps were detached and samples were stored in liquid nitrogen not longer than one week before XAS measurements at the synchrotron. For further information on this ‘freeze quench’ method, *i.e.* on the production of quasi *in-situ* samples by freezing small electrochemical cells, see Risch et al. 2015.

For testing the long-term equilibration, the NiCat samples were electrodeposited on ITO/glass under the conditions described above (see 6.1.1 Electrodeposition of the NiCat), and then potentials of 0.90 V for 24 h, 1.40 V for 3 h, or 1.40 V for 24 h were applied. The NiCats were washed with buffer solution, mounted to the sample holders, and frozen in liquid nitrogen before the synchrotron measurements.

6.1.6 XAS measurements

The X-ray absorption spectroscopy (XAS) data at the nickel *K*-edge were gathered at beamline KMC-1 (Schaefers, Mertin et al. 2007) of the Helmholtz-Zentrum Berlin for Materials and Energy (HZB). The characteristics of the beamline and its optics have been described in detail in Schaefers, Mertin et al. 2007. A liquid helium cryostat (Oxford Danfysk, heat conduction by helium gas at 0.2 bar in the sample compartment) was employed to establish a temperature of 20 K in order to preserve the sample state and prevent radiation damage of the samples. The excitation energies were selected by a double-crystal monochromator (Si-111), such that the scan range was 8215-9378 eV (Ni *K*-edge XAS). An energy-resolving fluorescence detector with 13 germanium elements (Ultra-LEGe detector elements, Canberra GmbH) was used. Each spot on the examined NiCat films was exposed for less than 35 min to synchrotron radiation at 20 K. After each scan the spot location was changed vertically by 0.5 mm. Two overlaying sheets of cobalt foil (0.01 mm thickness, 99.9 %, Goodfellow) were used as filter foil, which were mounted in front of the sample facing the fluorescence detector. At least six different sample spots of two different samples were scanned. For each spot on the sample the spectra of 13 channels were averaged.

Energy calibration was achieved by measuring simultaneously the *K*-edge inflection point of a nickel foil (5 μm , 99.9% purity, Goodfellow) at 8333 eV. We did not detect any radiation induced damages including oxidation state changes or structure changes at the NiCat samples due to minimised exposure time (< 35 min), high distance between cryostat and focal point of the beamline (> 3 m), low temperature (20 K), and thus low X-ray dosage per irradiated area.

6.1.7 XAS data extraction

The XAS data evaluation requires several steps of data extraction. A picture of the end part of the XAS setup is given in Figure 6.2. The following data is simultaneously recorded: four ionisation chambers (I_{00} after the monochromator and before the focal point of the beamline, I_0 before the sample, I_1 after the sample, and I_2 after the energy standard chamber), the total incoming count rates (*ICR*) and raw fluorescence signals of the 13 detector elements. Thus, the energy calibrated, normalised, and averaged fluorescence spectrum of one sample has still to be processed regarding these simultaneously detected signals.

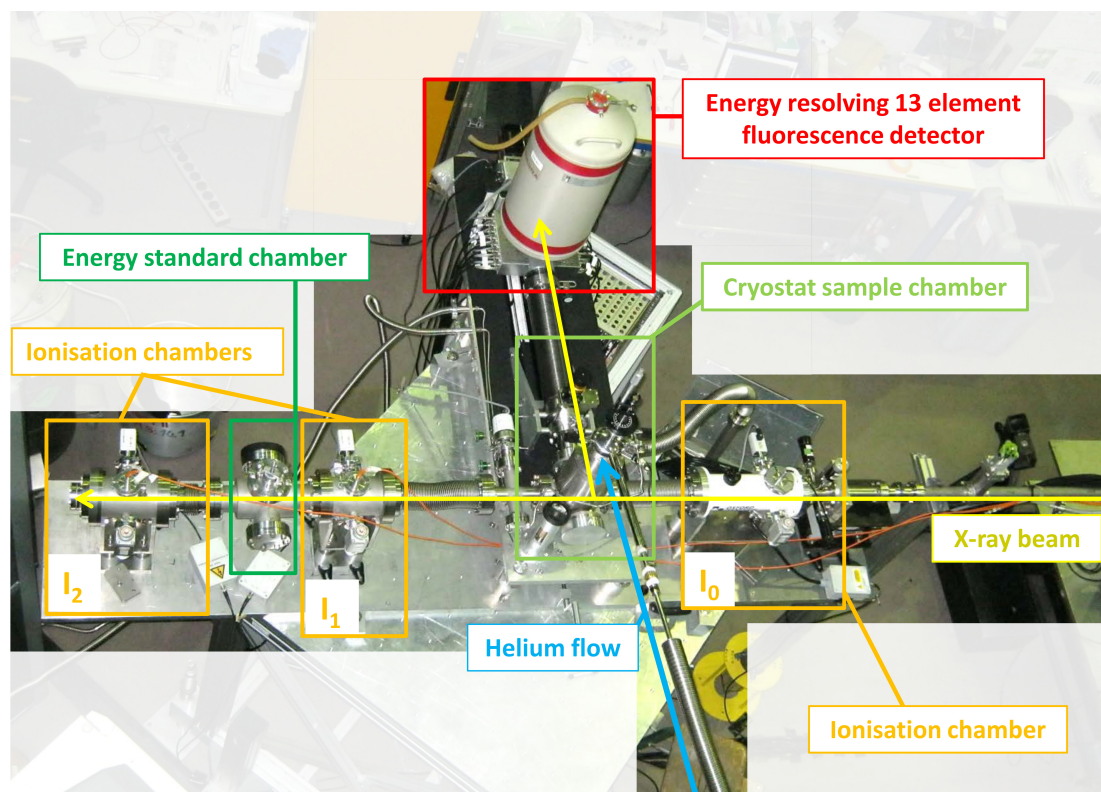


Figure 6.2. The XAS setup at the BESSY synchrotron (Berlin-Adlershof) operated by the Helmholtz-Zentrum Berlin (HZB). The photo shows the XAS setup of the beamline KMC-1 (Schaefers, Mertin et al. 2007). Simultaneous detection of 13 fluorescence signals with an energy-resolving 13 germanium element detector (Ultra-LEGe detector elements, Canberra GmbH) in windowless mode can be achieved. In addition the currents of three ionisation chambers I_0 , I_1 , and I_2 (absorption mode) are recorded.

XAS data extraction starts with a dead time correction for all signals. Time scans at a fixed energy for the corresponding shaping time of the 13 detector elements are recorded, and then plotted in a saturation curve. Hereby, the out-coming count rate (*OCR*) is correct by an exponential fit from the *ICR* values (Equation 6.2).

$$OCR = A \cdot (1 - e^{-k \cdot ICR}) \quad (\text{Eq. 6.2})$$

Then, the absorption by $-\ln(I_1/I_0)$, I_2' by $-\ln(I_2/I_1)$, and the fluorescence by dividing by I_0 were calculated. A finer energy calibration was performed the following: the I_2' spectra were background corrected by subtraction of a straight line, normalised by dividing by a 3rd order polynomial between 8396 and 9357 eV, and its derivative calculated. The 13 channels were averaged. The first peak of the derivative of I_2' was fit with a combined linear and Gaussian function (between 8312 and 8325 eV) to the known literature value of 8333 eV (Bearden and Burr 1967). Finally, energy

calibration was completed by shifting the energy axis of the experimental data by an offset such that the pre-edge of the fluorescence aligned to 8333 eV (Bearden and Burr 1967).

Subsequently, 6 to 8 scans for each sample were averaged. The fluorescence spectra were normalised by background subtraction of a linear fit (between 8222 and 8326 eV), followed by division of a 2nd order polynomial (between 8379 and 9362 eV).

The signal to noise ratio was calculated, and spectra rms-noise weighted as described in Risch, Klingan et al. 2011. Extraction of the EXAFS oscillations was conducted by subtracting a ‘knot-spline’ with 5 knots between 8335 and 9353 eV from the fluorescence data. Then, the energy axis was shifted by subtraction of 8335 eV (E_0) (Penner-Hahn 1999) and assigned into the wave vector space (Fourier-transformation in k -domain).

6.1.8 EXAFS simulations

The in-house software package ‘SimXLite’ (developed by Dr. P. Chernev, FU Berlin, Biophysics and Photosynthesis, AG Dau) was used for all simulations.

The phase functions for simulation of the nickel K -edge EXAFS were obtained by *ab-initio* simulations using FEFF 9.05 (Rehr and Albers 2000, Rehr, Kas et al. 2009). Coordinates were taken from a cluster of 10 nickel atoms and 32 oxygen atoms (NiO₂ layer) from a LiCoO₂ structure, where the cobalt atoms were replaced with nickel atoms (Risch, Klingan et al. 2011). Multi-scattering paths between nickel atoms were included up to a radius of 6 Å. Simulations of the electro-conditioned samples were performed with the following phase functions for a NiO₂ layer: Ni-O 1.9 Å, Ni-Ni₁ 2.8 Å, Ni-Ni₂ 4.9 Å, and Ni-Ni₃ with a multi-scattering path at 5.6 Å (‘three-legged’ and ‘four-legged’), the Ni-O distance of 2.02 Å in 0.85 V with the corresponding phase function from [Ni(H₂O)₆]²⁺, and the Jahn-Teller distorted distances were simulated with phase functions built from β-NiOOH (Demourgues, Gautier et al. 1997, Villars 2015). Reference compounds [Ni(H₂O)₆]²⁺, LiNiO₂ (Dyer, Borie et al. 1954), and K₂Ni(H₂IO₆)₂ were simulated with phase functions, built from their own coordinates. The energy shift of the nickel phase functions was 7.0 eV. Parameters were determined by curve-fitting to the experimental data in a k -range of 3-13.5 Å⁻¹. The amplitude reduction factor S_0^2 was 0.6.

6.2 Results

6.2.1 Coulometry

Coulometry shows that in a maximally oxidised film (1.45 V) approximately 1.6 electrons per nickel centre contribute to the changing of oxidation states between 0.45 V and 1.45 V vs. NHE (Figure 6.3). A lower limit of the NiCat's redox-charge during water oxidation is also obtained by the integration of the negative current densities of the CV in Figure 6.4 (in its suitable time domain), which gives 20.4 mC cm^{-2} , respectively 153% redox charge. The quantitative character of nickel oxidation in the NiCat is important, as these two results suggest that a 'non-operated' NiCat can use between 1.5 (CV) and 1.6 (coulometry) electrons per nickel centre for oxidation/reduction. Furthermore, this implies that the 'non-operated' NiCat already possess a high capacity for accumulating reduction equivalents.

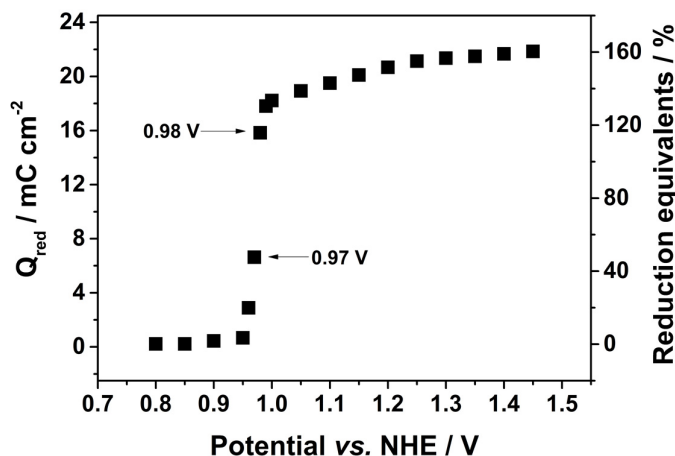


Figure 6.3. Reduction charge, Q_{red} , (left y-axis) and reduction equivalents (in percent on the right y-axis) of the nickel oxide catalyst at different potentials. The reduction charge, Q_{red} , was calculated from coulometry by the integration of the potential jump (between the potential indicated at the x-axis and 0.45 V vs. NHE) in 0.1 M $\text{B}(\text{OH})_3$ pH 9.2. The reduction equivalents of the NiCat were calculated by dividing the reductive charge, Q_{red} , by the total deposited charge, Q_{dep} , identified by TXRF, at different potentials. The arrows indicate data points at 0.97 V and 0.98 V, where a huge jump also for the corresponding absorption values is observed (Figure 6.4).

6.2.2 Electrochemical absorption changes

Figure 6.4 shows the second CV of a NiCat containing ~ 140 nmol of Ni, which was electrodeposited in 0.1 M $\text{B}(\text{OH})_3$, 0.5 mM $\text{Ni}(\text{NO}_3)_2$ at pH 9.2 at 1.15 V, in 0.1 M $\text{B}(\text{OH})_3$ at pH 9.2. Similar to the CoCat three prominent features can be attributed to the electrochemical function

of the NiCat as water oxidation catalyst: An anodic oxidative current wave, which is surprisingly sharp when compared to other transition metal catalysts like the CoCat and the MnCat (Zaharieva, Chernev et al. 2012, Klingan, Ringleb et al. 2014, Risch, Ringleb et al. 2015), a catalytic wave corresponding to water oxidation and oxygen evolution, and a well pronounced cathodic reductive current wave. The anodic peak potential is found to be at 1.14 V vs. NHE which relates to Ni oxidation, the cathodic peak potential is at 0.83 V vs. NHE, corresponding to Ni reduction, and the onset of the catalytic wave of the water oxidation region starts at 1.29 V. The midpoint potential for the $\text{Ni}_{\text{Ox/Red}}$ is at 0.99 V vs. NHE. The sharpness of the redox-waves points to a rather sudden charge-transfer in a defined and narrow potential range, whereas for Co and Mn oxides (Zaharieva, Chernev et al. 2012, Klingan, Ringleb et al. 2014, Risch, Ringleb et al. 2015) redox reactions occur over an extended potential range (compare to CoCat CVs in Figures 2.3, 3.1, and 4.1).

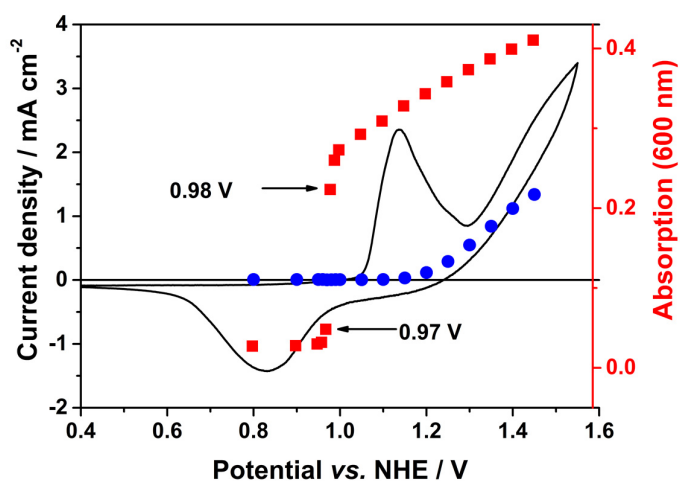


Figure 6.4. Cyclic voltammogram of the 2nd cycle for a 140 nmol NiCat film in 0.1 M B(OH)_3 at pH 9.2 with a scan rate of 20 mV s^{-1} (black line), steady state current density (blue circles), and absorption values at 600 nm (red squares) at the corresponding potentials after 3 min. The corresponding absorption spectra can be found in Figure 6.5.

Figure 6.4 also includes the steady state current density (after applying a potential for 3 minutes) at its corresponding potential values and the respective UV-vis absorption intensities at 600 nm. The wavelength of 600 nm was chosen because major modifications of absorption bands are absent at this value. The overall absorption intensity increases for any increase in potential suggesting that oxidation of Ni ions can be traced by monitoring of UV-vis absorption, which was also demonstrated for the CoCat (Risch, Ringleb et al. 2015). An amazing major jump in absorption is observed between 970 mV and 980 mV. This astonishing spectral change is also relevant regarding the position of the corresponding absorption peaks (Figure 6.5 and 6.6). Reductive potentials

between 800 mV and 970 mV only slightly change the optical transparency of the NiCat by a minor intensity change at 600 nm. No absorption maximum (≥ 400 nm) could be detected for potentials smaller than 980 mV. Between 1.00 V and 1.45 V, the absorption increases linearly with a slope of 0.3 V^{-1} (Figure 6.4).

The results from the electrochemical *in-situ* experiments at room temperature are depicted in Figure 6.5, showing UV-vis spectra for a series of electro-conditioned NiCats (panel A) and their difference spectra, which were obtained by subtracting the 0.98 V NiCat spectrum from every single other one (panel B). The absorption values are rather low for reductive potentials between 0.80 V and 0.97 V, thus show a steep augmentation in their intensities beginning at 0.98 V, which are continuously enhanced till 1.45 V. UV-vis spectra of NiCats in the potential region [0.80 V, 0.97 V] exhibit no apparent maximum, where spectra of potentials ≥ 0.98 V result in a broad absorption band.

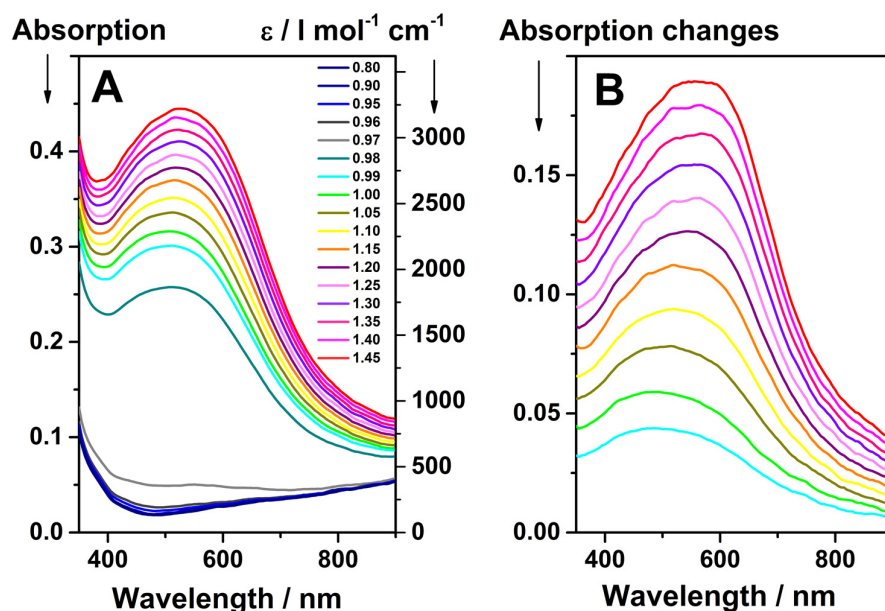


Figure 6.5. (A) UV-vis absorption spectra of the NiCat film with oxygen evolution activity recorded after 3 min of the applied potentials. The background spectrum of a blank ITO electrode was subtracted from every single NiCat spectrum. (B) Difference spectra: The shown difference spectra were obtained by subtracting the 0.98 V spectrum from the spectra recorded at the indicated potentials. We observe a major change in the spectral shape between 0.97 V and 0.98 V. However, the overall intensity increases for any increase in potential suggesting that oxidation of Ni ions can be traced by monitoring of UV-vis absorption.

The difference spectra in Figure 6.5 B highlight in a more pronounced way the shift in the position of the absorption maxima. The position change of the absorption maximum, which is induced by

different applied potentials, and the occurrence of a transparent potential region infer that structural changes within in the NiCat result in different spectroscopic properties.

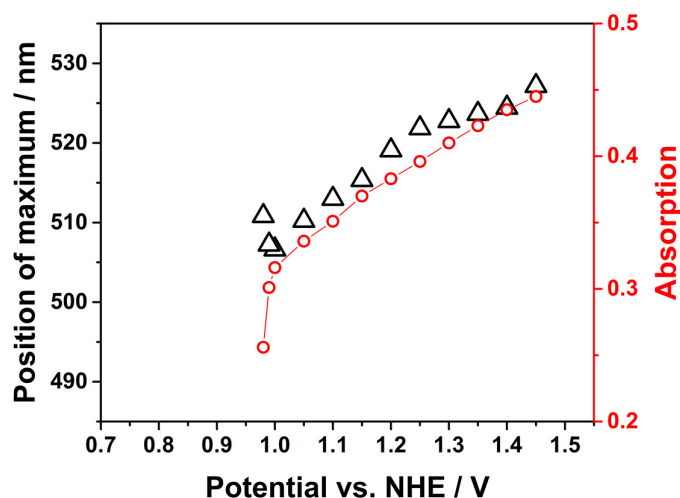


Figure 6.6. Position-changes of the absorption maximum for NiCat films poised at different potentials between 0.98 V and 1.45 V (black triangles). The peak position was determined by fitting a Gaussian curve through the UV-vis data of Figure 6.5. The corresponding absorption intensities for band maxima of NiCat films poised at different potentials between 0.98 V and 1.45 V are shown in red circles.

Inducing an electrochemical steady state between potentials of 0.80 V and 0.97 V gives molar extinction coefficients, ϵ , between ~ 130 and $360 \text{ l mol}^{-1} \text{ cm}^{-1}$ (Figure 6.5). Thus, the molar extinction coefficient, ϵ , varied between 1855 and $3225 \text{ l mol}^{-1} \text{ cm}^{-1}$ at the corresponding absorption maxima (Figure 6.5), when the potential was increased from 0.98 to 1.45 V vs. NHE. Moreover, the absorption bands experience a position shift, which is depicted in Figure 6.6. The maxima of the absorption vary between 507 and 525 nm, a wavelength where the photon energy is sufficiently high for supporting charge transfer transitions both ligand-metal and metal-metal as well as d-d transitions in transition metal oxides (Ertl, Knözinger et al. 2008). Recently, *in-situ* UV-vis experiments for the CoCat (Risch, Ringleb et al. 2015) conditioned at different potentials revealed extinction coefficients at its absorption maximum that were one order in magnitude higher than for the NiCat at 0.80 V, but gave comparable values for the high potential region. Charge transfer processes were assigned to the CoCat spectra, based on the extinction coefficients and the octahedral coordination of $[\text{CoO}_6]$ (Frei 2009, Risch, Ringleb et al. 2015). On these grounds, charge transfer transitions may also be the dominating processes for the NiCats, which were electro-conditioned between 0.98 V and 1.45 V, as the latter explicated EXAFS results (section 6.2.5) ascertained an octahedral coordination of Ni atoms in this potential region, and the extinction

coefficients, ϵ , are between ~ 2 and $3 \times 10^3 \text{ l mol}^{-1} \text{ cm}^{-1}$. Complementary, the lower potential region (0.80 V- 0.97 V) is characterised by minor extinction coefficients between $\sim 1 \times 10^2$ and $3 \times 10^2 \text{ l mol}^{-1} \text{ cm}^{-1}$. In this region the NiCat has almost optical transparency; almost all the light can pass through the catalyst without being scattered.

If one compares the potential-dependent *in-situ* CoCat UV-vis spectra (Risch, Ringleb et al. 2015) with the ones of the NiCat, the most prominent feature is missing for the CoCat. The CoCat spectra lack the huge absorption change of the NiCat from low to high potential regime. Instead the CoCat exhibits an absorption maximum at 405 nm at low potentials, which shapes into a broad shoulder at higher potentials (Risch, Ringleb et al. 2015). The overall spectral shape for the CoCat is almost identical for its different oxidation states as well as the position of the absorption maximum (405 nm) (Risch, Ringleb et al. 2015). Figure 6.5 and Figure 6.6 indicate that the spectral situation for the NiCat is far more intricate. Between 0.80 V and 0.97 V the NiCat spectra do not have a maximum in absorption, the overall intensity in absorption is very low, and no striking peaks are dominating the spectrum (Figure 6.5). When the potential is increased from 0.98 V to 1.45 V, the spectra are dominated by one outstanding maximum featuring a position change between 507 and 527 nm (Figure 6.5 and Figure 6.6). Between 1.00 V and 1.45 V the absorption at the corresponding maximum is linearly increased (slope of 0.28 V^{-1}).

6.2.3 Electrochemical operation of the NiCat

Recently the effects of short-term electrolysis at 1.1 V vs. NHE (or 3.5 mA cm⁻² for 2.5 hours in 1 M B_i) on the NiCat had been studied (Bediako, Lassalle-Kaiser et al. 2012, Bediako, Surendranath et al. 2013), where activation resulted in current density values, which were 2 orders of magnitude enhanced compared to the ‘as-deposited’ film. The change in current density when performing electrolysis of a NiCat film at high potential (1.40 V vs. NHE) in a time range of 24 h is shown in Figure 6.7. In the first 10 minutes the absolute activity of the NiCat stays constant, but in the first two hours a steep increase in current density is observed. The maximum of activity is reached after 6.5 hours (gain of ~26 % activity). After this point no further activation is possible, on the contrary, the current density starts to level off to the range of the initial activity level. Overall, the activity of the NiCat is not significantly affected, if a potential of 1.40 V vs. NHE is applied for 24 hours.

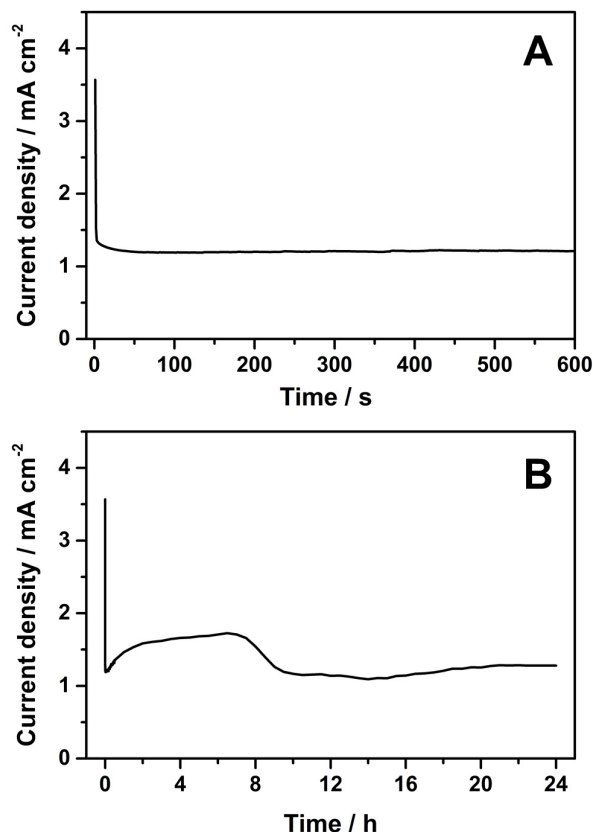


Figure 6.7. Potentiostatic current response of a NiCat (~40 nmol Ni) in 0.1 M B(OH)₃ at pH 9.2 over time. A constant potential of 1.40 V vs. NHE was applied for 24 h. (A) The first 10 min of the current response are displayed. (B) The full time response over 24 h is plotted.

Comparing a ‘non-operated’ catalyst film and one after 3 h of operation at 0.90 V (Figure 6.8 A), the current density is not profoundly enhanced in the oxygen evolution regime, but a maximum of catalytic activity is reached. Long term application for longer than 8 h at 0.90 V somewhat reduces the maximum current density, but the overall electrochemical performance of the film is maintained. Electrolysis at 1.4 V stabilises and activates the NiCat (Figure 6.8 B), so that after 8 h the highest current densities for oxygen evolution are reached.

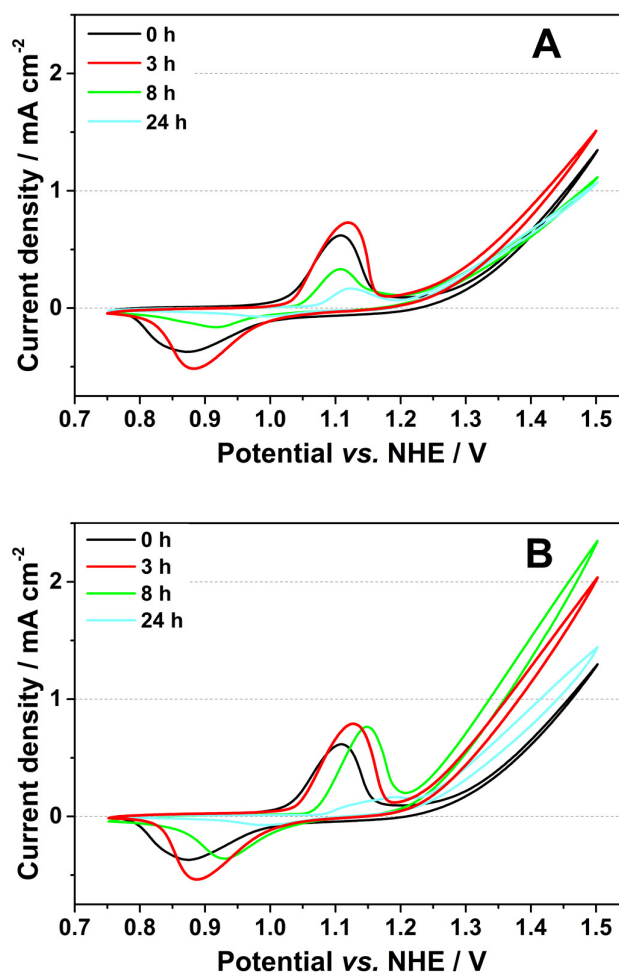


Figure 6.8. Cyclic voltammograms for selected NiCat films of ~40 nmol Ni content in 0.1 M B(OH)₃ at pH 9.2 with a scan rate of 20 mV s⁻¹ (A) after deposition (0 h-black), after 3 h (red), 8 h (green), 24 h (cyan) of operation at 0.90 V, and (B) after deposition (0 h-black), after 3 h (red), 8 h (green), 24 h (cyan) of operation at 1.40 V.

6.2.4 X-ray absorption near-edge structure (XANES)

The Ni *K*-edge X-ray absorption near-edge structure (XANES) spectra for NiCats, electro-conditioned at different potentials are shown in panel A of Figure 6.9, while a spectral comparison between ‘non-operated’ films and catalysts after electrolysis is provided in panel B of Figure 6.9. Commonly, features of XANES spectra such as edge and pre-edge positions, as well as intensities are consequences of bound transitions of the ejected photoelectron to unoccupied energy levels (Rougier, Delmas et al. 1995). Fundamental information about the oxidation state of the absorber atom and its coordination geometry can be gained from the position, height, and width of these spectroscopic features.

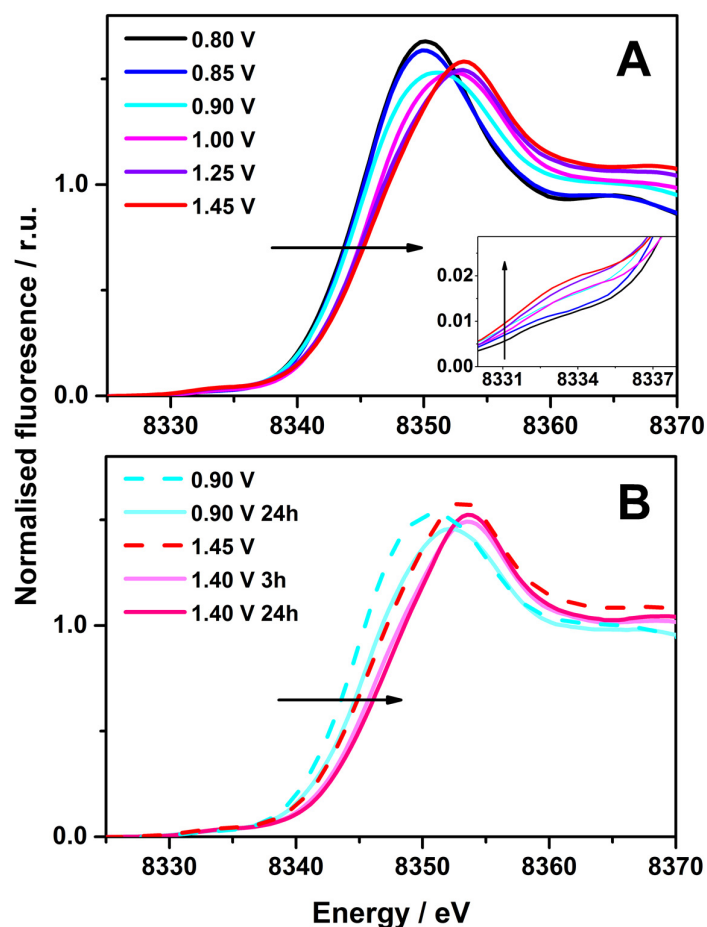


Figure 6.9. Nickel *K*-edge XANES spectra for catalyst film samples electro-conditioned at the indicated potentials (vs. NHE, pH 9.2). **(A)** ‘Non-operated’ catalyst films: at 0.80 V (black), 0.85 V (blue), 0.90 V (cyan), 1.00 V (magenta), 1.25 V (violet), and 1.45 V (red). The arrow indicates the shift of the X-ray edge for more oxidised NiCats to more positive energy values. The inset gives an enlarged picture of the pre-edge region. The arrow shows the rise in intensity of the pre-edges for higher electro-conditioned NiCats. **(B)** ‘Non-operated’ catalyst films: at 0.90 V (dashed cyan), 1.45 V (red dashed), and NiCats after long-term application of 0.90 V for 24 h (light cyan), of 1.40 V for 3h (light magenta), and of 1.40 V for 24 h (pink).

In Figure 6.9 A the positions of the X-ray edges are displaced to higher energy values for higher conditioning potentials applied to the NiCat. A positive shift of the main edge feature is usually interpreted as an increase in the corresponding Ni oxidation state and a simultaneous decrease in the first absorber-backscatter (Ni-O) bond length (Natoli 1984, Teo 1986, Dau and Haumann 2003, de Vries, Hozoi et al. 2003, Glatzel, Smolentsev et al. 2009). Exposure of a NiCat at 0.90 V for 24 h results in a severe shift of the edge position (of 0.9 eV) towards higher energies. Moreover, also the spectra of ‘the NiCats operated for 3 h and 24 h at a potential of 1.40 V indicate a higher oxidation state than found in the 1.45 V sample.

In addition, the intensity of the pre-edge rises for higher applied potentials, *i.e.* higher oxidation states of the NiCat (inlet of Figure 6.9 A). The pre-edge feature of the nickel oxide spectra can be assigned to the 1s to 3d electronic transition, which is usually forbidden for complete centrosymmetric geometry (dipole selection rule), but a slight distortion due to a weak quadrupole transition (Rougier, Delmas et al. 1995) or hybridisation of p and d states (Yang, Takada et al. 2008) result in weak pre-edge features around 8334 eV as depicted in Figure 6.9. The more oxidised Ni-oxo species are predicted to exhibit higher intensities in pre-edges than the reduced ones, and the overall small intensity in comparison to that of the main edge feature is characteristic for octahedral oxygen coordination around the nickel absorber with a slight distortion (Pandya, O'Grady et al. 1990, Kim, Tryk et al. 1994). Besides, the intensity of the pre-edges is very sensitive to the extent of coordination symmetry respectively asymmetry of the Ni-site (Yang, Takada et al. 2008).

These attributes entirely apply to the behaviour of the different states of the NiCat, as attested in Figure 6.9 A, and the following analysis of oxidation state and phase structure. The intensity at the maximum of the pre-edge (8334 eV) is nearly identical for the ‘non-operated’ 0.90 V and 1.00 V samples. Thus, the same extent of change in the main edge position (Table 6.1) between 0.80 V and 0.90 V NiCats results in intensity rise of the pre-edge. In the case of the 0.90 V and 1.00 V NiCat, a change in symmetry must occur to explain this behaviour of accordance in pre-edge intensities. The reason might be that the atomic structure of the catalyst is characterised by a strong distortion around the centre of the NiO₆ octahedra. Hence, we deduce that changes of the oxidation state of NiCat films, as well a change in local symmetry can be tracked down in Ni *K*-edge XANES spectra.

Table 6.1. X-ray edge position energies calculated from Figure 6.9 for different electro-conditioned NiCat films and nickel reference compounds shown in Figure 6.10. (*) The integral method described elsewhere (Dau, Liebisch et al. 2003) was used (integration: $0.15 < \mu < 1.0$) for determination of edge energies. Oxidation states are calculated from calibration curve shown in Figure 6.10.

	Edge position* (eV)	Oxidation state
0.80 V	8342.8	2.1
0.85 V	8342.9	2.2
0.90 V	8343.0	2.3
1.00 V	8343.9	2.9
1.25 V	8343.9	2.9
1.45 V	8344.2	3.1
0.90 V 24 h	8343.9	2.9
1.40 V 3 h	8345.0	3.7
1.40 V 24 h	8345.4	4.0
Ni^{II}O	8342.3	2.0
Ni^{II}(OH)₂	8343.0	2.0
LiNiO₂	8344.0	3.0
K₂Ni^{IV}(H₂IO₆)₂	8345.5	4.0

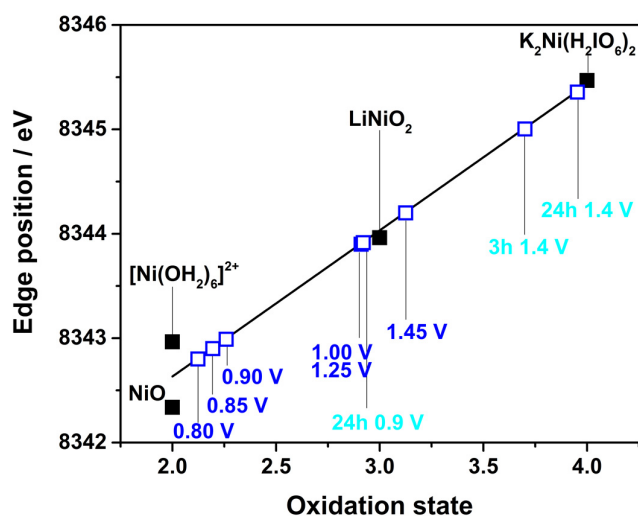


Figure 6.10. Calibration curve defined by a linear fit to Ni integral edge positions of reference materials, namely $[\text{Ni}^{\text{II}}(\text{OH}_2)_6]^{2+}$, $\text{Ni}^{\text{II}}\text{O}$, $\text{LiNi}^{\text{III}}\text{O}_2$, and $\text{K}_2\text{Ni}^{\text{IV}}(\text{H}_2\text{IO}_6)_2$. Edge positions were determined from Ni *K*-edge XANES spectra by the integral method (Dau, Liebisch et al. 2003). The open symbols indicate the X-ray edge positions of the NiCat samples, electro-conditioned at the displayed potentials vs. NHE.

The X-ray edge position energies for NiCats poised at different potentials are given in Table 6.1, where the XANES spectra from Figure 6.9 were analysed by the integral method (Dau, Liebisch et al. 2003). The shift of edge positions to higher energies, *i.e.* the rise of higher oxidation states with increasing applied potential to the sample, is reflected by the numbers of Table 6.1. A precise determination of the oxidation state (Figure 6.10 and Table 6.1) *via* calibration of the shift of the integral edge position with only four reference materials is problematic, but still provides a first estimate of NiCat oxidation state changes during the oxygen evolution reaction. An alternative calibration method (Risch, Klingan et al. 2011), which uses literature values of EXAFS Ni-O bond length, to determine correctly the oxidation state by means of XAS is described in section 6.2.5.

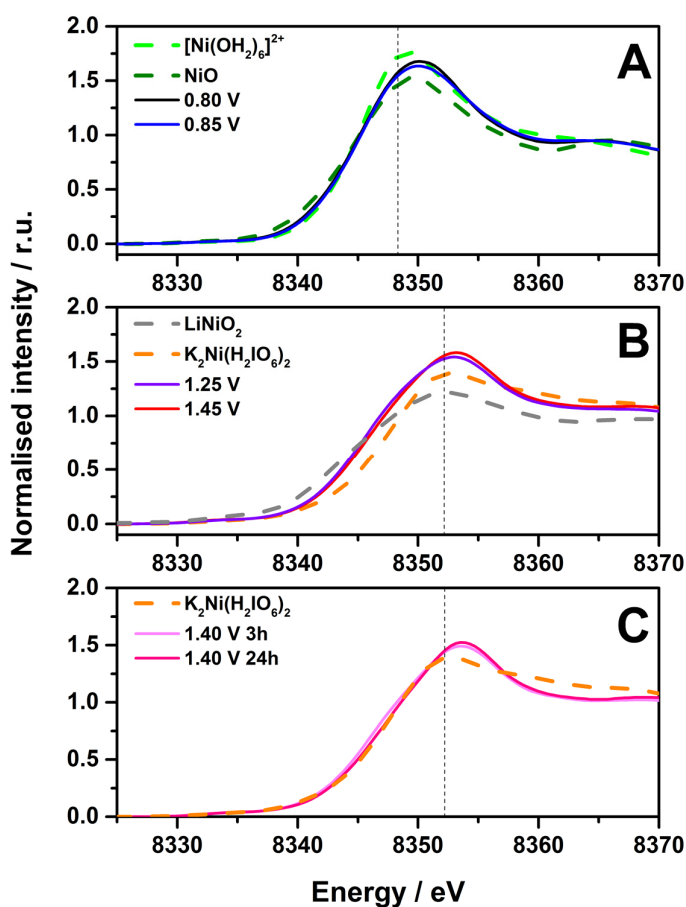


Figure 6.11. Nickel *K*-edge XANES spectra for nickel reference materials and catalyst film samples electro-conditioned at different indicated potentials: **(A)** $[\text{Ni}^{\text{II}}(\text{OH})_6]^{2+}$ (green dotted line), $\text{Ni}^{\text{II}}\text{O}$ (olive dotted line) are compared to NiCats electro-conditioned at 0.80 V (black) and 0.85 V (blue), **(B)** $\text{LiNi}^{\text{III}}\text{O}_2$ (grey dotted line), $\text{K}_2\text{Ni}^{\text{IV}}(\text{H}_2\text{IO}_6)_2$ (orange dotted line) are compared to NiCats electro-conditioned at 1.25 V (violet) and 1.45 V (red), and **(C)** $\text{K}_2\text{Ni}^{\text{IV}}(\text{H}_2\text{IO}_6)_2$ (orange dotted line) is compared to NiCats after electrolysis at 1.40 V for 3h (light magenta) and 24 h (pink).

Figure 6.11 depicts a comparison between selected XANES spectra of the NiCat and reference compounds. In panel A, the similarities in energy edge position and spectral shape in the 0.80 V and 0.85 V poised NiCat and the nickel-hexaquo-complex in solution are illustrated, while these low potential exposed spectra are explicitly different from Ni^{II}O powder. By contrast with the energy edge position of the Ni^{II} reference compounds, it follows that the most reduced states of the ‘non-operated’ NiCat may have an oxidation state close to +2. We exclude the possibility that the NiCat simply dissolves at this potentials, because control experiments showed the same characteristic NiCat CV (Figure 6.4), when the NiCat was electro-conditioned at 0.80 V and 0.85 V and then immediately after measured in a fresh buffering electrolyte. Moreover, the EXAFS data (Figure 6.12) confirmed the integrity of the catalyst due to the prominent existence of Ni-Ni interactions in the Fourier-transformed spectra.

Panel B in Figure 6.11 features the differences in spectral shape for the high potential NiCats poised at 1.25 V and 1.45 V, and the reference powder samples LiNiO₂ and K₂Ni(H₂IO₆)₂. Even though the edge positions (Table 6.1) for LiNiO₂ bear a substantial likeness to the 1.25 V and 1.45 V catalysts, shape and height of edge features are prominently different. The potassium nickel(IV) paraperiodate reference has iodate in its second coordination sphere (connected *via* di- μ -oxo-bridges), while for the different NiCat samples di- μ -oxo bridged nickel atoms are expected in the second coordination sphere. Regardless the difference, the energy edge position is considerably higher for Ni(IV). Hence, it can be concluded that none of the ‘non-operated’ NiCat reaches an oxidation state of +4, even when a highly positive potential promoting water oxidation is applied.

Figure 6.11 C compares NiCats, which were tested for electrolysis at 1.40 V for either 3 h or 24 h and the reference powder sample K₂Ni^{IV}(H₂IO₆)₂. Obviously, long-term electrolysis influences the oxidation state of the NiCat: the NiCat does not reach a maximum oxidation state in a ‘non-operated’ state. However, the X-ray edge position of the catalyst film after long-term application at 1.40 V for 24 hours reaches the highest oxidation state observed in this experimental series, namely close to +4.0 (Table 6.1). Similar slopes in the main absorption edge between this film and the Ni^{IV} powder reference can be detected (Figure 6.11 C).

6.2.5 Extended X-ray absorption fine-structure (EXAFS)

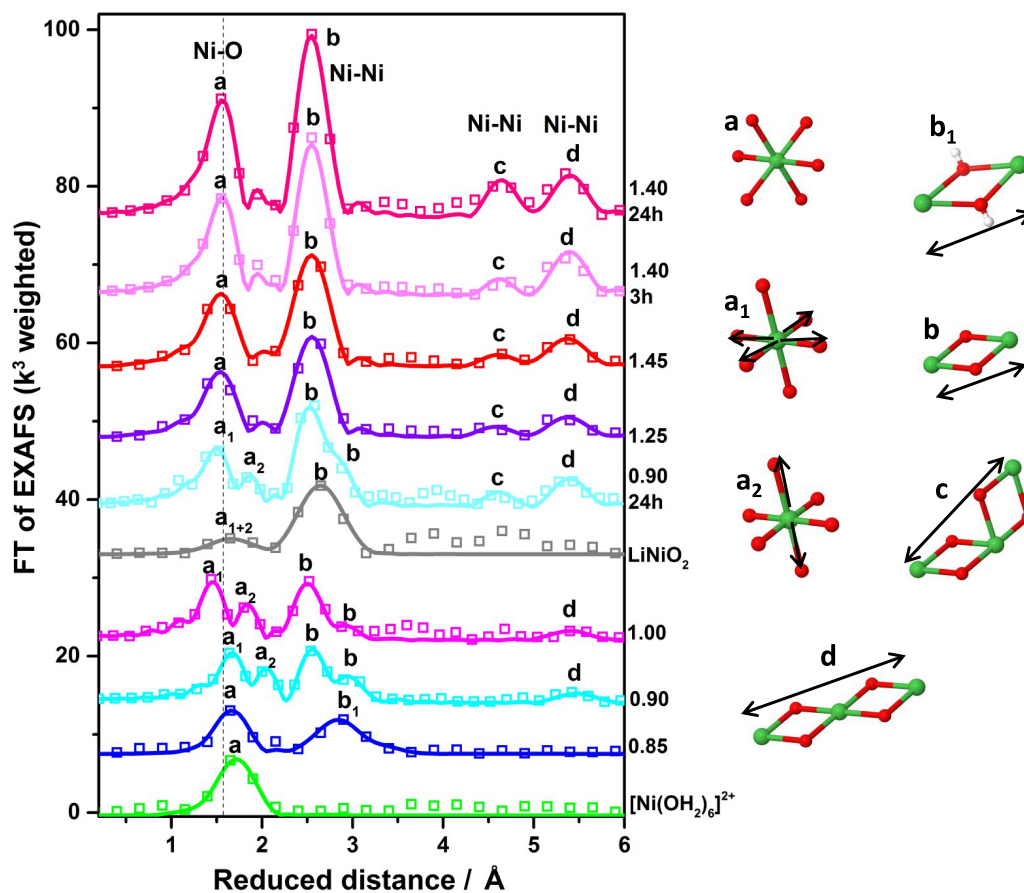


Figure 6.12. Fourier-transformed EXAFS spectra of ‘non-operated’ NiCats (electro-conditioned at indicated potentials); 0.85 V (blue), 0.90 V (cyan), 1.00 V (magenta), 1.25 V (violet), and 1.45 V (red) are compared to selected references $[\text{Ni}(\text{OH}_2)_6]^{2+}$ (green, Ni(II)) and LiNiO_2 (grey, Ni(III)), and long-term electrolysis NiCats at 0.90 V for 24 h (light cyan), at 1.40 V for 3h (light magenta), and at 1.40 V for 24 h (pink). Experimental data are indicated by symbols and EXAFS simulations (parameters given in Table 6.2) are shown as lines. Note that the distance on the x-axis is reduced by 0.3-0.4 Å relative to the real distance. The peaks marked with a_x , b_x , c, d denote distances belonging to structural motifs displayed on the right side. Colour codes are the following: nickel, green; oxygen, red; and hydrogen, white.

Table 6.2. Complete parameters of the EXAFS simulations of the nickel *K*-edge spectra of Figure 6.12. N_i , EXAFS coordination number (atoms per X-ray absorbing Ni atom); R_i , atom–atom distance; σ_i , Debye–Waller parameter. The parameter errors correspond to the 68% confidence interval. The NiCat samples were electro-conditioned at the indicated potentials in 0.1 M B(OH)₃, pH 9.2.

Sample	Ni-O (a _x)			Ni-Ni ₁ (b _x)		
	N_o	$R_o(\text{Å})$	$\sigma_o(\text{Å})$	N_{Ni}	$R_{Ni}(\text{Å})$	$\sigma_{Ni}(\text{Å})$
[Ni(OH ₂) ₆] ²⁺	6.1±0.1	2.05±0.01	0.065±0.004	-	-	-
0.85 V	4.9±0.3	2.03±0.01	0.061±0.005	1.7±0.2	3.08±0.01	0.037±0.005
0.90 V	3.8±0.2	1.96±0.01	0.066*	4.3±0.3	2.84±0.01	0.072*
	1.7±0.2	2.08±0.01	0.032*	1.8±0.3	3.05±0.01	0.058*
LiNiO₂	3.7±0.2	1.94±0.01	0.066*	4.5±0.3	2.91±0.01	0.051±0.004
	1.0±0.2	2.06±0.01	0.032*	-	-	-
0.90 V 24h	4.8±0.3	1.88±0.01	0.066*	4.2±0.3	2.82±0.01	0.072*
	2.1±0.3	2.06±0.01	0.032*	2.3±0.3	3.06±0.01	0.058*
1.00 V	4.3±0.2	1.86±0.01	0.066*	3.8±0.4	2.85±0.01	0.072*
	1.6±0.2	2.01±0.01	0.032*	2.2±0.3	3.07±0.01	0.058*
1.25 V	4.9±0.4	1.88±0.01	0.057±0.005	4.2±0.4	2.83±0.01	0.043±0.005
1.45 V	5.8±0.4	1.88±0.01	0.062±0.005	5.9±0.4	2.82±0.01	0.046±0.003
1.40 V 3h	5.6±0.4	1.88±0.01	0.058±0.005	6.3±0.4	2.82±0.01	0.054±0.003
1.40 V 24h	6.7±0.4	1.87±0.01	0.052±0.004	6.8±0.4	2.81±0.01	0.049±0.003
K₂Ni(H₂IO₆)₂	4.5±0.3	1.86±0.01	0.033±0.005	-	-	-

Sample	Ni-Ni ₂ (c)			Ni-Ni ₃ (d)		
	N_{Ni}	$R_{Ni}(\text{Å})$	$\sigma_{Ni}(\text{Å})$	N_{Ni}	$R_{Ni}(\text{Å})$	$\sigma_{Ni}(\text{Å})$
0.90 V	-	-	-	0.7±0.2	5.64±0.01	0.032*
1.00 V	-	-	-	0.8±0.2	5.64±0.01	0.032*
0.90 V 24h	1.8±0.5	4.87±0.02	0.039*	1.5±0.2	5.63±0.01	0.032*
1.25 V	1.5±0.4	4.88±0.02	0.039*	1.9±0.2	5.63±0.01	0.032*
1.45 V	2.2±0.4	4.91±0.01	0.039*	2.7±0.2	5.63±0.01	0.032*
1.40 V 3h	2.1±0.5	4.90±0.01	0.039*	2.4±0.2	5.62±0.01	0.032*
1.40 V 24h	4.9±0.5	4.90±0.01	0.039*	2.3±0.2	5.62±0.01	0.032*

The parameters marked by an asterisk (*) were fixed; all other parameters were determined by curve fitting to the experimental data (k -range 3-13.5 Å⁻¹). For LiNiO₂ only the first 2 shells of interest for comparing the Jahn-Teller effect in respect to the Ni catalyst films are depicted. The amplitude reduction factor S_0^2 was 0.6 and the maximum value of the filtered R_f -factor was 12.

In the following we will focus on the EXAFS results for the differently poised NiCats and compare these to selected reference materials. The Fourier-transformed (FT) EXAFS spectra are shown in Figure 6.12. The amplitude of the peaks in the FT reflects an approximate proportion of the abundance of the structural motif at its allocated Ni-O or Ni-Ni distance. The distances in Figure 6.12 are reduced by 0.3-0.4 Å relative to the real distances between the atoms.

The results from the EXAFS simulations can be found in Table 6.2. When going from 0.85 V to 1.45 V, it is explicitly visible that the long-range order ($> 4 \text{ \AA}$) of the ‘non-operated’ NiCat samples increases, which is indicated by the rise in the coordination number for the different Ni-Ni distances, and especially within the well-defined peaks c at 4.90 \AA and d at 5.6 \AA , especially for 1.25 V and 1.45 V. Thus, beyond the first coordination sphere a gain of structural order for NiCats electro-conditioned at higher potentials is observed. This insight should not be understood in a confusing way that the NiCat gains crystallinity, it still remains amorphous for all applied potentials, instead the cluster size of ordered material rises, *i.e.* an increase in interconnected $\{\text{Ni}_x(\mu_{2/3}\text{-O})_y\}$ assemblies. In contrast microcrystalline materials either have broad and damped EXAFS oscillations caused by many similar adjacent distances (see LiNiO_2 in Figure 6.12) or high FT amplitudes above 4 \AA (for example see LiCoO_2 FT spectrum in Risch et al. 2009). Upon long-term electrolysis the increase in long-range order is as well observed. The intensities of all peaks in the EXAFS spectrum of the 24 h long-term performance at 0.90 V NiCat are higher than for the corresponding as-deposited 0.90 V film. Moreover, it is also visible that for the 24 h treated catalyst sample that the oxidation state is increased as Ni-O peaks a_1 and a_2 are found at shorter distances. The same observations prevail for the operated NiCats at 1.40 V: ‘Activation’ results in a gain of structural order and a reduced Ni-O distance (evidence of higher oxidation state).

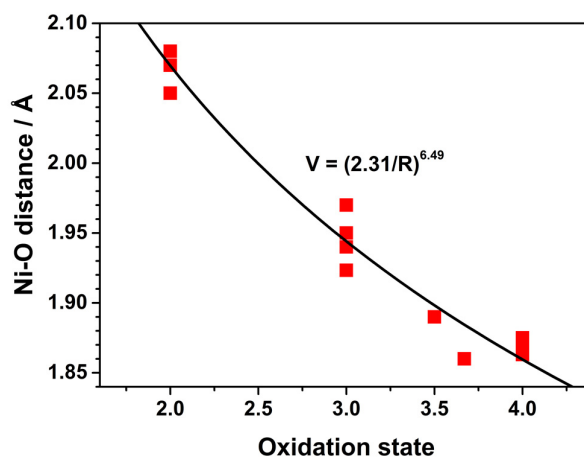


Figure 6.13. Calibration curve for the determination of the Ni oxidation state from the Ni—O bond length. Only the average EXAFS bond length (red squares) was used in the calibration. The black curve was obtained by fitting $y = (a/x)^b$ to the data. Adapted from Risch, Klingan et al. 2011 with permission from The Royal Society of Chemistry.

The Ni-O distances are of special interest as they can be an estimate of the oxidation state. Our previous work (Risch, Klingan et al. 2011) clarified the structure of the ‘resting state’ NiCat. There, a literature survey for different coordinated nickel oxide compounds was undertaken to determine

the oxidation state of the NiCat from a calibration curve of Ni-O distances (Figure 6.13). EXAFS literature values of 17 octahedrally coordinated nickel compounds spanning four nickel oxidation states were gathered. Mean Ni-O distances of 2.07 Å, 1.95 Å and 1.87 Å were found for oxidation states of Ni^{II}, Ni^{III}, and Ni^{IV} (Risch, Klingan et al. 2011). Calculated oxidation states for the herein investigated Ni catalyst thin films are given in Table 6.3.

Table 6.3. Calculated oxidation states, which are obtained by using a mathematical relation ($V=(2.31/R)^{6.49}$) obtained from the calibration curve in Figure 6.13. The calibration curve contains mean EXAFS literature bond lengths of nickel-oxo compounds (Risch, Klingan et al. 2011). For NiCat samples exhibiting a splitting of the Ni-O distances, mean distances (weighting by the simulated coordination numbers) are used.

	Ni-O distance (Å)	Oxidation state
[Ni(OH ₂) ₆] ²⁺	2.05	2.2
0.85 V	2.03	2.3
0.90 V	2.00	2.6
LiNiO₂	1.97	2.9
0.90 V 24h	1.94	3.2
1.00 V	1.90	3.5
1.25 V	1.88	3.8
1.45 V	1.88	3.8
1.40 V 3h	1.88	3.8
1.40 V 24h	1.87	3.9
K₂Ni^{IV}(H₂IO₆)₂	1.86	4.1

As given in Table 6.2 and 6.3, for the 0.85 V sample a Ni-O distance of 2.03 Å was estimated, which translates by application of the aforementioned calibration curve in an oxidation state of 2.3. Interestingly, this sample in the most reduced state at 0.85 V exhibits a similar Ni-O distance as the reference compound [Ni^{II}(OH₂)₆]²⁺. The coordination number of the Ni-O shell is expected to be six for an octahedral coordination; the lower value of around five suggests that some defects in terms of incomplete octahedra may occur. Moreover, its Ni-Ni bond length is found at 3.08 Å, which reflects an elongation of the di-μ-oxo-bridges caused by protonation (distance b₁ in Figure 6.12). This Ni-Ni distance is identical with the one found in α-Ni(OH)₂, which is contracted compared to the EXAFS bond length of β-Ni(OH)₂ of 3.13 Å, due to hydrogen bonding of OH groups (Pandya, O'Grady et al. 1990). On the basis of the results of mean EXAFS bond lengths and coordination numbers for the investigated samples, they are compared to different known and not fully crystalline nickel hydroxides, when striking similarities in their structures occur. To facilitate the further discussion of the NiCat samples and their comparison with nickel (oxy)hydroxides structures, the variety of possible nickel (oxy)hydroxides is schematically depicted in Figure 6.14.

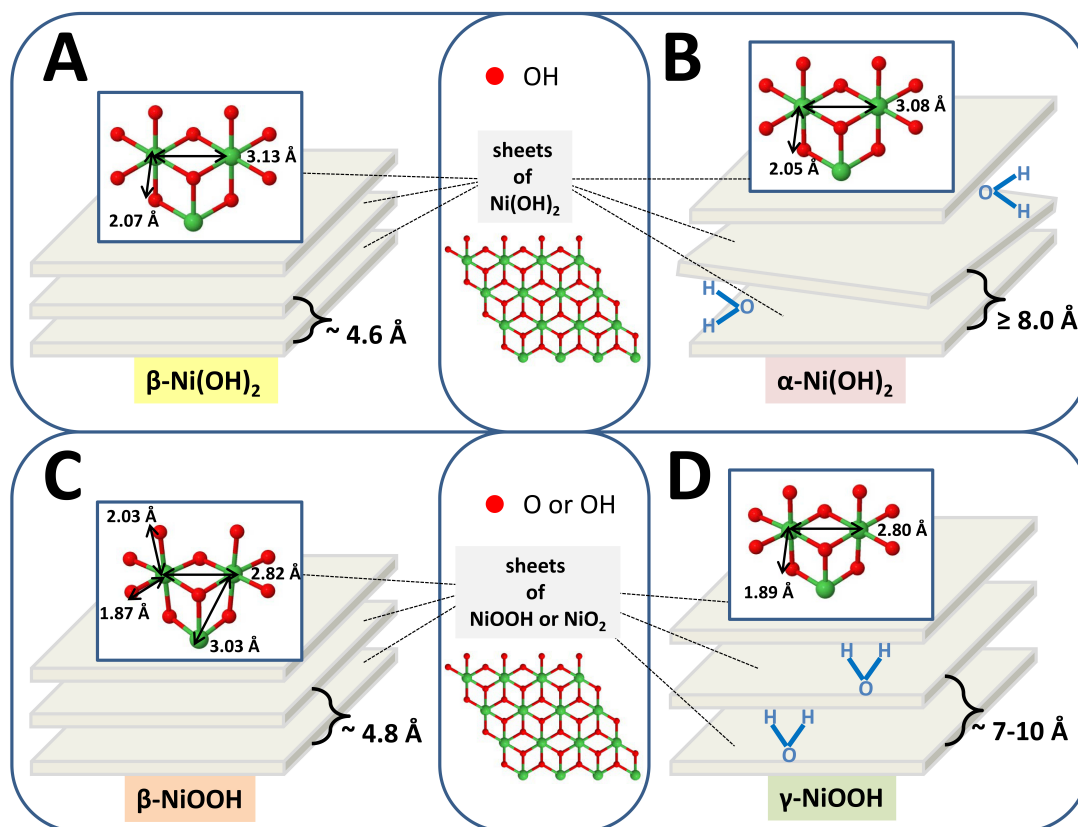


Figure 6.14. Schematically and idealised structures of different nickel (oxy)hydroxides; β -Ni(OH)₂, α -Ni(OH)₂, β -NiOOH, and γ -NiOOH. Hydrogen atoms are omitted for convenience. **(A)** The pseudopolymorph β -Ni(OH)₂ (Pandya, O'Grady et al. 1990, Ramesh, Kamath et al. 2006) has a brucite structure (Mg(OH)₂). Hydration of β -Ni(OH)₂ is not the usual case, but can occur between $0.1 \leq x \leq 0.4$ as [Ni(H₂O)_x](OH)₂, where water molecules are just weakly associated (Dennstedt and Löser 1971, Hall, Lockwood et al. 2015). Because of the weak interactions between the Ni(OH)₂ sheets, a stacking fault disorder in between these layers occurs frequently (translation and/or rotation of sheets). Herein the ideal stacking is displayed with a distance of ~ 4.6 Å (McEwen 1971) between adjacent layers. Each layer has a hexagonal arrangement of Ni ions, which are octahedrally coordinated by oxygen atoms.

(B) The other polymorph α -Ni(OH)₂·xH₂O (Pandya, O'Grady et al. 1990) consists of layers of β -Ni(OH)₂ and intrinsic water. In between the layers water molecules are intercalated. Water molecules are not close-packed structures with the OH⁻ and do not sit on fixed positions, but have rotational and translational freedom. Thus, neighbouring sheets are randomly orientated to each other ('turbostratic' structure). The distance between the sheets is ≥ 8.0 Å (Pandya, O'Grady et al. 1990, Hall, Lockwood et al. 2015). The 'ideal' degree of hydration varies between $0.41 \leq x \leq 0.7$, but often reaches higher values (McEwen 1971, Hall, Lockwood et al. 2015). Incorporation of anions in between the sheets is common. The Ni-Ni₁ distance is 0.05 Å shorter than for β -Ni(OH)₂ and may result from the addition of hydrogen bonding (Pandya, O'Grady et al. 1990). In both Ni(OH)₂ polymorphs a high degree of structural disorder is frequently observed (Hall, Lockwood et al. 2015).

(C) The low spin electronic configuration of trivalent Ni in β -NiOOH (Glemser and Einerhand 1950, Demourgues, Gautier et al. 1997) leads to a macroscopic Jahn-Teller distortion. The two axial distances are elongated and the four equatorial distances are contracted. The octahedral distortion affects a splitting of the Ni-O distances and of the Ni-Ni distances (cooperative Jahn-Teller effect) in EXAFS FT spectra.

(D) The structure of γ -NiOOH (Glemser and Einerhand 1950, Demourgues, Gautier et al. 1997) contains small quantities of alkali metal ions and water in between the sheets. Its structure can be formulated as A_xH_yNiO₂(H₂O)_z ($x, y \leq 1$, A = alkali metal ions) (Yang, Takada et al. 2008) and has an interlayer distance between 7 Å (Oliva, Leonardi et al. 1982) and 9.9 Å (Delmas, Fouassier et al. 1980).

The ‘non-operated’ 0.90 V and 1.00 V NiCats, as well as the 24 h treated 0.90 V film show two different oxygen distances, which is characteristic for a cooperative Jahn-Teller effect due to an axial elongation of NiO₆ octahedra (reduction in symmetry). In a FT EXAFS spectrum the distortion of the Jahn-Teller effect can be denoted as either cooperative or non-cooperative. A cooperative effect describes for example the splitting of the Ni-O (a) distance in Figure 6.12 into two different distances a_1 and a_2 and as well the splitting of the adjacent Ni-Ni₁ (b) distance into two differently populated states. In the non-cooperative case as it can be demonstrated for LiNiO₂ only a splitting of the Ni-O distances can be seen (Table 6.2) and the neighbouring Ni-Ni₁ (b) distance is characterised by only one peak.

For the ‘non-operated’ 0.90 V, around four short bonds at 1.96 Å and two long bonds at 2.08 Å are found (Table 6.2). Its mean weighted distances relate to an oxidation state of 2.6. Upon operation for 24 h the oxidation state of the 0.90 V film is increased to 3.2 (Table 6.3). In addition, also in the second coordination sphere a splitting of the Ni-Ni₁ (b) distance arises, so that two distinct peaks visible in the data in Figure 6.12 can be simulated. In a cooperative Jahn-Teller effect, the distortion around the NiO₆ centre is strong enough to influence also the adjacent Ni atoms. At the moment the assignment of a known nickel oxide phase to the ‘non-operated’ 0.90 V NiCat sample suggests a distorted, amorphous β-NiOOH phase with some defects and/or additional OH⁻, which lower the oxidation state from Ni^{3.2} (β-NiOOH) to Ni^{2.6} (0.90 V NiCat). This may be conceivable due to the extent of the Jahn-Teller effect. Also the operated sample is very similar to EXAFS data of β-NiOOH (Demourgues, Gautier et al. 1997) and exhibits the very same oxidation state of β-NiOOH; +3.2.

For the 1.00 V NiCat sample, the splitting of the oxygen distances occurs at 1.86 Å (close to 4 interactions) and 2.01 Å (close to 2 interactions). An average distance weighted by the coordination number implies a valence of 3.5 for 1.00 V. When going from 0.90 V to 1.00 V the oxidation state is increased by 0.9, which is the most drastic rise in this series and coincides with the results from *in-situ* electrochemical UV-vis spectroscopy in Figure 6.5. This ‘non-operated’ catalyst film, poised at 1.00 V, exhibits EXAFS spectral features, and especially split bond lengths of Ni-O and Ni-Ni, which are comparable with β-NiOOH.

The 1.25 V and 1.45 V samples mostly resemble the structure of our previously analysed NiCat (Risch, Klingan et al. 2011). Ni-O bond lengths of 1.88 Å are longer than the average reported Ni^{IV}-O distances of 1.87 Å and thus may be assigned to an oxidation state close to 3.8 (Table 6.3). Operation at 1.40 V increases the structural order of the catalyst film, a progression of the extent of long-range order is not completed after 3 h as the augmented peak intensities of the corresponding film suggests in Figure 6.12. Still, within long-term operation a slight increase in oxidation state

from 3.8 to 3.9 is seen, while the Ni-O distance is reduced by 0.1 Å for long-term operation. These four most oxidative NiCat states can be associated with a nickel oxide with extended layer fragments. Furthermore, the higher potential poised NiCats show the characteristic di- μ -O(H)-bridging with edge-sharing octahedra at 2.8 Å. The first multiple of the 2.8 Å distance occurs at 5.6 Å, which is representative for a layered structure and was reported for γ -NiOOH·xH₂O (McBreen 2007). The amplitude of the Ni-Ni₂ (c) distance at 4.9 Å is rather low, indicating the amorphous character of these NiCat films. In conclusion, the structure of the ‘non-operated’ high potential NiCats and the operated high-potential NiCats assembles a sheet like γ -NiOOH structure with water and borate in between the sheets.

6.3 Discussion

6.3.1 Structural changes by comparison with nickel (oxy)hydroxides

The proposed structural changes of the nickel oxide catalyst in dependence of the applied potential are schematically displayed in Figure 6.15. The catalyst in the most reduced state in this experimental series (steady state at 0.85 V vs. NHE) shows structural similarities with α -Ni(OH)₂. The overall characteristic of α -Ni(OH)₂ is its highly hydrated structure (Figure 6.14). The pseudopolymorph α -Ni(OH)₂ consists of randomly orientated layers of β -Ni(OH)₂, which are separated by intercalated water molecules (Le Bihan and Figlarz 1972, Chigane, Ishikawa et al. 2000, Hall, Lockwood et al. 2015). The intercalated water molecules do not occupy fixed positions, but possess some rotational and vibrational freedom (Hall, Lockwood et al. 2015). The incorporation of foreign anions and additional water molecules from a buffer medium into the interlayer region of α -Ni(OH)₂ takes place very commonly (Hall, Lockwood et al. 2015), so that we may assume a dominating structure similar to α -Ni(OH)₂ with intercalated borate and water molecules between stacking of β -Ni(OH)₂ at a potential of 0.85 V applied to the NiCat.

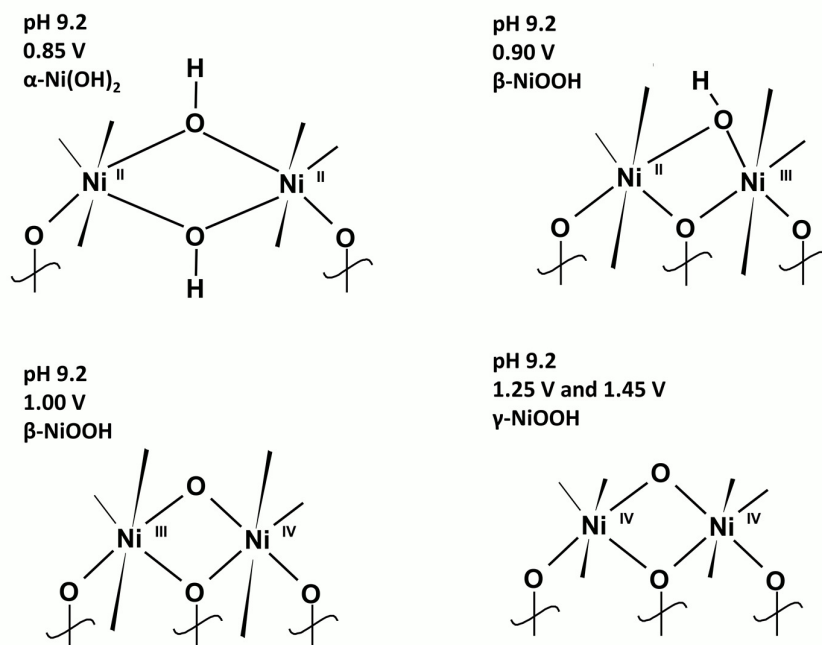


Figure 6.15. Highly idealised scheme of nickel structures contributing to the oxygen-evolving reaction (OER) at pH 9.2 in 0.1 M B₃ within the NiCat after inducing an electrochemical steady state. Note that oxidation states have been rounded for convenience.

β -NiOOH is known for its hexagonal layered structure of nickel with distorted octahedrally coordinated oxygen (Figure 6.14). In EXAFS studies β -NiOOH exhibits a Jahn-Teller distortion along Ni-O with four short bonds at 1.87 Å and two long bonds at 2.03 Å (Demourgues, Gautier et al. 1997).

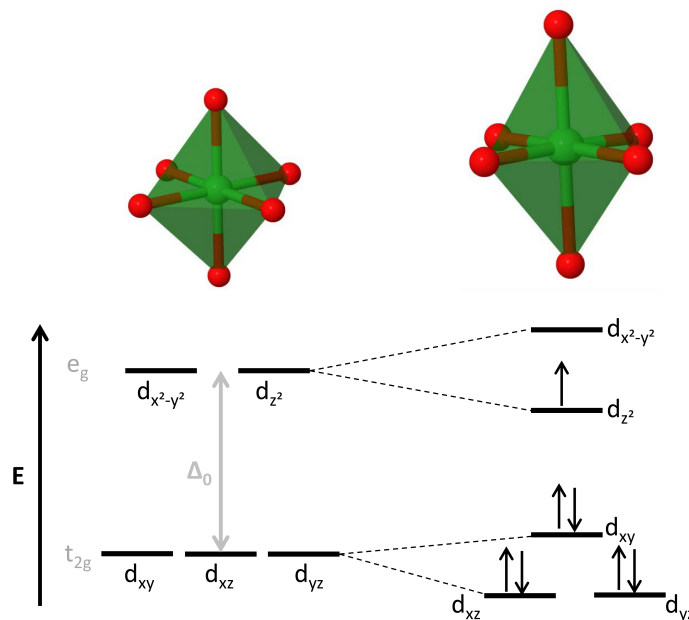


Figure 6.16. Scheme of electronic low spin configuration in Jahn-Teller distorted octahedral nickel-oxo complexes $t_{2g}^6e_g^1$ (NaNiO_2 , LiNiO_2 , β -NiOOH). In comparison to tetravalent nickel ions like in γ -NiOOH, the trivalent state can benefit from a strong stabilisation of one electron in the e orbital leading to the macroscopic Jahn-Teller-effect (Demourgues, Gautier et al. 1997).

Although a large Jahn-Teller distortion is predicted for NaNiO_2 and a non-cooperative one for LiNiO_2 , their bond lengths (Rougier, Delmas et al. 1995, Demourgues, Gautier et al. 1997, Kalyani and Kalaiselvi 2005) are considerable longer than the ones of the 1.00 V NiCat. Differences between the NiCat samples, undergoing a Jahn-Teller distortion and LiNiO_2 are revealed in Figure 6.12, where the split Ni-O distances a_1 and a_2 are hidden in the broad first peak in the Ni K-edge EXAFS Fourier-transform (FT) spectrum of LiNiO_2 . Hence, the results of the EXAFS simulation refer to an identification of the ‘non-operated’ 1.00 V catalyst with β -NiOOH. According to literature NaNiO_2 , LiNiO_2 , and β -NiOOH have a $t_{2g}^6e_g^1$ degeneracy with a strong stabilisation of one electron in the e orbital by the Jahn-Teller-effect (Demourgues, Gautier et al. 1997). Experimentally a non-cooperative local Jahn-Teller effect is observed for LiNiO_2 (only splitting of O distance) and a cooperative one for NaNiO_2 and β -NiOOH (splitting of O and Ni distances) (Demourgues, Gautier et al. 1997). The electronic configuration of these Jahn-Teller affected

compounds is schemed in Figure 6.16. The EXAFS data of the NiCat poised at 0.90 V and 1.00 V is comparable to the local distortion around the nickel centre in β -NiOOH and may account for an initial d^7 low-spin-configuration, which results in a lowered energy of a trivalent state ($t_2^6e^1$) in an octahedral elongated Jahn-Teller-effect.

Both intermediate states (0.90 V and 1.00 V) have around four short Ni-O interactions and around two long Ni-O interactions, an effect driven by the local distortion of the NiO₆ octahedra (elongation). The presence of NaNiO₂ can be largely excluded, because of its longer Ni-O bond length (1.95 and 2.17 Å) (Demourgues, Gautier et al. 1997). Hence, we may assume a sheet-like structure assimilable to that one in β -NiOOH, with some possible intercalated water for the mediocre states (0.90 V and 1.00 V) of the NiCat.

γ -NiOOH is a layered nickel oxide, which always contains sizeable quantities of both alkali ions and water in between the layers, and has an oxidation state close to Ni^{IV} (McBreen 2007). In the same way the four most oxidative NiCat states (≥ 1.25 V) can be best described as a nickel oxide with extended layer fragments (Risch, Klingan et al. 2011); a sheet like γ -NiOOH structure, where the nickel oxide layer fragments likely are separated by water and borate molecules. We note that – in spite of the designation as γ -NiOOH – the dominating structural motif is a layered nickel dioxide. Structure and protonation states at the margins of layer fragments likely will allow for charge compensation at potentials where the catalyst is in an average oxidation state close to Ni^{III}; also cations in the interlayer space may play a role.

One has to keep in mind that quantitative EXAFS analysis provides mean atom-atom distances and coordination numbers. The just proposed identification of nickel (oxy)hydroxide structures in different electrochemical induced states of a NiCat does not mean that the catalyst material exclusively consists of the aforementioned nickel (oxy)hydroxides. Thus, only the dominating structural motifs can be determined, which do not exclude the presence of other phases. Even nowadays electrochemical synthesis of pure nickel hydroxides and oxyhydroxides is still challenging, often mixtures of two or even three phases are obtained (Demourgues, Gautier et al. 1997). Moreover, X-ray diffraction lines of nickel (oxy)hydroxides are very broad supporting their not completely crystalline character (Demourgues, Gautier et al. 1997). The EXAFS simulations yielded striking similarities with known nickel hydroxides and oxyhydroxides, but not identical results which one can expect in a ‘pure’ material. Hence, the real nickel-oxo catalyst in its different states during the water oxidation reaction is in all likelihood a mixture of several nickel hydroxides and/or oxyhydroxides where one structure might be present at larger scale and thus dominating.

6.3.2 Electrochromism of the NiCat

The herein investigated NiCat does not only exhibit good qualities as water oxidation catalyst, it also shows the characteristic behaviour of electrochromic materials. Sputtered nickel oxides are known to be well working electrochromic materials, being able to change their optical properties by the appliance of an electric potential (Niklasson and Granqvist 2007). Their application is highly interesting for the material design of electrochromic smart windows that might have a large energy saving potential (Granqvist, Azens et al. 1997). Different sputtered electrochromic nickel oxides (Svensson and Granqvist 1986, Azens, Isidorsson et al. 2002, Avendaño, Azens et al. 2003, Avendano, Azens et al. 2003, Avendaño, Azens et al. 2004) are known to change from a transparent state to an absorbing state upon extraction of protons or insertion of hydroxide ions (Niklasson and Granqvist 2007). This characteristic electrochromism of nickel oxides is accountable due to a structural change and different protonation: β -Ni(OH)₂, α -Ni(OH)₂, and NiO were identified as optical transparent materials, while γ -NiOOH, and Ni₂O₃ as coloured ones (Niklasson and Granqvist 2007). Besides, in the sputtering synthesis of nickel oxides the higher O₂ content in the sputtering atmosphere was the primary driving power in transforming the optical transparency to a brown colour (Niklasson and Granqvist 2007). These insights are beneficial for understanding the optical properties of the NiCat, which change upon oxidation its colour from transparent to brown (Figure 6.5).

The EXAFS analysis pointed to an octahedral Jahn-Teller elongation at potentials of 0.90 and 1.00 V vs. NHE and pH 7. Thus, we might expect two absorption bands (in case of charge transfer) for two electronic transitions instead of one absorption band for an octahedral complex. Usually, a Jahn-Teller elongation is detectable in UV-Vis absorbance spectra as a splitting of bands caused by a reduction in symmetry. In the case of the NiCat it will be nearly impossible to see two distinct peaks below 0.97 V as the NiCat in these states is transparent and absorption values too low. Though, usually the highest practical relevance in terms of distortion strength are found when the degenerate electrons are in the e_g level (d⁹, high-spin d⁴ complexes, and low-spin d⁷ complexes), which results in a distinctive distortion of bond lengths (Figure 6.16), but additional selection rules may be induced due to geometry effects.

Between 0.98 V and 1.00 V one broad peak characterises the optical absorbance. The existence of an equatorial contraction of Ni-O bonds and an axial elongation for these NiCat states can also not be utterly excluded on the basis of the UV-vis spectra, because a possible splitting of absorption peaks may be hidden in the very broad band. Another explanation is that due to the very amorphous properties of the NiCat the Jahn-Teller distortions cannot be seen in UV-vis spectra, because of the co-existence of different unordered nickel hydroxide and nickel oxyhydroxide phases.

Interestingly, the position of the absorption maximum differs for different conditioning potentials, which may reflect the differences in atomic geometry. In conclusion, a precise geometry attribution is not possible *via* in-situ near UV-vis spectroscopy at the NiCat, but with quantitative EXAFS analysis.

In conclusion, changes in colour and oxidation state can be followed qualitatively with UV-vis spectroscopy, which suggest that these changes are accompanied by structural changes, but do not give any information about the extent and nature of these changes. Thus, further characterisation with the aid of XAS-analysis is essential to gain exact structural information on the different states of the amorphous NiCat. The combined results of *in-situ* UV-vis spectroscopy and EXAFS simulations can provide useful explanations on geometry effects of biomimetic transition metal catalysts like the NiCat.

6.3.3 Oxidation state changes

It has been reported before for a similar nickel-borate catalyst (Bediako, Lassalle-Kaiser et al. 2012) that the oxidation state of an anodically activated film was determined as 3.6, exhibiting a strong similarity to the structure of γ -NiOOH with the very same oxidation state. In the same work, a ‘non-operated’ film at 1.00 V *vs.* NHE beard more resemblance with β -NiOOH and had an oxidation state of +3.2. The reported Jahn-Teller effect for 1.00 V at a ‘non-operated’ NiCat is also found in this work, though we could identify further structural motifs during the overall oxygen-evolution reaction of the ‘non-operated’ NiCat. We propose that, based on the EXAFS results gathered herein, the ‘non-operated’ NiCat undergoes far more atomic rearrangements than initially identified by Bediako et al. (see Figure 6.15 and 6.17). We are aware that the obtained absorber-backscatter distances in Bediako, Lasalle-Kaiser et al. 2012 differ from our results as well as the overall intensity in FT EXAFS oscillations, which may be due to differences in technique (*in-situ/ex-situ*), temperature (room temperature/20 K), or deposition conditions (film thickness). Generally, in our data the distortion of the low spin d^7 nickel centres is in better compliance with the atomic features depicted in Demourgues, Gautier et al. 1997.

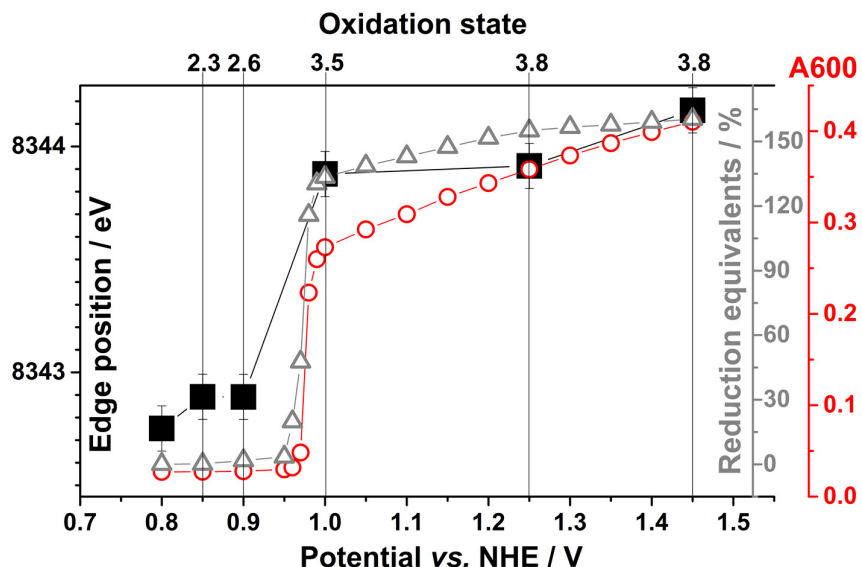


Figure 6.17. Oxidative charging of the NiCat film followed by X-ray and optical absorption spectroscopy, and electrochemical coulometry. The values for the edge position (black squares) are determined by the integral method (Dau, Liebisch et al. 2003) (Table 6.1) from Ni *K*-edge XANES spectra. The optical absorption (red squares) was detected at 600 nm. The reduction equivalents are shown as grey triangles. The reduction equivalents are given in terms of the one-electron reduction equivalent (in percent), estimated by dividing the reduced charge (Q_{red} , from coulometry) by the total deposited charge (Q_{Ni} , from elemental analysis). The oxidation states were calculated from the average EXAFS Ni-O bond length. The indicated lines are a guide for the eye in between the data points. Oxidation states, determined *via* simulation results of Ni-O distances, are indicated on the top x-axis.

Between 0.85 V and 1.45 V vs. NHE the differences in the nickel oxidation states in the ‘non-operated’ films cover up to 1.5 formal oxidation state units (2.3 at 0.85 V and 3.8 at 1.45 V). Calculation of the reduction equivalents from CVs and coulometry yields 1.5 - 1.6 electrons per active nickel centre. Independently, the XAS experiments provided the same number of electrons per active nickel centre during a redox-reaction as electrochemistry (Figure 6.17). Moreover, the absorption values at 600 nm follow the trend of the XAS and coulometry results, but differ in a constant increase above 1.00 V for every further potential increment. Two factors may be responsible for this effect; on one side bubble formation at the electrode from oxygen evolution in the water oxidation regime can influence the scattered light, and on the other hand an extended ordering can cause spectral enhancement (Goldner, Chapman et al. 1986, Conell, Corrigan et al. 1992).

6.3.4 Possibility of Fe contaminations

Recently, it has been stated that the major catalytic activity of amorphous nickel oxide water oxidation catalysts may be due to Fe contaminations (Landon, Demeter et al. 2012, Trotochaud, Ranney et al. 2012, Trotochaud, Young et al. 2014). The increased activity was explained by a partial charge transfer between Ni and Fe (Trotochaud, Young et al. 2014). Synthesis of a catalyst consisting of $\text{Ni}_{0.9}\text{Fe}_{0.1}\text{O}_x$ resulted in the most active oxidation catalyst in basic media among other Ni/Fe concentrations (Trotochaud, Ranney et al. 2012). In our case, we may rule out severe Fe contaminations, as we do not work in KOH media, where most of the iron leaches out from the glass ware and then gets incorporated into the catalyst film. Furthermore, we applied proper cleaning procedures to the glass/plastic ware and all the electrodes/material parts used in the electrochemical experiments. TXRF showed an iron concentration of $\sim 0.3\%$ of the total nickel concentration of the NiCat (or 0.41 ± 0.2 nmol Fe). We did not detect a reasonable high iron peak at the Fe *K*-edge that could descend from the NiCat samples during synchrotron measurements (to minor extent Fe is part of the sample holders and the ITO, so that Fe fluorescence will be visible in all samples). Unlike the results of our NiCat EXAFS spectra (Figure 6.12), iron containing Ni-oxides incorporate Fe^{3+} in an inverse spinel structure of NiFe_2O_4 (Chinnasamy, Narayanasamy et al. 2001, Perron, Mellier et al. 2007, Landon, Demeter et al. 2012), which should differ clearly from the structure of NiO_6 fragments in our case. Another work elucidated by *in operando* XAS that Fe^{3+} in $\text{Ni}_{1-x}\text{Fe}_x\text{OOH}$ catalysts occupies octahedral sites of the $[\text{NiO}_6]$ (Friebel, Louie et al. 2015). A partial replacement of edge-sharing octahedra with iron could not be extracted from our EXAFS spectra (Figure 6.12). We note that in alkaline electrolysis, incorporation of iron into nickel oxides can enhance the catalytic currents by 1-3 orders of magnitude. In clear contrast, the activity of Ni-only and Ni-Fe oxides at neutral pH is of comparable magnitude (unpublished results). In conclusion, the herein studied NiCat is free of any contaminations of iron atoms, which exceed 0.4 % of the nickel concentration. Therefore we consider any significant influence of iron contributions unlikely.

6.4 Summary

Both oxidation state and atomic structure of the NiCat change with applied electrode potential. Compared to the CoCat, distinctly different NiO_x structures contribute to the redox transitions and possibly also the catalytic cycle. At low potentials (0.85 V vs. NHE), the NiCat is transparent, and mainly Ni^{II} prevails connected *via* protonated di- μ -oxo-bridges of edge-sharing octahedra, similar to the ones in α -Ni(OH)₂. Intermediate potentials create a deprotonation of di- μ -hydroxo-bridges and an elongated Jahn-Teller distortion in the NiCat. These films are comparable to β -NiOOH and their oxidation states range between Ni^{+2.6} (0.90 V), Ni^{+3.2} (0.90 V 24 h operated), and Ni^{+3.5} (1.00 V). High potentials and operation above 1.25 V give extended layer fragments of nickel dioxide and di- μ -O-bridging with edge-sharing octahedra. In this oxygen evolution regime, the NiCat is comparable to a γ -NiOOH structure with water and borate intercalated between the sheets. Thus, an increase in the applied electrode potential results in an extended long-range order in terms of a rise in interconnected NiCat domains, and an elevated oxidation state. The overall amorphous character of the NiCat, which is of clear relevance for heterogeneous water oxidation catalysts, is retained in different potential states. Long-term operation of the NiCat surprisingly involves a further overall gain in the structural ordering and a higher oxidation state compared to the ‘non-operated’ catalyst film.

Key results

Structure-function correlations in amorphous and hydrated cobalt oxide (CoCat) and nickel oxide (NiCat) catalysts, which are active in the water oxidation reaction at moderate pH, were identified *e.g.* by varying the applied electrode potential, by tuning the film thickness, and by calcination. The results have been discussed in the respective chapters. In the following, key results are summarised:

Results for electrochemical water oxidation by the Co-based catalyst film (CoCat)

- At low overpotentials, the current density is directly proportional to the catalyst volume. This volume activity is explainable by catalysis at the margins of numerous cobalt oxide fragments of molecular dimensions, which together with an intercalated quasi-electrolyte constituted the bulk catalyst material. Catalysis does not take place exclusively at the bulk oxide/bulk electrolyte surface, but throughout the hydrated oxide material. → *Chapter 2* (Klingan, Ringleb et al. 2014)
- Proton transfer to bases of the electrolyte buffer (*e.g.* 100 mM phosphate buffer) is essential for water oxidation at moderate pH. In electrolytes without proton-accepting buffer molecules, the catalytic currents are negligibly small. At high current densities, the availability of the unprotonated form of the respective proton-accepting buffer molecule controls the rate of water oxidation. The pH-dependence of the catalytic currents reflects the protonation state of the buffer base, rather than the pH dependence of the O₂-formation step itself. → *Chapter 2* (Klingan, Ringleb et al. 2014)
- At high overpotentials, the catalytic current increased proportionally with the square root of the amount of deposited cobalt ions (and thus catalyst volume), which is explained by an increased catalyst-internal proton concentration, because of rate limitation by proton transfer to the buffer base at the bulk-catalyst—bulk-electrolyte interface. → *Chapter 2* (Klingan, Ringleb et al. 2014)
- The rate of catalysis per transition metal ion is drastically improved for CoCat films containing less than 20 nmol Co per cm². These films contain more atomic defects and consist of less ordered oxide layers and/or smaller oxide fragments. The enhanced catalytic activity per Co ion may either relate to this lowered structural order throughout the

deposited CoCat material (larger variety of structural motifs in the bulk catalyst) or it may be explainable by surface-specific processes (surface or near-surface catalysis). We consider more likely that the high catalytic rate results from superior reactivity of special surface exposed sites or domains. → *Chapter 3* (Gonzalez-Flores, Sanchez et al. 2015)

- Within the same transition metal catalyst, volume and surface catalysis may occur simultaneously. The dominating process depends (inter alia) on the film thickness. It is of clear importance to consider both modes of catalysis for a complete understanding of heterogeneous water oxidation. → *Chapter 3* (Gonzalez-Flores, Sanchez et al. 2015)
- Calcination transforms parts of the catalyst material into a spinel-like structure ($\text{Co}^{\text{II}}\text{Co}^{\text{III}}_2\text{O}_4$), which is associated with a severe loss of catalytic activity. → *Chapter 4* (prepared for publication)
- A molecular polyoxometalate, $\text{Co}_4\text{-POM}$ (**1**), can be stable under catalytic conditions and thus is indeed a promising water oxidation catalyst. Avoiding relatively harsh electrocatalytic conditions and using a chemical oxidant at neutral pH, there are no indications of formation of a catalytically active cobalt oxide catalyst (CoCat) on homogenous POM water oxidation. The polyoxometalates also may be promising as molecular models of the heterogeneous Co-oxo catalyst. → *Chapter 5* (Schiwon, Klingan et al. 2014)

Results for electrochemical water oxidation by the Ni-based catalyst film (NiCat)

→ *Chapter 6* (prepared for publication)

- Both oxidation state and atomic structure of the catalyst change with applied electrode potential clearly more drastically than observed in the CoCat.
- In borate buffer at pH 9.2, between 0.85 V and 1.45 V (vs. NHE) the number of electrons contributing to oxidation/reduction of the catalyst material was determined as 1.5 - 1.6 electrons per transition-metal ion (versus 0.6 in the Co-based catalyst). XAS analysis indicates the formation of Ni^{III} and Ni^{IV} (at high potentials) from Ni^{II} (at low potentials).
- Whereas in the CoCat, relatively minor changes in the Co coordination and bridging type are observed, a phase transition between distinctly different NiO_x structures is detected for the NiCat:

1. At low potentials, the NiCat is transparent, and mainly Ni^{II} prevails connected *via* protonated di- μ -oxo-bridges of edge-sharing octahedra similar to the ones in α -Ni(OH)₂.
2. Intermediate potentials create a deprotonation of di- μ -hydroxo-bridges and result in Ni sites with an elongated Jahn-Teller effect in the catalyst. These films are comparable to β -NiOOH spanning oxidation states of +2.6, +3.2, and +3.5.
3. High potentials and long-term operation entail a brown film consisting of extended layer fragments of nickel oxide and di- μ -O-bridging with edge-sharing octahedra with oxidation states close to +4. In this oxygen evolution regime the NiCat is comparable to a γ -NiOOH structure with water and borate intercalated between the oxide sheets.

References

- Abdi, F. F., Firet, N. and van de Krol, R. (2012). "Efficient BiVO₄ thin film photoanodes modified with cobalt phosphate catalyst and W-doping." *ChemCatChem* **5**: 490-496.
- Abdi, F. F. and van de Krol, R. (2012). "Nature and light dependence of bulk recombination in Co-P₁-catalyzed BiVO₄ photoanodes." *J. Phys. Chem. C* **116**: 9398-9404.
- Alstrum-Acevedo, J. H., Brennaman, M. K. and Meyer, T. J. (2005). "Chemical approaches to artificial photosynthesis. 2." *Inorg. Chem.* **44**: 6802-6827.
- Amatucci, G. G., Tarascon, J. M., Larcher, D. and Klein, L. C. (1996). "Synthesis of electrochemically active LiCoO₂ and LiNiO₂ at 100°C." *Solid State Ionics* **84**: 169-180.
- Ankudinov, A. L., Ravel, B., Rehr, J. J. and Conradson, S. D. (1998). "Real-space multiple-scattering calculation and interpretation of X-ray-absorption near-edge structure." *Phys. Rev. B: Condens. Matter* **58**: 7565-7576.
- Aricò, A. S., Siracusano, S., Briguglio, N., Baglio, V., Di Blasi, A. and Antonucci, V. (2013). "Polymer electrolyte membrane water electrolysis: status of technologies and potential applications in combination with renewable power sources." *J. Appl. Electrochem.* **43**: 107-118.
- Armaroli, N. and Balzani, V. (2007). "The future of energy supply: challenges and opportunities." *Angew. Chem. Int. Ed.* **46**: 52-66.
- Artero, V., Chavarot-Kerlidou, M. and Fontecave, M. (2011). "Splitting water with cobalt." *Angew. Chem. Int. Ed.* **50**: 7238-7266.
- Avendaño, E., Azens, A., Isidorsson, J., Karmhag, R., Niklasson, G. A. and Granqvist, C. G. (2003). "Optimized nickel-oxide-based electrochromic thin films." *Solid State Ionics* **165**: 169-173.
- Avendano, E., Azens, A., Niklasson, G. and Granqvist, C. (2003). "Nickel-oxide-based electrochromic films with optimized optical properties." *J. Solid State Electrochem.* **8**: 37-39.
- Avendaño, E., Azens, A., Niklasson, G. and Granqvist, C. (2004). "Electrochromism in nickel oxide films containing Mg, Al, Si, V, Zr, Nb, Ag, or Ta." *Sol. Energy Mater. Sol. Cells* **84**: 337-350.
- Azens, A., Isidorsson, J., Karmhag, R. and Granqvist, C. G. (2002). "Highly transparent Ni-Mg and Ni-V-Mg oxide films for electrochromic applications." *Thin Solid Films* **422**: 1-3.
- Bajdich, M., García-Mota, M., Vojvodic, A., Nørskov, J. K. and Bell, A. T. (2013). "Theoretical investigation of the activity of cobalt oxides for the electrochemical oxidation of water." *J. Am. Chem. Soc.* **135**: 13521-13530.

Baktash, E., Zaharieva, I., Schroder, M., Goebel, C., Dau, H. and Thomas, A. (2013). "Cyanamide route to calcium manganese oxide foams for water oxidation." *Dalton Trans.*: 16920–16929.

Bard, A. J. and Fox, M. A. (1995). "Artificial photosynthesis: solar splitting of water to hydrogen and oxygen." *Acc. Chem. Res.* **28**: 141-145.

Barroso, M., Cowan, A. J., Pendlebury, S. R., Grätzel, M., Klug, D. R. and Durrant, J. R. (2011). "The role of cobalt phosphate in enhancing the photocatalytic activity of α -Fe₂O₃ toward water oxidation." *J. Am. Chem. Soc.* **133**: 14868-14871.

Bearden, J. A. and Burr, A. F. (1967). "Reevaluation of X-ray atomic energy levels." *Rev. Mod. Phys.* **39**: 125-142.

Bediako, D. K., Costentin, C., Jones, E. C., Nocera, D. G. and Savéant, J.-M. (2013). "Proton–electron transport and transfer in electrocatalytic films. Application to a cobalt-based O₂-evolution catalyst." *J. Am. Chem. Soc.* **135**: 10492-10502.

Bediako, D. K., Lassalle-Kaiser, B., Surendranath, Y., Yano, J., Yachandra, V. K. and Nocera, D. G. (2012). "Structure-activity correlations in a nickel-borate oxygen evolution catalyst." *J. Am. Chem. Soc.* **134**: 6801-6809.

Bediako, D. K., Surendranath, Y. and Nocera, D. G. (2013). "Mechanistic studies of the oxygen evolution reaction mediated by a nickel–borate thin film electrocatalyst." *J. Am. Chem. Soc.* **135**: 3662-3674.

Bergmann, A., Martinez-Moreno, E., Teschner, D., Chernev, P., Gliech, M., de Araujo, J. F., Reier, T., Dau, H. and Strasser, P. (2015). "Reversible amorphization and the catalytically active state of crystalline Co₃O₄ during oxygen evolution." *Nat Commun* **6**.

Bergmann, A., Zaharieva, I., Dau, H. and Strasser, P. (2013). "Electrochemical water splitting by layered and 3D cross-linked manganese oxides: correlating structural motifs and catalytic activity." *Energy Environ. Sci.* **6**: 2745-2755.

Bledowski, M., Wang, L., Ramakrishnan, A., Bétard, A., Khavryuchenko, O. V. and Beranek, R. (2012). "Visible-light photooxidation of water to oxygen at hybrid TiO₂–polyheptazine photoanodes with photodeposited Co-P_i (CoO_x) cocatalyst." *ChemPhysChem* **13**: 3018-3024.

Brimblecombe, R., Dismukes, G. C., Swiegers, G. F. and Spiccia, L. (2009). "Molecular water-oxidation catalysts for photoelectrochemical cells." *Dalton Trans.*: 9374-9384.

Burke, L. D. and O'Sullivan, E. J. M. (1981). "Oxygen gas evolution on hydrous oxides — An example of three-dimensional electrocatalysis?" *J. Electroanal. Chem.* **117**: 155-160.

Cady, C. W., Crabtree, R. H. and Brudvig, G. W. (2008). "Functional models for the oxygen-evolving complex of photosystem II." *Coord. Chem. Rev.* **252**: 444-455.

Calle-Vallejo, F., Inoglu, N. G., Su, H.-Y., Martinez, J. I., Man, I. C., Koper, M. T. M., Kitchin, J. R. and Rossmeisl, J. (2013). "Number of outer electrons as descriptor for adsorption processes on transition metals and their oxides." *Chem. Sci.* **4**: 1245-1249.

Car, P.-E., Guttentag, M., Baldrige, K. K., Alberto, R. and Patzke, G. R. (2012). "Synthesis and characterization of open and sandwich-type polyoxometalates reveals visible-light-driven water oxidation via POM-photosensitizer complexes." *Green Chemistry* **14**: 1680-1688.

Carmo, M., Fritz, D. L., Mergel, J. and Stolten, D. (2013). "A comprehensive review on PEM water electrolysis." *Int. J. Hydrogen Energy* **38**: 4901-4934.

Chigane, M., Ishikawa, M. and Inoue, H. (2000). "Further XRD characterization of electrochromic nickel oxide thin films prepared by anodic deposition." *Sol. Energy Mater. Sol. Cells* **64**: 65-72.

Chinnasamy, C. N., Narayanasamy, A., Ponpandian, N., Chattopadhyay, K., Shinoda, K., Jeyadevan, B., Tohji, K., Nakatsuka, K., Furubayashi, T. and Nakatani, I. (2001). "Mixed spinel structure in nanocrystalline NiFe₂O₄." *Phys. Rev. B* **63**: 184108.

Coehn, A. and Gläser, M. (1902). "Studien über die Bildung von Metalloxyden I. Über das anodische Verhalten von Kobalt- und Nickel-Lösungen." *Zeitschrift für anorganische Chemie* **33**: 9-24.

Conell, R. S., Corrigan, D. A. and Powell, B. R. (1992). "The electrochromic properties of sputtered nickel oxide films." *Sol. Energy Mater. Sol. Cells* **25**: 301-313.

Conway, B. E. (1991). "Transition from "supercapacitor" to "battery" behavior in electrochemical energy storage." *J. Electrochem. Soc.* **138**: 1539-1548.

Conway, B. E., Birss, V. and Wojtowicz, J. (1997). "The role and utilization of pseudocapacitance for energy storage by supercapacitors." *J. Power Sources* **66**: 1-14.

Conway, B. E. and Pell, W. G. (2003). "Double-layer and pseudocapacitance types of electrochemical capacitors and their applications to the development of hybrid devices." *J. Solid State Electrochem.* **7**: 637-644.

Creutz, C., Schwarz, H. A. and Sutin, N. (1984). "Homogenous catalysis of the photoreduction of water by visible-light. 5. Free-radical route to formation of the metal hydride complex hydrido-aquo-bis(2,2'-bipyridine)cobalt(III)." *J. Am. Chem. Soc.* **106**: 3036-3037.

Dau, H. and Haumann, M. (2003). "X-ray absorption spectroscopy to watch catalysis by metalloenzymes: status and perspectives discussed for the water-splitting manganese complex of photosynthesis." *J. Synchrotron Rad.* **10**: 76-85.

Dau, H. and Haumann, M. (2008). "The manganese complex of photosystem II in its reaction cycle—basic framework and possible realization at the atomic level." *Coord. Chem. Rev.* **252**: 273-295.

- Dau, H., Liebisch, P. and Haumann, M. (2003). "X-ray absorption spectroscopy to analyze nuclear geometry and electronic structure of biological metal centers—potential and questions examined with special focus on the tetra-nuclear manganese complex of oxygenic photosynthesis." *Anal. Bioanal. Chem.* **376**: 562-583.
- Dau, H., Limberg, C., Reier, T., Risch, M., Roggan, S. and Strasser, P. (2010). "The mechanism of water oxidation: from electrolysis via homogeneous to biological catalysis." *ChemCatChem* **2**: 724-761.
- Dau, H. and Zaharieva, I. (2009). "Principles, efficiency, and blueprint character of solar-energy conversion in photosynthetic water oxidation." *Acc. Chem. Res.* **42**: 1861-1870.
- de Vries, A. H., Hozoi, L. and Broer, R. (2003). "Origin of the chemical shift in x-ray absorption near-edge spectroscopy at the Mn K-edge in manganese oxide compounds." *Int. J. Quantum Chem.* **91**: 57-61.
- Delmas, C., Fouassier, C. and Hagemuller, P. (1980). "Structural classification and properties of the layered oxides." *Physica B+C* **99**: 81-85.
- Demourgues, A., Gautier, L., Chadwick, A. V. and Delmas, C. (1997). "EXAFS study of the Jahn-Teller distortion in layered nickel oxyhydroxide." *Nuclear Instruments and Methods in Physics Research Section B: Beam Interactions with Materials and Atoms* **133**: 39-44.
- Dennstedt, W. and Löser, W. (1971). "Zur Kenntnis der Nickelhydroxid-Elektrode—III. Thermogravimetrische Untersuchungen an Nickel(II)-hydroxiden." *Electrochim. Acta* **16**: 429-435.
- Dincă, M., Surendranath, Y. and Nocera, D. G. (2010). "Nickel-borate oxygen-evolving catalyst that functions under benign conditions." *Proc. Natl. Acad. Sci. USA* **107**: 10337-10341.
- Ding, C., Shi, J., Wang, D., Wang, Z., Wang, N., Liu, G., Xiong, F. and Li, C. (2013). "Visible light driven overall water splitting using cocatalyst/BiVO₄ photoanode assisted with the minimized bias." *Phys. Chem. Chem. Phys.* **15**: 4589-4595.
- Doyle, R. L., Godwin, I. J., Brandon, M. P. and Lyons, M. E. G. (2013). "Redox and electrochemical water splitting catalytic properties of hydrated metal oxide modified electrodes." *Phys. Chem. Chem. Phys.* **15**: 13737-13783.
- Du, P. W., Kokhan, O., Chapman, K. W., Chupas, P. J. and Tiede, D. M. (2012). "Elucidating the domain structure of the cobalt oxide water splitting catalyst by X-ray pair distribution function analysis." *J. Am. Chem. Soc.* **134**: 11096-11099.
- Duan, L., Bozoglian, F., Mandal, S., Stewart, B., Privalov, T., Llobet, A. and Sun, L. (2012). "A molecular ruthenium catalyst with water-oxidation activity comparable to that of photosystem II." *Nat. Chem.* **4**: 418-423.
- Dyer, L. D., Borie, B. S. and Smith, G. P. (1954). "Alkali metal-nickel oxides of the type MNiO₂." *J. Am. Chem. Soc.* **76**: 1499-1503.

Ertl, G., Knözinger, H., Schüth, F. and Weitkamp, J. (2008). Handbook of heterogeneous catalysis. Weinheim, Wiley-VCH.

Esswein, A. J., Surendranath, Y., Reece, S. Y. and Nocera, D. G. (2011). "Highly active cobalt phosphate and borate based oxygen evolving catalysts operating in neutral and natural waters." *Energy Environ. Sci.* **4**: 499-504.

Farrow, C. L., Bediako, D. K., Surendranath, Y., Nocera, D. G. and Billinge, S. J. L. (2013). "Intermediate-range structure of self-assembled cobalt-based oxygen-evolving catalyst." *J. Am. Chem. Soc.* **135**: 6403-6406.

Fedorov, F. S., Linnemann, J., Tschulik, K., Giebeler, L., Uhlemann, M. and Gebert, A. (2013). "Capacitance performance of cobalt hydroxide-based capacitors with utilization of near-neutral electrolytes." *Electrochim. Acta* **90**: 166-170.

Finke, R. G., Droege, M., Hutchinson, J. R. and Gansow, O. (1981). "Trivalent heteropolytungstate derivatives: the rational synthesis, characterization, and tungsten-183 NMR spectra of $P_2W_{18}M_4(H_2O)_2O_{68}^{10-}$ (M = cobalt, copper, zinc)." *J. Am. Chem. Soc.* **103**: 1587-1589.

Finke, R. G., Droege, M. W. and Domaille, P. J. (1987). "Trivalent heteropolytungstate derivatives. 3. Rational syntheses, characterization, two-dimensional tungsten-183 NMR, and properties of tungstometallophosphates $P_2W_{18}M_4(H_2O)_2O_{68}^{10-}$ and $P_4W_{30}M_4(H_2O)_2O_{112}^{16-}$ (M = cobalt, copper, zinc)." *Inorg. Chem.* **26**: 3886-3896.

Fischer, M., Werber, M. and Schwartz, P. V. (2009). "Batteries: higher energy density than gasoline?" *Energy Policy* **37**: 2639-2641.

Frei, H. (2009). "Polynuclear photocatalysts in nanoporous silica for artificial photosynthesis." *Chimia* **63**: 721-730.

Friebel, D., Louie, M. W., Bajdich, M., Sanwald, K. E., Cai, Y., Wise, A. M., Cheng, M.-J., Sokaras, D., Weng, T.-C., Alonso-Mori, R., Davis, R. C., Bargar, J. R., Nørskov, J. K., Nilsson, A. and Bell, A. T. (2015). "Identification of highly active Fe sites in (Ni,Fe)OOH for electrocatalytic water splitting." *J. Am. Chem. Soc.* **137**: 1305-1313.

Gardner, G. P., Go, Y. B., Robinson, D. M., Smith, P. F., Hadermann, J., Abakumov, A., Greenblatt, M. and Dismukes, G. C. (2012). "Structural requirements in lithium cobalt oxides for the catalytic oxidation of water." *Angew. Chem. Int. Ed.* **51**: 1616-1619.

Geletii, Y. V., Botar, B., Kögerler, P., Hillesheim, D. A., Musaev, D. G. and Hill, C. L. (2008). "An all-inorganic, stable, and highly active tetra-ruthenium homogeneous catalyst for water oxidation." *Angew. Chem. Int. Ed.* **47**: 3896-3899.

Geletii, Y. V., Huang, Z., Hou, Y., Musaev, D. G., Lian, T. and Hill, C. L. (2009). "Homogeneous light-driven water oxidation catalyzed by a tetra-ruthenium complex with all inorganic ligands." *J. Am. Chem. Soc.* **131**: 7522-7523.

- Gerken, J. B., Landis, E. C., Hamers, R. J. and Stahl, S. S. (2010). "Fluoride-modulated cobalt catalysts for electrochemical oxidation of water under non-alkaline conditions." *ChemSusChem* **3**: 1176-1179.
- Gerken, J. B., McAlpin, J. G., Chen, J. Y. C., Rigsby, M. L., Casey, W. H., Britt, R. D. and Stahl, S. S. (2011). "Electrochemical water oxidation with cobalt-based electrocatalysts from pH 0–14: the thermodynamic basis for catalyst structure, stability, and activity." *J. Am. Chem. Soc.* **133**: 14431-14442.
- Glatzel, P., Smolentsev, G. and Bunker, G. (2009). "The electronic structure in 3d transition metal complexes: Can we measure oxidation states?" *J. Physics: Conf. Series* **190**: 012046.
- Glemser, O. and Einerhand, J. (1950). "Über höhere Nickelhydroxyde." *Zeitschrift für anorganische Chemie* **261**: 26-42.
- Golden, D. C., Chen, C. C. and Dixon, J. B. (1987). "Transformation of birnessite to buserite, todorokite, and manganite under mild hydrothermal treatment." *Clays Clay Miner.* **35**: 271-280.
- Goldner, R. B., Chapman, R. L., Foley, G., Goldner, E. L., Haas, T., Norton, P., Seward, G. and Wong, K. K. (1986). "Recent research related to the development of electrochromic windows." *Solar Energy Materials* **14**: 195-203.
- Gonzalez-Flores, D., Sanchez, I., Zaharieva, I., Klingan, K., Heidkamp, J., Chernev, P., Menezes, P. W., Driess, M., Dau, H. and Montero, M. L. (2015). "Heterogeneous water oxidation: surface activity versus amorphization activation in cobalt phosphate catalysts." *Angew. Chem. Int. Ed.* **54**: 2472-2476.
- Gorlin, Y., Lassalle-Kaiser, B., Benck, J. D., Gul, S., Webb, S. M., Yachandra, V. K., Yano, J. and Jaramillo, T. F. (2013). "In situ X-ray absorption spectroscopy investigation of a bifunctional manganese oxide catalyst with high activity for electrochemical water oxidation and oxygen reduction." *J. Am. Chem. Soc.* **135**: 8525-8534.
- Grahame, D. C. (1947). "The electrical double layer and the theory of electrocapillarity." *Chem. Rev.* **41**: 441-501.
- Granqvist, C. G., Azens, A., Isidorsson, J., Kharrazi, M., Kullman, L., Lindström, T., Niklasson, G. A., Ribbing, C. G., Rönnow, D., Strømme Mattsson, M. and Veszelei, M. (1997). "Towards the smart window: progress in electrochromics." *J. Non-Cryst. Solids* **218**: 273-279.
- Grimaud, A., Carlton, C. E., Risch, M., Hong, W. T., May, K. J. and Shao-Horn, Y. (2013). "Oxygen evolution activity and stability of Ba₆Mn₅O₁₆, Sr₄Mn₂CoO₉, and Sr₆Co₅O₁₅: the influence of transition metal coordination." *J. Phys. Chem. C* **117**: 25926-25932.
- Grimaud, A., May, K. J., Carlton, C. E., Lee, Y.-L., Risch, M., Hong, W. T., Zhou, J. and Shao-Horn, Y. (2013). "Double perovskites as a family of highly active catalysts for oxygen evolution in alkaline solution." *Nat. Commun.* **4**.

- Gust, D., Moore, T. A. and Moore, A. L. (2009). "Solar fuels via artificial photosynthesis." *Acc. Chem. Res.* **42**: 1890-1898.
- Hall, D. S., Lockwood, D. J., Bock, C. and MacDougall, B. R. (2015). "Nickel hydroxides and related materials: a review of their structures, synthesis and properties." *Proceedings. Mathematical, physical, and engineering sciences / the Royal Society.* **471**: 20140792.
- Harriman, A., Pickering, I. J., Thomas, J. M. and Christensen, P. A. (1988). "Metal-oxides as heterogeneous catalysts for oxygen evolution under photochemical conditions." *J. Chem. Soc.-Farad. T 1* **84**: 2795-2806.
- Haumann, M., Müller, C., Liebisch, P., Iuzzolino, L., Dittmer, J., Grabolle, M., Neisius, T., Meyer-Klaucke, W. and Dau, H. (2005). "Structural and oxidation state changes of the photosystem II manganese complex in four transitions of the water oxidation cycle ($S_0 \rightarrow S_1$, $S_1 \rightarrow S_2$, $S_2 \rightarrow S_3$, and $S_{3,4} \rightarrow S_0$) characterized by X-ray absorption spectroscopy at 20 K and room temperature." *Biochemistry* **44**: 1894-1908.
- Higashi, M., Domen, K. and Abe, R. (2012). "Highly stable water splitting on oxynitride TaON photoanode system under visible light irradiation." *J. Am. Chem. Soc.* **134**: 6968-6971.
- Hong, W. T., Risch, M., Stoerzinger, K. A., Grimaud, A., Suntivich, J. and Shao-Horn, Y. (2015). "Toward the rational design of non-precious transition metal oxides for oxygen electrocatalysis." *Energy Environ. Sci.* **8**: 1404-1427.
- Hong, Y.-R., Liu, Z., Al-Bukhari, S. F. B. S. A., Lee, C. J. J., Yung, D. L., Chi, D. and Hor, T. S. A. (2011). "Effect of oxygen evolution catalysts on hematite nanorods for solar water oxidation." *Chem. Commun.* **47**: 10653-10655.
- Huang, Z., Luo, Z., Geletii, Y. V., Vickers, J. W., Yin, Q., Wu, D., Hou, Y., Ding, Y., Song, J., Musaev, D. G., Hill, C. L. and Lian, T. (2011). "Efficient light-driven carbon-free cobalt-based molecular catalyst for water oxidation." *J. Am. Chem. Soc.* **133**: 2068-2071.
- Kalyani, P. and Kalaiselvi, N. (2005). "Various aspects of LiNiO_2 chemistry: A review." *Science and Technology of Advanced Materials* **6**: 689.
- Kanan, M. W. and Nocera, D. G. (2008). "In situ formation of an oxygen-evolving catalyst in neutral water containing phosphate and Co^{2+} ." *Science* **321**: 1072-1075.
- Kanan, M. W., Surendranath, Y. and Nocera, D. G. (2009). "Cobalt-phosphate oxygen-evolving compound." *Chem. Soc. Rev.* **38**: 109-114.
- Kanan, M. W., Yano, J., Surendranath, Y., Dinca, M., Yachandra, V. K. and Nocera, D. G. (2010). "Structure and valency of a cobalt-phosphate water oxidation catalyst determined by in situ X-ray spectroscopy." *J. Am. Chem. Soc.* **132**: 13692-13701.

- Kenney, M. J., Gong, M., Li, Y., Wu, J. Z., Feng, J., Lanza, M. and Dai, H. (2013). "High-performance silicon photoanodes passivated with ultrathin nickel films for water oxidation." *Science* **342**: 836-840.
- Kerr, R. A. and Service, R. F. (2005). "What can replace cheap oil--and when?" *Science* **309**: 101.
- Khayzer, R. S., Mara, M. W., Huang, J., Shelby, M. L., Chen, L. X. and Castellano, F. N. (2012). "Structure and activity of photochemically deposited "CoP_i" oxygen evolving catalyst on titania." *ACS Catalysis* **2**: 2150-2160.
- Kim, S., Tryk, D. A., Antonio, M. R., Carr, R. and Scherson, D. (1994). "In situ x-ray absorption fine structure studies of foreign metal ions in nickel hydrous oxide electrodes in alkaline electrolytes." *J. Phys. Chem.* **98**: 10269-10276.
- Klingan, K., Ringleb, F., Zaharieva, I., Heidkamp, J., Chernev, P., Gonzalez-Flores, D., Risch, M., Fischer, A. and Dau, H. (2014). "Water oxidation by amorphous cobalt-based oxides: volume activity and proton transfer to electrolyte bases." *ChemSusChem* **7**: 1301-1310.
- Koper, M. T. M. (2013). "Theory of multiple proton-electron transfer reactions and its implications for electrocatalysis." *Chem. Sci.* **4**: 2710-2723.
- Koroidov, S., Anderlund, M. F., Styring, S., Thapper, A. and Messinger, J. (2015). "First turnover analysis of water-oxidation catalyzed by Co-oxide nanoparticles." *Energy Environ. Sci.* **8**: 2492-2503.
- Kühn, T.-J., Caliebe, W., Matoussevitch, N., Bönnemann, H. and Hormes, J. (2011). "Site-selective X-ray absorption spectroscopy of cobalt nanoparticles." *Appl. Organomet. Chem.* **25**: 577-584.
- Kurz, R. (2012). *Geld ohne Wert. Grundrisse zu einer Transformation der Kritik der politischen Ökonomie*, Horlemann.
- Landon, J., Demeter, E., İnoğlu, N., Keturakis, C., Wachs, I. E., Vasić, R., Frenkel, A. I. and Kitchin, J. R. (2012). "Spectroscopic characterization of mixed Fe-Ni oxide electrocatalysts for the oxygen evolution reaction in alkaline electrolytes." *ACS Catalysis* **2**: 1793-1801.
- Le Bihan, S. and Figlarz, M. (1972). "Croissance de l'hydroxyde de nickel Ni(OH)₂ à partir d'un hydroxyde de nickel turbostratique." *J. Cryst. Growth* **13-14**: 458-461.
- Lee, S. W., Carlton, C., Risch, M., Surendranath, Y., Chen, S., Furutsuki, S., Yamada, A., Nocera, D. G. and Shao-Horn, Y. (2012). "The nature of lithium battery materials under oxygen evolution reaction conditions." *J. Am. Chem. Soc.* **134**: 16959-16962.
- LeRoy, R. L. (1983). "Industrial water electrolysis - present and future." *Int. J. Hydrogen Energy* **8**: 401-417.

- Levine, S. and Smith, A. L. (1971). "Theory of differential capacity of oxide/aqueous electrolyte interface." *Discussions of the Faraday Society* **52**: 290-301.
- Lewis, N. S. and Nocera, D. G. (2006). "Powering the planet: chemical challenges in solar energy utilization." *Proc. Natl. Acad. Sci. USA* **103**: 15729-15735.
- Li, Z., Luo, W., Zhang, M., Feng, J. and Zou, Z. (2013). "Photoelectrochemical cells for solar hydrogen production: current state of promising photoelectrodes, methods to improve their properties, and outlook." *Energy Environ. Sci.* **6**: 347-370.
- Lieb, D., Zahl, A., Wilson, E. F., Streb, C., Nye, L. C., Meyer, K. and Ivanović-Burmazović, I. (2011). "Water exchange reactivity and stability of cobalt polyoxometalates under catalytically relevant pH conditions: insight into water oxidation catalysis." *Inorg. Chem.* **50**: 9053-9058.
- Liu, X. and Prewitt, C. T. (1990). "High-temperature X-ray diffraction study of Co_3O_4 : Transition from normal to disordered spinel." *Phys. Chem. Miner.* **17**: 168-172.
- Liu, Y. and Nocera, D. G. (2014). "Spectroscopic studies of nanoparticulate thin films of a cobalt-based oxygen evolution catalyst." *J. Phys. Chem. C* **118**: 17060-17066.
- Louie, M. W. and Bell, A. T. (2013). "An investigation of thin-film Ni-Fe oxide catalysts for the electrochemical evolution of oxygen." *J. Am. Chem. Soc.* **135**: 12329-12337.
- Lutterman, D. A., Surendranath, Y. and Nocera, D. G. (2009). "A self-healing oxygen-evolving catalyst." *J. Am. Chem. Soc.* **131**: 3838-3839.
- Lv, H., Geletii, Y. V., Zhao, C., Vickers, J. W., Zhu, G., Luo, Z., Song, J., Lian, T., Musaev, D. G. and Hill, C. L. (2012). "Polyoxometalate water oxidation catalysts and the production of green fuel." *Chem. Soc. Rev.* **41**: 7572-7589.
- Marx, K. (2008 (1876)). *Das Kapital - Kritik der politischen Ökonomie, Erster Band. Der Produktionsprozeß des Kapitals*, MEW 23, Dietz Berlin.
- Mattioli, G., Risch, M., Bonapasta, M. A., Dau, H. and Guidoni, L. (2011). "Protonation states in a cobalt-oxide catalyst for water oxidation: fine comparison of ab initio molecular dynamics and X-ray absorption spectroscopy results." *Phys. Chem. Chem. Phys.* **13**: 15437-15441.
- May, K. J., Carlton, C. E., Stoerzinger, K. A., Risch, M., Suntivich, J., Lee, Y.-L., Grimaud, A. and Shao-Horn, Y. (2012). "Influence of oxygen evolution during water oxidation on the surface of perovskite oxide catalysts." *J. Phys. Chem. Lett.* **3**: 3264-3270.
- McBreen, J. (2007). Nickel hydroxides. *Handbook of Battery Materials*, Wiley-VCH Verlag GmbH: 135-151.
- McClintock, Lisa F. and Blackman, Allan G. (2010). "A structural model for HPO_4^{2-} binding to Co in a water oxidation catalyst." *Chemistry - An Asian Journal* **5**: 756-758.

- McDermott, G. P., Jones, P., Barnett, N. W., Donaldson, D. N. and Francis, P. S. (2011). "Stable Tris(2,2'-bipyridine)ruthenium(III) for chemiluminescence detection." *Anal. Chem.* **83**: 5453-5457.
- McDonald, K. J. and Choi, K. S. (2011). "Photodeposition of Co-based oxygen evolution catalysts on α -Fe₂O₃ photoanodes." *Chem. Mater.* **23**: 1686-1693.
- McEwen, R. S. (1971). "Crystallographic studies on nickel hydroxide and the higher nickel oxides." *J. Phys. Chem.* **75**: 1782-1789.
- Meng, Y., Song, W., Huang, H., Ren, Z., Chen, S.-Y. and Suib, S. L. (2014). "Structure–property relationship of bifunctional MnO₂ nanostructures: highly efficient, ultra-stable electrochemical water oxidation and oxygen reduction reaction catalysts identified in alkaline media." *J. Am. Chem. Soc.* **136**: 11452-11464.
- Midilli, A., Ay, M., Dincer, I. and Rosen, M. A. (2005). "On hydrogen and hydrogen energy strategies: I: current status and needs." *Renewable and Sustainable Energy Reviews* **9**: 255-271.
- Natali, M., Berardi, S., Sartorel, A., Bonchio, M., Campagna, S. and Scandola, F. (2012). "Is [Co₄(H₂O)₂(α -PW₉O₃₄)₂]¹⁰⁻ a genuine molecular catalyst in photochemical water oxidation? Answers from time-resolved hole scavenging experiments." *Chem. Commun.* **48**: 8808-8810.
- Natoli, C. R. (1984). EXAFS and near edge structure III. Chapter: Distance dependence of continuum and bound state of excitonic resonances in X-Ray absorption near edge structure (XANES), Springer.
- Nicholson, W. (1800). "Account of the new electrical or galvanic apparatus of Sig. Alex Volta, and experiments performed with the frame." *Journal of Natural Philosophy, Chemistry, and the Arts* **4**: 179.
- Niklasson, G. A. and Granqvist, C. G. (2007). "Electrochromics for smart windows: thin films of tungsten oxide and nickel oxide, and devices based on these." *J. Mater. Chem.* **17**: 127-156.
- Nocera, D. G. (2009). "Chemistry of personalized solar energy." *Inorg. Chem.* **48**: 10001-10017.
- Nocera, D. G. (2012). "The artificial leaf." *Acc. Chem. Res.* **45**: 767-776.
- Ohlin, C. A., Harley, S. J., McAlpin, J. G., Hocking, R. K., Mercado, B. Q., Johnson, R. L., Villa, E. M., Fidler, M. K., Olmstead, M. M., Spiccia, L., Britt, R. D. and Casey, W. H. (2011). "Rates of water exchange for two cobalt(II) heteropolyoxotungstate compounds in aqueous solution." *Chem. Eur. J.* **17**: 4408-4417.
- Oliva, P., Leonardi, J., Laurent, J. F., Delmas, C., Braconnier, J. J., Figlarz, M., Fievet, F. and Deguibert, A. (1982). "Review of the structure and the electrochemistry of nickel hydroxides and oxy-hydroxides." *J. Power Sources* **8**: 229-255.

Pandya, K. I., O'Grady, W. E., Corrigan, D. A., McBreen, J. and Hoffman, R. W. (1990). "Extended x-ray absorption fine structure investigations of nickel hydroxides." *J. Phys. Chem.* **94**: 21-26.

Penner-Hahn, J. E. (1999). "X-ray absorption spectroscopy in coordination chemistry." *Coord. Chem. Rev.* **190-192**: 1101-1123.

Perron, H., Mellier, T., Domain, C., Roques, J., Simoni, E., Drot, R. and Catalette, H. (2007). "Structural investigation and electronic properties of the nickel ferrite NiFe_2O_4 : a periodic density functional theory approach." *J. Phys.: Condens. Matter* **19**: 346219.

Pilli, S. K., Deutsch, T. G., Furtak, T. E., Turner, J. A., Brown, L. D. and Herring, A. M. (2012). "Light induced water oxidation on cobalt-phosphate (Co-P_i) catalyst modified semi-transparent, porous SiO_2 - BiVO_4 electrodes." *Phys. Chem. Chem. Phys.* **14**: 7032-7039.

Pilli, S. K., Furtak, T. E., Brown, L. D., Deutsch, T. G., Turner, J. A. and Herring, A. M. (2011). "Cobalt-phosphate (Co-P_i) catalyst modified Mo-doped BiVO_4 photoelectrodes for solar water oxidation." *Energy Environ. Sci.* **4**: 5028-5034.

Pintauro, P. N. (2015). "Perspectives on membranes and separators for electrochemical energy conversion and storage devices." *Polymer Reviews* **55**: 201-207.

Post, J. E. (1999). "Manganese oxide minerals: crystal structures and economic and environmental significance." *Proc. Natl. Acad. Sci. USA* **96**: 3447-3454.

Quionero, D., Kaledin, A. L., Kuznetsov, A. E., Geletii, Y. V., Besson, C., Hill, C. L. and Musaev, D. G. (2010). "Computational studies of the geometry and electronic structure of an all-inorganic and homogeneous tetra-Ru-polyoxotungstate catalyst for water oxidation and its four subsequent one-electron oxidized forms." *J. Phys. Chem. A* **114**: 535-542.

Ramesh, T. N., Kamath, P. V. and Shivakumara, C. (2006). "Classification of stacking faults and their stepwise elimination during the disorder \rightarrow order transformation of nickel hydroxide." *Acta Crystallographica Section B-Structural Science* **62**: 530-536.

Reece, S. Y., Hamel, J. A., Sung, K., Jarvi, T. D., Esswein, A. J., Pijpers, J. J. H. and Nocera, D. G. (2011). "Wireless solar water splitting using silicon-based semiconductors and earth-abundant catalysts." *Science* **334**: 645-648

Rehr, J. J. and Albers, R. C. (2000). "Theoretical approaches to X-ray absorption fine structure." *Rev. Mod. Phys.* **72**: 621-654.

Rehr, J. J., Kas, J. J., Prange, M. P., Sorini, A. P., Takimoto, Y. and Vila, F. (2009). "Ab initio theory and calculations of X-ray spectra." *Comptes Rendus Physique* **10**: 548-559.

Risch, M. (2011). Structure-function relations in water-oxidizing cobalt oxides investigated by X-ray absorption spectroscopy PhD, Free University Berlin.

- Risch, M., Grimaud, A., May, K. J., Stoerzinger, K. A., Chen, T. J., Mansour, A. N. and Shao-Horn, Y. (2013). "Structural changes of cobalt-based perovskites upon water oxidation investigated by EXAFS." *J. Phys. Chem. C* **117**: 8628-8635.
- Risch, M., Khare, V., Zaharieva, I., Gerencser, L., Chernev, P. and Dau, H. (2009). "Cobalt-oxo core of a water-oxidizing catalyst film." *J. Am. Chem. Soc.* **131**: 6936-6937.
- Risch, M., Klingan, K., Fischer, A. and Dau, H. (2013). The structure of water-oxidizing cobalt oxide film and comparison to the photosynthetic manganese complex. *Photosynthesis Research for Food, Fuel and Future*. T. Kuang, C. Lu and L. Zhang. Heidelberg, Springer: 257-261.
- Risch, M., Klingan, K., Heidkamp, J., Ehrenberg, D., Chernev, P., Zaharieva, I. and Dau, H. (2011). "Nickel-oxido structure of a water-oxidizing catalyst film." *Chem. Commun.* **47**: 11912-11914.
- Risch, M., Klingan, K., Ringleb, F., Chernev, P., Zaharieva, I., Fischer, A. and Dau, H. (2012). "Water oxidation by electrodeposited cobalt oxides - role of anions and redox-inert cations in structure and function of the amorphous catalyst." *ChemSusChem* **5**: 542-549.
- Risch, M., Klingan, K., Zaharieva, I. and Dau, H. (2014). Water oxidation by Co-based oxides with molecular properties. *Molecular Water Oxidation Catalysts*. A. Llobet, Wiley-VCH.
- Risch, M., Ringleb, F., Khare, V., Chernev, P., Zaharieva, I. and Dau, H. (2009). "Characterisation of a water-oxidizing Co-film by XAFS." *J. Physics: Conf. Series* **190**: 012167.
- Risch, M., Ringleb, F., Kohlhoff, M., Bogdanoff, P., Chernev, P., Zaharieva, I. and Dau, H. (2015). "Water oxidation by amorphous cobalt-based oxides: in situ tracking of redox transitions and mode of catalysis." *Energy Environ. Sci.* **8**: 661-674.
- Risch, M., Shevchenko, D., Anderlund, M. F., Styring, S., Heidkamp, J., Lange, K. M., Thapper, A. and Zaharieva, I. (2012). "Atomic structure of cobalt-oxide nanoparticles active in light-driven catalysis of water oxidation." *Int. J. Hydrogen Energy* **37**: 8878-8888.
- Ritorto, M. D., Anderson, T. M., Neiwert, W. A. and Hill, C. L. (2004). "Decomposition of A-type sandwiches. Synthesis and characterization of new polyoxometalates incorporating multiple d-electron-centered units." *Inorg. Chem.* **43**: 44-49.
- Robinson, D. M., Go, Y. B., Mui, M., Gardner, G., Zhang, Z., Mastrogiovanni, D., Garfunkel, E., Li, J., Greenblatt, M. and Dismukes, G. C. (2013). "Photochemical water oxidation by crystalline polymorphs of manganese oxides: structural requirements for catalysis." *J. Am. Chem. Soc.* **135**: 3494-3501.
- Romero, I., Rodríguez, M., Sens, C., Mola, J., Kollipara, M. R., Francàs, L., Mas-Marza, E., Escriche, L., Llobet, A. (2008). "Ru complexes that can catalytically oxidize water to molecular dioxygen." *Inorg. Chem.* **47**: 1824-1834.

Rosa, V. M., Santos, M. B. F. and DaSilva, E. P. (1995). "New materials for electrolysis diaphragms." *Int. J. Hydrogen Energy* **20**: 697-700.

Rougier, A., Delmas, C. and Chadwick, A. V. (1995). "Non-cooperative Jahn-Teller effect in LiNiO₂: An EXAFS study." *Solid State Commun.* **94**: 123-127.

Sala, X., Romero, I., Rodríguez, M., Escriche, L. and Llobet, A. (2009). "Molecular catalysts that oxidize water to dioxygen." *Angew. Chem. Int. Ed.* **48**: 2842-2852.

Sartorel, A., Carraro, M., Scorrano, G., Zorzi, R. d., Geremia, S., McDaniel, N. D., Bernhard, S. and Bonchio, M. (2008). "Polyoxometalate embedding of a tetraruthenium(IV)-oxo-core by template-directed metalation of [γ -SiW₁₀O₃₆]⁸⁻: a totally inorganic oxygen-evolving catalyst." *J. Am. Chem. Soc.* **130**: 5006-5007.

Schaefer, F., Mertin, M. and Gorgoi, M. (2007). "KMC-1: a high resolution and high flux soft X-ray beamline at BESSY." *Rev. Sci. Instrum.* **78**: 123102.

Schiwon, R., Klingan, K., Dau, H. and Limberg, C. (2014). "Shining light on integrity of a tetracobalt-polyoxometalate water oxidation catalyst by X-ray spectroscopy before and after catalysis." *Chem. Commun.* **50**: 100-102.

Seabold, J. A. and Choi, K. S. (2011). "Effect of a cobalt-based oxygen evolution catalyst on the stability and the selectivity of photo-oxidation reactions of a WO₃ photoanode." *Chem. Mater.* **23**: 1105-1112.

Sheehan, S. W., Thomsen, J. M., Hintermair, U., Crabtree, R. H., Brudvig, G. W. and Schmittenmaer, C. A. (2015). "A molecular catalyst for water oxidation that binds to metal oxide surfaces." *Nat. Commun.* **6**: 6469.

Shevchenko, D., Anderlund, M. F., Thapper, A. and Styring, S. (2011). "Photochemical water oxidation with visible light using a cobalt containing catalyst." *Energy Environ. Sci.* **4**: 1284-1287.

Singh, A., Chang, S. L. Y., Hocking, R. K., Bach, U. and Spiccia, L. (2013). "Highly active nickel oxide water oxidation catalysts deposited from molecular complexes." *Energy Environ. Sci.* **6**: 579-586.

Sivula, K., Le Formal, F. and Grätzel, M. (2011). "Solar water splitting: progress using hematite (α -Fe₂O₃) photoelectrodes." *ChemSusChem* **4**: 432-449.

Smith, R. D. L., Prévot, M. S., Fagan, R. D., Trudel, S. and Berlinguette, C. P. (2013). "Water oxidation catalysis: electrocatalytic response to metal stoichiometry in amorphous metal oxide films containing iron, cobalt, and nickel." *J. Am. Chem. Soc.* **135**: 11580-11586.

Smith, W. L. and Hobson, A. D. (1973). "The structure of cobalt oxide, Co₃O₄." *Acta Crystallographica Section B* **29**: 362-363.

- Srinivasan, V. and Weidner, J. W. (2002). "Capacitance studies of cobalt oxide films formed via electrochemical precipitation." *J. Power Sources* **108**: 15-20.
- Steinmiller, E. M. P. and Choi, K. S. (2009). "Photochemical deposition of cobalt-based oxygen evolving catalyst on a semiconductor photoanode for solar oxygen production." *Proc. Natl. Acad. Sci. USA* **106**: 20633-20636.
- Stracke, J. J. and Finke, R. G. (2011). "Electrocatalytic water oxidation beginning with the cobalt polyoxometalate $[\text{Co}_4(\text{H}_2\text{O})_2(\text{PW}_9\text{O}_{34})_2]^{10-}$: identification of heterogeneous CoO_x as the dominant catalyst." *J. Am. Chem. Soc.* **133**: 14872-14875.
- Stracke, J. J. and Finke, R. G. (2013). "Water oxidation catalysis beginning with $2.5 \mu\text{M}$ $[\text{Co}_4(\text{H}_2\text{O})_2(\text{PW}_9\text{O}_{34})_2]^{10-}$: investigation of the true electrochemically driven catalyst at $\geq 600 \text{ mV}$ overpotential at a glassy carbon electrode." *ACS Catalysis* **3**: 1209-1219.
- Su, H.-Y., Gorlin, Y., Man, I. C., Calle-Vallejo, F., Norskov, J. K., Jaramillo, T. F. and Rossmeisl, J. (2012). "Identifying active surface phases for metal oxide electrocatalysts: a study of manganese oxide bi-functional catalysts for oxygen reduction and water oxidation catalysis." *Phys. Chem. Chem. Phys.* **14**: 14010-14022.
- Suga, M., Akita, F., Hirata, K., Ueno, G., Murakami, H., Nakajima, Y., Shimizu, T., Yamashita, K., Yamamoto, M., Ago, H. and Shen, J.-R. (2015). "Native structure of photosystem II at 1.95 Å resolution viewed by femtosecond X-ray pulses." *Nature* **517**: 99-103.
- Sun, K., McDowell, M. T., Nielander, A. C., Hu, S., Shaner, M. R., Yang, F., Brunschwig, B. S. and Lewis, N. S. (2015). "Stable solar-driven water oxidation to $\text{O}_2(\text{g})$ by Ni-oxide-coated silicon photoanodes." *J. Phys. Chem. Lett.* **6**: 592-598.
- Sun, K., Park, N., Sun, Z., Zhou, J., Wang, J., Pang, X., Shen, S., Noh, S. Y., Jing, Y., Jin, S., Yu, P. K. L. and Wang, D. (2012). "Nickel oxide functionalized silicon for efficient photo-oxidation of water." *Energy Environ. Sci.* **5**: 7872-7877.
- Sun, K., Saadi, F. H., Lichterman, M. F., Hale, W. G., Wang, H.-P., Zhou, X., Plymale, N. T., Omelchenko, S. T., He, J.-H., Papadantonakis, K. M., Brunschwig, B. S. and Lewis, N. S. (2015). "Stable solar-driven oxidation of water by semiconducting photoanodes protected by transparent catalytic nickel oxide films." *Proc. Natl. Acad. Sci. USA* **112**: 3612-3617.
- Suntivich, J., May, K. J., Gasteiger, H. A., Goodenough, J. B. and Shao-Horn, Y. (2011). "A perovskite oxide optimized for oxygen evolution catalysis from molecular orbital principles." *Science* **334**: 1383-1385.
- Surendranath, Y., Dinca, M. and Nocera, D. G. (2009). "Electrolyte-dependent electrosynthesis and activity of cobalt-based water oxidation catalysts." *J. Am. Chem. Soc.* **131**: 2615-2620.
- Surendranath, Y., Kanan, M. W. and Nocera, D. G. (2010). "Mechanistic studies of the oxygen evolution reaction by a cobalt-phosphate catalyst at neutral pH." *J. Am. Chem. Soc.* **132**: 16501-16509.

Surendranath, Y., Lutterman, D. A., Liu, Y. and Nocera, D. G. (2012). "Nucleation, growth, and repair of a cobalt-based oxygen evolving catalyst." *J. Am. Chem. Soc.* **134**: 6326-6336.

Svensson, J. S. E. M. and Granqvist, C. G. (1986). "Electrochromic hydrated nickel oxide coatings for energy efficient windows: optical properties and coloration mechanism." *Appl. Phys. Lett.* **49**: 1566-1568.

Swierk, J. R. and Mallouk, T. E. (2013). "Design and development of photoanodes for water-splitting dye-sensitized photoelectrochemical cells." *Chem. Soc. Rev.* **42**: 2357-2387.

Symes, M. D., Lutterman, D. A., Teets, T. S., Anderson, B. L., Breen, J. J. and Nocera, D. G. (2013). "Photo-active cobalt cubane model of an oxygen-evolving catalyst." *ChemSusChem* **6**: 65-69.

Symes, M. D., Surendranath, Y., Lutterman, D. A. and Nocera, D. G. (2011). "Bidirectional and unidirectional PCET in a molecular model of a cobalt-based oxygen-evolving catalyst." *J. Am. Chem. Soc.* **133**: 5174-5177.

Tanaka, S., Annaka, M. and Sakai, K. (2012). "Visible light-induced water oxidation catalyzed by molybdenum-based polyoxometalates with mono- and dicobalt(III) cores as oxygen-evolving centers." *Chem. Commun.* **48**: 1653-1655.

Teo, B. (1986). EXAFS: Basic principles and data analysis. Berlin, Germany, Springer Verlag.

Thomas, M. G. S. R., Bruce, P. G. and Goodenough, J. B. (1985). "Lithium mobility in the layered oxide $\text{Li}_{1-x}\text{CoO}_2$." *Solid State Ionics* **17**: 13-19.

Trasatti, S. (1980). "Electrocatalysis by oxides - Attempt at a unifying approach." *J. Electroanal. Chem.* **111**: 125-131.

Trasatti, S. (1984). "Electrocatalysis in the anodic evolution of oxygen and chlorine." *Electrochim. Acta* **29**: 1503-1512.

Trasatti, S. (1999a). "1799-1999: Alessandro Volta's 'electric pile': two hundred years, but it doesn't seem like it." *J. Electroanal. Chem.* **460**: 1.

Trasatti, S. (1999b). "Water electrolysis: who first?" *J. Electroanal. Chem.* **476**: 90-91.

Trotochaud, L., Ranney, J. K., Williams, K. N. and Boettcher, S. W. (2012). "Solution-cast metal oxide thin film electrocatalysts for oxygen evolution." *J. Am. Chem. Soc.* **134**: 17253-17261.

Trotochaud, L., Young, S. L., Ranney, J. K. and Boettcher, S. W. (2014). "Nickel-iron oxyhydroxide oxygen-evolution electrocatalysts: the role of intentional and incidental iron incorporation." *J. Am. Chem. Soc.* **136**: 6744-6753.

- Vickers, J. W., Lv, H., Sumliner, J. M., Zhu, G., Luo, Z., Musaev, D. G., Geletii, Y. V. and Hill, C. L. (2013). "Differentiating homogeneous and heterogeneous water oxidation catalysis: confirmation that $[\text{Co}_4(\text{H}_2\text{O})_2(\alpha\text{-PW}_9\text{O}_{34})_2]^{10-}$ is a molecular water oxidation catalyst." *J. Am. Chem. Soc.* **135**: 14110-14118.
- Villars, P., Karin Cenzual and Roman Gladyshevskii (2015). Handbook of Inorganic Substances. Berlin, Boston, De Gruyter.
- Wackernagel, M., Schulz, N. B., Deumling, D., Linares, A. C., Jenkins, M., Kapos, V., Monfreda, C., Loh, J., Myers, N., Norgaard, R. and Randers, J. (2002). "Tracking the ecological overshoot of the human economy." *Proc. Natl. Acad. Sci. USA* **99**: 9266-9271.
- Wang, D., Li, R., Zhu, J., Shi, J., Han, J., Zong, X. and Li, C. (2012). "Photocatalytic water oxidation on BiVO_4 with the electrocatalyst as an oxidation cocatalyst: essential relations between electrocatalyst and photocatalyst." *J. Phys. Chem. C* **116**: 5082-5089.
- Wang, L.-P. and Van Voorhis, T. (2011). "Direct-coupling O_2 bond forming a pathway in cobalt oxide water oxidation catalysts." *J. Phys. Chem. Lett.* **2**: 2200-2204.
- Wiechen, M., Zaharieva, I., Dau, H. and Kurz, P. (2012). "Layered manganese oxides for water-oxidation: alkaline earth cations influence catalytic activity in a photosystem II-like fashion." *Chem. Sci.* **3**: 2330-2339.
- Wood, R. M. and Palenik, G. J. (1998). "Bond valence sums in coordination chemistry: a simple method for calculating the oxidation state of cobalt in complexes containing only Co-O bonds." *Inorg. Chem.* **37**: 4149-4151.
- Xiao, X., Liu, X., Zhao, H., Chen, D., Liu, F., Xiang, J., Hu, Z. and Li, Y. (2012). "Facile shape control of Co_3O_4 and the effect of the crystal plane on electrochemical performance." *Adv. Mater.* **24**: 5762-5766.
- Yagi, M., Syouji, A., Yamada, S., Komi, M., Yamazaki, H. and Tajima, S. (2009). "Molecular catalysts for water oxidation toward artificial photosynthesis." *Photochem. Photobiol. Sci.* **8**: 139-147.
- Yamamoto, T. (2008). "Assignment of pre-edge peaks in K-edge X-ray absorption spectra of 3d transition metal compounds: electric dipole or quadrupole?" *X-Ray Spectrom.* **37**: 572-584.
- Yamazaki, H., Shouji, A., Kajita, M. and Yagi, M. (2010). "Electrocatalytic and photocatalytic water oxidation to dioxygen based on metal complexes." *Coord. Chem. Rev.* **254**: 2483-2491.
- Yang, X., Takada, K., Itose, M., Ebina, Y., Ma, R., Fukuda, K. and Sasaki, T. (2008). "Highly swollen layered nickel oxide with a trilayer hydrate structure." *Chem. Mater.* **20**: 479-485.
- Ye, H., Park, H. S. and Bard, A. J. (2011). "Screening of electrocatalysts for photoelectrochemical water oxidation on W-doped BiVO_4 photocatalysts by scanning electrochemical microscopy." *J. Phys. Chem. C* **115**: 12464-12470.

Yeo, B. S. and Bell, A. T. (2012). "In situ Raman study of nickel oxide and gold-supported nickel oxide catalysts for the electrochemical evolution of oxygen." *J. Phys. Chem. C* **116**: 8394-8400.

Yilanci, A., Dincer, I. and Ozturk, H. K. (2009). "A review on solar-hydrogen/fuel cell hybrid energy systems for stationary applications." *Prog. Energy Combust. Sci.* **35**: 231-244.

Yin, Q., Tan, J. M., Besson, C., Geletii, Y. V., Musaev, D. G., Kuznetsov, A. E., Luo, Z., Hardcastle, K. I. and Hill, C. L. (2010). "A fast soluble carbon-free molecular water oxidation catalyst based on abundant metals." *Science* **328**: 342-345.

Young, K. J., Martini, L. A., Milot, R. L., Snoeberger Iii, R. C., Batista, V. S., Schmuttenmaer, C. A., Crabtree, R. H. and Brudvig, G. W. (2012). "Light-driven water oxidation for solar fuels." *Coord. Chem. Rev.* **256**: 2503-2520.

Zaharieva, I., Chernev, P., Risch, M., Klingan, K., Kohlhoff, M., Fischer, A. and Dau, H. (2012). "Electrosynthesis, functional and structural characterization of a water-oxidizing manganese oxide." *Energy Environ. Sci.* **5**: 7081-7089.

Zaharieva, I., Najafpour, M. M., Wiechen, M., Haumann, M., Kurz, P. and Dau, H. (2011). "Synthetic manganese-calcium oxides mimic the water-oxidizing complex of photosynthesis functionally and structurally." *Energy Environ. Sci.* **4**: 2400-2408.

Zeng, K. and Zhang, D. (2010). "Recent progress in alkaline water electrolysis for hydrogen production and applications." *Prog. Energy Combust. Sci.* **36**: 307-326.

Zhang, C., Chen, C., Dong, H., Shen, J.-R., Dau, H. and Zhao, J. (2015). "A synthetic Mn₄Ca-cluster mimicking the oxygen-evolving center of photosynthesis." *Science* **348**: 690-693.

Zhang, M., de Respinis, M. and Frei, H. (2014). "Time-resolved observations of water oxidation intermediates on a cobalt oxide nanoparticle catalyst." *Nat. Chem.* **6**: 362-367.

Zhang, Y., Lu, Z. G., Chung, C. Y. and Zhu, M. (2007). "Kinetics of Li⁺ transport and capacity retention capability of HT-LiCoO₂ films." *Phys. Scr.* **2007**: 38.

Zhong, D. K., Cornuz, M., Sivula, K., Grätzel, M. and Gamelin, D. R. (2011). "Photo-assisted electrodeposition of cobalt-phosphate (Co-P_i) catalyst on hematite photoanodes for solar water oxidation." *Energy Environ. Sci.* **4**: 1759-1764.

Zhu, G., Glass, E. N., Zhao, C., Lv, H., Vickers, J. W., Geletii, Y. V., Musaev, D. G., Song, J. and Hill, C. L. (2012). "A nickel containing polyoxometalate water oxidation catalyst." *Dalton Trans.* **41**: 13043-13049.

Zou, X. and Zhang, Y. (2015). "Noble metal-free hydrogen evolution catalysts for water splitting." *Chem. Soc. Rev.* **44**: 5148-5180.

List of publications

2015 **Electrosynthesis of biomimetic manganese-calcium oxides for water-oxidation catalysis – atomic structure and functionality for variation of the calcium content**

Diego González-Flores, Ivelina Zaharieva, Jonathan Heidkamp, Petko Chernev, Elías Martínez-Moreno, Chiara Pasquini, Mohammad Reza Mohammadi, Katharina Klingan, Ulrich Gernet, Anna Fischer, Holger Dau

ChemSusChem (Impact Factor: 7.7), accepted

2015 **Hydrophobic nanoreactor soft-templating –A supramolecular approach to yolk@shell materials**

Amandine Guet, Caren Göbel, Katharina Klingan, Michael Lublow, Tobias Reier, Ulla Vainio, Ralph Kraehnert, Helmut Schlaad, Peter Strasser, Ivelina Zaharieva, Holger Dau, Matthias Driess, Jörg Polte, Anna Fischer

Advanced Functional Materials (Impact Factor 11.8), <http://dx.doi.org/10.1002/adfm.201502388>

2015 **Heterogeneous water oxidation: surface activity versus amorphization activation in cobalt phosphate catalysts**

Diego González-Flores, Irene Sánchez, Ivelina Zaharieva, Katharina Klingan, Jonathan Heidkamp, Petko Chernev, Prashanth W. Menezes, Matthias Driess, Holger Dau, Mavis L. Montero

Angewandte Chemie International Edition (Impact Factor 11.3), 54(8):2472–2476, <http://dx.doi.org/10.1002/anie.201409333>

2014 **Water oxidation by amorphous cobalt-based oxides: volume activity and proton transfer to electrolyte bases**

Katharina Klingan, Franziska Ringleb, Ivelina Zaharieva, Jonathan Heidkamp, Petko Chernev, Diego Gonzalez-Flores, Marcel Risch, Anna Fischer, Holger Dau

ChemSusChem (Impact Factor: 7.7), 7(5):1301-10, <http://dx.doi.org/10.1002/cssc.201301019>

2014 Water oxidation by Co-based oxides with molecular properties

Marcel Risch, Katharina Klingan, Ivelina Zaharieva, Holger Dau

In book: *Molecular Water Oxidation Catalysis: A Key Topic for New Sustainable Energy Conversion Schemes* (ed A. Llobet), John Wiley & Sons, Ltd, Chichester, UK. ISBN: 9781118413371, <http://dx.doi.org/10.1002/9781118698648.ch9>

2014 Electronic and molecular structures of the active-site H-cluster in [FeFe]-hydrogenase determined by site-selective X-ray spectroscopy and quantum chemical calculations

Camilla Lambertz, Petko Chernev, Katharina Klingan, Nils Leidl, Kajsa G.V. Sigfridsson, Thomas Happe, Michael Haumann

Chemical Science (Impact Factor: 9.2), 5(3):1187-1203, <http://dx.doi.org/10.1039/c3sc52703d>

2014 Shining light on integrity of a tetracobalt-polyoxometalate water oxidation catalyst by X-ray spectroscopy before and after catalysis

Rafael Schiwon, Katharina Klingan, Holger Dau, Christian Limberg

Chemical Communications (Impact Factor: 6.8), 50(1):100-102, <http://dx.doi.org/10.1039/c3cc46629a>

2013 The structure of a water-oxidizing cobalt oxide film and comparison to the photosynthetic manganese complex

Marcel Risch, Katharina Klingan, Anna Fischer, Holger Dau

In book: *Photosynthesis Research for Food, Fuel and the Future*, Chapter: 53, Springer Berlin Heidelberg. ISBN: 9783642320330, http://dx.doi.org/10.1007/978-3-642-32034-7_53

2012 Electrosynthesis, functional, and structural characterization of a water-oxidizing manganese oxide

Ivelina Zaharieva, Petko Chernev, Marcel Risch, Katharina Klingan, Mike Kohlhoff, Anna Fischer, Holger Dau

Energy & Environmental Science (Impact Factor: 20.5), 5(5):7081-9, <http://dx.doi.org/10.1039/c2ee21191b>

2012 Water oxidation by electrodeposited cobalt oxides—role of anions and redox-inert cations in structure and function of the amorphous catalyst

Marcel Risch, Katharina Klingan, Franziska Ringleb, Petko Chernev, Ivelina Zaharieva, Anna Fischer, Holger Dau

ChemSusChem (Impact Factor: 7.7), 5(3):542-549, <http://dx.doi.org/10.1002/cssc.201100574>

2011 Nickel-oxido structure of a water-oxidizing catalyst film

Marcel Risch, Katharina Klingan, Jonathan Heidkamp, David Ehrenberg, Petko Chernev, Ivelina Zaharieva, Holger Dau

Chemical Communications (Impact Factor: 6.8), 47(43):11912-11914, <http://dx.doi.org/10.1039/c1cc15072c>

Selbstständigkeitserklärung

Hiermit versichere ich, dass die vorliegende Dissertation eigenständig und ausschließlich unter Verwendung der angegebenen Hilfsmittel angefertigt wurde. Alle Literaturquellen sind als solche kenntlich gemacht. Die vorliegende Arbeit ist in dieser oder anderer Form zuvor nicht als Prüfungsarbeit zur Begutachtung vorgelegt worden.

Berlin, den 15. Dezember 2015

.....
Katharina Klingan